

Electrical anisotropy and shear-resistant topology in the quasi one-dimensional van-der-Waals material  $\alpha\text{-Bi}_4\text{Br}_4$ 

Jonathan Karl Hofmann

Information
Band / Volume 117
ISBN 978-3-95806-869-8



Forschungszentrum Jülich GmbH Peter Grünberg Institut (PGI) Quantum Nanoscience (PGI-3)

# Electrical anisotropy and shear-resistant topology in the quasi one-dimensional van-der-Waals material $\alpha$ -Bi $_4$ Br $_4$

Jonathan Karl Hofmann

Schriften des Forschungszentrums Jülich Reihe Information / Information

Bibliografische Information der Deutschen Nationalbibliothek. Die Deutsche Nationalbibliothek verzeichnet diese Publikation in der Deutschen Nationalbibliografie; detaillierte Bibliografische Daten sind im Internet über http://dnb.d-nb.de abrufbar.

Herausgeber Forschungszentrum Jülich GmbH

und Vertrieb: Zentralbibliothek, Verlag

52425 Jülich

Tel.: +49 2461 61-5368 Fax: +49 2461 61-6103 zb-publikation@fz-juelich.de

www.fz-juelich.de/zb

Umschlaggestaltung: Grafische Medien, Forschungszentrum Jülich GmbH

Druck: Grafische Medien, Forschungszentrum Jülich GmbH

Copyright: Forschungszentrum Jülich 2025

Schriften des Forschungszentrums Jülich Reihe Information / Information, Band / Volume 117

D 82 (Diss. RWTH Aachen University, 2025)

ISSN 1866-1777 ISBN 978-3-95806-869-8

Vollständig frei verfügbar über das Publikationsportal des Forschungszentrums Jülich (JuSER) unter www.fz-juelich.de/zb/openaccess.



This is an Open Access publication distributed under the terms of the <u>Creative Commons Attribution License 4.0</u>, which permits unrestricted use, distribution, and reproduction in any medium, provided the original work is properly cited.

steals the morn upon the night, And melts the shades away: So Truth does Fancy's charm dissolve, And rising Reason puts to flight The fumes that did the mind involve, Restoring intellectual day.

> Charles Jennens and George Frideric Handel L'Allegro, 11 Penseroso ed 11 Moderato (HWV 55)

#### **Abstract**

The quasi one-dimensional van-der-Waals material  $\alpha$ -Bi<sub>4</sub>Br<sub>4</sub> crystallizes in a monoclinic crystal structure consisting of covalently bonded Bi<sub>4</sub>Br<sub>4</sub> chains parallel to the lattice vector  $\underline{b}$ . The van-der-Waals interaction connects these chains to form 2D layers. These layers are then stacked in  $\underline{c}$ -direction.  $\alpha$ -Bi<sub>4</sub>Br<sub>4</sub> features AB stacking. In contrast to well-known van-der-Waals materials such as WTe<sub>2</sub> or MoS<sub>2</sub>,  $\alpha$ -Bi<sub>4</sub>Br<sub>4</sub> features two van-der-Waals gaps. A monolayer of  $\alpha$ -Bi<sub>4</sub>Br<sub>4</sub> is a quantum spin Hall insulator.

 $\alpha$ -Bi<sub>4</sub>Br<sub>4</sub> showing the same surface can be prepared by mechanical exfoliation. Electrical transport measurements are preformed using a four-tip scanning tunneling microscope (STM) to investigate the anisotropy of the resistivity of  $\alpha$ -Bi<sub>4</sub>Br<sub>4</sub>. A four-tip STM integrates four individual STMs into a tight unit, in order to enable transport measurements on surfaces. The piezo-drives of the individual STMs allow flexible tip configurations to be set up as needed for a transport measurement. Furthermore, a four-tip STM still can image the surface by scanning a single tip and perform scanning tunneling microscopy. Due to the small resistances measured here, the exact calibration of the voltage measurement in the four-tip STM became a major issue for the measurement. This calibration is therefore addressed in chapter 3.

Chapter 5 presents a modified surface structure of the  $\alpha$ -Bi<sub>4</sub>Br<sub>4</sub>(001) surface. Atomically resolved STM images show that the parallel Bi<sub>4</sub>Br<sub>4</sub> chains exhibit a mutual shift different from the one expected for this surface. Density functional theory calculations by *Mingqian Zheng and Jin-Jian Zhou* indicate, that a monolayer of this new structure is also a quantum spin Hall insulator. The modified structure arises due to shear stress which is able to shift the parallel chains with respect to each other because neighboring chains are only connected by weak van-der-Waals forces.

Two different methods to disentangle the resistivity tensor  $\rho$  of  $\alpha$ -Bi<sub>4</sub>Br<sub>4</sub> are implemented: In chapter 6, the in-plane anisotropy is first measured on the (001) surface of a bulk  $\alpha$ -Bi<sub>4</sub>Br<sub>4</sub> crystal. For this, two measurements of the resistance in a square tip configuration are used. Then, the value of resistivity in b-direction is determined using a distance-dependent measurement on a thin flake. Assuming that the influence of the off-diagonal element of the resistivity tensor can be neglected, an in-plane anisotropy of  $A = \rho_{\rm a}/\rho_{\rm b} = 6.4 \pm 0.5$  is obtained at room temperature. Furthermore, the anisotropy normal to the ab plane is found to be  $A_z = \rho_z/\rho_b = 1300$ . Thus, the resistivity in <u>b</u>-direction, parallel to the chains, is the smallest, as expected from the crystal structure. At 77 K,  $A = 5.0 \pm 0.3$  and  $A_z = 6500$  were measured. Chapter 7 demonstrates an alternative approach to disentangle the three elements on the main diagonal of the resistivity tensor  $\rho$ when the off-diagonal element is neglected. Here, the tips are positioned in the corners of a large, rectangular flake. The anisotropy can then be obtained by the Bierwagen-Simon method. While it is possible to demonstrate the disentanglement of the three components of the resistivity tensor, the in-plane anisotropy A measured with the second method was substantially smaller than the result obtained before. The origin of this discrepancy is traced back to imperfections of the flake.

# Kurzfassung

Das quasi-eindimensionale van-der-Waals-Material  $\alpha$ -Bi $_4$ Br $_4$  kristallisiert in einer monoklinen Kristallstruktur von kovalent gebundenen Ketten aus Bi $_4$ Br $_4$ -Einheiten, die parallel zum Gittervektor  $\underline{b}$  verlaufen. Diese Ketten sind durch die van-der-Waals-Wechselwirkung zu 2D-Lagen verbunden, die in  $\underline{c}$ -Richtung gestapelt sind.  $\alpha$ -Bi $_4$ Br $_4$  zeigt eine AB-Stapelung. Im Gegensatz zu bekannten van-der-Waals-Materialien wie WTe $_2$  oder MoS $_2$  weist  $\alpha$ -Bi $_4$ Br $_4$  zwei van-der-Waals gaps auf. Eine Monolage  $\alpha$ -Bi $_4$ Br $_4$  ist ein Quanten-Spin-Hall-Isolator.

Die  $(0\,0\,1)$ -Ebene ist eine Spaltfläche von  $\alpha$ -Bi $_4$ Br $_4$ -Volumenkristallen. Die gleiche Oberfläche zeigen  $\alpha$ -Bi $_4$ Br $_4$ -Flocken, die durch mechanische Exfolierung hergestellt werden können. Zur Untersuchung der Anisotropie der Resistivität von  $\alpha$ -Bi $_4$ Br $_4$  werden elektrische Transportmessungen mit einem Vier-Spitzen-Rastertunnelmikroskop (STM) durchgeführt. Ein Vier-Spitzen-STM integriert vier einzelne STMs zu einer zusammenhängenden Einheit, um Transportmessungen auf Oberflächen zu ermöglichen. Die Piezomotoren der einzelnen STMs erlauben es, flexible Spitzenkonfigurationen für die Transportmessung einzustellen. Zusätzlich kann mit dem Vier-Spitzen-STM die Oberfläche abgebildet und Rastertunnelspektroskopie durchgeführt werden. Aufgrund der kleinen hier gemessenen Widerstände ist die genaue Kalibrierung der Spannungsmessung des Vier-Spitzen-STMs von großer Bedeutung. Daher wird diese Kalibrierung in Kapitel 3 im Detail dargestellt.

In Kapitel 5 wird eine modifizierte Oberflächenstruktur von  $\alpha$ -Bi $_4$ Br $_4$ (001) vorgestellt. Atomar aufgelöste STM-Aufnahmen zeigen, dass die parallelen Bi $_4$ Br $_4$ -Ketten eine andere gegenseitige Verschiebung aufweisen, als auf dieser Oberfläche zu erwarten wäre. Dichtefunktionaltheorie-Berechnungen von *Mingqian Zheng und Jin-Jian Zhou* deuten darauf hin, dass eine Monolage dieser neuen Struktur ebenfalls ein Quanten-Spin-Hall-Isolator ist. Die modifizierte Struktur entsteht durch eine Scherspannung, welche die parallelen Ketten gegeneinander verschieben kann, da benachbarte Ketten nur durch schwache van-der-Waals-Kräfte aneinander gebunden sind.

Zur Bestimmung der Elemente des Resistivitätstensors  $\rho$  von  $\alpha$ -Bi<sub>4</sub>Br<sub>4</sub> werden zwei verschiedene Methoden verwendet: In Kapitel 6 wird zunächst die Anisotropie in der (001)-Ebene eines α-Bi<sub>4</sub>Br<sub>4</sub>-Volumenkristalls gemessen. Dazu werden zwei Messungen in einer quadratischen Spitzenanordnung durchgeführt. Anschließend wird der Wert der Resistivität in b-Richtung mittels einer abstandsabhängigen Messung auf einer dünnen Flocke bestimmt. Unter der Annahme, dass die Nichtdiagonalelemente des Resistivitätstensors  $\rho$  von  $\alpha$ -Bi $_4$ Br $_4$  vernachlässigt werden können, ergibt sich bei Raumtemperatur die Anisotropie  $A=\rho_{\rm a}/\rho_{\rm b}=6.4\pm0.5$ . Zusätzlich wird die Anisotropie senkrecht zur ab-Ebene bestimmt:  $A_z = \rho_z/\rho_b = 1300$ . Somit ist die Resistivität in  $\underline{b}$ -Richtung parallel zu den Ketten am kleinsten, wie auch von der Kristallstruktur zu erwarten ist. Bei 77 K werden  $A = 5.0 \pm 0.3$  und  $A_z = 6500$  gemessen. In Kapitel 7 wird ein alternativer Ansatz zur Entflechtung der drei Hauptdiagonalelemente von  $\rho$  vorgestellt, bei dem die Nichtdiagonalelemente ebenfalls vernachlässigt werden. Die Spitzen werden hier in den Ecken einer großen, rechteckigen Flocke positioniert. Die Anisotropie kann dann mit der Bierwagen-Simon-Methode bestimmt werden. Obwohl es möglich ist, die Entflechtung der drei Komponenten auf der Hauptdiagonalen des Resistivitätstensors zu demonstrieren, ist der gemessene Wert der Oberflächenanisotropie A erheblich kleiner als der zuvor erhaltene. Diese Diskrepanz wird auf Unvollkommenheiten der Flocke zurückgeführt.

# List of publications

- Jonathan K. Hofmann, Hoyeon Jeon, Saban M. Hus, Yuqi Zhang, Mingqian Zheng, Tobias Wichmann, An-Ping Li, Jin-Jian Zhou, Zhiwei Wang, Yugui Yao, Bert Voigtländer, F. Stefan Tautz, and Felix Lüpke, Shear-resistant topology in the quasi-one-dimensional van der Waals material Bi<sub>4</sub>Br<sub>4</sub>, Physical Review B 111, 245415, (2025) doi.org/10.1103/tdp5-wmqc
- 2. <u>Jonathan K. Hofmann</u>\*, Serhii Kovalchuk\*, Yuqi Zhang, Vasily Cherepanov, Timofey Balashov, Zhiwei Wang, Yugui Yao, Irek Morawski, F. Stefan Tautz, Felix Lüpke, Bert Voigtländer, *Disentangling three anisotropic resistivities of the topological insulator*  $\alpha$ - $Bi_{\perp}Br_{\perp}$ , in preparation

<sup>\*</sup> These authors contributed equally.

# **List of Acronyms**

2D two-dimensional3D three-dimensionalac alternating current

ADC Analogue-to-digital converter

ARPES Angle-resolved photoemission spectroscopy

**DAC** Digital-to-analogue converter

dc direct current

DFT Density functional theoryDSP Digital signal processorFEM Finite-element modeling

**HOTI** Higher-order topological insulator

RT Room temperature SOI Silicon-on-insulator SOC Spin-orbit coupling

STI Strong topological insulator

STM Scanning tunneling microscope/microscopy

STS Scanning tunneling spectroscopy TCI Topological crystalline insulator

**QSH** Quantum spin Hall

WTI Weak topological insulator

# **Contents**

Ι.	intro	duction		1
2.	Resi	stance ar	nd resistivity	3
2.1. Four probe resistance of isotropic samples				4
		2.1.1. B	Bulk	4
		2.1.2. T	Thin film samples	6
	2.2.	Crystal p	physics and anisotropic resistivity	9
	2.3.	The Was	sscher Transformation	11
		2.3.1. E	Example: Derivation of an equation for $R_{\rm arb}$ on an anisotropic sample	13
	2.4.	Anisotro	py and resistance	14
		2.4.1. S	heet resistivity of anisotropic samples	15
		2.4.2. V	Van-der-Pauw equation for anisotropic samples	16
	2.5.	Methods	for disentangling the elements of the resistivity tensor	17
		2.5.1. B	Sierwagen-Simon method	17
		2.5.2. M	Montgomery method	19
	2.6.	Correction	on Factors	20
		2.6.1. E	Equidistant, linear tip placement on a sample of finite thickness .	20
		2.6.2. R	dectangular tip geometry next to an insulating boundary	22
		2.6.3. R	tectangular tip geometry on a laterally infinite sample of finite	
		tl	hickness	27
		2.6.4. C	Cuboid and rectangular samples	30
	2.7.	Permuta	tion of tips	31
3.	Mea	suring re	sistances with a four-tip STM	35
-	3.1.		-tip STM	35
			The Black Box	37
		3.1.2. T	The four-tip STMs used in this thesis	39
	3.2.		ion measurement electronics	39
	3.3.	Measurer	ment of resistances with the four-tip STM	41
	3.4.		try of four-probe measurements	43
	3.5.		nties in the resistance measurements	44
1	The	higher o	rder topological insulator $lpha$ -Bi $_4$ Br $_4$	47
₹.		_	, ,	47
			1 0	49
				51
				54

5.		Shear-resistant topology in quasi one-dimensional van-der-Waals material						
	Bi <sub>4</sub> Br <sub>4</sub>		57					
	5.1. Method	${ m ls}$	57					
	5.2. Results		57					
	5.2.1.	Surface structure	57					
	5.2.2.	Electronic structure	60					
	5.3. Origin	of the $b/3$ structure	65					
	5.4. Résume	ś <sup>'</sup>	67					
6.	_	ng the anisotropic resistivity tensor of the topological insulator	60					
	$\alpha$ -Bi <sub>4</sub> Br <sub>4</sub>	A DID	69					
		sistivity tensor of $\alpha$ -Bi <sub>4</sub> Br <sub>4</sub>						
		Diagonalization of the resistivity tensor						
		Contribution of the off-diagonal element						
		${\bf l}$ to disentangle the diagonal components of the resistivity tensor .						
		Determination of the anisotropy $A$ (Square Measurement)						
		Determination of the resistivity $\rho_{\rm b}$ (Linear Measurement)						
	6.2.3.	Determination of $\rho_a$ and $\rho_z$						
	-	8						
	6.4. Results		76					
		Sizes of the relevant flakes						
	6.4.2.	Room Temperature	80					
	6.4.3.	Low temperature transport on flakes	84					
	6.5. Discuss	sion	88					
	6.6. Résume	<u> </u>	90					
7.	_	the anisotropy of an $lpha ext{-Bi}_4Br_4$ flake by the Bierwagen-Simon	01					
	method		91					
		agling the three components of an orthorombic resistivity tensor $$ .	91					
		sion						
		Effect of moving the tips out of the corners						
		Influence of flake defects of flake E						
	7.4. Résum	<u> </u>	98					
8.	Conclusion	and outlook	99					
Bil	bliography		101					
9.	Acknowledg	ment	113					
Α.	Solving Ea.	2.50 and 2.51 for the three components of the resistivity tensor	or115					
		,						
В.	Calibration		117					
		AC Calibration	117					
		Salibration						
		ting the offset of the current amplifier						
	K/L ('alibra	ting the gain of the voltage-probe mode	112					

	B.5. Calibrating the offset of the bias voltage in the Black Box	119
C.	Contacting procedure	<b>12</b> 1
D.	Crystal structures of Bi <sub>4</sub> I <sub>4</sub>	123
E.	Extended data: evaluation of the band gap of the $\it b/3$ structure	125
F.	Diagonalisation of the conductivity tensor	127
G.	Extended data: Damage to flake E	129

# 1. Introduction

Following a steady path of miniaturization has enabled the semiconductor industry to produce microprocessors and other devices with increased performance. Currently, the smallest metal-to-metal distance on microprocessors is 24 nm [1, 2]. Thus, there is still some "room at the bottom" [3] left for further improvement by miniaturization [2]. Quantum computing is an alternative to the conventional design of microprocessors that uses elemental quantum states for computations, the qubits [4]. A qubit is a two-state system, that is generally in a superposition of its two bases states [5, pp. 35-38]. This superposition state is described by two complex numbers per qubit. These complex numbers, however, are analogue signals making a quantum computer more susceptible to noise [5, pp. 35-38]. Nevertheless, similar to error-correction code in conventional computing [5, p. 34], it is possible to design error-corrected quantum computers [5, p. 52]. However, error-corrected quantum computers lead to a very high overhead due to the large number of qubits needed to form a single, error-corrected logical qubit [5, pp. 72-79].

One way to create fault-tolerant qubits is through topological quantum computing. [4, 6]. Majorana bound states are a possible way to realize fault-tolerant quantum qubits. These Majorana bound states can be realized by combining topological insulators with superconductors [7]. In simple terms, topological insulators combine an insulating interior with a conductive surface [8]. Topological insulators are described by topological invariants, e.g., the  $\mathbb{Z}_2$  topological invariant, which can take the values  $\nu=0$  and  $\nu=1$  for a topologically trivial and non-trivial insulator, respectively [8, 9]. A two-dimensional (2D) topological insulator (quantum spin Hall insulator) hosts topologically protected edge states at its boundaries, that allow ballistic transport [10]. These edge states also exhibit spin-momentum locking, i.e. spin-up electrons are transported in one direction, while spin-down electrons are transported in the opposite direction [8]. A three-dimensional (3D) topological insulator hosts topologically non-trivial surface states on some or all of its faces [8, 11].

In the present thesis, the quasi-one dimensional van-der-Waals material  $\alpha$ -Bi<sub>4</sub>Br<sub>4</sub> is studied [12].  $\alpha$ -Bi<sub>4</sub>Br<sub>4</sub> is a member of the emerging group of bismuth halides, Bi<sub>4</sub>X<sub>4</sub> (X = I,Br), that all consist of quasi-one dimensional, covalently bonded Bi<sub>4</sub>X<sub>4</sub> chains [12–14]. Parallel chains, connected by van-der-Walls forces, form 2D layers, which are then stacked to form the quasi-one dimensional crystal structures [12, 13, 15]. Thus, the bismuth halides feature two van-der-Waals gaps. The topological properties of the different bismuth halide compounds depend critically on their stacking:  $\beta$ -Bi<sub>4</sub>I<sub>4</sub> features AA stacking [13, 16] and has been shown to be a weak topological insulator featuring topologically protected surface states only on certain facets [16, 17].  $\alpha$ -Bi<sub>4</sub>I<sub>4</sub> features AA' stacking [14]. The topological properties of  $\alpha$ -Bi<sub>4</sub>I<sub>4</sub> are somewhat unclear at present: Based on angle-resolved photoemission spectroscopy supported by theory,  $\alpha$ -Bi<sub>4</sub>I<sub>4</sub> was classified as trivial insulator [18]. Recent scanning tunneling microscopy results, however, indicate that  $\alpha$ -Bi<sub>4</sub>I<sub>4</sub> is a 3D quantum spin Hall insulator [19].  $\alpha$ -Bi<sub>4</sub>Br<sub>4</sub>, on the other hand, features AB stacking [12, 14, 20] and was recently shown to be a higher-order

topological insulator [20–22]. As a higher order topological insulator,  $\alpha$ -Bi<sub>4</sub>Br<sub>4</sub> features so-called *hinge states*: topologically protected one-dimensional states that extent along the line at which certain crystal facets meet. A monolayer of  $\alpha$ -Bi<sub>4</sub>Br<sub>4</sub> has been shown to be a quantum spin hall insulator [20, 23]. The edge states of  $\alpha$ -Bi<sub>4</sub>Br<sub>4</sub> were observed in scanning tunneling spectroscopy up until room temperature [20]. Due to its quasi-one dimensional crystal structure,  $\alpha$ -Bi<sub>4</sub>Br<sub>4</sub> is expected to exhibit a pronounced electrical anisotropy [12].

To investigate the anisotropy, a four-tip scanning tunneling microscope is used [24]. A (single-tip) scanning tunneling microscope (STM) is a tool to investigate surfaces of conductive materials in real space [25, 26]. An image of the surface is obtained by scanning it with a metallic tip which is placed in so called tunneling contact. The purpose of the four-tip STM is to use the nano-positioning capabilities of an STM and its metallic STM tip to measure the resistance of surfaces and bulk crystals. In order to separate the contact resistance from the surface or bulk resistance that is to be measured, the four-point method is used [27, 28]: The tips are navigated into a predefined configuration (e.g. linear equidistant) and then contacted to the surface. From the measured resistance and the tip configuration, the resistivity of an isotropic sample can then be obtained [27, 28]. This treatment can be extended to anisotropic samples, where multiple independent measurements are needed to disentangle all components of the resistivity tensor [29, 30].

In the present thesis, the anisotropy of the resistivity of  $\alpha$ -Bi<sub>4</sub>Br<sub>4</sub> arising from its quasi-one dimensional crystal structure is studied. The methods used to disentangle the elements of the resistivity tensor  $\underline{\rho}$  are presented together with the results in chapters 6 and 7. In chapter 2, the relationship between measured resistance and the elements of the resistivity tensor is discussed in detail. Furthermore, correction factors needed for measurements on finite samples are introduced in chapter 2. Correction factors for a rectangular tip configuration, which could not be found in the literature are also derived. Chapter 3 introduces the four-tip STM. During the measurements, the correct calibration of the voltage measurement became a major concern; consequently, chapter 3 focuses on the electronics of the four-tip STM and their calibration. In chapter 4, the higher-order, quasi-one dimensional topological insulator  $\alpha$ -Bi<sub>4</sub>Br<sub>4</sub> is introduced.

Chapter 5 presents a modified surface structure of the  $\alpha$ -Bi<sub>4</sub>Br<sub>4</sub>(001). Atomically resolved STM images show that the parallel Bi<sub>4</sub>Br<sub>4</sub> chains exhibit a mutual shift different from the one expected for this surface [12]. Density functional theory calculations by *Mingqian Zheng and Jin-Jian Zhou* indicate, that a monolayer of this new structure is also a quantum spin hall insulator [31]. The modified structure arises due to shear stress which is able to shift the parallel chains with respect to each other because neighboring chains are only connected by weak van-der-Waals forces.

# 2. Resistance and resistivity

The four-probe method to measure resistivities with four equal distant electrodes was first proposed by Wenner [27]. This method features a line of four equidistantly placed (distance s) electrodes at an equal depth b in the soil. The two outer electrodes inject a dc-current, the two inner electrodes measure the voltage drop. Wenner obtained for the resistivity

$$\rho = \frac{4\pi sR}{1 + \frac{2}{\sqrt{1 + 4\left(\frac{s}{b}\right)^2}} - \frac{1}{\sqrt{1 + \left(\frac{s}{b}\right)^2}}}.$$
 (2.1)

The measurements were intended e.g. to analyze the return current path of electrical railways, or to find natural resources [27]. In geophysics, the electrode configuration originally proposed by Wenner is referred to as the *Wenner method* [32] or the *Wenner configuration* [33, pp. 128-173].

Valdes introduced a version of the Wenner method into condensed matter physics, originally to assist in the manufacturing of germanium transistors [28]. Figure 2.1 shows a simple model of such a four-probe measurement and an equivalent circuit. Since the four-probe method excludes the effect of the contact resistance by virtue of the two potential measuring contacts [27, 28], it is ideally suited for materials such as semiconductors (or earth), where good (i.e. low resistance, ohmic) contacts are difficult to establish. In principle, this is a variation of the long known four-terminal sensing method, first introduced by Thomson [34, pp. 891-892; 35; 36], with the key difference being a physical separation between the current injection contacts and the voltage probing contacts.

When computing the resistivity  $\rho$  from the four-probe resistance  $R_{4P}$  [(see Fig. 2.1(b)] two geometric effects have to be taken into account:

- 1. The contact configuration, and
- 2. The finite extent of the sample.

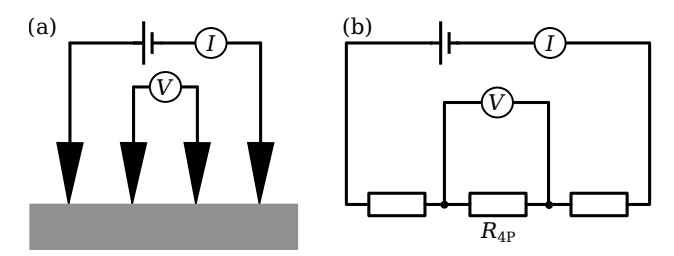


Fig. 2.1.: (a) A simple model of a four-probe resistance measurement according to Wenner and Valdes [27, 28]. (b) The equivalent circuit of a four-probe resistance measurement. The two outer resistors contain both the resistance of the sample and the contact resistances. The resistance obtained from the four-probe measurement is  $R_{\rm 4P}$ .

Even on infinite samples, geometrical configuration factors arise, describing the contact layout [e.g. Eq.(2.1)]. For example, there are specific factors linking the resistance R to the resistivity  $\rho$  for the in-line and for the square contact configuration. These factors can be derived from the potential of the current injection tips placed in an infinitely large 2D or 3D sample [27, 28, 37]. Anisotropic materials are described with the resistivity tensor, having up to six independent elements [38, Chapter 11], further complicating the relationship between geometry, resistivity, and the measured resistance R. Moreover, real samples are not infinitely large. To contend with this problem, correction factors exist [28, 37, 39].

Since all transport measurements were carried out using a four-tip STM (see the following chapter), contacts will also be referred to as *tips*.

# 2.1. Four probe resistance of isotropic samples

#### 2.1.1. Bulk

For an arbitrary tip setup [40; 41, pp. 6-7], the resistance is given by

$$R_{\text{arb,3D}} = \frac{\Delta V_{23}}{I_{14}} = \frac{V_2 - V_3}{I_{14}} = \frac{\rho}{2\pi} \left( \underbrace{\left[ \frac{1}{|\underline{s}_2 - \underline{s}_1|} - \frac{1}{|\underline{s}_2 - \underline{s}_4|} \right]}_{V_2} - \underbrace{\left[ \frac{1}{|\underline{s}_3 - \underline{s}_1|} - \frac{1}{|\underline{s}_3 - \underline{s}_4|} \right]}_{V_3} \right). \tag{2.2}$$

Figure 2.2(a) depicts an arbitrary tip geometry, where the position vectors  $\underline{s}_i$  are measured from an arbitrary point  $\underline{r}_0$  on the surface. In addition to the numbering from 1 to 4, the tips are labeled with I and V according to their function in the four probe measurement described by Eq. (2.2). The voltage drop  $\Delta V$  is measured across tips 2 and 3, while the current flows from tip 1  $(I^+)$  to 4  $(I^-)$ . When the injection voltage is applied across tips 1 and 4 as shown in Fig. 2.1, the voltage drop is positive. The current then flows from tip 1 to tip 4, so the resistance is also positive  $R_{\rm arb,3D}$ . In Eq. 2.2, the terms in parenthesis can be understood as follows: The first term,  $|\underline{s}_2 - \underline{s}_1|^{-1}$ , describes the potential at tip 2 due to the current injected at tip 1. The second term,  $-|\underline{s}_2 - \underline{s}_4|^{-1}$ , describes the potential at tip 2 due to the current flowing through tip 4, etc. Using Eq. (2.2) expressions for the resistance measured in a particular configuration of the tips on the surface of a semi infinite sample can be derived. Eq. (2.2) can be derived from the electrostatic potential of a point source, placed on the surface of a infinitely large object, see e.g. [27; 42, Chapter 3; 43, Chapter 2; 44, Chapter 9].

<sup>&</sup>lt;sup>1</sup>Obviously, this uses the technical definition of current direction. If the majority carriers in the sample are electrons, the physical current direction would be inverse.

<sup>&</sup>lt;sup>2</sup>By exchanging the two current injection tips or the two voltage probing tips with each other, the sign of the resistance can be reversed, see section 2.7. Furthermore, during the experiment, current flowing into the sample will be counted as negative current by the electronics. Thus, during data analysis, the magnitude of  $R_{4P}$  is considered.

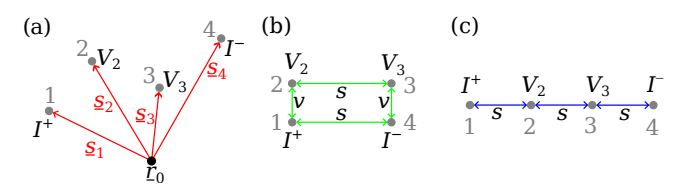


FIG. 2.2.: Tip geometries after [40]. Current is always injected from Tip 1  $(I^+)$  to tip 4  $(I^-)$ . (a) An arbitrary placement of tips. (b) The tips are placed in a rectangle with the distance s between the two current injection tips and the distance v between a current injection tip and its neighboring voltage probing tip. (c) An in-line (or linear) tip geometry with an equal distance s between all neighboring tips.

#### 2.1.1.1. Calculating resistances for rectangular tip configurations

In the following, an equation describing the resistance measured in a rectangular tip configuration as shown in Fig. 2.2(b) will be derived. Formulas describing different tip geometries can easily be derived using the same methods. The rectangular tip configuration is particularly important for correction factors, which will be calculated in section 2.6. Here and in the following, s always refers to the distance between the two current injection contacts; v refers to the distance between a given current injection tip and a voltage probing tip.

First, the potentials  $V_2$  and  $V_3$  below the voltage probing tips 2 and 3 are calculated. From the schematic in Fig. 2.2(b), the inter-tip distances needed can be obtained:

$$|\underline{s}_3 - \underline{s}_1| = \sqrt{s^2 + v^2}, \quad |\underline{s}_3 - \underline{s}_4| = v, \quad |\underline{s}_2 - \underline{s}_1| = v, \quad |\underline{s}_2 - \underline{s}_4| = \sqrt{s^2 + v^2}. \tag{2.3}$$

As all tips are placed on the surface of the semi-infinite bulk sample, all vectors  $\underline{s}_i$  lie in the plane with z = 0. Plugging these inter-tip distances into Eq. (2.2), the potentials

$$V_2 = \frac{\rho I}{2\pi} \left( \frac{1}{v} - \frac{1}{\sqrt{v^2 + s^2}} \right) \tag{2.4}$$

$$V_3 = \frac{\rho I}{2\pi} \left( \frac{1}{\sqrt{v^2 + s^2}} - \frac{1}{v} \right) \tag{2.5}$$

can be found. From this, the potential voltage drop  $\Delta V = V_2 - V_3$  and the resistance R

$$\Delta V = \frac{\rho I}{2\pi} \left( \frac{2}{v} - \frac{2}{\sqrt{v^2 + s^2}} \right) \tag{2.6}$$

$$R = \frac{\rho}{2\pi} \left( \frac{2}{v} - \frac{2}{\sqrt{v^2 + s^2}} \right) \tag{2.7}$$

can be found. Solving for  $\rho$  yields

$$\rho = \frac{2\pi v}{2 - \frac{2}{\sqrt{1 + \frac{s^2}{v^2}}}} R. \tag{2.8}$$

#### 2.1.1.2. Further tip configurations

By letting s = v, the well known equation for a square tip configuration [32, 39]

$$\rho = \frac{2\pi s}{2 - \sqrt{2}}R\tag{2.9}$$

can be recovered. Another important tip configuration is the in-line, equidistant tip configuration, as shown in Fig. 2.2(c). In this case, the relationship between measured resistance R and the resistivity  $\rho$  is given by [28, 32; 41, p. 7]

$$\rho = 2\pi sR. \tag{2.10}$$

Note the linear dependence of  $\rho$  on s for bulk samples. In practice, of course, the inverse relation is much more important:  $R \propto 1/s$  in Eq. (2.9) and Eq. (2.10). Consequently, for a material with a given resistivity  $\rho$ , the measured resistance R increases with decreasing s. Hence, measuring R as a function of s can serve as a simple test for 2D (see below) or 3D behavior. In addition, if  $\rho$  is small, the resistivity R might be difficult to measure at large inter-tip distances s. The last consideration has to be balanced with the increased relative uncertainty at small inter-tip distances (see section 3.5).

#### 2.1.2. Thin film samples

Sufficiently thin samples can be described as an infinitely large two-dimensional sheet. What exactly constitutes a "sufficiently thin sample" will be discussed in section 2.6.1. In the 2D case, the electrostatic potential is no longer described by the 1/r-function, but by the  $\ln(r)$ -function. As a result, the resistance of an arbitrary tip configuration is described by [40: 41, p. 10]

$$R = \frac{\rho}{2\pi t} \ln \left( \underbrace{\frac{|\underline{s}_2 - \underline{s}_1|}{|\underline{s}_2 - \underline{s}_4|}}_{V_2} \cdot \underbrace{\frac{|\underline{s}_3 - \underline{s}_4|}{|\underline{s}_3 - \underline{s}_1|}}_{V_3} \right), \tag{2.11}$$

where t is the thickness of the sheet. Figure 2.2(a) illustrates also the tip positions for the 2D case. Similar to Eq. (2.2), Eq. (2.11) can be derived from the electrostatic potential of a point source. However, in this case the point source is placed within a two-dimensional sheet, see e.g. [42, Chapter 3; 43, Chapter 2; 44, Chapter 9].

In the 2D case, instead of the resistivity  $\rho$ , the sheet resistivity  $R_{\rm s}$ 

$$R_{\rm s} = \frac{\rho}{t} \tag{2.12}$$

is often used. In the literature, sometimes the symbol  $\rho_{\rm 2D}$ , or indeed  $\sigma_{\rm 2D}$  for the sheet conductivity, are used. In this work, however, the symbol  $R_{\rm s}$  is used for better clarity. The SI-unit of  $R_{\rm s}$  is  $\Omega$ . In practice, the unit  $\Omega \square^{-1}$  is used [40].

As the distances listed in Eq. (2.3) were calculated for the surface of a bulk sample (with constant z), they can also be applied in the 2D case. Substituting Eq. (2.3) into Eq. (2.11) yields

$$\rho = \frac{2\pi tR}{\ln\left(1 + \left(\frac{v}{s}\right)^2\right)} \tag{2.13}$$

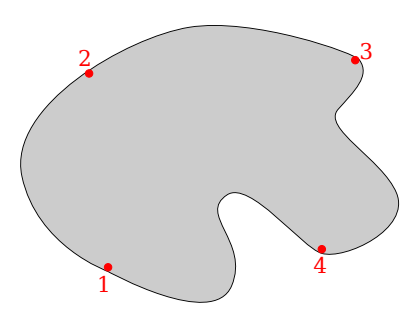


Fig. 2.3.: A thin, singly connected sample with arbitrary shape for the van-der-Pauw method.

The contacts are indicated with red circles.

for the case of a rectangle [c.f. Fig. 2.2(b)] on a 2D sheet. When s=v, one easily obtains the known result [32] for a square:

$$\rho = \frac{2\pi tR}{\ln(2)}.\tag{2.14}$$

For a linear, equidistant tip setup, it holds that [32, 37; 41, pp. 9-10; 45]:

$$\rho = \frac{\pi t R}{\ln(2)}.\tag{2.15}$$

Comparing Eq. (2.14) and (2.15) to the ones found for the 3D case [Eq. (2.9) and Eq. (2.10)] in the previous section, in the 2D case there is obviously no dependence on the inter-tip distance s. Thus, for the geometries discussed here and a given resistivity  $\rho$ , the resistance is constant. As already discussed above, this allows for a rather straightforward way to distinguish between 2D and 3D samples.

#### 2.1.2.1. The van-der-Pauw method

With the van-der-Pauw method, the resistivity  $\rho$  of finite, thin samples of arbitrary shape can be found. The tips have to be placed at the sample boundary and the sample has to be singly connected, i.e. it must not have holes [46, 47]. A sketch of such a sample is shown in Fig. 2.3.

According to van der Pauw, it then holds [32, 46, 47]:

$$1 = \exp\left(-\pi R_{12,34} \frac{t}{\rho}\right) + \exp\left(-\pi R_{23,41} \frac{t}{\rho}\right). \tag{2.16}$$

 $R_{12,34}$  is the resistance measured when current is injected from tip 1 to tip 2, and the corresponding voltage drop is measured across tips 3 and 4. Should there be a hole in the sample, this equality is only fulfilled for specific contact positions, which would have to be found using simulations before the measurement [48]. The resistivity can then be found from [46; 41, pp. 14-18; 32, 47]

$$\rho = \frac{\pi t}{\ln(2)} \frac{R_{12,34} + R_{23,41}}{2} f, \tag{2.17}$$

where f has to satisfy

$$\frac{R_{12,34} - R_{23,41}}{R_{12,34} + R_{23,41}} = \frac{f}{\ln(2)} \operatorname{arccosh}\left(\frac{\exp\left(\frac{\ln(2)}{f}\right)}{2}\right). \tag{2.18}$$

If the sample is symmetrical and two contacts are placed on the symmetry line, Eq. (2.17) simplifies to

$$\rho = \frac{\pi t}{\ln(2)} R,\tag{2.19}$$

with  $R = R_{12.34} = R_{23.41}$ .

Following van der Pauw [47], the relationship between Eq. (2.17) and (2.18) and Eq. (2.16) can be easily seen. First, the shorthand

$$\xi_1 = \pi R_{12,34}t$$
 and  $\xi_2 = \pi R_{23,41}t$  (2.20)

is defined. Thus Eq. (2.16) becomes

$$1 = \exp\left(-\frac{\xi_1}{\rho}\right) + \exp\left(-\frac{\xi_2}{\rho}\right). \tag{2.21}$$

Eq. (2.20) can also be written as (this corresponds to adding a "zero")

$$\xi_1 = \frac{1}{2} (\xi_1 + \xi_2 - \xi_2 + \xi_1) = \frac{1}{2} [(\xi_1 + \xi_2) + (\xi_1 - \xi_2)]$$
 (2.22)

$$\xi_2 = \frac{1}{2} (\xi_1 + \xi_2 - \xi_1 + \xi_2) = \frac{1}{2} [(\xi_1 + \xi_2) - (\xi_1 - \xi_2)]. \tag{2.23}$$

Plugging into Eq. (2.16) yields

$$\exp\left(-\frac{\xi_1 + \xi_2}{2\rho}\right) \cdot \left[\exp\left(-\frac{\xi_1 - \xi_2}{2\rho}\right) + \exp\left(\frac{\xi_1 - \xi_2}{2\rho}\right)\right] = 1 \tag{2.24}$$

$$\exp\left(-\frac{\xi_1 + \xi_2}{2\rho}\right) \cosh\left(\frac{\xi_1 - \xi_2}{2\rho}\right) = \frac{1}{2}.\tag{2.25}$$

One can now define

$$\frac{\xi_1 + \xi_2}{2\rho} = \frac{\ln(2)}{f},\tag{2.26}$$

which already recovers Eq. (2.17). Replacing the exponent of Eq. (2.25) and the numerator of the argument of the cosh-function with Eq. (2.26) yields

$$\exp\left(-\frac{\ln(2)}{f}\right)\cosh\left(\frac{\xi_1 - \xi_2}{\xi_1 + \xi_2}\frac{\ln(2)}{f}\right) = \frac{1}{2},\tag{2.27}$$

which checks Eq. (2.18) [47].

The factor f can be found graphically, e.g. from plots in references [41, p. 15; 46; 47]. Furthermore, Hurand  $et\,al$  published a convenient fit to f, with adequate precision for most practical purposes [49]. f can also be calculated from iterative methods, e.g.

[50]. On the other hand, Eq. (2.16) can also be solved for  $\rho$  using numerical root finding procedures. This requires a good starting value. The latter procedure together with the one introduced by Hurand *et al.* [49] is used for this work.

For finite samples, that possess at least one symmetry plane, Thorsteinsson et al. proposed a variation of the van-der-Pauw method, based on the realization that for such a sample, the current density flowing across the mirror plane vanishes if the contacts are placed on the mirror plane [51]. The authors assume a micro-four-point probe, which features four in-line contacts with a pitch of a few 10 µm. While a varying inter-tip distance s cannot induce a positioning error in the van-der-Pauw method, shifting contacts away from the sample edge still induces an error [49, 52, 53]. Consequently, placing the tip array not exactly on the symmetry line will induce a positioning error as well. Thorsteinsson et al. analyzed this positioning error for a linear probe array on different sample geometries (e.g. square and rectangular samples) by calculating the lines of equal error, the isoerror contours. This analysis provides a guideline for the selection of the optimal symmetry plane for the measurement. For example, on a rectangular sample, the optimal symmetry plane is the one parallel to the short edges of the sample [51]. Since each tip is navigated independently in a four-tip STM, applying the method by Thorsteinsson et al. here could introduce additional errors, if some tips are placed at one side of the symmetry line, and others are placed at the other side. Furthermore, while this method allows to measure the resistivity  $\rho$  without the need for correction factors, it prohibits a simple check of the 2D or 3D nature of a sample by changing the inter-tip distance s. Furthermore, placing the tips at the circumference of the sample can permit large inter-tip distances, which in turn might change the character of the sample from 3D to 2D (see section 2.6.1 below). Due to the positioning error, the conditions for the use of Eq. (2.16) can be violated. To allow for this, Thorsteinsson et al. suggest a modified van-der-Pauw equation

$$1 = \exp\left(-\pi R_{12,34} \frac{t}{\chi \rho}\right) + \exp\left(-\pi R_{23,41} \frac{t}{\chi \rho}\right), \tag{2.28}$$

with  $0 < \chi \le 2$  [51].

# 2.2. Crystal physics and anisotropic resistivity

For electrical current in an anistropic crystal, Ohm's law holds [38, pp. 205-214]

$$j_i = \sum_{k=1}^3 \sigma_{ik} E_k = -\sum_{k=1}^3 \sigma_{ik} \frac{\partial \Phi}{\partial x_k}.$$
 (2.29)

The  $\sigma_{ik}$  are the components of the conductivity tensor [38, pp. 205-214]

$$\underline{\underline{\sigma}} = \begin{pmatrix} \sigma_{xx} & \sigma_{xy} & \sigma_{xz} \\ \sigma_{yx} & \sigma_{yy} & \sigma_{xz} \\ \sigma_{zx} & \sigma_{zy} & \sigma_{zz} \end{pmatrix}. \tag{2.30}$$

At first glance, this means that there are nine components and thus nine measurements necessary, to fill the complete tensor. However,  $\underline{\underline{\sigma}}$  is in fact symmetrical,  $\sigma_{ij} = \sigma_{ji}$ , reducing the number of independent components to six [32; 38, Chapter 11; 54, 55]. Due

to Neumann's principle, the symmetry of the crystal can further reduce this number. Neumann's principle relates the symmetry elements (e.g. an n-fold rotation axis) of the crystal to those of its physical properties. Nye states it as: "The symmetry elements of any physical property of a crystal must include the symmetry elements of the point group of the crystal" [38, p. 20]. Basically, Neumann's principle poses a lower limit on the symmetry elements of the physical property, which may have more symmetry elements than the crystal it belongs to [38, pp. 20-21]. In the case of the conductivity tensor  $\underline{\sigma}$  this means, that according to the symmetry elements of a crystal, certain elements  $\sigma_{ij}$  must have the value 0. However, it may still turn out that further elements are equal to 0.

Tensors representing physical properties are written out using a set of mutual perpendicular axes which are related to the crystallographic lattice directions according to a set of conventions [38, p. 282]. For this thesis, two crystal structures are relevant: the monoclinic<sup>3</sup> crystal structure, in which in addition to the main diagonal, also the element  $\sigma_{zx}$  is not 0

$$\underline{\underline{\sigma}}_{\text{mono}} = \begin{pmatrix} \sigma_{xx} & 0 & \sigma_{xz} \\ 0 & \sigma_{yy} & 0 \\ \sigma_{zx} & 0 & \sigma_{zz} \end{pmatrix}, \tag{2.31}$$

and the orthorombic crystal structure, that retains only the elements on the main diagonal, all off-diagonal elements are zero due to symmetry

$$\underline{\underline{\sigma}}_{\text{ortho}} = \begin{pmatrix} \sigma_{xx} & 0 & 0\\ 0 & \sigma_{yy} & 0\\ 0 & 0 & \sigma_{zz} \end{pmatrix}. \tag{2.32}$$

For a cubic crystal, this reduces further, as all elements on the main diagonal are equal [38, p. 23; 55]. One should therefore speak of an isotropic crystal. The resistivity tensor  $\underline{\rho}$  is given by the matrix inverse of the conductivity tensor. While in principle, there is no relevant difference between reporting the resistivity or the conductivity of a material, resistivities are used in this thesis to facilitate comparison with the available literature.

Since the conductivity tensor  $\underline{\underline{\sigma}}$ , and thus also the resistivity tensor  $\underline{\underline{\rho}}$ , is symmetric, it is possible to find a coordinate system K', such that the tensor  $\underline{\underline{\rho}}'$  becomes diagonal [38, pp.195-196; 54; 56, pp.218-220]. These axes are also called the main axes and the elements on the main diagonal, the main resistivities. While this seems to be very useful at first glance, this transformation does not reduce the number of free parameters. Instead of the off-diagonal elements, now the numbers (or rather angles) pertaining to the transformation from the coordinate system K to the coordinate system K' have to be found [54].

<sup>&</sup>lt;sup>3</sup>There are two different indexing conventions for the monoclinic system. In the one used here, the off-diagonal element is  $\sigma_{zx}$  following [38]. In the one used elsewhere in the literature, e.g. [55], the off-diagonal element is  $\sigma_{xy}$ .

#### 2.3. The Wasscher Transformation

The so called Wasscher transformation<sup>4</sup> can be used to transform a given anisotropic sample into an *equivalent isotropic* sample [30, 32; 38, p. 201]. The equivalent isotropic sample is the image of the Wasscher transformation with isotropic resistivity. Furthermore, if a resistance R is measured on the anisotropic sample in an arbitrary contact (or in the case of a four-tip STM: tip) configuration, then the same resistance R is obtained under the Wasscher transformation, if both the contact configuration and the sample are transformed. This is achieved by the coordinate transformation [29]

$$x' = x\sqrt{\frac{\rho_x}{\bar{\rho}}}, \quad y' = y\sqrt{\frac{\rho_y}{\bar{\rho}}}, \quad z' = z\sqrt{\frac{\rho_z}{\bar{\rho}}}.$$
 (2.33)

This assumes a diagonal resistivity tensor  $\underline{\rho}$ . However, as noted in the previous section,  $\underline{\rho}$  can always be diagonalized. The parameter  $\bar{\rho}$ , used in Eq. (2.33) is given by the geometric mean of components of the resistivity [29, 30]

$$\bar{\rho} = \sqrt[3]{\rho_x \rho_y \rho_z}.\tag{2.34}$$

The electrical field is given by  $\underline{E} = -\underline{\nabla}\Phi(x,y,z)$ . The electrical potential  $\Phi(x,y,z)$  is required to be identical in corresponding points, i.e.,  $\Phi(x',y',z') = \Phi(x,y,z)$ . By the chain rule, the components of  $\underline{E}$  after the transformation are [29]

$$E'_{x} = -\frac{\partial \Phi(x', y', z')}{\partial x'} = -\sqrt{\frac{\bar{\rho}}{\rho_{x}}} \frac{\partial \Phi(x, y, z)}{\partial x} = \sqrt{\frac{\bar{\rho}}{\rho_{x}}} E_{x},$$

$$E'_{y} = -\frac{\partial \Phi(x', y', z')}{\partial y'} = -\sqrt{\frac{\bar{\rho}}{\rho_{y}}} \frac{\partial \Phi(x, y, z)}{\partial y} = \sqrt{\frac{\bar{\rho}}{\rho_{y}}} E_{y},$$

$$E'_{z} = -\frac{\partial \Phi(x', y', z')}{\partial z'} = -\sqrt{\frac{\bar{\rho}}{\rho_{z}}} \frac{\partial \Phi(x, y, z)}{\partial z} = \sqrt{\frac{\bar{\rho}}{\rho_{z}}} E_{z}.$$

$$(2.35)$$

Furthermore, the transformation is constructed such that the same current flows through corresponding surface elements. Therefore, the current densities  $\underline{j}$  of the sample and its equivalent isotropic sample are not the same. For the y component of the current density, it holds that [29]

$$j_y \mathrm{d}x \mathrm{d}z = j_y' \mathrm{d}x' \mathrm{d}z'. \tag{2.36}$$

With Eq. (2.33)

$$j_y' = \sqrt{\frac{\bar{\rho}^2}{\rho_x \rho_z}} j_y \tag{2.37}$$

follows. Similar results can be obtained for the other two components of j' [29]:

$$j_x' = \sqrt{\frac{\bar{\rho}^2}{\rho_y \rho_z}} j_x \mathbf{x}, \quad j_z' = \sqrt{\frac{\bar{\rho}^2}{\rho_x \rho_y}} j_z. \tag{2.38}$$

<sup>&</sup>lt;sup>4</sup>While the transformation is associated with Wasscher's name in the literature, see e.g. Ref. [32], Wasscher himself cites van der Pauw [29]. However, this transformation can be found in the literature even earlier, e.g. [38, p. 201].

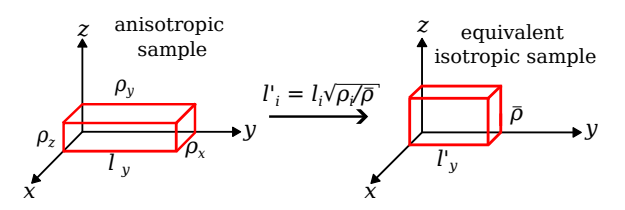


FIG. 2.4.: Wasscher transformation after [30]. If  $\rho_i < \bar{\rho}$ , the length  $l_i$  is compressed, if  $\rho_i > \bar{\rho}$ , the length  $l_i$  is stretched.

Substituting Eq. (2.35), (2.37), and (2.38) into Ohm's law [29; 38, pp. 205-214]

$$E_x = \rho_x j_x,$$

$$E_y = \rho_y j_y,$$

$$E_z = \rho_z j_z,$$
(2.39)

yields

$$E'_{x} = \rho_{x} \sqrt{\frac{\bar{\rho}}{\rho_{x}}} \cdot \sqrt{\frac{\rho_{y}\rho_{z}}{\bar{\rho}^{2}}} j'_{x} = \sqrt{\frac{\rho_{x}^{2}\rho_{y}\rho_{z}}{\rho_{x} \cdot \bar{\rho}}} j'_{x} = \sqrt{\frac{\bar{\rho}^{3}}{\bar{\rho}}} j'_{x} = \bar{\rho}j'_{x},$$

$$E'_{y} = \bar{\rho}j'_{y},$$

$$E'_{z} = \bar{\rho}j'_{z}.$$

$$(2.40)$$

Thus, the image of the Wasscher transformation indeed has an isotropic resistivity.

Now, the second property of the Wasscher transformation, the invariance of the resistance R, will be demonstrated for the case of a simple contact geometry: Figure 2.4 shows a drawing of a cuboid, whose sides are normal to one of the coordinate axes. Applying the Wasscher transformation to this cuboid then compresses or stretches its lengths according to

$$l_i' = l_i \sqrt{\frac{\rho_i}{\bar{\rho}}},\tag{2.41}$$

with  $i \in \{x, y, z\}$ . Now contacts are applied to the side surfaces at y = 0 and  $y = l_y$ , covering the complete surfaces. Once voltages are applied to the two surfaces, a homogeneous current density  $j_y$  will flow through sample. The contact resistance is neglected in these considerations. The total current is related to the current density  $j_y$  flowing through a given cross section of the sample by

$$I = \int_0^{l_x} \int_0^{l_z} j_y dx dz = j_y l_x l_z.$$
 (2.42)

The current

$$I' = \int_0^{l_x'} \int_0^{l_z'} j_y' dx' dz' = j_y' l_x' l_z'$$
(2.43)

flows through the equivalent isotropic sample. With Eq. 2.37, it follows directly, that I' = I, since

$$j_x' l_x' l_z' = \sqrt{\frac{\overline{\rho^2}}{\rho_x \rho_z}} j_y \cdot l_x \sqrt{\frac{\rho_x}{\overline{\rho}}} \cdot l_z \sqrt{\frac{\rho_z}{\overline{\rho}}} = j_y l_x l_z.$$
 (2.44)

The same voltage is applied to both the sample and its equivalent isotropic sample. Moreover, as noted above, it is part of the definition of the Wasscher transformation, that the potentials at corresponding points are the same, e.g.  $V(l_y) = V(l'_y)$ . Hence, for the case of a uniform current density arising from a voltage applied to two contacts on opposing sides of a cuboid,

$$R' = R \tag{2.45}$$

is obtained. It should be noted, that due to the construction of the Wasscher transformation, the same result can be obtained for the case of an arbitrary tip configuration on the surface of an anisotropic sample.

# 2.3.1. Example: Derivation of an equation for $R_{ m arb}$ on an anisotropic sample

In the following, as an example, the Wasscher transformation is applied to find an expression of the resistance of an arbitrary tip geometry on an anisotropic bulk sample. First, Eq. (2.2) is rewritten to apply it to the equivalent isotropic sample. Recall from section 2.1, that the current flows between the tips 1 and 4. As the tips are placed on the surface of the bulk sample, at z = 0, Eq. (2.2) can be rewritten as

$$R_{\rm arb} = \frac{\bar{\rho}}{2\pi} \left( \frac{1}{\sqrt{(x_2' - x_1')^2 + (y_2' - y_1')^2}} - \frac{1}{\sqrt{(x_2' - x_4')^2 + (y_2' - y_4')^2}} - \frac{1}{\sqrt{(x_3' - x_1')^2 + (y_3' - y_1')^2}} + \frac{1}{\sqrt{(x_3' - x_4')^2 + (y_3' - y_4')^2}} \right). \quad (2.46)$$

Now, the coordinate transformations [29, 30] [c.f. Eq. (2.33)]

$$x'_k = x_k \sqrt{\frac{\rho_x}{\bar{\rho}}}; \qquad y'_k = y_k \sqrt{\frac{\rho_y}{\bar{\rho}}}$$
 (2.47)

are applied. Note,  $x_k$  and  $y_k$  are the x and y coordinates of the four tips. This yields after some trivial rearranging

$$R = \frac{\bar{\rho}}{2\pi} \left( \frac{1}{\sqrt{(x_2 - x_1)^2 \frac{\rho_x}{\bar{\rho}} + (y_2 - y_1)^2 \frac{\rho_y}{\bar{\rho}}}} - \frac{1}{\sqrt{(x_2 - x_4)^2 \frac{\rho_x}{\bar{\rho}} + (y_2 - y_4)^2 \frac{\rho_y}{\bar{\rho}}}} - \frac{1}{\sqrt{(x_3 - x_1)^2 \frac{\rho_x}{\bar{\rho}} + (y_3 - y_1)^2 \frac{\rho_y}{\bar{\rho}}}} + \frac{1}{\sqrt{(x_3 - x_4)^2 \frac{\rho_x}{\bar{\rho}} + (y_3 - y_4)^2 \frac{\rho_y}{\bar{\rho}}}} \right). \quad (2.48)$$

Thus, by applying the following substitutions

$$l_i \to l_i' = l_i \sqrt{\frac{\rho_i}{\bar{\rho}}};$$
 and  $\rho \to \bar{\rho} = \sqrt[3]{\rho_x \rho_y \rho_z},$  (2.49)

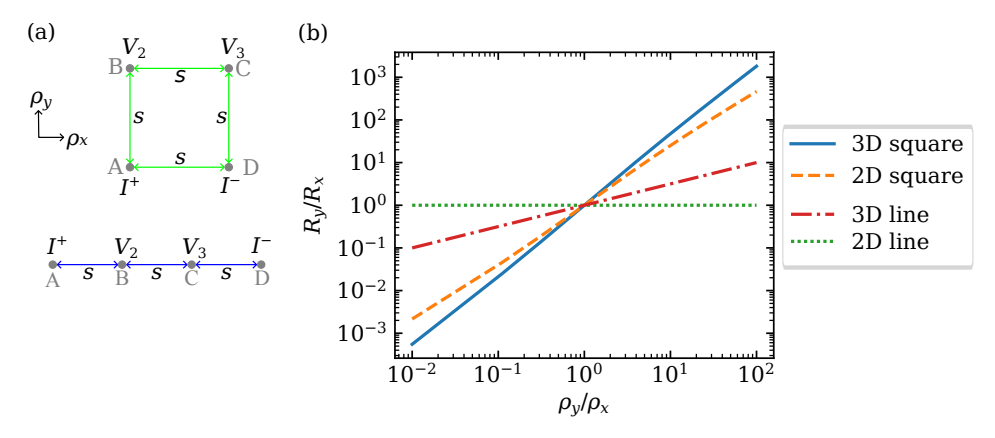


FIG. 2.5.: (a) Tip positions for the square and in-line measurement on an anisotropic sample. The current injection tips are aligned with  $\rho_{xx}$ , such that the resistances  $R_x$  are measured. (b) Sensitivity of the resistance ratio on the anisotropy  $A = \rho_{yy}/\rho_{xx}$ .

the Wasscher transformation can be used to apply equations calculated for isotropic samples to anisotropic samples.

# 2.4. Anisotropy and resistance

As discussed in the previous section, the Wasscher transformation can be used to derive equations for anisotropic samples from known equations for isotropic samples (see also Refs. [30, 32]). Rewriting equations Eq. (2.7), (2.10), (2.14), and (2.15) yields for bulk samples (3D)

$$R_x = \frac{\sqrt{\rho_{yy}\rho_{zz}}}{2\pi s}$$
 (in-line) (2.50)

$$R_x = \frac{\sqrt{\rho_{xx}\rho_{zz}}}{\pi s} \left( 1 - \frac{1}{\sqrt{1 + \frac{\rho_{xx}}{\rho_{yy}}}} \right)$$
 (square)

and thin-film samples (2D)

$$R_x = \frac{\sqrt{\rho_{xx}\rho_{yy}}\ln(2)}{\pi t}$$
 (in-line) (2.52)

$$R_{x} = \frac{\sqrt{\rho_{xx}\rho_{yy}}\ln(2)}{\pi t}$$
 (in-line) (2.52)  

$$R_{x} = \frac{\sqrt{\rho_{xx}\rho_{yy}}}{2\pi t}\ln\left(1 + \frac{\rho_{xx}}{\rho_{yy}}\right)$$
 (square), (2.53)

where the  $\rho_{ii}$  are the elements on the main diagonal of the resistivity tensor [30, 32]. The index x of the resistance illustrates that the measured resistance now depends on the alignment of the tip configuration with directions of the main resistivities. For the resistance  $R_x$ , the corresponding tip configuration are shown in Fig. 2.5(a). As the index x already implies, another set of equations can be found for current flowing in the ydirection (and in principle, also for current flowing in the z-direction.) The equations for  $R_y$  can readily be retrieved, by exchanging  $\rho_{xx}$  with  $\rho_{yy}$ .

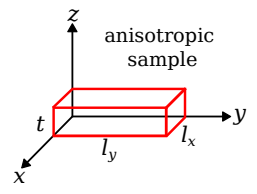


FIG. 2.6.: Sketch of a thin anisotropic sample, which is aligned with the main directions of the anisotropy.

Using Eq. (2.50), (2.51), (2.52) or (2.53), the surface anisotropy

$$A = \frac{\rho_{yy}}{\rho_{yy}} \tag{2.54}$$

is determined. From measurements of  $R_x$  and  $R_y$ , A is found by considering the ratio  $R_y/R_x$ . For the geometries discussed above, one obtains

$$\frac{R_y}{R_x} = \sqrt{\frac{\rho_{yy}}{\rho_{xx}}} \tag{in-line}$$

$$\frac{R_y}{R_x} = \frac{\sqrt{1 + \frac{\rho_{yy}}{\rho_{xx}}} - 1}{\sqrt{1 + \frac{\rho_{yx}}{\rho_{xy}}} - 1}$$
(square)

for a bulk sample, and

$$\frac{R_y}{R_-} = 1 \tag{in-line}$$

$$\frac{R_y}{R_x} = \frac{\ln\left(1 + \frac{\rho_{yy}}{\rho_{xx}}\right)}{\ln\left(1 + \frac{\rho_{xx}}{\rho_{yy}}\right)}$$
 (square)

for the case of a thin sheet [30, 32]. Using the equations above [except for Eq. (2.57)], the anisotropy A can be found by solving for  $\rho_{yy}/\rho_{yy}$ . As shown in Fig. 2.5(b), the sensitivity of the ratio  $R_y/R_x$  on the anisotropy depends on the tip configuration. It is clearly advantageous to measure the anisotropy A using the square tip geometry. Methods to disentangle all three components of the resistivity tensor from measurements of the resistance are addressed in the following section.

#### 2.4.1. Sheet resistivity of anisotropic samples

As discussed in section 2.1.2, for thin, isotropic sheet samples, the resistivity is normally expressed by the sheet resistivity:

$$R_{\rm S} = \frac{\rho}{t},\tag{2.59}$$

with the bulk resistivity  $\rho$  and the sheet thickness t. In the anisotropic case, an equivalent definition has to be found. Assuming that the sample is oriented as depicted in Fig 2.6, i.e., the three main resistivities are aligned with the coordinate axes. This also implies

that the sample material must be of orthorombic or higher symmetry. In this case, the average sheet resistivity  $R_{\rm S,avg}$  can then be found using the Wasscher transformation [30]: by replacing  $\rho$  with  $\bar{\rho} = \sqrt[3]{\rho_x \rho_y \rho_z}$  and t with  $t' = t \sqrt{\rho_z/\bar{\rho}}$ , see section 2.3 and Eq. (2.49). Then

$$R_{\text{S,avg}} = \frac{\sqrt[3]{\rho_x \rho_y \rho_z}}{t\sqrt{\rho_z/\bar{\rho}}} = \frac{\left(\sqrt[3]{\rho_x \rho_y \rho_z}\right)^{\frac{3}{2}}}{t\sqrt{\rho_z}} = \frac{\sqrt{\rho_x \rho_y \rho_z}}{t\sqrt{\rho_z}}$$
(2.60)

$$R_{\rm S,avg} = \frac{\sqrt{\rho_x \rho_y}}{t}.$$
 (2.61)

Van der Pauw found a more general expression for  $R_{S, \text{avg}}$ , without assuming that the sample and the main resistivity directions are aligned [29]. Van der Pauw's result for  $R_{S,\text{avg}}$  simplifies to the one presented here, if the sample is aligned with the main resistivity directions.

#### 2.4.2. Van-der-Pauw equation for anisotropic samples

As discussed in section 2.1.2.1, according to van der Pauw,

$$1 = \exp\left(-\pi \frac{R_x t}{\rho}\right) + \exp\left(-\pi \frac{R_y t}{\rho}\right) \tag{2.62}$$

holds for thin, isotropic samples [46, 47]. Using the Wasscher transformation and replacing  $\rho$  with  $\bar{\rho}=\sqrt[3]{\rho_x\rho_y\rho_z}$  and t with  $t'=t\sqrt{\rho_z/\bar{\rho}}$ , as was done in the previous section, Eq. (2.62) can also be applied to thin, anistropic samples. For convenience, the Wasscher transformation [30] is applied only to the argument of the exponential function.

$$-\pi \frac{R_x t'}{\bar{\rho}} = -\pi \frac{R_x t \sqrt{\rho_z/\bar{\rho}}}{\sqrt[3]{\rho_x \rho_y \rho_z}} = -\pi \frac{R_x t \sqrt{\rho_z}}{\left(\sqrt[3]{\rho_x \rho_y \rho_z}\right)^{\frac{3}{2}}} = -\pi \frac{R_x t}{\sqrt{\rho_x \rho_y}} = -\pi \frac{R_x}{R_{\text{S,avg}}}$$
(2.63)

Thus, the van-der-Pauw-equation

$$1 = \exp\left(-\pi \frac{R_x}{R_{\text{S,avg}}}\right) + \exp\left(-\pi \frac{R_y}{R_{\text{S,avg}}}\right). \tag{2.64}$$

can also be applied to anisotropic samples. See also [57–59].

Due to Eq. (2.63), the modified van-der-Pauw method proposed by Thorsteinsson *et al.* [51] will also yield  $R_{S,avg}$  on thin anisotropic samples, when the tips are placed along a line of mirror symmetry. However, it should be noted that the Wasscher transformation may also change the isoerror curves computed in Ref. [51]. Therefore, a reevaluation of the optimal symmetry line for the measurement might be necessary. Furthermore, due to the electric anisotropy, the mirror symmetries of the samples might be reduced, e.g. the diagonals of a square sample are no longer mirror planes, if the edges of the sample are aligned with the two main resistivity directions.

# 2.5. Methods for disentangling the elements of the resistivity tensor

At first glance, it seems that with Eq. (2.50) and (2.51) (considering that equations for  $R_y$  can be obtained by exchanging x and y), there should be sufficient information to disentangle all three components of the resistivity tensor. However, it is not possible to solve for  $\rho_{xx}$ ,  $\rho_{yy}$ , and  $\rho_{zz}$  using these expressions for  $R_x$  and  $R_y$ : The two measurements of  $R_x$  (or  $R_y$ ), one in the linear configuration and one in the square configuration, are not independent (see A on page 115). Therefore, methods presented in the literature to disentangle all three components of the resistivity tensor rely on resistance measurements on at least two different samples. In principle, a number of long bars of the material under study cut in low index directions could be prepared. On each of these samples, one of the diagonal components of  $\underline{\rho}$  can be measured [29]. For an example, see Ref. [60]. Airapetyants  $et \, al$ . first suggested to measure the three components of the resistivity tensor using the four-probe method in a linear tip configuration [61]. They suggest three measurements on two different (orthogonal) crystal surfaces to obtain all three components. The tips must be aligned with the main directions of the resistivity tensor  $\underline{\rho}$  [61].

Using the formulas presented in section 2.4, a method to measure the three components on the main diagonal of  $\underline{\rho}$  can be devised. However, on a three-dimensional sample, measurements on two different samples are necessary: Either two different crystal surfaces are measured (as presented in Ref. [61]), or measurements on 3D and on a 2D sample are combined [32]. The equations presented in section 2.4 are not linearly independent (as long as multiple measurements on the same crystallographic facet are considered). Thus, performing multiple measurements in the square and the in-line geometry on the same surface of a 3D sample only yields the ratio of the two in-plane components of the resistivity tensor  $\underline{\rho}$ . In chapter 6 of the present thesis, a measurement method using eq. (2.51) (square geometry on a bulk sample) and a linear, distance dependent measurement on a thin flake is introduced.

In the literature, two different methods to disentangle the elements of the resistivity tensor for finite samples have been presented:

- 1. the Bierwagen-Simon method for thin flake samples [59], and
- 2. the Montgomery method for 3D cuboid samples [62].

The Montgomery method was recently rewritten by Dos Santos *et al.* [63] as Montgomery relied on cumbersome graphical solutions of the equations. The Bierwagen-Simon method is employed in chapter 7 as an alternative method to the one presented in chapter 6.

# 2.5.1. Bierwagen-Simon method

For the Bierwagen-Simon method [59], a thin rectangular sample is prepared. The contacts (red) are placed in the corners, as displayed in Fig. 2.7(a).  $R_x$  and  $R_y$  are the resistances measured along the x and y side of the sample, respectively.

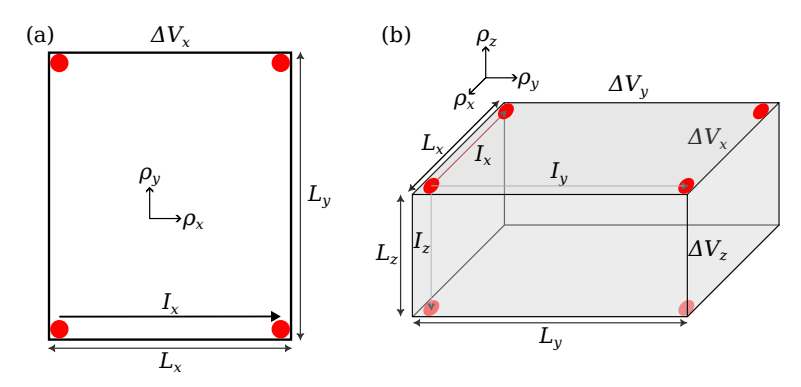


Fig. 2.7.: (a) Sketch of a thin rectangular sample for the Bierwagen-Simon method. The locations of the contacts are indicated with red circles. The sketch shows the measurement of the resistance  $R_x$ ; after [59, Fig. 1]. (b) Sketch of a cuboid sample for the Montgomery method. The six contacts necessary to measure  $R_x$ ,  $R_y$ , and  $R_z$  are indicated in red. The contacts on the bottom surface of the sample are indicated in a light red. After [63, Fig. 1].

The measurement of the anisotropy is based on an equation for  $R_x$  first published by Simon [64] for a slightly different geometry. For the resistance  $R_x$ , it holds that<sup>5</sup>

$$R_{x} = \frac{8}{\pi} \frac{\sqrt{\rho_{x}\rho_{y}}}{\sum_{n=0}^{\infty} \left[ (2n+1)\sinh\left(\pi\sqrt{\frac{\rho_{x}L_{x}^{2}}{\rho_{y}L_{y}^{2}}}(2n+1)\right) \right]},$$
(2.65)

under the assumption, that the principle axes of the resistivities align with the sample edges [64]. Using the shorthand

$$A_{\text{eff}} = \frac{\rho_y}{\rho_x} \left(\frac{L_y}{L_x}\right)^2 = A \left(\frac{L_y}{L_x}\right)^2 \tag{2.66}$$

one can write [59]

$$\frac{R_{y}}{R_{x}} = \frac{\sum_{n=0}^{\infty} \left[ (2n+1) \sinh\left(\sqrt{A_{\text{eff}}^{-1}}\pi(2n+1)\right) \right]^{-1}}{\sum_{n=0}^{\infty} \left[ (2n+1) \sinh\left(\sqrt{A_{\text{eff}}}\pi(2n+1)\right) \right]^{-1}}.$$
 (2.67)

The anisotropy A is obtained by solving Eq. (2.67) numerically for  $A_{\text{eff}}$  and then using Eq. 2.66.

Once the average sheet resistivity  $R_{S,avg}$  has been measured using the van-der-Pauw method (Eq. (2.64)), the two in-plane components of the resistivity tensor can then be calculated according to [59]

$$\frac{\rho_x}{t} = \frac{\sqrt{\rho_x \rho_y}}{t} \cdot \sqrt{A^{-1}}$$
 and  $\frac{\rho_y}{t} = \frac{\sqrt{\rho_x \rho_y}}{t} \cdot \sqrt{A}$ . (2.68)

<sup>&</sup>lt;sup>5</sup>Note, there is a misprint in Eq. (10) and (11) in Ref. [59]:  $L_x$  and  $L_y$  were swapped.

#### 2.5.2. Montgomery method

Montgomery proposed a widely used method to obtain the resistivities of an anisotropic sample [62]. The contacts are again placed in the corners of the sample. To obtain all three resistivities, either a second sample has to be measured, or the first sample is contacted both on the top and the bottom surface. The analysis uses the Wasscher transformation [30] to apply solutions for the potential of an isotropic sample from an accompanying theoretical paper [65] to the anisotropic sample under study. In the original method, the equations by Logan *et al.* [65] are solved graphically [62].

Dos Santos  $et\,al.$  published a modified version of the Montgomery method, where the equations are solved analytically [63]. Note that in Refs. [62, 63, 65] and in the relevant sections of [32], primed dimensions describe the anisotropic sample and unprimed the equivalent isotropic sample. In the present thesis, however, the Wasscher's nomenclature is used: The primed dimensions describe the equivalent isotropic sample. Ref. [63] provides the appropriate procedures to find the  $\rho_x$  and  $\rho_y$  of a thin sample and, in addition,  $\rho_z$  for a bulk sample. Thus, the Montgomery method could be applied to a rectangular 2D sample instead of the Bierwagen-Simon method.

In all cases, a relationship between the  $R_y/R_x$  and  $L'_y/L'_x$  is used in the analysis:

$$\frac{R_y}{R_x} = \frac{\sinh\left(\pi \frac{L_y'}{L_x'}\right)}{\sinh\left(\pi \frac{L_x'}{L_y'}\right)}.$$
(2.69)

Already Montgomery observed, that this relationship is only weakly dependent on the thickness [62]. For the mean resistivity

$$\bar{\rho} = H_x E' R_x = H_y E' R_y \tag{2.70}$$

holds [63]. E' is an effective thickness of the equivalent isotropic sample and depends on the electrostatic potential [62, 63, 65]. If the thickness  $l'_z$  is small, E' can be replaced by  $l'_z$ , for thicker samples, E' is also dependent on the lateral sample dimensions [62]. Thus one obtains  $R_y/R_x = H_x/H_y$ . With

$$\frac{1}{H_x} = \frac{4}{\pi} \sum_{n=0}^{\infty} \frac{2}{(2n+1)\sinh\left(\pi(2n+1)\frac{L_y'}{L_x'}\right)}$$
(2.71)

[63], one obtains

$$\frac{R_y}{R_x} = \frac{\sum_{n=0}^{\infty} (2n+1) \sinh\left(\pi (2n+1) \frac{L_y'}{L_x'}\right)}{\sum_{n=0}^{\infty} (2n+1) \sinh\left(\pi (2n+1) \frac{L_x'}{L_y'}\right)}.$$
 (2.72)

Eq. (2.69) is recovered, when terminating the series after n=0. On the other hand, using the Wasscher transformation  $L'_i = L_i \sqrt{\rho_i/\bar{\rho}}$  one finds

$$\frac{L_y'}{L_x'} = \frac{L_y \sqrt{\frac{\rho_y}{\bar{\rho}}}}{L_x \sqrt{\frac{\rho_x}{\bar{\rho}}}} = \frac{L_y \sqrt{\rho_y}}{L_x \sqrt{\rho_x}} = \sqrt{A_{\text{eff}}}.$$
(2.73)

Thus, also Eq. (2.67) is recovered. More importantly, Eq. (2.67) can also be applied when bulk samples are considered.

#### 2.6. Correction Factors

With some important exceptions, the previous sections of the present chapter dealt with geometric (configuration) factors relating the measured resistance to the resistivity. In this section, the effects of finite sample sizes are discussed. On finite samples, in contrast to the (semi-) infinite samples discussed above, parts of the current pathways are missing at the sample edge, changing the measured resistance R. Alternatively, a conductive sample edge can create new current pathways. Correction factors can then be used to calculate the correct resistivity  $\rho$ . Note, in some cases, both the configuration factor and the correction factor are included in the same calculation. This must be taken into account when applying specific correction factors from the literature.

As an example, consider a linear equidistant tip setup on a bulk sample [41, p. 7]

$$\rho = 2\pi sRF,\tag{2.74}$$

and recall that for a semi-infinite bulk sample, this equation [see Eq. (2.10)] was presented without the factor F. This already highlights an important constraint for the correction factors: They have to attain the value F=1, when distance between the tips and the boundary is large. The correction factor F can be calculated for different geometries, e.g. the tips are placed parallel to a non conductive boundary. If the correction factor F in Eq. (2.74) also includes the geometric factor,  $\rho = F'R$  would result. In some instances, correction factors are published in this form. Note also: As the potential of a point source is different in the 2D case compared to the 3D case, for 2D samples separate correction factors have to be calculated [37].

A summary of some relevant correction factors can be found in the review by Miccoli  $et\,al.$  [32] and the book by Schroder [41, Ch. 1]. Derivations of correction factors using the method of image charges are given in Refs. [28] and [39]. A derivation of the correction factor for in-line contacts on a thin sample is given by Weller [66]. For the latter case, Albers  $et\,al.$  obtained a closed analytical expression, which will be used in the following section [67].

The material used for experiments in this thesis,  $\alpha$ -Bi<sub>4</sub>Br<sub>4</sub>, tends to form long rectangular flakes (see chapter 4 for details): Perloff solved this problem for thin sheets using conformal mapping [45]. For 3D cuboid samples Yamashita *et al.* calculated correction factors for the in-line geometry [68] and for the square or rectangular geometry [69, 70].

Correction factors can also be used to show that a cumbersome correction of measurement results is not needed on a given sample, if the difference between corrected and uncorrected results would be smaller than the measurement error.

# 2.6.1. Equidistant, linear tip placement on a sample of finite thickness

For the resistance of a thin sample measured with a linear, equidistant contact setup, Albers et al. derived

$$R = \frac{\rho}{\pi t} \ln \left( \frac{\sinh\left(\frac{t}{s}\right)}{\sinh\left(\frac{t}{2s}\right)} \right), \tag{2.75}$$

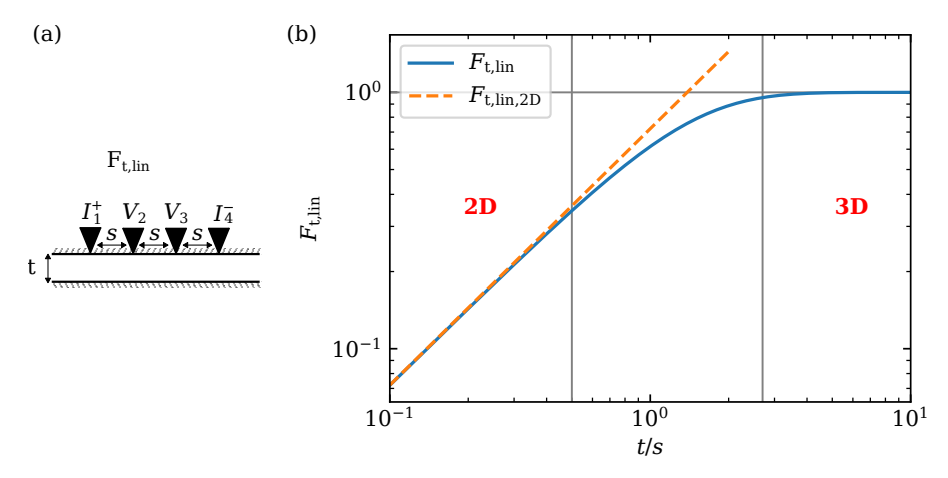


FIG. 2.8.: (a) Four tips placed in a line with equal inter-tip distances s on a sample with a finite thickness t and an insulating bottom surface. (b) The corresponding correction factor  $F_{\rm t,lin}$  has three distinct regions: the 2D region where the sample can be approximated as a 2D sheet, the 3D region where no correction of the bulk measurement is necessary, and an intermediate region in between.

with the sample thickness t. The tip placement is illustrated in Fig. 2.8(a). This only holds, when the bottom layer is insulating [67]. Note, also in this case the authors did not calculate a correction factor  $per\ se$ , but rather a new relation between R and  $\rho$  that takes into account the complete layout of the problem. Rewriting for  $\rho$  yields:

$$\rho = \pi t \frac{R}{\ln\left(\frac{\sinh\left(\frac{t}{s}\right)}{\sinh\left(\frac{t}{2s}\right)}\right)}.$$
(2.76)

When equating the coefficients of Eq. (2.76) and (2.74), a correction factor can be obtained:

$$F_{\text{t,lin}} = \frac{\frac{t}{s}}{2\ln\left(\frac{\sinh\left(\frac{t}{s}\right)}{\sinh\left(\frac{t}{2s}\right)}\right)}.$$
 (2.77)

See also [41, p. 8].

When considering small thicknesses t, sinh can be expanded as  $\sinh(x) \approx x$  [71, p. 85]. Thus,  $F_{\text{t,lin}}$  reduces to

$$F_{\text{t,lin, 2D}} \approx \frac{\frac{t}{s}}{2\ln(2)}.$$
 (2.78)

Plugging this result into Eq. (2.74), one finds [41, p. 9; 67]

$$\rho = \frac{\pi}{\ln(2)} tR. \tag{2.79}$$

This recovers Eq. (2.15), that was introduced at the beginning of this chapter for an equidistant, linear tip geometry on a 2D sample.

The plot of  $F_{\rm t,lin}$  in Fig. 2.8(b) can be separated into three different regions. The boundaries between the different regions are set according to the permitted deviation of a chosen approximation from  $F_{\rm t,lin}$ . At small t/s, the approximation  $F_{\rm t,lin,\ 2D}$  in Eq. (2.78) is used. On the other hand, at large values of t/s, the correction factor  $F_{\rm t,lin}$  is approximated as 1.

For small t/s, the used approximation of sinh is applicable until  $t/s \approx 0.5$ , considering a deviation of 5% between  $F_{\rm t,lin,\ 2D}$  and  $F_{\rm t,lin}$  permissible. By this simple argument, one can conclude, that in the case of an linear, equidistant measurement, a sample can be described as a 2D object, as long as  $t \leq s/2$  holds. Thus, in a transport measurement a two-dimensional behavior is not (or not necessarily) an intrinsic property of the sample, but also depends on the ratio of the inter-tip distance s to the sample thickness t. When considering large values of t/s, one finds  $t/s \approx 2.7$  for  $F_{\rm t,lin}$ , if a deviation of 5% between 1 and  $F_{\rm t,lin}$  is allowed. Therefore, if  $t \leq 2.7s$ , the correction factor  $F_{\rm t,lin}$  needs to be applied.

Consequently, for a sample of finite thickness t, there are three distinct regions: the 2D regime  $(t \le s/2)$ , the 3D regime  $(t \ge 2.7s)$ , and an intermediate regime  $(s/2 \ge t \le 2.7s)$ . These three regions are also displayed in Fig. 2.8(b). If one requires a smaller deviation than 5%, the boundary for the 2D regime moves to smaller values of t/s, whereas the boundary of the 3D regime moves to larger values of t/s. This can be easily verified in the plot in Fig. 2.8(b).

#### 2.6.2. Rectangular tip geometry next to an insulating boundary

A number of correction factors are derived for the present thesis, which could not be found in the literature. The correction factors describe the rectangular tip configuration adjacent to an insulating boundary or, in one case, a rectangular tip configuration placed on a sample of finite thickness. The need for these specific correction factors arose during the measurement of anisotropy using  $\alpha$ -Bi<sub>4</sub>Br<sub>4</sub> (see section 6.4.3). For the measurement, the tips were placed in a square in the middle of a flake. Due to the anisotropy of the sample, the Wasscher transformation [30] transforms this square into a rectangle. As a basis the treatment using the method of image currents by Valdes was used [28].

Here and in the following, s always refers to the distance between the two current injection contacts; v refers to the distance between a given current injection tip and a voltage probing tip. All correction factors calculated in the following, apply to a finite bulk sample. If the measurements were carried out on a thin 2D sample instead, similar correction factors could be calculated using the  $\ln(r)$  potential. The rectangular tip configuration on an infinitely large bulk sample was presented in section 2.1.1.1, at the beginning of this chapter.

#### 2.6.2.1. Current injection tips perpendicular to an insulting boundary

First, the case of current injected perpendicular to a non-conductive boundary is considered. The measurement geometry is depicted in Fig. 2.9(a). A side-view of the tips next to the boundary is depicted in Fig. 2.9(b). As the boundary is non-conductive, the signs of the image tips are the same as the signs of the object tips.

To start with, the potentials under the voltage probing tips 2 and 3 are calculated. The first two terms in both formulas represent the case of an infinitely large square as

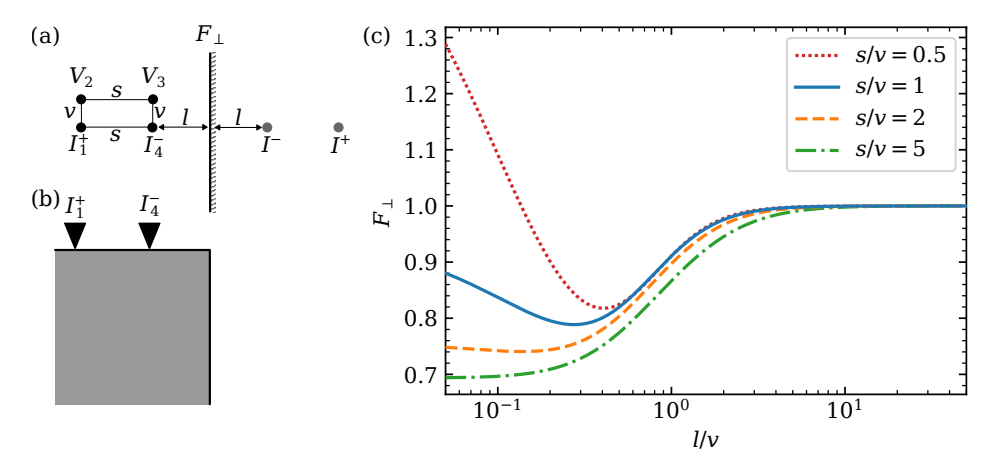


Fig. 2.9.: The correction factor  $F_{\perp}$ . (a) Top-view of the rectangle of tips on the surface, with the non conductive boundary indicated by the vertical line. The mirrored contacts are depicted in gray. (b) Side view. As the two voltage probing tips are behind the current injection tips, only the latter are visible. (c) Plot of  $F_{\perp}$  for different aspect ratios s/v.

discussed in section 2.1.1.1.

$$V_2 = \frac{\rho I}{2\pi} \left( \frac{1}{v} - \frac{1}{\sqrt{v^2 + s^2}} - \frac{1}{\sqrt{v^2 + (2l + s)^2}} + \frac{1}{\sqrt{v^2 + 4(s + l)^2}} \right)$$
(2.80)

$$V_3 = \frac{\rho I}{2\pi} \left( \frac{1}{\sqrt{v^2 + s^2}} - \frac{1}{v} - \frac{1}{\sqrt{v^2 + (2l)^2}} + \frac{1}{\sqrt{v^2 + (2l + v)^2}} \right). \tag{2.81}$$

The voltage difference reads:

$$\Delta V = \frac{\rho I}{2\pi} \left( \frac{2}{v} - \frac{2}{\sqrt{v^2 + s^2}} - \frac{2}{\sqrt{v^2 + (2l + s)^2}} + \frac{1}{\sqrt{v^2 + 4(s + l)^2}} + \frac{1}{\sqrt{v^2 + (2l)^2}} \right). \tag{2.82}$$

The first two terms correspond to the solution for an infinite sample. Solving for  $\rho$  and rearranging to separate the solution for an infinite sample yields:

$$\rho = \frac{2\pi Rv}{2 - \frac{2}{\sqrt{1 + \frac{s^2}{v^2}}}} \cdot \frac{1}{1 + \frac{1}{\frac{2}{v} - \frac{2}{\sqrt{v^2 + s^2}}} \left(\frac{1}{\sqrt{v^2 + 4(s+l)^2}} + \frac{1}{\sqrt{v^2 + (2l)^2}} - \frac{2}{\sqrt{v^2 + (2l+s)^2}}\right)}.$$
 (2.83)

The second fraction can then be identified as the correction factor  $F_{\perp}$ 

$$F_{\perp}\left(\frac{s}{v}, \frac{l}{v}\right) = \frac{1}{1 + \frac{1}{2 - \frac{2}{\sqrt{1 + (\frac{s}{v})^2}}} \left(\frac{1}{\sqrt{1 + 4(\frac{s}{v} + \frac{l}{v})^2}} + \frac{1}{\sqrt{1 + (2\frac{l}{v})^2}} - \frac{2}{\sqrt{1 + (2\frac{l}{v} + \frac{s}{v})^2}}\right)}.$$
 (2.84)

Figure 2.9(c) depicts  $F_{\perp}$  for different aspect ratios s/v as a function of the distance to the boundary l. Note, that local minimum around  $l/v \approx 0.4$  decreases with the aspect ratio. For large aspect ratios, the local minimum becomes a saddle point. If the aspect ratio is smaller than 1, the local minimum becomes sharper. Furthermore,  $F_{\perp}$  becomes larger than 1, if the contacts are too close to the boundary.

#### 2.6.2.2. Current injection parallel to an insulating boundary

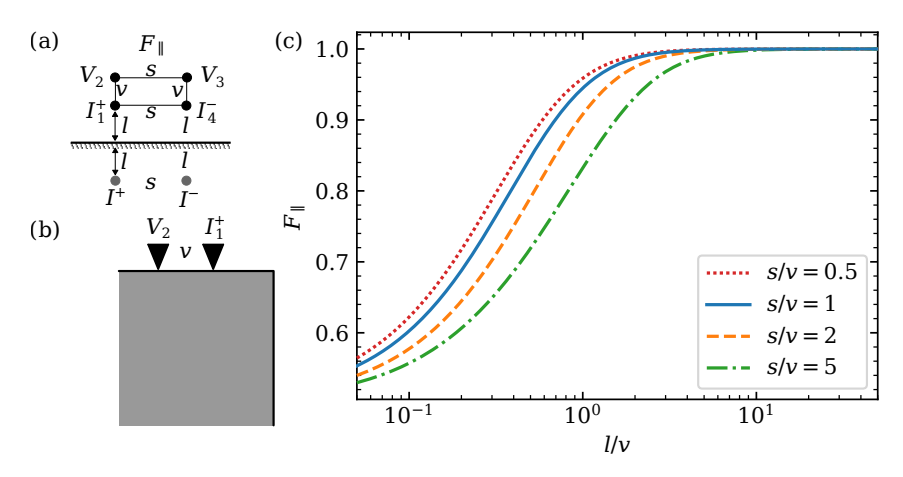


Fig. 2.10.: The correction factor  $F_{\parallel}$ . (a) Top-view of the rectangle of tips on the surface, with the non conductive boundary indicated by the vertical line. The mirrored contacts are depicted in gray. (b) Side view of the rectangle. In this projection, only two tips are visible. (c) Plot of  $F_{\parallel}$  for different aspect ratios s/v.

Next, the case of current flowing parallel to the boundary is treated. Figure 2.10(a) illustrates the tip placement next to the boundary. A side-view of the tips close to the boundary of the sample is depicted in Fig. 2.10(b). Again, the potentials below the voltage probing tips are calculated first:

$$V_2 = \frac{\rho I}{2\pi} \left( \frac{1}{v} - \frac{1}{\sqrt{v^2 + s^2}} - \frac{1}{\sqrt{s^2 + (2l + v)^2}} + \frac{1}{v + 2l} \right)$$
 (2.85)

$$V_3 = \frac{\rho I}{2\pi} \left( \frac{1}{\sqrt{v^2 + s^2}} - \frac{1}{v} - \frac{1}{v + 2l} + \frac{1}{\sqrt{s^2 + (2l + v)^2}} \right). \tag{2.86}$$

Hence, the voltage drop

$$\Delta V = \frac{\rho I}{\pi} \left( \frac{1}{v} - \frac{1}{\sqrt{v^2 + s^2}} - \frac{1}{\sqrt{s^2 + (v + 2l)^2}} + \frac{1}{v + 2l} \right)$$
 (2.87)

is calculated. This result is similar to Eq. (2.82). Therefore, following the treatment in

$$n = -3$$
  $n = -2$   $n = -1$   $n = 0$   $n = +1$   $n = +2$   $n = +3$ 
 $I^{+}$   $I^{-}$   $I^{-}$ 

FIG. 2.11.: Sketch of image currents for two parallel boundaries with equal distance l. The current is injected parallel to the non-conductive boundary. Below, the distances of the nth order based on the order (n-1) is shown. E.g. from n=-1, n=2 is calculated.

the previous section, the correction factor  $F_{\parallel}$  is then found immediately

$$F_{\parallel}\left(\frac{s}{v}, \frac{l}{v}\right) = \frac{1}{1 + \frac{1}{1 - \frac{1}{\sqrt{1 + \left(\frac{s}{v}\right)^{2}}}} \left(\frac{1}{1 + 2\frac{l}{v}} - \frac{1}{\sqrt{\left(\frac{s}{v}\right)^{2} + (2\frac{l}{v} + 1)^{2}}}\right)}$$
(2.88)

In Fig. 2.10(c) the dependence of  $F_{\parallel}$  on l/v for different aspect ratios s/v is plotted. In contrast to  $F_{\perp}$  discussed above, the  $F_{\parallel}$  for the different aspect ratio are similar.

#### 2.6.2.3. Current injection parallel to two insulating boundaries

For better understanding of the measurement geometry, the second boundary, opposite from first, also has to be taken into account. This leads to an infinite amount of reflections, and, therefore, image current sources. The most straightforward way to deal with this situation is to find a series describing the contributions of all image currents, as is done in the following section for a sample of finite thickness. In the present case, however, there was no obvious way of writing down such a series.

As a simple solution, all terms up to the third order are calculated. During the computation of F, the convergence of the terms is monitored. If necessary, more terms can be calculated. Figure 2.11 shows a sketch of the tip placement in the center of the sample. The distances of the nth image to the (n+1)st mirror is also indicated, allowing the calculation of terms until  $n=\pm 3$ . The individual terms are given in the following.

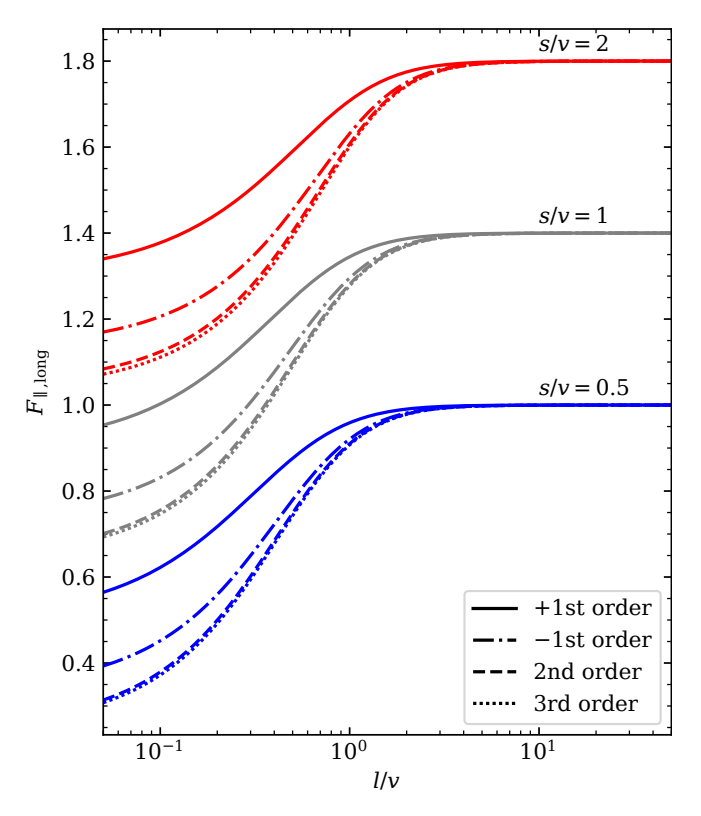


FIG. 2.12.: The correction factor  $F_{\parallel, \rm long}$  for three different aspect ratios s/v. For each aspect ratio,  $F_{\parallel, \rm long}$  involving terms until the positive first order (corresponding to  $F_{\parallel}$ , solid), the negative first order (dash-dotted), the second order (dashed), and the third order (dotted) are plotted. The aspect ratios 1 and 2 are shifted upwards by 0.4 and 0.8, respectively.

As  $V_2^n=-V_3^n$ , only  $V_2^n$ , n=-3 ... + 3, are given (compare also Fig. 2.11).

$$\begin{split} V_2^0 &= \frac{\rho I}{2\pi} \left( \frac{1}{v} - \frac{1}{\sqrt{v^2 + s^2}} \right) \\ V_2^{+1} &= \frac{\rho I}{2\pi} \left( \frac{1}{2l + v} - \frac{1}{\sqrt{s^2 + (2l + v)^2}} \right); \quad V_2^{-1} &= \frac{\rho I}{2\pi} \left( \frac{1}{2l + v} - \frac{1}{\sqrt{s^2 + (2l + v)^2}} \right) \\ V_2^{+2} &= \frac{\rho I}{2\pi} \left( \frac{1}{4l + 3v} - \frac{1}{\sqrt{s^2 + (4l + 3v)^2}} \right); \quad V_2^{-2} &= \frac{\rho I}{2\pi} \left( \frac{1}{4l + v} - \frac{1}{\sqrt{s^2 + (4l + v)^2}} \right) ^6 \\ V_2^{+3} &= \frac{\rho I}{2\pi} \left( \frac{1}{6l + 3v} - \frac{1}{\sqrt{s^2 + (6l + 3v)^2}} \right); \quad V_2^{-3} &= \frac{\rho I}{2\pi} \left( \frac{1}{6l + 3v} - \frac{1}{\sqrt{s^2 + (6l + 3v)^2}} \right) \end{split}$$

<sup>&</sup>lt;sup>6</sup>Sic! Since  $V_2^{+1} \neq V_2^{-1}$ ,  $V_2$  cannot be written as a series.

Thus, the inverse of the correction factor  $F_{\parallel, \text{long}}$  is

$$F_{\parallel,\log}^{-1}\left(\frac{s}{v}, \frac{l}{v}\right) = 1 + \frac{1}{1 - \frac{1}{\sqrt{1 + \left(\frac{l}{v}\right)^2}}} \left(\frac{2}{1 + 2\frac{s}{v}} - \frac{2}{\sqrt{\left(\frac{s}{v}\right)^2 + \left(2\frac{l}{v} + 1\right)^2}} + \frac{1}{3 + 4\frac{l}{v}} - \frac{1}{\sqrt{\left(\frac{s}{v}\right)^2 + \left(4\frac{l}{v} + 3\right)^2}} + \frac{1}{1 + 4\frac{l}{v}} - \frac{1}{\sqrt{\left(\frac{s}{v}\right)^2 + \left(4\frac{l}{v} + 1\right)^2}} + \frac{2}{3 + 6\frac{l}{v}} - \frac{2}{\sqrt{\left(\frac{s}{v}\right)^2 + \left(6\frac{l}{v} + 3\right)^2}}\right).$$

$$(2.89)$$

Plots of  $F_{\parallel, \mathrm{long}}$  are shown in Fig. 2.12 for three different aspect ratios. The positive first order corresponds to the correction factor  $F_{\parallel}$ . For small l/v ignoring the higher order contributions will induce a major error. The largest contribution stems from the negative first order. For l/v > 1, however, the deviation of  $F_{\parallel, \mathrm{long}}$  from  $F_{\parallel}$  becomes smaller than a few percent. Thus, calculating the terms until the 3rd order seems to be sufficient for most practical purposes.

# 2.6.3. Rectangular tip geometry on a laterally infinite sample of finite thickness

Finally, the correction factor  $F_{\rm t}$  to account for the finite thickness of the sample is derived. The calculations are based on cases 6 and 7 in Ref. [28]. The situation is sketched in Fig. 2.13(c) (side-view) and Fig. 2.13(d) (top-view).

As already noted in the previous section, due to the two parallel mirror planes, there is an infinite number of mirror images both below and above the sample. Figure 2.13(a) only shows the first order. The images above the sample surface are numbered with  $n \in \mathbb{Z}_{>0}$ . The images below the sample surface are numbered with  $n \in \mathbb{Z}_{<0}$ ; n = 0 corresponds to the formula for an infinitely thick sample. To begin, the first few orders of the  $V_2$  are calculated:

$$V_2^0 = \frac{\rho I}{2\pi} \left( \frac{1}{\sqrt{v^2}} - \frac{1}{\sqrt{v^2 + s^2}} \right) \tag{2.90}$$

$$V_2^1 = \frac{\rho I}{2\pi} \left( \frac{1}{\sqrt{v^2 + (1 \cdot 2t)^2}} - \frac{1}{\sqrt{v^2 + s^2 + (1 \cdot 2t)^2}} \right)$$
 (2.91)

$$V_2^{-1} = \frac{\rho I}{2\pi} \left( \frac{1}{\sqrt{v^2 + (-1 \cdot 2t)^2}} - \frac{1}{\sqrt{v^2 + s^2 + (-1 \cdot 2t)^2}} \right)$$
 (2.92)

$$V_2^2 = \frac{\rho I}{2\pi} \left( \frac{1}{\sqrt{v^2 + (2 \cdot 2t)^2}} - \frac{1}{\sqrt{v^2 + s^2 + (2 \cdot 2t)^2}} \right)$$
 (2.93)

$$V_2^{-2} = \frac{\rho I}{2\pi} \left( \frac{1}{\sqrt{v^2 + (-2 \cdot 2t)^2}} - \frac{1}{\sqrt{v^2 + s^2 + (-2 \cdot 2t)^2}} \right). \tag{2.94}$$

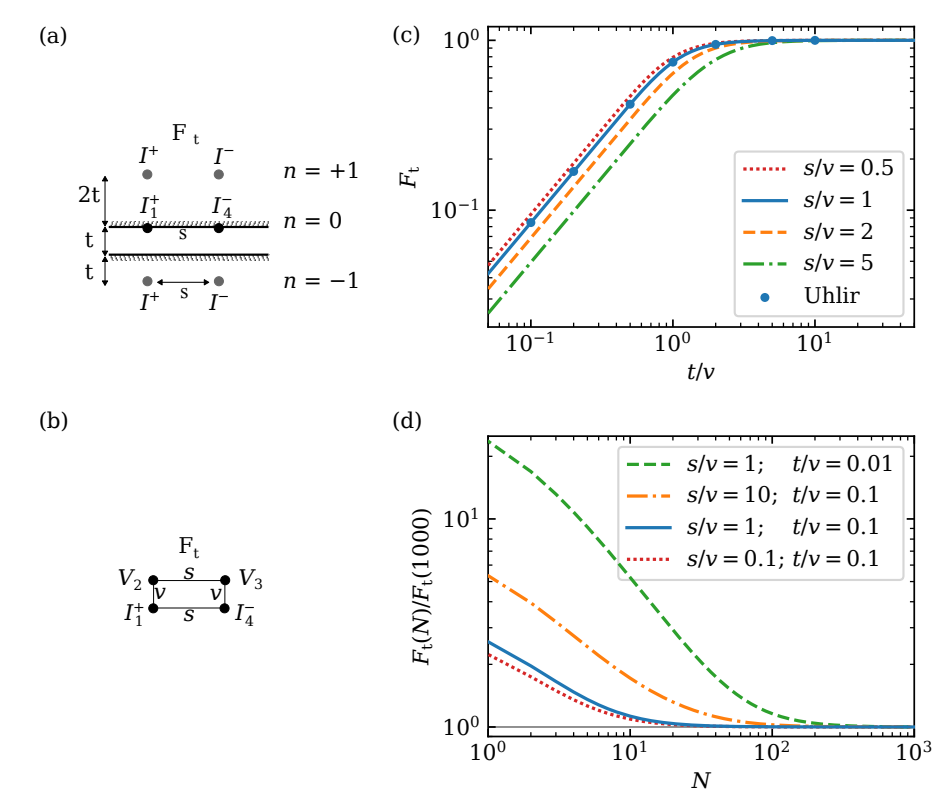


FIG. 2.13.: The correction factor  $F_{\rm t}$  for a rectangular tip configuration. (a) Side-view drawing of a square tip geometry on a finitely thick sample. The voltage probing tips are placed on the top surface behind the current injection tips. (b) Top-view drawing of the same tip geometry. (c) Plot of  $F_{\rm t}$  for different aspect ratios s/v. The dots indicate numerical values for a square on a thin sample given by Uhlir [39], showing excellent agreement with the values calculated here for s/v=1. (d) Convergence of the infinite series, needed to evaluate  $F_{\parallel}$  numerically. The plot shows  $F_{\rm t}$  for different parameters depending on N, after which the summation is terminated. The plot is normalized to  $F_{\rm t}\left(\frac{s}{v},\frac{t}{v},N=1000\right)$ , after which the series has converged sufficiently.

From this, two series can be found: as can be seen from section 2.1.1.1,  $V_3^n = -V_2^n$ , and  $\Delta V = 2V_2$  (compare section 2.1.1.1, note this does not hold for all correction factors). Thus, one can write down two series, one based on the first term of the parenthesis above, and the other one on the second term. Thus, the series  $I_4$  corresponds to the potential due to the source tip  $(I^-)$  and all its images and the series  $I_1$  corresponds to the drain tip  $(I^+)$  and all its images.

$$I_1 = \frac{\rho I}{2\pi} \sum_{n = -\infty}^{\infty} \frac{2}{\sqrt{v^2 + (2nt)^2}}$$
 (2.95)

$$I_4 = \frac{\rho I}{2\pi} \sum_{n = -\infty}^{\infty} \frac{2}{\sqrt{v^2 + s^2 + (2nt)^2}}$$
 (2.96)

Noticing  $(+n)^2 = (-n)^2$  and then taking the difference of  $I_1$  and  $I_4$ , the voltage difference

$$\Delta V = \frac{\rho I}{2\pi} \left[ \left( \frac{2}{v} - \frac{2}{\sqrt{v^2 + s^2}} \right) + 2 \sum_{n=1}^{\infty} \left( \frac{2}{\sqrt{v^2 + (2nt)^2}} - \frac{2}{\sqrt{v^2 + s^2 + (2nt)^2}} \right) \right]$$
(2.97)

is found. The correction factor thus reads

$$F_{t} = \frac{1}{1 + \left(\frac{2}{1 - \frac{1}{\sqrt{v^{2} + s^{2}}}}\right) \sum_{n=1}^{\infty} \left(\frac{1}{\sqrt{v^{2} + (2nt)^{2}}} - \frac{1}{\sqrt{v^{2} + s^{2} + (2nt)^{2}}}\right)}.$$
 (2.98)

Figure 2.13(c) shows plots of the correction factor  $F_t$ , again for different aspect ratios. As was already observed for  $F_{\parallel}$  in section 2.6.2.2,  $F_t$  is rather similar for different aspect ratios l/v. In this case, however, the correction factor in fact converges to 0 for small t/v. There is no straightforward limit of Eq. (2.98) for small t/v, as was the case for  $F_{t,\text{lin}}$  (compare section 2.6.1). Therefore, the 2D limit of Eq. (2.98) was not calculated. However, in a double logarithmic scale,  $F_t$  is similar to  $F_{t,\text{lin}}$ , thus a 2D limit of  $F_t$  is expected to exist. The change from the intermediate regime to the 3D regime at large t/v is now dependent on the aspect ratio s/v of the rectangle. Evaluating  $F_t$  when s=v, excellent numerical agreement with values published by Uhlir for a square on a finite sample was obtained [39].

Due to the infinite series in Eq. (2.98), the question arises, at which N the summation can be interrupted when  $F_t$  is evaluated. To aide in the selection of N, the convergence of Eq. (2.98) is analyzed in Fig. 2.13(d). The correction factor  $F_t$  is calculated for a few combinations of s/v and t/v as a function of the summation limit N. The plot shows  $F_t(N)$  normalized to  $F_t(1000)$ . Obviously, for smaller t/v, the number of summations N has to be larger in order to achieve a reasonable small error. A standard value of N = 1000 is selected, as it is deemed sufficient for all practical purposes. Comparing Fig. 2.13(d) with Fig. 2.12, there appears to be a significant difference in the convergence behavior of  $F_{\parallel,\log}$  and  $F_t$ . Equation (2.98) is similar to expressions for the correction factor  $F_{t,\text{lin}}$  (c.f. section 2.6.1) using a series [28, 66]. For small t/s, this series is known to converge very slowly [66]. In Eq. (2.89)  $(F_{\parallel,\log})$ , however, only every other term is the square root of two distances along orthogonal directions. Thus, the convergence behavior of Eq. (2.89) can be expected to differ from Eq. (2.98).

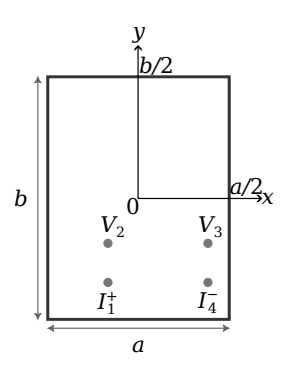


Fig. 2.14.: A rectangular flake with four tips in an arbitrary position. The origin of the coordinate system is in the center of the flake. After [45, Fig. 1].

#### 2.6.4. Cuboid and rectangular samples

Due to its crystal structure,  $\alpha$ -Bi<sub>4</sub>Br<sub>4</sub> tends to form long rectangular flakes. To describe these flakes two different correction factors can be combined, one for thin flakes [45] and another one for rectangular cuboid samples.

#### 2.6.4.1. Correction factor for 2D rectangular samples

Perloff derived a correction factor for an arbitrary tip geometry on a rectangular conductive sheet with insulating edges using conformal mapping [45]. Consequently, the Jacobi elliptic functions sn, cn, and dn  $^{7}$  [71] are needed to evaluate this correction factor. The correction factor is given by

$$k = \frac{4\pi}{\ln\left(\frac{\alpha_1 \alpha_2}{\alpha_3 \alpha_3}\right) + \ln\left(\frac{\beta_1 \beta_2}{\beta_3 \beta_3}\right)} \quad \text{with}$$
 (2.99)

$$\rho = ktR. \tag{2.100}$$

Thus, this correction factor also includes the geometrical factor. This offers the great advantage that the tips can be placed anywhere on the rectangular sample. An example for this tip placement is given in Fig. 2.14, note the choice of origin for the coordinate system. One only has to choose tip 1 and 4 as the current injection tips. The  $\alpha_i$  and  $\beta_i$  are given by:

$$\alpha_{1} = (v_{2} - v_{4})^{2} + (u_{2} - u_{4})^{2}$$

$$\alpha_{2} = (v_{2} + v_{4})^{2} + (u_{2} - u_{4})^{2}$$

$$\alpha_{3} = (v_{2} - v_{1})^{2} + (u_{2} - u_{1})^{2}$$

$$\beta_{2} = (v_{3} + v_{1})^{2} + (u_{3} - u_{1})^{2}$$

$$\beta_{3} = (v_{3} - v_{4})^{2} + (u_{3} - u_{4})^{2}$$

$$\beta_{4} = (v_{3} + v_{1})^{2} + (u_{3} - u_{1})^{2}$$

$$\beta_{4} = (v_{3} + v_{1})^{2} + (u_{3} - u_{1})^{2}$$

<sup>&</sup>lt;sup>7</sup>When computing the correction factor, it is advisable to verify the output of the Jacobi elliptic functions first!

The parameters  $v_i$  and  $u_i$  are calculated by first solving [45]

$$\frac{K(1-m)}{K(m)} = \frac{2b}{a} \tag{2.101}$$

numerically, where K(m) is the complete elliptic integral of the first kind [71], and a and b are the width and the length of the flake, respectively. Compare also Fig. 2.14. With the known parameter m, the normalized coordinates can be computed [45]

$$x' = 2K(m)\frac{x}{a},$$
  $y' = 2K(m)\frac{y+b/2}{a}.$  (2.102)

Now, the values of  $u_i$  and  $v_i$  can finally be computed:

$$u(x,y) = \frac{\operatorname{sn}(x',m) \cdot \operatorname{dn}(y',1-m)}{\left(\operatorname{cn}(y',1-m)\right)^2 + m\left(\operatorname{sn}(x',m) \cdot \operatorname{sn}(y',1-m)\right)^2}$$
(2.103)

$$u(x,y) = \frac{\operatorname{sn}(x',m) \cdot \operatorname{dn}(y',1-m)}{\left(\operatorname{cn}(y',1-m)\right)^2 + m\left(\operatorname{sn}(x',m) \cdot \operatorname{sn}(y',1-m)\right)^2}$$

$$v(x,y) = \frac{\operatorname{cn}(x',m) \cdot \operatorname{dn}(x',m) \cdot \operatorname{cn}(y',1-m) \cdot \operatorname{cn}(y',1-m)}{\left(\operatorname{cn}(y',1-m)\right)^2 + m\left(\operatorname{sn}(x',m) \cdot \operatorname{sn}(y',1-m)\right)^2}.$$
(2.103)

#### 2.6.4.2. Correction factors for 3D cuboid samples

Yamashita et al. derived a correction factor and equations for the potential in a cuboid with an in-line tip geometry. The two voltage probing tips are placed between the current injection tips. The correction factor can be found in Ref. [68].

Additionally Yamashita derived also a correction factor for a rectangular tip placement [69, 70]. The most readable print can be found in Ref. [70]. Note the choice of coordinate system for this correction factor. For thin samples, numerical evaluation of this correction factor yields the same result as Eq. (2.99) for 2D sample. This can be used to analyze, if a given combination of sample and tip configuration can be approximated as a 2D sample. This is especially useful, when a target sample thickness for exfoliation has to be selected.

The numerical evaluation of the correction factor is a somewhat difficult task. Depending on the input parameters, the convergence can be slow. Moreover, in some situations, NANs can turn up in some of the intermediate results, poisoning the complete result and hindering the evaluation of higher terms in the infinite sums. This problem can be solved by storing intermediate results in 128 bit float variables.

## 2.7. Permutation of tips

As will be discussed in detail the following section, the four-tip STM allows to use each individual tip both as a current injection tip and a voltage probing tip. Consequently, for a fixed but arbitrary contact geometry, there are 4! = 24 different resistances, that can be measured, by permuting the current and voltage contacts, without changing the physical position of the tips. The majority of these resistances, however, are not independent and do not yield any more information on the sample. Exchanging the two current injection tips, will only reverse the direction of current flow and thus the sign of the resistance. Similarly, interchanging the voltage probing tips will change the direction of the voltage drop and thus also the sign of the resistance. This already excludes the majority of the permutations, leaving six different tip configurations [72, 73].

The reciprocity theorem for linear passive electrical networks provides a further reduction in the number of different resistances that can be measured by changing the roles of the tips [36, 74; 75, pp. 148-153]. This theorem states, that in a passive, linear network, the points of observation and the points of excitation are interchangeable without changing the ratio of excitation to observation, as long as one of these is a voltage and the other a current [75, pp. 148-153]. This means in the case of a four-probe measurement, that the current injection tips can be exchanged with the voltage probing tips without changing the measured resistance. See also [42, pp. 33-36]. Thus, there are only three different resistances, that can be measured in a four probe transport measurement.

Rymaszewski gives a complete theory for finite thin film samples, linking the three resistances measurable in an arbitrary tip configuration [73]. The calculations are based on the method of conformal mapping. This method allows to calculate the correction factor for the given tip placement on a finite 2D sample from measurements of the resistivity in all three configurations [73]. Furthermore, there are some proofs in the literature showing a relation between these three resistances such that there are only two independent resistances that can be measured: [36, 72, 76], and [42, pp. 33-36]. Worledge alleges that "it is easy to show, that"

$$R_{\rm III} = R_{\rm I} - R_{\rm II}.$$
 (2.105)

for the 2D case [72].

In the following, Eq. (2.105) shall be proven both for the 2D and the 3D case using Eq. (2.11) and (2.2). The three configurations of the tips are shown in Fig. 2.15. Note, the actual tip placements are arbitrary with arbitrary inter-tip distances a to f. The three configurations refer only to the different tip permutations.

For configuration I, the voltage drop  $V_2 - V_3$  is proportional to

$$V_2 - V_3 \propto \ln(a) - \ln(c) - [\ln(b) - \ln(d)] = \ln\left(\frac{ad}{cb}\right)$$
 (2.106)

The voltage drops for the other two configurations can be found in the same manner. Thus, in the 2D case, Eq. (2.11) yields the resistances

$$R_{\rm I,2D} = \frac{\rho}{2\pi t} \ln\left(\frac{ad}{cb}\right),\tag{2.107}$$

$$R_{\rm II,2D} = \frac{\rho}{2\pi t} \ln\left(\frac{ef}{bc}\right)$$
, and (2.108)

$$R_{\rm III,2D} = \frac{\rho}{2\pi t} \ln\left(\frac{ad}{ef}\right). \tag{2.109}$$

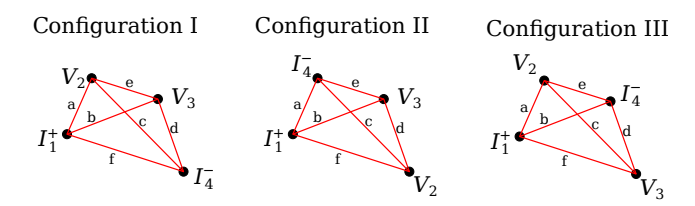


Fig. 2.15.: Sketch for diagonal current injection.

Now, the difference  $R_{\rm I}-R_{\rm II}$  can be calculated:

$$R_{\text{I,2D}} - R_{\text{II,2D}} = \frac{\rho}{2\pi t} \ln\left(\frac{ad}{cb}\right) - \frac{\rho}{2\pi t} \ln\left(\frac{ef}{bc}\right) - \frac{\rho}{2\pi t} \ln\left(\frac{ef}{bc}\right)$$

$$= \frac{\rho}{2\pi t} \left(\ln(ad) - \ln(cb) - \left[\ln(ef) - \ln(bc)\right]\right)$$

$$= \frac{\rho}{2\pi t} \ln\left(\frac{ad}{ef}\right). \tag{2.110}$$

Thus, the proposition in Eq. (2.105) is obviously proven for infinitely large, isotropic, two-dimensional sheets.

Similarly, using Eq. (2.2), the resistances in the 3D case can be calculated:

$$R_{\rm I,3D} = \frac{\rho}{2\pi} \left( \frac{1}{a} + \frac{1}{d} - \frac{1}{b} - \frac{1}{c} \right),$$
 (2.111)

$$R_{\rm II,3D} = \frac{\rho}{2\pi} \left( \frac{1}{e} + \frac{1}{f} - \frac{1}{b} - \frac{1}{c} \right)$$
, and (2.112)

$$R_{\rm III,3D} = \frac{\rho}{2\pi} \left( \frac{1}{a} + \frac{1}{d} - \frac{1}{e} - \frac{1}{f} \right).$$
 (2.113)

The difference is then

$$R_{\text{I,3D}} - R_{\text{II,3D}} = \frac{\rho}{2\pi} \left( \frac{1}{a} + \frac{1}{d} - \frac{1}{b} - \frac{1}{c} \right) - \frac{\rho}{2\pi} \left( \frac{1}{e} + \frac{1}{f} - \frac{1}{b} - \frac{1}{c} \right)$$

$$= \frac{\rho}{2\pi} \left( \frac{1}{a} + \frac{1}{d} - \frac{1}{b} - \frac{1}{c} - \left[ \frac{1}{e} + \frac{1}{f} - \frac{1}{b} - \frac{1}{c} \right] \right)$$

$$= \frac{\rho}{2\pi} \left( \frac{1}{a} + \frac{1}{d} - \frac{1}{e} - \frac{1}{f} \right)$$
(2.114)

Thus, the proposition in Eq. (2.105) is proven for the case of an isotropic, semi-infinite bulk sample, as well.

Since these proofs do not rely on any specific tip geometry, Eq. (2.105) is also valid for anisotropic samples. It is obviously valid for the equivalent isotropic sample with resistance  $\bar{\rho}$  and with inter-tip distances a' to f'. Rewriting a' using Eq. (2.33), however, is not as simple as presented in section 2.3: First, the inter-tip distances have to be separated into their x and y components:

$$\underline{a} = \begin{pmatrix} a_x \\ a_y \end{pmatrix}, \tag{2.115}$$

with  $a = \sqrt{a_x^2 + a_y^2}$ . Then a' can be expressed as

$$a' = \sqrt{{a_x'}^2 + {a_y'}^2} = \sqrt{{a_x}^2 \frac{\rho_x}{\bar{\rho}} + {a_y}^2 \frac{\rho_y}{\bar{\rho}}}.$$
 (2.116)

Similar expressions can be obtained for b' to f', which then could be used to write down Eq. (2.105) explicitly for anisotropic samples.

Lastly, the case of finite samples will be discussed. As stated in section 2.6.1, in the limit of a thin enough sample with insulating top and bottom surfaces, the sample can be described as two dimensional for a transport experiment in a linear, equidistant tip configuration. While this limit cannot be written down explicitly for the case of a rectangular tip configuration (see section 2.6.3), it seems reasonable to assume that this 2D limit exists in general. Indeed, it can be written down if a square tip configuration on a sample of finite thickness is considered [39]. Thus, the proposition Eq. (2.105) has been proven to be correct for both the limit of an infinitely thick sample and for thin sample. Therefore, the proposition is expected to be valid in general for samples of thickness t with insulating top and bottom surfaces. An explicit proof, however, would require to derive the correction factor  $F_t$  for the configurations I, II, and III.

As was already alluded to above, for two-dimensional samples, that are bound by a simple closed Jordan curve and that have an insulating boundary, Rymaszewski derived a complete theory using conformal mapping [73]. The explicit purpose of this theory is to obtain the correction factors for a given thin sample from a series of measurements. However, in Ref [73], no general proof of Eq. (2.105) is given. Also, the expressions that are derived in Ref. [73] are cumbersome to use except for specific sample geometries. In the case of finite bulk samples, such a general theory was not found in the literature. If necessary, the validity of Eq. (2.105) can be checked by calculating the relevant correction factors.

# 3. Measuring resistances with a four-tip STM

While the previous chapter dealt with the relationship of the four-probe resistance to the (anisotropic) resistivity, this chapter shall discuss the actual measurement of resistances using a four-tip scanning tunneling microscope (four-tip STM).

# 3.1. The four-tip STM

A four-tip STM [24, 40, 77] integrates four individual scanning tunneling microscopes (STM) [25, 26, 78] into a single unit. STMs have been in use in surface science for four decades, for a complete introduction refer to Ref. [79, 80]. In principle, a four-tip STM can still provide access to most single tip STM techniques, that are known from the literature, such as constant height, and constant current topography, scanning tunneling spectroscopy (STS) etc. However, the main focus of a four-tip STM is the measurement of electrical transport data, using the STM tips to inject currents and measure voltages [40]. For these measurement, the tips are placed in hard (i.e. ohmic) contact on the sample surface, using the tip configurations discussed in the previous chapter. Furthermore, while scanning tunneling potentiometry [81] can be implemented in a single tip STM (e.g. [82]), a four-tip STM allows to apply the transport field with contacts created in situ [83]. Therefore, also the hardware and software of a four-tip STM are adapted to this goal. Thus, the main purpose of a four-tip STM is to combine a nano-prober with an STM.

Figure 3.1(a) displays a cross section of a four-tip STM used for this work. While there are multiple different designs of four-tip STMs, this drawing still highlights the main design features [24, 40, 77, 84]:

- Each tip is mounted in one corner of the instrument on its own piezo motors for coarse and fine motion.
- The tips are mounted with an angle  $\sim 45^{\circ}$  with respect to the sample surface.
- A visual light microscope or scanning electron microscope (SEM) is mounted with its optical axis normal to the sample surface to facilitate tip positioning.

Figure 3.1(b) illustrates another main feature of a four-tip STM: to enable the transport experiments, current can be injected through each tip. Conversely, also the voltage can be measured at each tip. In the four-tip STM used in this work, this was achieved using special amplifiers: to measure currents, a biased preamplifier is used; a voltage follower measures the voltages. The room temperature four-tip STM used for most of the transport measurements is presented in more detail in Refs. [77; 44, pp. 34-50; 42; 43, pp. 3-5].

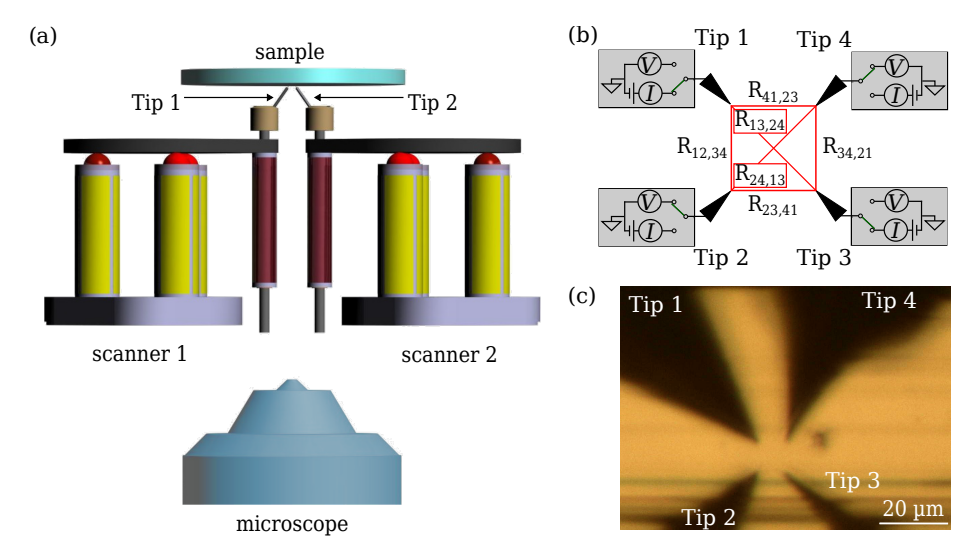


Fig. 3.1.: (a) A sketch illustrating the operational principle of a four-tip STM. Modified from [77] (b) Drawing showing the different resistance configurations, that can be measured. The gray boxes symbolize the biased preamplifiers/voltage followers. The electronics are set up to measure the resistance  $R_{13,24}$  (The first two indices indicate the current-injection tips). (c) View of the four tips through the optical microscope. The tips are arranged in a square on a sample.

As tips, standard electro-chemically etched tungsten tips are used [85; 79, pp. 344-346; 80, pp. 50-51]. In contrast to tips for standard single tip STM, the tips are etched to be longer to ensure that the sample is contacted with the tip apex and not with its shaft [44, pp. 10-11, pp. 27-30]. For some measurements, also commercial platin iridium tips by Unisoku [P-100PtIr(S)] are used. In the measurements, however, no appreciable difference between the Pt/Ir and the W tips is observed. Both kinds of tips can be seen in the optical micrograph displayed in Fig. 3.1(c): Tips 1 and 2 are PtIr-tips, whereas tips 3 and 4 are W-tips.

One main difference between a four-tip STM and a conventional single-tip STM are the electronics for generating the tunneling voltage  $V_{\rm bias}$  and measuring the tunnel current  $I_{\rm t}$ . The four-tip STM is operated by modified Createc hardware and software. The STM controller supplies the digital-to-analogue (DAC) and analogue-to-digital (ADC) converters necessary for each tip. The feedback-loops are run with a single digital signal processor (DSP). Due to the limited amount of Input-Output channels available with the single DSP, the DACs for the tunneling voltages  $V_{\rm bias}$  have only 16 bit, all other ADCs and DACs have 20 bit. The Createc electronics features two ADC inputs per tip, numbered from 0 to 7. The even numbered ADCs are used for measuring the current. The odd numbered ADCs can be used for to measure the voltage, however, if the gain set on the DLPCA-200 is known, the signal recorded by the even numbered ADCs can also be used for the voltage measurement. For each tip, there are two ADC inputs, one for

<sup>&</sup>lt;sup>1</sup>The voltage read at the even numbered ADCs is automatically multiplied by the gain set on the DLCPA-200 to recover the measured current in ampere.

the current (even numbered) and one for the voltage (odd numbered). See also Refs. [42, pp. 8-10; 44, p.37-39].

In a single-tip STM, the voltage source for biasing  $(V_{\text{bias}})$  either sample or tip is usually placed on one side of the tunneling junction and the (ideal) ampere meter to measure the tunneling current  $I_{\rm t}$  on the other. In principle, both the voltage source and the ampere meter can be placed on the same side of the tunnel junction without any issue. However, in an actual STM, due to the small current of typically a few 10 pA to nA, the tunneling current  $I_t$  is usually measured with a transimpedance amplifier. A transimpedance amplifier outputs a voltage  $V_t$ , that is proportional to the input current. This voltage is usually measured with respect to ground [34, pp. 504-508; 79, pp. 313-314; 80, pp. 86-88]. However, if the transimpedance amplifier is on bias potential (i.e. it is placed on the same side as the voltage source) as is the case here, its output voltage is in fact  $V_t + V_{\text{bias}}$ , from which  $V_{\text{bias}}$  has to subtracted [84]. In a single-tip STM, this complication is easily avoided. Of course, this complication can be avoided in a four-tip STM as well, but this sacrifices the ability to select the tunneling setpoint and the  $V_{\text{bias}}$  for each tip individually. Furthermore, by adding a voltage measurement circuit, the transport measurements can also be carried out with the STM hardware and electronics [84]. This eliminates a large number of possible errors when setting up a transport measurement. The electronics will be addressed in more detail in the following section.

#### 3.1.1. The Black Box

The Black Boxes are the current and voltage amplifiers of the four-tip STM used in this work. They are used both for STM measurements and for transport experiments. The Black Boxes expose one triaxial socket one side, used to connect each Black Box to its respective tip. On the other side, they feature four sockets for the measurement signal, the bias voltage to apply, a digital control signal, and the power supply. A standard Black Box has two different modes of operation: the voltage-probe mode and the currentprobe mode. Simplified circuit diagrams showing the main components of both modes are displayed in Fig. 3.2. Switching between the two modes is done with two relays: one at the triaxail socket, choosing which part of the circuitry the tip is connected to, and a second relay, choosing what the output of the Black Box is connected to. For current measurements, the Black Boxes use the variable gain transimpedance amplifier DLPCA-200, produced by Femto [86]. Voltages are measured with a voltage follower. The measurement software switches the operating mode and the gain of the DLPCA-200 using the digital connection. The digital control signal uses four bits, one for change from current probe mode into voltage probe mode, three for setting the gain of the Femto DLPCA-200. These control bits of each tip are represented as nibbles of a 32-bit control word, that is saved during the four-probe transport measurement. Thus, the use of the tips can be reconstructed from the data. However, in voltage probe mode, the measured voltage is read in using the same ADC as the current and thus stored in the same data channel as the current. To recover the voltage, the current amplification set at the DLPCA-200 needs to be known.

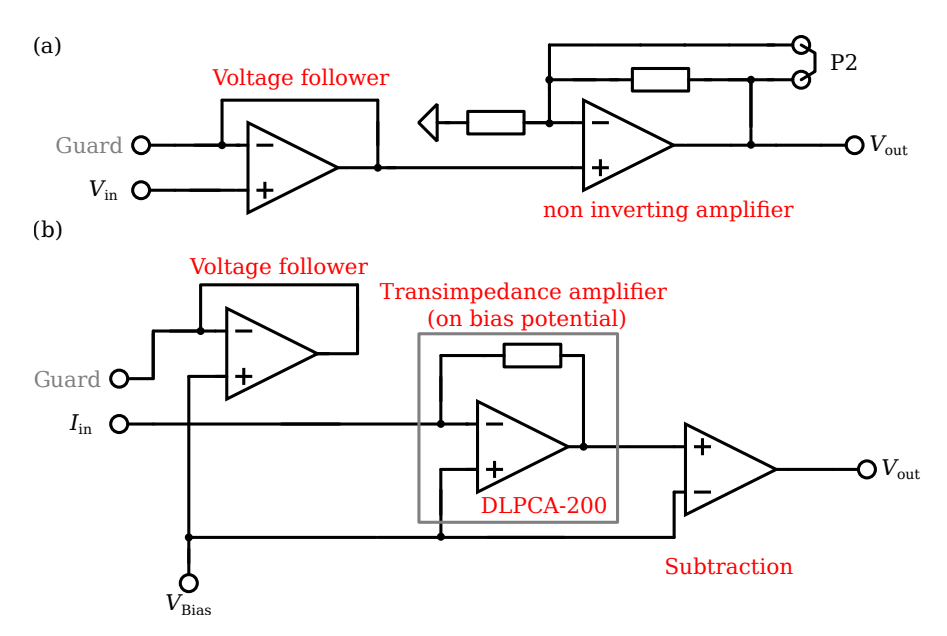


Fig. 3.2.: Simplified circuit diagrams of the Black Box for (a) the voltage-probe mode, and (b) the current-probe mode.

#### 3.1.1.1. Voltage-probe mode

In the voltage-probe mode, the tip (via the central conductor of the triaxial cable) is connected to the input of a voltage follower. For the voltage follower, an operational amplifier with a very high input resistance is used. The output voltage of the voltage follower is also connected to the inner shield of the triaxial cable (guard) to reduce the influence of the capacitance between the central conductor and ground. The other relevant part of the circuitry is a non-inverting amplifier [34, pp. 132-135]. Using the jumper P2, the gain 1 or 100 can be chosen. A simplified circuit diagram is shown in Fig. 3.2(a).

#### 3.1.1.2. Current-probe mode

A simplified circuit diagram of the current-probe mode is shown in Fig. 3.2(b): When the Black Box is set to current-probe mode, the tip (via the center conductor of the triaxial cable) is connected to the input of the DLPCA-200 [inverting input in equivalent circuit in Fig. 3.2(b)]. The ground input (non-inverting input) of the DLCPA-200 is connected to the bias voltage. Thus, the DLPCA-200 outputs  $V_t + V_{\text{bias}}$ , with  $V_t \propto I_t$ . A voltage difference amplifier then removes  $V_{\text{bias}}$  from the output voltage of the DLPCA-200 by analogue subtraction. The inner shield (guard) of the triaxial cable is connected to the output of the voltage follower, whose input is also connected to the bias voltage  $V_{\text{bias}}$ . Thus, the guard of the triaxial cable is kept at  $V_{\text{bias}}$ , reducing the influence of parasitic capacitances (e.g. the capacitance of the cables themselves) [87, pp. 352-353]. The current-probe mode mode is used for current injection during transport measurements and also for STM and STP measurements. According to measurements by  $Timofey\ Balashov$ , modulating the voltage applied to the bias voltage

input of the Black Box would give rise to a resonance like behavior of the measured current, even at low modulation frequencies ( $\sim 100\,\mathrm{Hz}$ ). Therefore, all measurements were taken as quasi-dc measurements using long times ( $t \sim 10\,\mathrm{s}$ ) for the voltage ramps (see section 3.3).

#### 3.1.2. The four-tip STMs used in this thesis

For the work presented in this thesis, the two four-tip STMs of PGI-3 at the Forschungszentrum Jülich GmbH were used. Furthermore, the Scienta-Omicron four-probe STM of the Oak Ridge National Laboratory, Tennessee, USA, was used. At the latter instrument, however, mainly single tip measurements were performed.

The first Jülich four-tip STM used here is operated at room temperature and uses an optical microscope for tip positioning. The instrument is presented in more detail in Refs. [77; 42, pp. 8-12; 44, p. 35-53].

The second system used in Jülich features an STM of slightly different design, which, nevertheless follows the principles outlined above. The key features of this instrument, however, are a cryostat, enabling operation at 77 K and 4 K, and a scanning electron microscope (SEM) with electrostatic lenses. SEM images are recorded using the sample current as signal (c. f. Ref. [88, p. 233]). Therefore, the SEM cannot be used when a tip is in hard contact. Due to the bandwidth of the transimpedance amplifier, using the sample current for images also limits the SEM scan speed. Furthermore, the shadow of the tips cannot be used as an aid during approach, c.f. Ref. [89, pp. 26-27 & pp. 44-45]. The low-temperature four-tip STM is introduced in more detail in Ref. [90, pp. 45-68].

#### 3.2. Calibration measurement electronics

In principle, two components of the four-tip STM electronics need to be calibrated: the amplifiers and the ADCs and DACS of the control electronics. Calibration procedures are given in appendix B on page 117. All ADCs and the bias DACs have two parameters, that can be adjusted in the measurement software: the gain, g, and the offset, o. During data analysis of a four-probe transport measurement, the resistance is found from a linear fit of the measured current and voltage drop [compare Fig. 3.3(e)]. Both of these quantities are critically influenced by the gain of the ADCs. The offset merely shifts the y-intercept of the fit. The ADC-calibration is applied by the STM software during the measurement. Consequently, applying a correction to the data after the measurement is difficult.

For four-probe resistance measurements, the ADCs of the STM electronics have to be calibrated. Calibrating the even numbered ADCs used to measure the current removes them as a source of systematic error of the current measurement. Furthermore, uncalibrated ADC offsets may create spurious dc-current signal even when  $0\,\mathrm{V}$  are applied between the current injection tips. For the four-probe measurement, the voltage difference  $\Delta V$  is calculated. Uncalibrated ADCs can drastically alter the measured voltage drop, consequently an accurate calibration of the gain is critical for a reliable measurement of the resistance. The odd numbered ADCs need to be calibrated, if they are used to read in the voltage measurement signals. The bias DACs can also be calibrated; however, as the injection voltage does not enter into the four-probe resistance, this calibration is not necessary. Nevertheless, it is still advantageous to calibrate the bias DACs, as

uncalibrated DACs can cause spurious currents when nominally  $0\,\mathrm{V}$  is applied between the current injection tips. Furthermore, calibrated bias DACs are needed for two-probe measurements. Both the DACs and the ADCs were calibrated using two Keithley-2000  $6\,1/2$  digit digital multimeters. In principle, a calibrated DAC can be used as a voltage source for the ADC calibration. Nevertheless, it is advisable to verify the input voltage with a multimeter.

Furthermore, also the voltage measured with the voltage-probe mode of the Black Box has to be calibrated. Correct calibration of the voltage measurement is of special importance when the non-inverting amplifier (see Fig. 3.2) is used, as this amplifier is rather sensitive to the tolerances of the individual resistors. A difference in gain between the two voltage-probing Black Boxes can easily induce a spurious voltage drop. This is illustrated in Fig. 3.3(d), where the voltage drop  $\Delta V$  is plotted before (orange line) and after (blue dots) applying the calibration to the measurement data. The amplifier is used, if a highly conductive sample is measured. In most practical cases, the injected current cannot be increased substantially, as high currents might damage the sample. Consequently, the actual voltage drop across the voltage-probing tips is small and a spurious voltage drop due to a missing calibration can easily cover the actual voltage drop. To calibrate a Black Box, a known voltage is applied to the triaxial tip input of the Black Box, using a coaxial to triaxial adapter, that drops the inner shield. The corresponding output voltage is then measured. The correction of the voltage measurement has to be applied during data analysis. The different gains of the Black Boxes prohibit a differential read in of the voltage drop (see [44, p. 92]). Instead, both voltage signals are read into two different ADCs. After applying the voltage correction to the data, the voltage drop is computed. As disadvantage the noise of both ADCs enters into the measurement.

In principle, also the current-probe mode of the Black Box could be calibrated. In this work, the gain of the current measurement was not calibrated. The DLPCA-200 transimpedance amplifier has a gain accuracy of 1% [86]. In most practical cases, the uncertainty of the measurement result created by this gain accuracy is negligible (see below). Furthermore, in contrast to the measurement of the voltage drop, the difference of the two measured currents is not used in the final result. Thus, minor differences in gain between the two current measuring Black Boxes cannot create a spurious measurement signal. The offset of the black-box in current probe mode can be easily included into the calibration of the ADCs. To this end, the tunnel junction is replaced by a  $1\,\mathrm{G}\Omega$  resistor, and a VI curve is measured. The offset of the respective ADC is adjusted such that  $I=0\,\mathrm{nA}$  at  $V_\mathrm{bias}=0\,\mathrm{V}$ . This procedure requires a calibrated bias DAC.

An STP measurement uses a feedback loop to set  $V_{\rm bias}$ , such that no current is flowing over the tunnel junction. If  $I_{\rm t}=0$ , then  $V_{\rm bias}$  compensates the surface potential  $\Phi$  and thus  $\Phi=V_{\rm bias}$ . It is therefore obvious, that a good calibration of the bias DACs is imperative. In this case, not only the gain, but also the offset is important. The bias circuitry of the Black Box can create a further bias offset in the range of a few mV. If deemed necessary, this last offset can first be measured using another Black Box in voltage-probe mode and corrected by adjusting the offset of the relevant DAC. For four-tip transport measurements, correcting this bias offset can be omitted.

<sup>&</sup>lt;sup>2</sup>Only the eight bias DACs can be calibrated. The bias DACs have only 16 bits. In order to reduce noise, it is advisable to use one of the other DACs (e.g. the X1 output; 20 bits) for the ADC calibration.

## 3.3. Measurement of resistances with the four-tip STM

In order to measure a four-probe resistance, the tips are first approached to the sample and placed in a specific configuration (see previous chapter). To avoid an accidental tip crash, large lateral movements are done a few z coarse steps away from tunneling contact. In the next step, the tips are approached to tunneling contact. For approach and subsequent tunneling, reasonable tunneling parameters for the material should be set (e.g.  $I_{\rm t} \sim 100\,{\rm pA}$ ;  $V_{\rm bias} \sim -0.3\,{\rm V}$  for  $\alpha$ -Bi<sub>4</sub>Br<sub>4</sub>). No voltage is applied to the sample; the sample is grounded for approach and tunneling. During this process, small positioning errors can be corrected using coarse motion with small sawtooth amplitudes, or using the fine motion piezo drives. Once a tip is in tunneling contact, one should refrain from executing coarse motion steps with any other tip. In principle, the electronics controlling the four-tip STM allow to place all four tips in tunneling contact at the same time. Care should be taken when then bringing the tips successively into hard contact, as establishing hard contact with the first tip can radically alter the potential underneath the tunneling tips. Thus, it is advisable to set a slightly different  $V_{\text{bias}}$  at each tip and also set  $V_{\text{bias}} = 0 \text{ V}$ , once hard contact has been established. The last step also prevents very high currents from occurring when the second tip is contacted. To establish hard contact, after placing the tip in tunneling contact, it is recommended to wait until the effect of piezo creep has subsided. Then, using the z-limiter function, the tip is retracted (not more than a few nm). Next, the current set-point is changed to a few hundred mA, consequently the feedback controller sets z-piezo position to the maximum extension permitted by the z-limiter, afterwards, the gain of the DLPCA-200 is set to  $10^6 \,\mathrm{VA^{-1}}$  (or similar). The tip is approached to the sample surface in small steps using the z-limiter until the measured current changes noticeably. On most samples, the current from the tip to ground of  $I \sim 0.1 \,\mu\text{A}$  can be considered to indicate a sufficiently low contact resistance. If the sample-ground contact is very insulating, a noticeable change in the tip current may only be observable once a second tip is placed in hard contact. Once all tips are in hard contact, the quality of the tip-sample contacts may be improved by pressing more with the z-limiter. A detailed contacting procedure used for the measurements on  $\alpha$ -Bi<sub>4</sub>Br<sub>4</sub> is given in appendix C on page 121.

When in hard contact, switching the gain of the DLPCA-200 or switching a Black Box to voltage probe mode may cause a voltage pulse, that can change the tip-sample contact. Therefore, switching the Black Boxes should be avoided as much as possible. However, as some measurements require different tip configurations (see section 2.7) and establishing hard contact is a rather time consuming procedure, the Black Boxes need to be switched in hard contact. In this case, the Black Boxes are switched sequentially, while the software also allows to switch all Black Boxes at the same time. Furthermore, for switching  $V_{\rm bias}=0~{\rm V}$  should be set at every tip.

After having established satisfactory contacts and having removed the ground connection of the sample, the Black Boxes are switched to the desired mode (see above) and the transport data are recorded. The two-probe measurement consisting of the measured current and the injection voltage clearly indicates the contact quality. On  $\alpha$ -Bi<sub>4</sub>Br<sub>4</sub>, the two-probe measurement needs to exhibit a linear IV-curve and a resistance of a few

<sup>&</sup>lt;sup>3</sup>This is sometimes referred to as "disabling the feedback loop". While it is true, that the feedback no longer directly changes the z-position, the feedback loop is still necessary to keep the tip at the z-piezo extension required by the z-limiter.

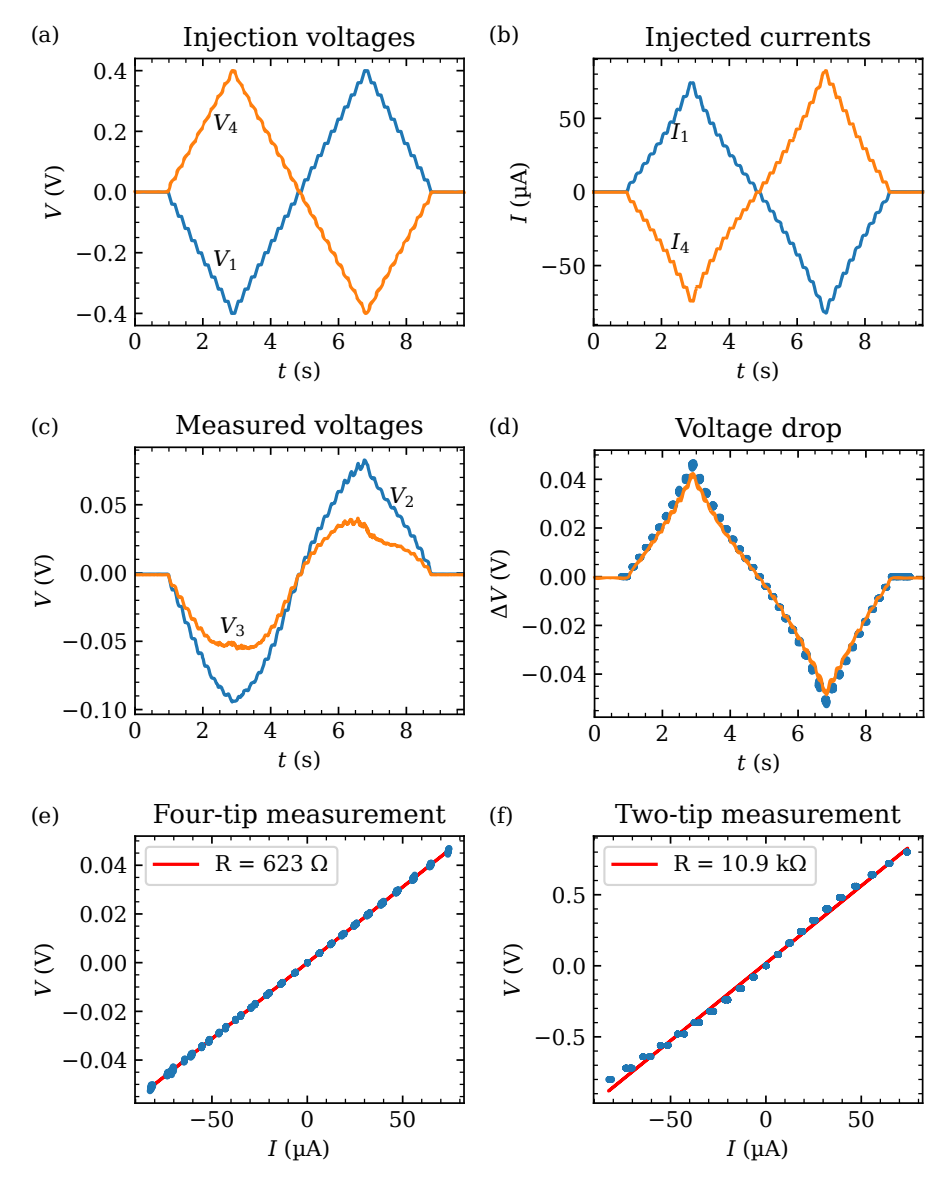


Fig. 3.3.: Example of a four-probe in-line transport experiment. (a) The symmetric voltage ramps at the current injection tips, with visible plateaus. (b) The two measured currents. Due to voltage dependent contact resistances, the maximum current is higher in the second half of the four-probe measurement. (c) The two measured voltages, without the voltage calibration of the Black Boxes. (d) The voltage drop with (blue points) and without calibration (orange line). Displaying the calibrated voltage drop as points makes the noise close to the peaks more obvious. (e) The result of the four-probe measurement. (f) The two-probe resistance. The *IV*-curve starts to show some minor non-linearities.

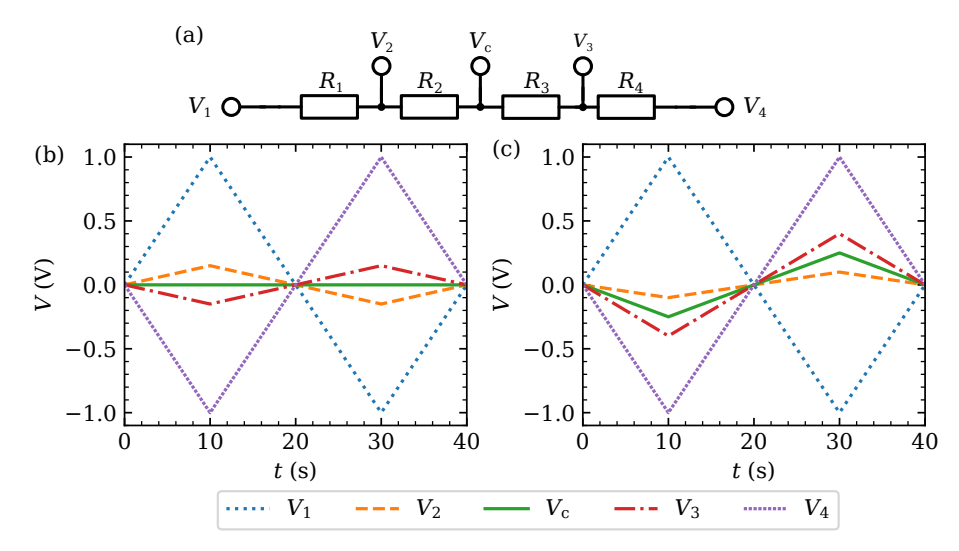


FIG. 3.4.: Asymmetry of four-probe resistance measurements. (a) Resistor chain model for the four-probe experiment. (b) Simulation of a symmetric four-probe experiment with  $R_1=R_4=850\,\Omega,\,R_2=R_3=150\,\Omega.$  Note, that  $V_{\rm c}=0\,{\rm V}$  for the complete simulation. (b) Simulation of a symmetric four-probe experiment with  $R_1=1100\,\Omega,\,R_4=600\,\Omega,$  and  $R_2=R_3=150\,\Omega.$  Now,  $V_2,\,V_{\rm c},$  and  $V_3$  are positive, when  $V_4$  is also positive and vice versa.

 $10\,\mathrm{k}\Omega$ . During a transport experiment, an anti-symmetric voltage ramp is applied to the two current injection tips, see Fig. 3.3(a). This voltage ramp features distinct plateaus, allowing for a measurement in steady-state conditions [44, pp. 87-88]. A standard ramp has a length of 10 000 points, while each plateau is 100 points wide. For analysis, the data points measured on the plateaus is extracted. The measurement time for the complete ramp is typically set to t=5 ... 60 s. If the measurement time is insufficient, the influence of parasitic capacitances becomes significant. In the example in Fig. 3.3,  $t=10\,\mathrm{s}$  was set. Thus, the effect of parasitic capacitances and the bad frequency response of the Black Boxes can be neglected. When the contact resistances are highly asymmetric, also two asymmetric voltage ramps can be chosen. A slight case of of asymmetry can be seen in the example transport measurement shown in Fig. 3.3 and will be discussed below in more detail.

# 3.4. Asymmetry of four-probe measurements

In a simple model, a four-probe measurement can be thought of as a chain of resistors, such a displayed in Fig. 3.4(a). For an in-line tip configuration, the contact  $V_c$  would correspond to a fifth tip, placed in the center of the tip configuration. For a symmetric configuration, with  $R_1 = R_4$ , and  $R_2 = R_3$ , the central voltage is always  $V_c = 0$ , as long as it holds  $V_1 = -V_4$ . Consequently, if an anti-symmetrical voltage ramp is applied to the current injection contacts  $V_1$  and  $V_4$ , then  $V_2 > 0$  when also  $V_1 > 0$ . This is demonstrated by the simulation shown in Fig. 3.4(b).

This behavior, however, is not observed in the measurement data [see Fig. 3.3(c)]. Obviously, the four-probe experiment cannot be simulated as a symmetric chain of resistors. From experimental experience [e.g. Fig. 3.3(e) and (f)], the two-probe resistance is made up almost completely of the two contact resistances. Since the current injection contacts are formed by pressing the tips into the sample, it is obvious that these tip-sample contacts are not well defined. In addition, in this example the  $R_{4P}$  only makes up  $\sim 5\%$  of the total resistance. Thus, a small difference between  $R_1$  and  $R_4$  suffices to create an asymmetric situation. This behavior can also be demonstrated by a simulation: In the simulation shown in Fig. 3.4(c), an asymmetric chain with  $R_1 = 1100 \,\Omega$ ,  $R_4 = 600 \,\Omega$ , and  $R_2 = R_3 = 150 \Omega$  was modeled. The two voltages  $V_2$  and  $V_3$  show qualitatively similar behavior as the voltages measured in the experiment [Fig. 3.3(c)]. Note, in order to make all voltages visible in the plot, the differences of the resistors was exaggerated. Furthermore, the contact resistances are weakly voltage dependent and depend on the polarity. This can be seen both in the non-linearity of the two-probe measurement displayed in Fig. 3.3(f) and from the different maximum currents in the two halves of probe measurement [Fig. 3.3(b)]. Depending on the tip-sample contacts, the asymmetry can become more pronounced. The range of the voltage measurement is  $\pm 0.1 \,\mathrm{V}$ , when the 100 times amplification of the Black Box is used. If necessary, the asymmetry of the contact resistances may be counteracted by making the voltage ramp asymmetric. The asymmetric voltage ramp is created by setting different scaling factors for the voltages applied to the two current injection tips. Thus, voltage ramps in Fig. 3.3(a) would have different heights.

#### 3.5. Uncertainties in the resistance measurements

While the calibration of the voltage measurement discussed above removes one main source of uncertainty, there are other sources of uncertainty, that will be discussed briefly. The DLPCA-200 has a gain accuracy of  $\pm 1\,\%$  [86]. Thus, the current measurement has a systematic uncertainty of the same amount. Furthermore, there is random noise in the measurement electronics. The latter uncertainty can easily be captured by repeating a transport experiment and then calculating the averages. A main source of uncertainty is related to the placement of the tips: the tip-placement error. With a simple estimate, it can be shown, that the tip-placement error is the leading source of uncertainty. For example, for a linear tip configuration on a bulk sample with the inter-tip distance  $s=20\,\mu\mathrm{m}$ , one can estimate a relative error of the resistance R of up to 20 % when assuming an uncertainty of  $1\,\mu\mathrm{m}$  for the positioning [43, pp. 12-13]. These estimates indicate an upper limit of the measurement uncertainty.

The tip-placement error is due to two factors:

- 1. the resolution of the microscope, and
- 2. a difficulty in identifying the actual contacting point of a tip.

The resolution of the optical microscope is  $\sim 1\,\mu\text{m}$ . In principle, this can be improved by using an SEM. However, the SEM installed in the low temperature system also comes with some disadvantages, such as not being able to image while the tips are in hard contact, since the sample current is used for imaging. The second factor contributing to

the tip placement error, is a difficulty in actually ascertaining the point of contact of a tip. As can be seen in Fig 3.1(c), even at their apex, the tips have a finite width. While a better resolution of the microscope might reduce this uncertainty, the possibilities of reducing this source of uncertainty are limited. The actual point of contact cannot be seen with the microscope. Furthermore, successive attempts of establishing hard contact will tend to bend the tips. This bending will move the point of contact outwards along the tip axis, compare also [43, pp. 29-31].

Instead of trying to improve upon the analytical treatment of the tip-placement error by Leis [43, pp. 12-13], a different approach to estimate the measurement uncertainty will be introduced: A numeric approach, the Monte-Carlo propagation of uncertainty, is applied to the problem [91]. As the name suggests, for each quantity entering into an equation, a distribution is assumed and a number of random samples are drawn from it. In this case, the normal distribution is used. For standard deviation of the normal distribution, the estimated error is used. For example, for a tip placed at the coordinates  $x = (20 \pm 1) \,\mu\text{m}$ , N samples are drawn from a normal distribution with mean  $\bar{x} = 20 \,\mu\text{m}$  and standard deviation  $s = 1 \,\mu\text{m}$ . Figure 3.5(a) displays such a distribution. For each set of samples, the equation is solved, yielding a new distribution, from which the mean and standard deviation can then be calculated. The resulting distribution for the example of a resistance is shown in Fig. 3.5(b). The Monte-Carlo propagation of uncertainty does not require the equations to be solved analytically. Instead, for each set of samples, the equation can also be solved numerically, provided that sufficient computation time and power is given. All computations in this thesis were done with  $N = 10\,000\,000$ .

As an example for this method, the resistance of linear measurements on a 3D and a 2D sample are simulated. Figure 3.5(c) and (e) show the dependence of the average resistance R on the inter-dip distance d, if an error of  $s=1\,\mu\mathrm{m}$  is assumed. An isotropic resistivity of  $\rho=1\,\Omega\,\mathrm{cm}$  and a thickness of the 2D layer of  $t=10\,\mathrm{nm}$  was used. The resistances were computed using Eq. (2.2) and (2.11), with the tips being placed in an in-line configuration. Note, that as expected from the discussions in section 2.1, the resistance  $R_{3\mathrm{D}}$  of the bulk sample Fig. 3.5(e) decreases  $\propto d^{-1}$  whereas the  $R_{2\mathrm{D}}$  remains constant. There is a small  $R_{2\mathrm{D}}$  for  $d<5\,\mu\mathrm{m}$ . At these small distances between the individual tips, the measurement can no longer be assumed to be equidistant, due to the uncertainty of  $1\,\mu\mathrm{m}$ . Figure 3.5(d) and (f) display the relative uncertainties. As expected, the relative uncertainties decrease with d. For the bulk sample, the relative uncertainty for  $d>5\,\mu\mathrm{m}$  is more than 1, thus it is not advisable to measure at these small distances without considerably reducing the tip-placement error. The relative uncertainty calculated using the method by Leis [43, p. 12] [red dots in Fig. 3.5(d) and (f)] is almost always larger than the relative uncertainties obtained from the Monte-Carlo method.

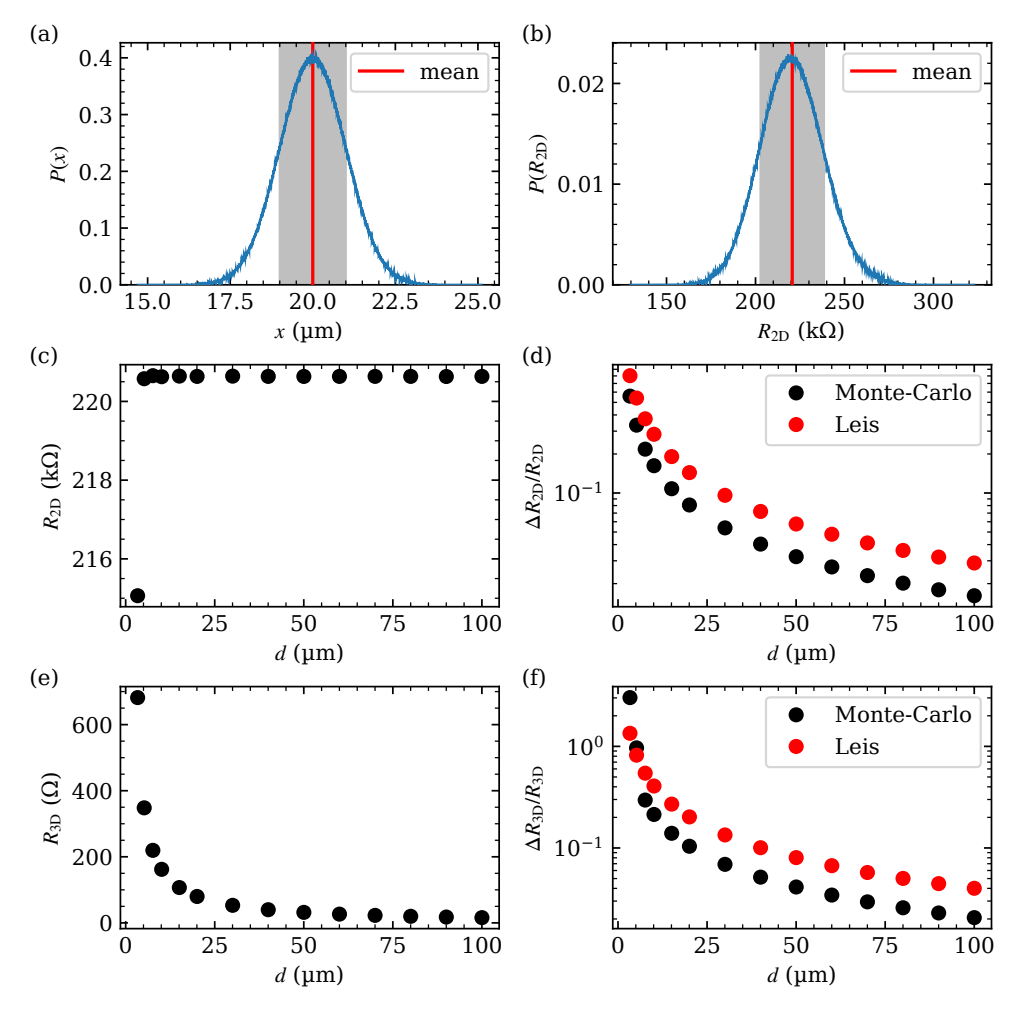


Fig. 3.5.: Monte-Carlo propagation of uncertainty for linear measurements on a 2D sheet and a 3D bulk sample with  $\rho=1\,\Omega\,\mathrm{cm},\ t=10\,\mathrm{nm},\ \mathrm{and}\ N=10\,000\,000.$  (a) Example of the distribution of for the x coordinate of one tip. (b) Resulting distribution for  $R_{\mathrm{2D}}$ . (c) Calculated resistance  $R_{\mathrm{2D}}$  for a 2D sample. (d) Resulting relative errors: The black dots are the obtained from the Monte-Carlo calculation, the red dots are calculated from the estimation in [43, p. 12]. (e) Calculated resistance  $R_{\mathrm{3D}}$  for a bulk sample. (f) Resulting relative errors: The black dots are the obtained from the Monte-Carlo calculation, the red dots are calculated from the estimation in [43, p. 12].

# 4. The higher-order topological insulator $\alpha$ -Bi<sub>4</sub>Br<sub>4</sub>

Bismuth halogenides (Bi<sub>4</sub>X<sub>4</sub>, X = Br, I) are a new family of topological materials. Bi<sub>4</sub>Br<sub>4</sub> and Bi<sub>4</sub>I<sub>4</sub> crystallize in similar structures consisting of isolated Bi<sub>4</sub>X<sub>4</sub>-chains, which are bonded by van-der-Waals forces, forming layers and finally the crystals. The known stable polymorphs Bi<sub>4</sub>Br<sub>4</sub> and Bi<sub>4</sub>I<sub>4</sub> crystallize in the same, monoclinic space group C2/m [12–14, 92, 93]. However, the stacking order is specific to the individual phases. While  $\alpha$ -Bi<sub>4</sub>Br<sub>4</sub> [12],  $\alpha$ -Bi<sub>4</sub>I<sub>4</sub>, and  $\beta$ -Bi<sub>4</sub>I<sub>4</sub> [13, 92] have been synthesized,  $\beta$ -Bi<sub>4</sub>Br<sub>4</sub> has not been observed [14]

The bulk  $\alpha$ -Bi<sub>4</sub>Br<sub>4</sub> crystal used in this thesis were grown by Yuqi Zhang and Zhiwei Wang. Bulk crystals can be grown by various methods from solid or solid and gaseous precursors [12, 13, 17, 18, 22, 94]. Furthermore,  $\alpha$ -Bi<sub>4</sub>Br<sub>4</sub> nanowires were grown on TiSe<sub>2</sub> by epitaxy [95, 96]. Furthermore, the structurally rather similar Bi<sub>4</sub>I<sub>4</sub> was grown on a SiC-substrate by epitaxy [97].

# 4.1. A brief introduction to topological insulators

A topological classification of matter rests on the observation that insulators behave similarly, even though the properties of their electronic band structures can be rather different. Indeed, vacuum can be described as an insulator with a band gap  $E_{\rm g}$ , a conduction band (electrons), and a valence band (positrons) [8]. A counter example to such topological trivial insulators is the integer quantum Hall effect. In the quantum Hall state, a two-dimensional electron gas is placed in an external magnetic field. Due to this external magnetic field, the electrons occupy quantized energy levels, the Landau levels. Similar to an insulator, in the quantum Hall state, an energy gap separates the highest occupied from the lowest unoccupied states. Nevertheless, applying an electric field leads to an electric current with the conductivity

$$\sigma_{xy} = N \frac{1}{R_K},\tag{4.1}$$

where N is an integer and  $R_{\rm K}=h/e^2$  is the von-Klitzing constant, which is the ratio of the elementary charge e and Planck's constant h, two exact natural constants in the International System of Units [98, p. 454]. Thus, the quantum Hall effect is an example of a state of matter which exhibits a band gap and electric conductivity at the same time. Consequently, the integer quantum Hall effect can be described as a different, topological nontrivial state of matter [8].

To classify the topological properties of matter, topological invariants are used. The first topological invariant is the Chern number  $n \in \mathbb{Z}$ , which remains constant while the Hamiltonian describing the band structure is varied, as long as the band gap is not closed

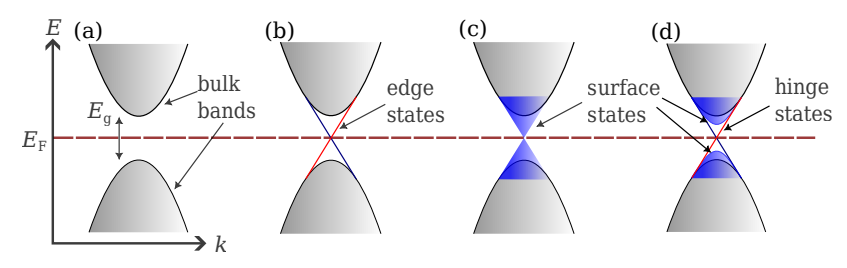


Fig. 4.1.: Simplified Band structures of (topological) insulators. The gray, filled paraboloids represent the bulk bands. (a) The band structure of a trivial insulator. (b) The band structure of a 2D quantum spin hall (QSH) insulator with the two one-dimensional, helical edge states. The colors (red and dark blue) indicate the spin polarization of the two edge states. (c) The band structure of a 3D topological insulator. The blue cone indicates the topological surface state. (d) Band structure of a higher-order topological insulator with a gapped topological surface state and one-dimensional hinge states (red lines).

[8]. The vacuum is topologically trivial and thus it has the Chern number n=0. In contrast, a quantum Hall state is topologically not trivial (n=1). Consequently, at the boundary of the quantum Hall state with the vacuum, the band gap has to be closed. The closed band gap at the boundary is the origin of the topologically protected edge states. For the presence of these edge states at the boundary of the quantum Hall state, there is an intuitive explanation. Due to the applied magnetic field, the electrons in a quantum hall state move in quantized, circular orbits. At the boundary, these circular cannot be completed. Thus, the electrons move on along the edge on (in the simplest case) connected semicircles, each individual semicircle terminating at the boundary [8].

Spin-orbit coupling (SOC) may also lead to a different topological class of band structures [8]. If a band inversion is present, SOC causes the quantum spin Hall (QSH) effect. SOC can also give rise to the band inversion, e.g. in  $\alpha$ -Bi<sub>4</sub>Br<sub>4</sub> [23, 99, 100]. The QSH effect is similar to the quantum Hall effect in that an applied electric field leads to spin polarized currents with up and down spin electrons flowing in opposite directions. However, the SOC effectively takes over the role of the applied magnetic field [8]. This effect is time-reversal invariant and can no longer be described with the Chern number n. Instead, the  $\mathbb{Z}_2$  invariant with  $\nu=0$  or  $\nu=1$  is used [8, 9]. As summarized in Ref. [8], there are different approaches to calculating the  $\mathbb{Z}_2$  invariant from a band structure, obtained from DFT calculations.

Figure 4.1 illustrates the band structures of different insulators. In Fig. 4.1(a) the standard band structure of an insulator is displayed. The top of the valence band is separated from the top of the conduction band by the band gap  $E_{\rm g}$ . Close to the band gap, the bands can be approximated by parabolas.

In addition to the bulk bands, a quantum spin hall 2D (QSH) insulator also hosts two topologically protected edge states. Its band structure is depicted in Fig. 4.1(b). A QSH insulator is characterized by  $\nu=1$ . In real space, a QSH insulator consists of a finite, insulating 2D sheet, with the two counter propagating edge states located on its boundaries. A QSH insulator can e.g. be realized as HgTe-quantum wells or monolayers of WTe<sub>2</sub>, featuring a quantized conductance given by  $1/R_{\rm K}$  [8, 10, 101].

A three-dimensional topological insulator can fall into one of multiple categories. It is characterized by four topological  $\mathbb{Z}_2$  invariants  $(\nu_0;\nu_1\nu_2\nu_3)$  [8, 11]. A strong topological insulator (STI) hosts topologically protected surface states on all of its surfaces. Thus, on all surfaces, the band structure of an STI is represented by Fig. 4.1(c). The linear dispersion relation is characteristic of the surface states of a 3D topological insulator. Because of its linearity, this feature of the band structure is also called a Dirac cone. In Fig. 4.1(c) the blue filled area represents the cone, which is rotationally symmetric about its central axis. STIs are characterized by  $\nu_0 = 1$  [11]. Weak topological insulators (WTI) are rather similar to STIs. However, the topologically protected surface states are present only on some specific surfaces. WTIs have  $\nu_0 = 0$ , while at least one  $\nu_i = 1$  (i = 1, 2, 3). A WTI can be visualized as a stack of QSH insulators [11]. An example of such a WTI is  $\beta$ -Br<sub>4</sub>I<sub>4</sub> [17].

Higher-order topological insulators (HOTI) combine the topologically protected surface states present on some surfaces known from WTIs with *gapped* surface states on other surfaces and one-dimensional hinge states [102, 103]. A HOTI is a generalized topological crystalline insulator (TCI) [104]. The band structure of a TCI is classified as topologically trivial or non-trivial due to the crystals symmetries in addition to time reversal symmetry [104]. The hinge states of a HOTI are reminiscent of the edge states on a QSH insulator. A HOTI, however, hosts these hinge states only where two specific surfaces meet [102]. Figure 4.1(d) presents the band structure of a HOTI with the bulk band gap (gray), the gapped topological surface states (blue) and the one-dimensional hinge states (red and dark blue lines) [22].

As already touched upon, in the QSH effect, spin up and spin down electrons will flow in opposite directions in an applied field. Thus, one hallmark property of the topological edge and surface states is the spin-momentum locking [105]. As the name implies, spin-momentum locking links the direction of movement of an electron in a topological edge or surface state to its spin. Edge states that feature spin momentum locking and that allow transport in both directions along a boundary are referred to as *helical* edge states. Consequently, a scattering from one edge state to the other in Fig. 4.1(b) necessitates an additional change of spin. When using a ferromagnetic tip for one voltage-probing contact in a four-probe measurement, this leads to the spin voltage, an additional voltage offset [106]. In an ultra thin (a few nm) STI, the scattering between the top and bottom surface states becomes dominant, lifting the spin-momentum locking [107]. Furthermore, transport through topological edge and surface states is ballistic [8, 10].

# 4.2. Crystal structure of $\alpha$ -Bi<sub>4</sub>Br<sub>4</sub>

 $\alpha$ -Bi<sub>4</sub>Br<sub>4</sub> crystallizes in a base-centered monoclinic structure with space group C2/m [12]. The lattice constants are  $a=1.3064\,\mathrm{nm},\ b=0.4338\,\mathrm{nm},\ c=2.0061\,\mathrm{nm},\ \mathrm{and}$   $\triangleleft ac\equiv\beta=107.42^\circ$  [12]. Figure 4.2(a) shows an atomic model of  $\alpha$ -Bi<sub>4</sub>Br<sub>4</sub> projected along the b axis. The unit cell is indicated with a black parallelogram.  $\alpha$ -Bi<sub>4</sub>Br<sub>4</sub> has two cleavage surfaces [22], the (100) and the (001) surfaces. The two planes are indicated by the red and blue dashed lines, respectively.  $\alpha$ -Bi<sub>4</sub>Br<sub>4</sub> exhibits AB-type stacking along the c-direction, with chains with S- and Z-shaped cross sections stacked on top of each other. Due to the AB stacking, the (001) surface can either consist of an A or of a B layer. In the projection of Fig. 4.2(a), the layers are distinguished by the topmost Br

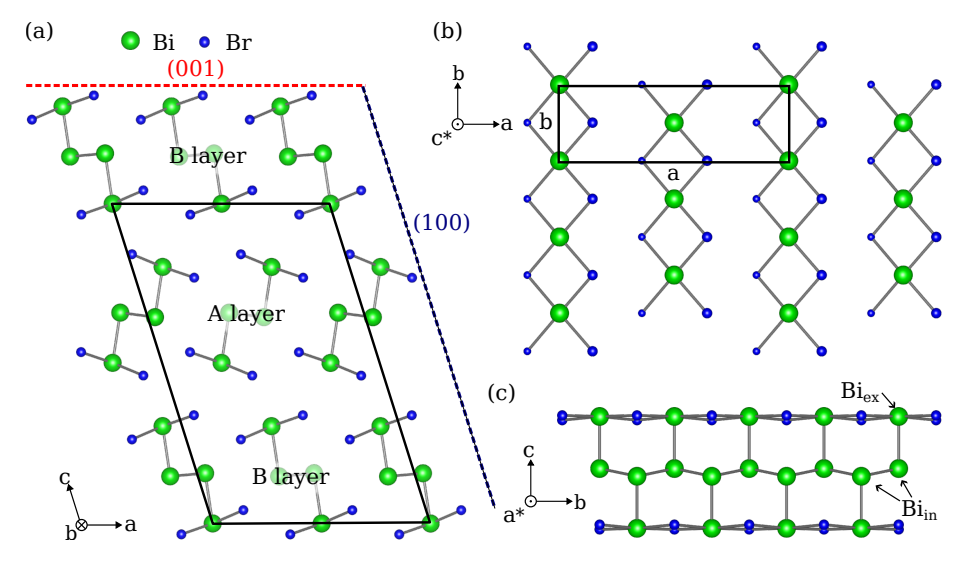


Fig. 4.2.: Atomic crystal models of  $\alpha$ -Bi<sub>4</sub>Br<sub>4</sub> [12]. (a) A side-view of the unit cell, projected along  $\underline{b}$ -direction. The AB stacking is clearly visible. The unit cell is indicated by the black parallelogram. The two cleavage surfaces are indicated using red and blue dashed lines. This side view of the unit cell also corresponds to the (010) surface. (b) Top-view of (001) surface. Due to the AB stacking, there are two (001) surfaces per unit cell, that differ in whether the top-most Br atom is left or right of the Bi atom. In this case, the (001)B surface is depicted. The lower Br is indicated by a smaller size. For clarity, only the topmost atoms are shown. (c) Side-view of a single chain, projected along the  $\underline{a}^*$  direction.

atom placed either to left (A) or to the right (B) of the Bi atom [20, 108]. The side-view of the unit cell [Fig. 4.2(a)] also corresponds to a model of the (010) surface. This surface cuts through the chains and is consequently impossible to access via cleaving.

Figure 4.2(b) displays a top-view of the  $(0\,0\,1)$ B surface. The model is projected along its surface normal, the reciprocal lattice vector  $\underline{c}^*$ . The projected bulk unit cell is indicated by the black parallelogram, the lower Br atoms are indicated by a smaller diameter. Two neighboring chains are shifted by b/2 with respect to each other. This can be clearly seen in the rectangular surface unit cell spanned by the lattice vectors  $\underline{a}$  and  $\underline{b}$ . In the top-view,  $(0\,0\,1)$ A surface would be distinguished from the  $(0\,0\,1)$ B surface by the upper Br atoms lying on the other (i.e. the right) side of the Bi atoms.

The single chain depicted in Fig. 4.2(c) illustrates the internal structure of the chains; the model is projected along the reciprocal lattice vector  $\underline{a}^*$ , which is also the surface normal of the  $\alpha$ -Bi<sub>4</sub>Br<sub>4</sub>(100). The outer Bi atoms (Bi<sub>ex</sub>) are bonded to a central chain of (Bi<sub>in</sub>) atoms. In between two neighboring outer Bi atoms, there are two Br atoms. The Bi<sub>in</sub> atoms are coordinated similarly to Bi atoms in elemental bismuth. The Bi<sub>ex</sub> atoms, in contrast, are coordinated as is to be expected from atoms with five ligands and a pair of free electrons [12]. All intra-chain bonds are of the van-der-Waals type. Consequently, unlike in other well known van-der-Waals materials such as WTe<sub>2</sub> and MoS<sub>2</sub> [109, 110],  $\alpha$ -Bi<sub>4</sub>Br<sub>4</sub> features two van-der-Waals gaps. These two van-der-Waals gaps correspond to

the two cleavage surfaces, indicated in Fig. 4.2(a). Due to this crystal structure,  $\alpha$ -Bi<sub>4</sub>Br<sub>4</sub> is classified as a quasi one-dimensional crystal.

On the  $\alpha$ -Bi<sub>4</sub>Br<sub>4</sub>(001), a step encompasses an integer number of monolayers. A monolayer consists of an individual A or B layer. The height of the unit cell is  $h=c\sin(\beta)=1.91\,\mathrm{nm}$ . Thus, a monolayer step is  $h/2=0.96\,\mathrm{nm}$  high. This height also corresponds to the change from an A to a B surface, or vice versa.

The two modifications of  $Bi_4I_4$ ,  $\alpha$ - $Bi_4I_4$  and  $\beta$ - $Bi_4I_4$ , have similar crystal structures [13, 15, 92]. Atomic models of  $\alpha$ - $Bi_4I_4$  and  $\beta$ - $Bi_4I_4$  are displayed in appendix D on page 123. They both feature similar chains with slightly different bond lengths and bond angles [13]. In the case of  $\beta$ - $Bi_4I_4$ , the stacking order is AA. The stacking order of  $\alpha$ - $Bi_4I_4$  is AA': the vertical stacking is the same as AA stacking, however, every second layer is shifted by a distance of b/2 in b-direction [13, 17]. The mutual shifts of the adjacent chains in the plane and the stacking of shifted layers then produces the AA' stacking.  $\beta$ - $Bi_4I_4$  is metastable and will undergo a phase change to return to  $\alpha$ - $Bi_4I_4$  at room temperature [15].  $\beta$ - $Bi_4Br_4$  is expected to feature AA stacking but has not been observed in experiment [14, 111].

## 4.3. Electronic structure of $\alpha$ -Bi<sub>4</sub>Br<sub>4</sub>

According to DFT calculations, the conduction band minimum is located at the L-point. The valence band maximum is slightly offset from the L-point, on the  $\Gamma$  to L path [22]. However, at the L-point, the gap is only slightly larger, as both the conduction band and the valence band are almost flat on the  $\Gamma$  to L path close to the L-point. DFT finds a band gap at the L point to be  $E_{\rm g}=0.18\,{\rm eV}$  [22]. Experimentally, different methods have been used to measure the bulk band gap, yielding a range of values from 0.2 eV to 0.3 eV [20, 21, 96, 108, 112].

A single monolayer of  $\alpha$ -Bi<sub>4</sub>Br<sub>4</sub> was predicted to be a QSH insulator [23, 99, 100]. Due to the difference in electronegativity of bromine and bismuth, the energy of the Br-4p orbitals is much lower than the energy of the Bi-6p orbitals. Thus, at the band gap, the valence band and the conduction band consist of Bi-6p orbitals. Furthermore, due to the Bi-Br bonds, Bi<sub>in</sub>-6p orbitals and the Bi<sub>ex</sub>-6p orbitals differ slightly in energy. Consequently, without SOC, the valence band is made up of Bi<sub>in</sub>- $p_x^+$ - orbitals<sup>1</sup>, while the conduction consists of Bi<sub>in</sub>- $p_x^-$ + orbitals [23, 100]. The x-direction (as well as the y-direction) lies in the plane spanned by the lattice vectors  $\underline{a}$  and  $\underline{b}$ , with the z-direction normal to this plane. At the  $\Gamma$ -point<sup>2</sup> these two orbitals are exchanged due the strong spin-orbit coupling of Br yielding an inverted band gap. The corresponding topological invariant is  $\mathbb{Z}_2 = 1$  [23].

When multiple layers are stacked, the inter-layer coupling can alter the electronic properties. However, the band splitting depends on the strength of the hopping parameter, which is larger for the out-of-plane  $p_z$  orbitals than for the in-plane  $p_x$  and  $p_y$  orbitals. Obviously, this hopping parameter is also larger for the  $\text{Bi}_{\text{ex}}$ -atoms than it is for the  $\text{Bi}_{\text{in}}$ -atoms. As indicated above, the low energy bands are predominantly made up of

<sup>&</sup>lt;sup>1</sup>The plus refers to an inversion operation on two bonded Bi atoms in the chain, the minus refers to a linear combination of bonding and anti-bonding orbitals, when inter-chain coupling is considered. See Refs. [23, 99].

<sup>&</sup>lt;sup>2</sup>Ref. [23] treats only a monolayer, with the fundamental band gap at the Γ-point. Note also a different nomenclature in Refs. [22, 23, 99].

 $p_x$  bands. Thus, the edge states of a monolayer of  $\alpha$ -Bi<sub>4</sub>Br<sub>4</sub>, resting on a bulk  $\alpha$ -Bi<sub>4</sub>Br<sub>4</sub>, are mostly unaffected. Therefore, bulk  $\alpha$ -Bi<sub>4</sub>Br<sub>4</sub> can act as a substrate for monolayer  $\alpha$ -Bi<sub>4</sub>Br<sub>4</sub> [99, 100]. From this, it could be expected, that the topological properties of a stack of n monolayers is not affected by n. This, however, is not the case. Zhou et al. predict a bilayer to be a trivial insulator and a triple layer to be a non-trivial insulator; correlated with the number of band inversions [99]. While the behavior of  $\alpha$ -Bi<sub>4</sub>Br<sub>4</sub> is in fact even more involved, this is also the basis of the higher-order topological insulator properties of bulk  $\alpha$ -Bi<sub>4</sub>Br<sub>4</sub>.

Bulk  $\alpha$ -Bi<sub>4</sub>Br<sub>4</sub> is a HOTI with the topological invariants  $\mathbb{Z}_{2,2,2,4} = \{0,0,0,2\}$  <sup>3</sup> [103]. Figure 4.3 illustrates how the stacking of  $\alpha$ -Bi<sub>4</sub>Br<sub>4</sub> monolayers builds up a higher-order topological insulator. Panels (a) to (d) show two neighboring stacks, that are one to four monolayers high. The stacks rest on a further monolayer of  $\alpha$ -Bi<sub>4</sub>Br<sub>4</sub> that symbolizes a bulk  $\alpha$ -Bi<sub>4</sub>Br<sub>4</sub> substrate. As discussed above, using  $\alpha$ -Bi<sub>4</sub>Br<sub>4</sub> as substrate will not cause a major change in the properties of an  $\alpha$ -Bi<sub>4</sub>Br<sub>4</sub> monolayer [99]. The two neighboring stacks give an insight into the location of edge or hinge states at a trench on the  $\alpha$ -Bi<sub>4</sub>Br<sub>4</sub>(001), formed by two parallel steps. Since a monolayer of  $\alpha$ -Bi<sub>4</sub>Br<sub>4</sub> is a QSH insulator, each stack presents an edge state on both sides. This is illustrated in Fig. 4.3(a). When two monolayers are stacked in c-direction, they form two different angles at their ends as shown in Fig. 4.3(b): one angle is obtuse (left side of the stack), while on the other side there is a reflex angle. Thus, the protruding ends of the chains separate the two edge states on the right side. On the left side, there are no such protruding ends. Therefore, the two edge states on the left side of the stack hybridize (indicated by the orange ellipse) [20, 22, 100, 108]. This hybridization forms a gap in the Dirac cone. For reasons that will become clear when more layers are stacked, the two remaining edge states on the right side of the stacks are referred to as hinge states. If another layer is added to the stacks, the pattern formed by the hybridizing edge states is different, see Fig. 4.3(c). Now, edge states on both sides of the stacks hybridize, leaving one hinge state on the top left and one hinge state on the bottom right. This also explains the name hinge state, as the remaining gapless states are located at the hinge between the top and the side surface of the stacks. If four monolayers are stacked on top of each other, both hinge states are located at the top and bottom of the same side of the stack. This is shown in Fig. 4.3(d).

In general, a stack of an even number of monolayers will feature two hinge states, both located at the same side of the stack, one at the top, the other at the bottom. A stack of an odd number of monolayers will feature two hinge states on opposite sides, one at the top, the other at the bottom [20, 22, 100, 108]. For an even number of layers, the top monolayer (or equivalently, the bottom monolayer) determines which side of the stack the hinge states are on. If, as is the case in Fig. 4.3(d), the top monolayer is a B layer, then the hinge states are on the right of the stack, when looking along the lattice vector b. If the top monolayer were an A layer, both hinge states would be located on the left side of the stack when looking along the lattice vector b. For an odd number of layers, the same reasoning applies. To assign the labels top and bottom unambiguously, the top surface is defined to be a  $(0\,0\,1)$  surface. Correspondingly, the bottom surface is a  $(0\,0\,1)$  surface, see also Ref. [100].

<sup>&</sup>lt;sup>3</sup>The topological invariants depend on the space group of the crystal [113, 114]. The three weak indices  $\nu_i$  (i = 1, 2, 3) are all zero [103].

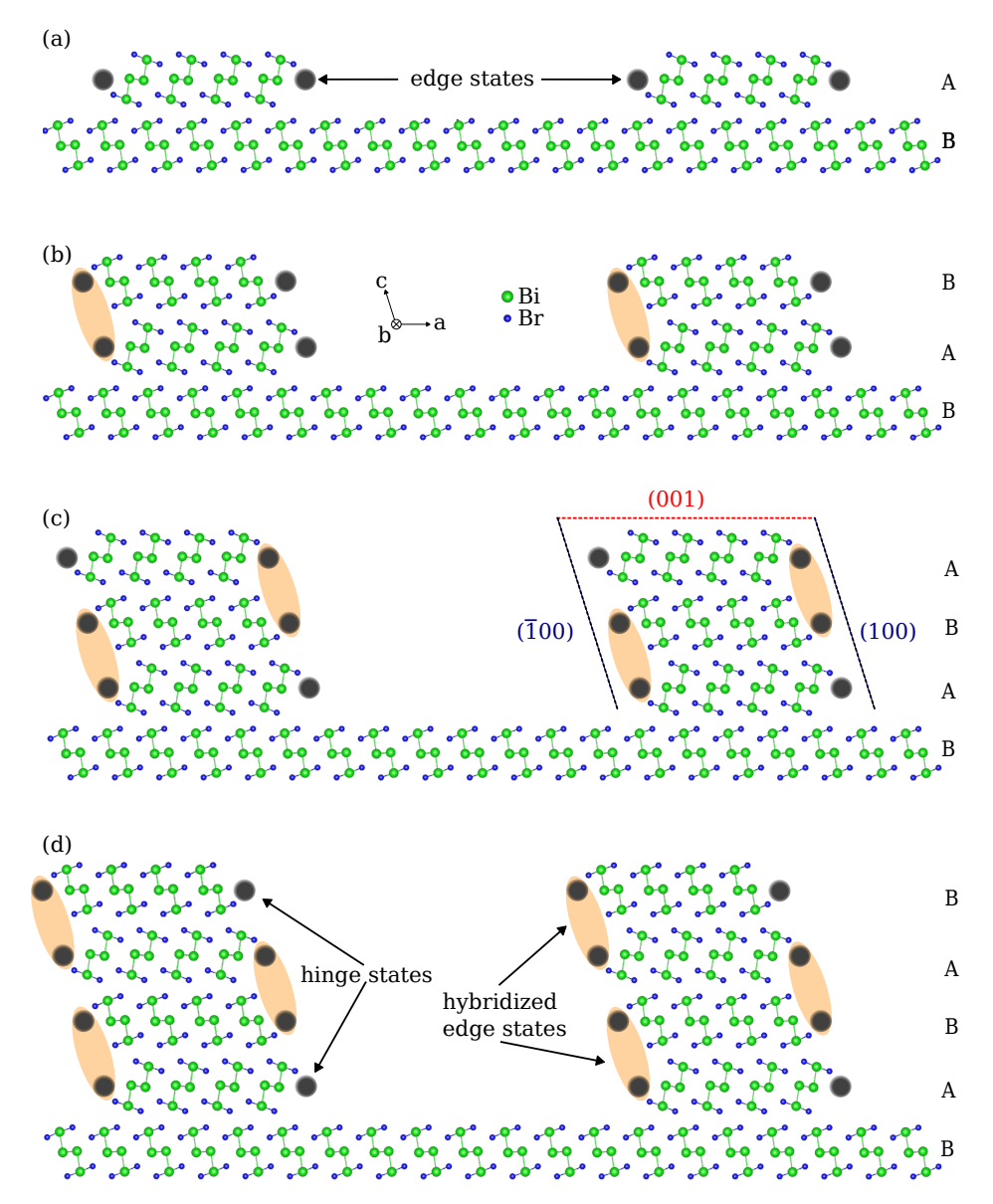


FIG. 4.3.: Formation of the hinge states observable at a trench on the  $\alpha$ -Bi $_4$ Br $_4$  (001) surface. (a) single monolayer stacks. (b) Two monolayer stacks. (c) Three monolayer stacks. (d) Four monolayer stacks. Especially (c) and (d) illustrate how the hybridization of the edge states of the individual QSH layers leads to the formation of hinge states where the  $\{1\,0\,0\}$  and  $\{0\,0\,1\}$  surfaces meet. The (001) top surface and the (100) and ( $\overline{1}\,0\,0$ ) side surfaces are indicated in panel (c). Adapted and modified from from Ref. [31].

Consequently, on the (100) and the (001) surface, different surface band gaps can be observed. Since there are no surface states on  $\alpha$ -Bi<sub>4</sub>Br<sub>4</sub>(001), the bulk band is observed with angle-resolved photoemission spectroscopy (ARPES) [21, 22] and STS [20, 108]. This finding is also consistent with a monolayer of  $\alpha$ -Bi<sub>4</sub>Br<sub>4</sub> being a QSH insulator, as the  $\alpha$ -Bi<sub>4</sub>Br<sub>4</sub>(001) forms the interior of this QSH insulator. Meanwhile, on the  $\alpha$ -Bi<sub>4</sub>Br<sub>4</sub>(100) surface, there is a gapped topological protected surface state resulting from the hybridization. Thus, using ARPES, a much smaller band gap of 40 meV (compared to the bulk band gap of  $\sim 300\,\mathrm{meV}$ ) was observed on the  $\alpha$ -Bi<sub>4</sub>Br<sub>4</sub>(100) surface [22].

The QSH edge state of a single monolayer of  $\alpha$ -Bi<sub>4</sub>Br<sub>4</sub> is also present on the  $\alpha$ -Bi<sub>4</sub>Br<sub>4</sub>(0 1 0) surface. The pristine (0 1 0) surface does not exhibit any large kinks, which would lead to the pattern of hybridizing surface states on the  $\alpha$ -Bi<sub>4</sub>Br<sub>4</sub>(1 0 0) surface. Therefore, it is predicted to host a non-trivial surface state, protected by a two-fold rotation symmetry [20, 22, 100, 103]. However, due to the experimental challenge in preparing samples showing the  $\alpha$ -Bi<sub>4</sub>Br<sub>4</sub>(0 1 0) surface, the topological surface state has not been observed in the literature. Indeed, in the available literature the (0 0 2) surface is preferred [20, 96, 108, 112], with only a few studies also investigating the (1 0 0) surface [21, 22].

In the literature, the presence of the edge/hinge states on the  $\alpha$ -Bi<sub>4</sub>Br<sub>4</sub>(001) surface was detected by STS [20, 96, 108, 112] and ARPES [18, 22]. In all these cases, additional DFT simulations were performed in order to attribute the measured features to topological surface, edge, or hinge states. In one instance, the edge states on a 1 nm step were observed even at room temperature [20]. The gapped topological surface states on the  $\alpha$ -Bi<sub>4</sub>Br<sub>4</sub>(100) surface were also observed by ARPES [22]. Shubnikov-de Haas oscillations observed during transport experiments were interpreted as evidence of the presence of surface states [115, 116]. Similarly, Aharonov-Bohm oscillations were observed on  $\alpha$ -Bi<sub>4</sub>Br<sub>4</sub> with an even number of layers. This is an additional experimental indication of the presence of hinge states on these flakes [108].

# 4.4. Preparation of exfoliated Bi<sub>4</sub>Br<sub>4</sub> flakes

Since the introduction of mechanical exfoliation to prepare single monolayers of graphite (graphene) and other strongly layered materials [110], mechanical exfoliation and stacking of 2D monolayers has become a standard procedure for the preparation of these materials. Stacking of exfoliated monolayers of different van-der-Waals materials allows to assemble heterostructures from materials with widely different lattice constants, without being limited by the lattice mismatch [117]. To assemble a van-der-Waals heterostructure, first the required (mono-) layers are exfoliated on some intermediate substrate, e.g. SiO<sub>2</sub>. On these intermediate substrates, flakes of desired shape and thickness can be identified. Then, the heterostructure is stacked step by step using a dedicated set of micropositioniers and a light microscope. The flakes are picked up using a polymer stamp [117].

At PGI-3, a glovebox is available for the exfoliation and stacking of sensitive 2D materials. Inside the glovebox, an Ar atmosphere is maintained. The partial pressures of  $O_2$  and  $H_2O$  are kept below 5 ppm. Sensitive samples are transferred to the STM using a vacuum suitcase.

While in this thesis, no  $\alpha$ -Bi<sub>4</sub>Br<sub>4</sub> heterostructures are stacked, this transfer procedure can still be useful. The  $\alpha$ -Bi<sub>4</sub>Br<sub>4</sub>, flakes can be exfoliated on SiO<sub>2</sub> substrate, providing

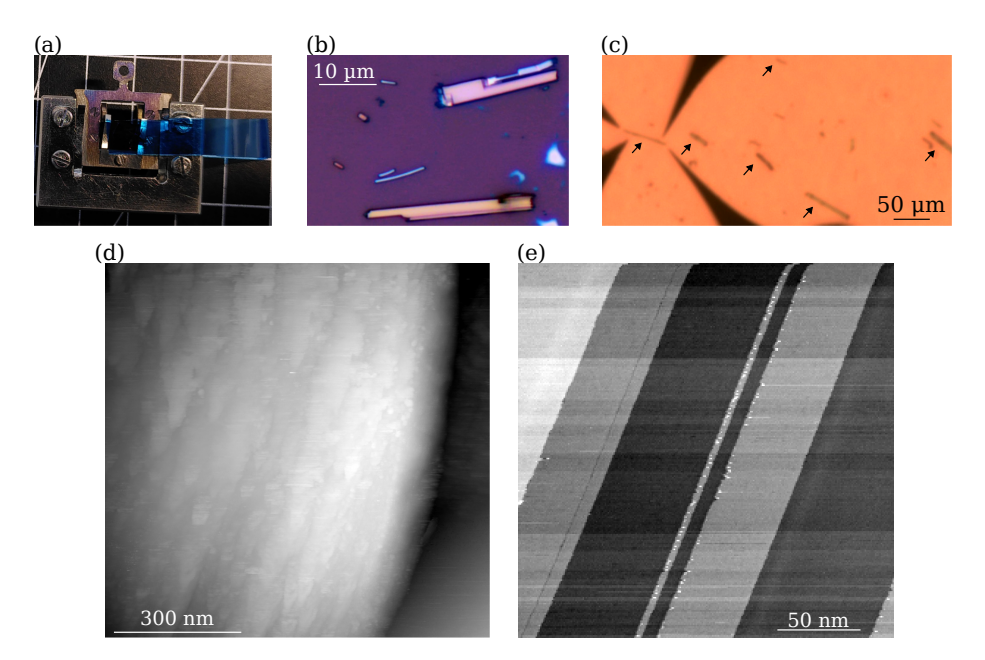


FIG. 4.4.: (a) Sample holder with a silicon sample and an attached tape with  $\mathrm{Bi_4Br_4}$  flakes. (b)  $\mathrm{Bi_4Br_4}$  flakes exfoliated onto  $\mathrm{SiO_2}$  inside the glovebox. (c) Flakes exfoliated in vacuo onto a SOI substrate, due to the inferior optical contrast, arrows point out the flakes. (d) STM topography of a flake with polymer remnants from transfer inside the glovebox. (e) STM topography of a flake exfoliated in vacuo, showing the parallel steps typical for  $\alpha\text{-Bi_4Br_4}(0\,0\,1)$  with flat terraces in between.

excellent optical contrast. The flakes were subsequently transferred to the measurement substrate [Si(111)] or H-terminated silicon-on-insulator (SOI)]. This procedure also allows to position a marker flake (e.g. a thick graphite flake). A marker flake simplifies locating and approaching the  $\alpha$ -Bi<sub>4</sub>Br<sub>4</sub>-flake in the four-tip STM. However, the method of transferring the flakes from an intermediate to the measurement substrate also has a major drawback: The polymer leaves remnants on the flake surface. In order to obtain clean surfaces for STM studies, a flip technique can be used: This technique requires the use of at least two polymer stamps, that touch only a part of the flake surface. A more detailed description can be found in Ref. [109]. In principle, polymer remnants on flakes of more chemically inert materials can also be removed by mechanical or chemical cleaning.

For this thesis, a different approach was developed. Exfoliation and thinning of  $\alpha$ -Bi<sub>4</sub>Br<sub>4</sub> flakes is done in the glovebox using standard exfoliation techniques and Ultron systems 1007R-6.0 dicing tape. In a final step, the tape containing the  $\alpha$ -Bi<sub>4</sub>Br<sub>4</sub> flakes is attached to the measurement substrate, which is already mounted in the sample holder. A photograph of the sample holder with the attached tape is shown in Fig. 4.4(a). The sample, while still covered with the tape, is then transferred to the four-tip STM through air and mounted to the vacuum system. The free end of the tape is fixed to the chamber wall. The tape is finally peeled off under vacuum conditions ( $p \sim 7 \times 10^{-5}$  Pa). On the

substrate, an assortment of flakes of different sizes remain. A suitable flake can then be selected using the optical microscope. The main drawback of this procedure is the limited resolution of the optical microscope mounted to the STM. Figures 4.4(b) and (c) show  ${\rm Bi}_4{\rm Br}_4$  flakes on the standard  ${\rm SiO}_2$  substrate and the SOI substrate, respectively. Note, the difference in optical contrast is both due to the different microscopes used inside the glovebox [Fig. 4.4(b)] and due to the different substrates.

The STM topography displayed in Fig. 4.4(d) shows the surface of a  $Bi_4Br_4$  flake contaminated with polymer remnants from the flake transfer discussed above. The polymer leads to a very high surface roughness, the defining features of the  $\alpha$ -Bi<sub>4</sub>Br<sub>4</sub>(001), the long parallel step edges, cannot be recognized anymore. The flat surface in the bottom right corner is the substrate. It is  $\sim 60\,\mathrm{nm}$  lower than the flake surface. In Fig. 4.4(e) an STM topography of a Bi<sub>4</sub>Br<sub>4</sub> flake after vacuum exfoliation is displayed. The surface shows the distinctive long parallel steps, that have been observed before using various methods [20, 21, 112]. The elongated steps form along the lattice vector  $\underline{b}$ , that is, in chain direction (c.f. Fig. 4.2). Step formation is favored along  $\underline{b}$ -direction, as the van-der-Waals forces binding the individual chains are much weaker than the covalent bonds linking the atoms inside the chains.

# 5. Shear-resistant topology in quasi one-dimensional van-der-Waals material Bi<sub>4</sub>Br<sub>4</sub>

In this chapter, a new surface structure of the  $\alpha$ -Bi<sub>4</sub>Br<sub>4</sub>(0 0 1) is discussed. Atomically resolved STM topography images show a mutual shift of  $s=\underline{b}/3$  for neighboring chains instead of the shift of  $s=\underline{b}/2$  observed in the literature [20, 108, 112, 118]. On terraces separated by a one monolayer high step, the AB stacking expected for  $\alpha$ -Bi<sub>4</sub>Br<sub>4</sub> is observed. Scanning tunneling spectra indicate the presence of quantum spin Hall (QSH) edge states at the monolayer step edges. This result is confirmed by DFT calculations, that find the new structure to be a QSH insulator with the topological invariant  $\mathbb{Z}_2 = 1$ .

#### 5.1. Methods

The  $\alpha$ -Bi<sub>4</sub>Br<sub>4</sub> single crystal, grown by the self-flux method [22], was glued to a standard sample plate using conductive epoxy. The sample was then introduced into UHV, where it was cleaved at room temperature using Kapton tape, which was peeled off along the  $\underline{b}$  direction. Experiments were carried out in the low-temperature four-tip scanning tunneling microscope (STM) at the Oak Ridge National Laboratory at 4.7 K using a commercial PtIr tip. Scanning tunneling spectroscopy (STS) was performed with a lockin amplifier, employing a modulation frequency  $f=500\,\mathrm{Hz}$  and modulation amplitudes  $V_{\mathrm{mod}}=10\,\mathrm{mV}$  to  $100\,\mathrm{mV}$ .

# 5.2. Results

#### 5.2.1. Surface structure

Figure 5.1(a) shows an atomically resolved STM topography image of the  ${\rm Bi_4Br_4}(001)$  surface. It clearly exhibits parallel chains, running along the  $\underline{b}$  axis (from top to bottom in the image). The mutual alignment of the chains, however, does not correspond to the one expected for the bulk terminated  $\alpha$ -Bi<sub>4</sub>Br<sub>4</sub>(001) surface. The bulk terminated  $\alpha$ -Bi<sub>4</sub>Br<sub>4</sub>(001) features parallel chains with each chain offset by  $\underline{s} = \underline{b}/2$  with respect to the adjacent chains. The atomic model in Fig. 5.1(b) illustrates this surface structure. This surface was already observed in the literature on cleaved bulk samples [20, 108, 112, 118]. In contrast, in the present case, the mutual shift of the chain is s = b/3 between neighboring chains, according to the STM topography [Fig. 5.1(a)]. This surface structure is no longer spanned by the two surface lattice vectors  $\underline{a}_s$  and  $\underline{b}_s$ , but by new lattice vectors  $\underline{a}_s'$  and  $\underline{b}_s'$ . Figure 5.1(c) shows an atomic model of the modified surface,

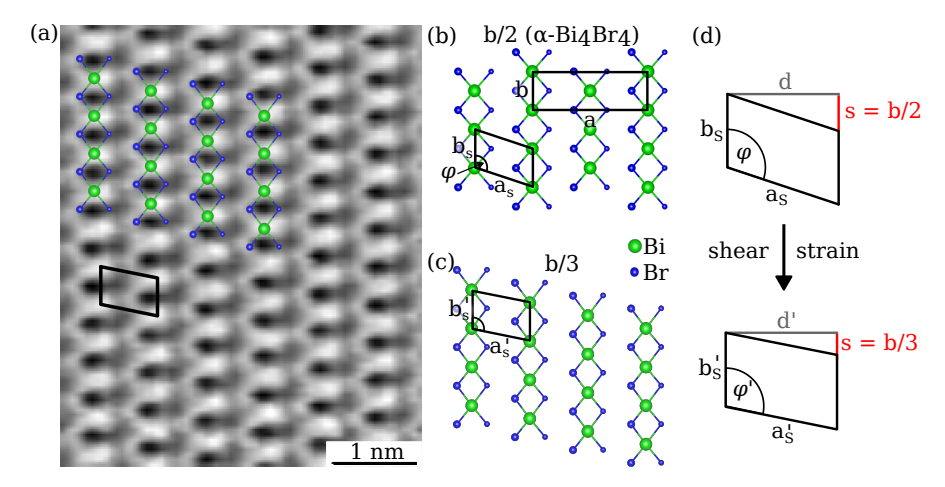


Fig. 5.1.: (a) STM topography recorded at  $I_{\rm t}=0.4\,{\rm nA}$  and  $V_{\rm tip}=-0.4\,{\rm V}$ . The atomic model from (c) is superimposed on the chains, showing good agreement. The image was upscaled using a linear interpolation. (b) Top-view of the bulk terminated  $\alpha$ -Bi<sub>4</sub>Br<sub>4</sub>(001)A surface. The lower Br atoms are indicated by smaller size. Neighboring chains are shifted by  $s=\underline{b}/2$  with respect to each other. The rectangle shows the projected monoclinic bulk unit cell (which equals the non-primitive centered surface unit cell), the parallelogram is the primitive surface unit cell. (c) The experimentally observed surface structure in which neighboring chains are shifted by b/3 against each other. The primitive surface unit cell is shown. (d) Defines  $\varphi$ , d, s,  $\underline{a}_{\rm s}$ ,  $\underline{b}_{\rm s}$ , d',  $\underline{a}'_{\rm s}$ , and  $\underline{b}'_{\rm s}$ . The panel further illustrates how the shear strain deforms the surface unit cell. Adapted from Ref. [31].

obtained by rigidly shifting the chains. Hereafter, the new surface structure is referred to a b/3 structure, while the commonly observed [20, 108, 112, 118] surface structure is denoted by b/2.

The observed length of the surface lattice vectors can be extracted from Fig. 5.1(a):  $a_s' = (0.69 \pm 0.04) \,\mathrm{nm}$  and  $b_s' = (0.45 \pm 0.03) \,\mathrm{nm}$  with an angle  $\varphi = (101 \pm 5)^\circ$  between them; the inter-chain distance is determined as  $d = (0.68 \pm 0.04) \,\mathrm{nm}$ . These values are averages obtained from multiple STM topographs, including Figs. 5.1(a) and 5.3. While the lattice vector  $\underline{b}_s'$  appears to be slightly larger than that of  $\alpha$ -phase  $\mathrm{Bi}_4\mathrm{Br}_4$  ( $b_s = 0.4338 \,\mathrm{nm}$  [12]), both still coincide within the experimental error of  $b_s'$ , i.e.  $b_s' \approx b_s$ . Figure 5.1(d) defines the lattice vectors used here. Comparing the STM topography with a simulated STM image from the literature [112, 118] and annotated STM topographies in Ref. [20] allows to identify the positions of the individual atoms: The large bright contrast separated in the vertical direction by large dark contrasts originate from the top Bi atoms (green). The zigzag pattern to the left of each vertical chain of Bi atoms are the topmost Br atoms (blue). The lower lying Br atoms right of the Bi atoms cause a depression in the STM topographies, compare also Refs. [20, 108, 112, 118].

Scan distortions can be excluded as the origin of the new structure: First, before the experiments on  $Bi_4Br_4$ , the calibration of the STM was verified on the Au(111) surface. Second, the fact that the structure is consistent both within one image and between multiple scans of the same area rules out piezo creep and drift. Third, on terraces

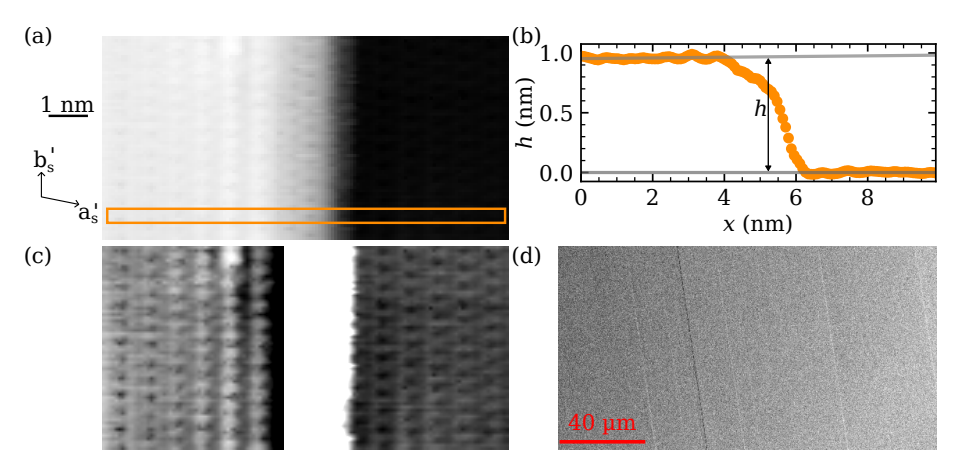


FIG. 5.2.: (a) STM topography of a step edge on the  ${\rm Bi_4Br_4(001)}$  surface, acquired at  $I_{\rm t}=0.1\,{\rm nA}$  and  $V_{\rm tip}=-0.3\,{\rm V}$ . The image shows a one-monolayer step edge with atomic resolution on both the upper and the lower terraces. (b) Line profile indicated by the orange box in (a). (c) Upper and lower terraces of (a) with individually adjusted contrast. Both terraces exhibit atomic resolution showing the b/3 structure. (d) SEM micrograph showing six parallel steps (higher than a monolayer) as lines due to the edge contrast. Panels (a) and (b) are adapted from Ref. [31].

separated by a monolayer step the same structure rotated by 180° is observed. The b/3 structure is either a surface reconstruction (which has not been observed on  $\alpha$ -Bi<sub>4</sub>Br<sub>4</sub>(0 0 1) [20, 108, 112, 118]) or derives from shear stress applied to the sample. The origin of the b/3 structure is further discussed in section 5.3. Figure 5.1(d) illustrates how the mutual shift of s = b/2 deforms the surface unit cell.

The Bi<sub>4</sub>Br<sub>4</sub>(001) surface has multiple parallel steps, running in  $\underline{b}'_s$  direction. Figure 5.2(a) shows a high resolution STM topography of such a step. According to the height profile displayed in Fig. 5.2(b), the step height is  $(0.97 \pm 0.05)$  nm. This step height compares well to experimental step heights reported in the literature [20, 112, 118]. According to the crystal model, presented in section 4.2, the height of the unit cell is 1.9 nm. Thus 0.96 nm corresponds to the height of a monolayer (c.f. section 4.2 on page 49). On  $\alpha$ -Bi<sub>4</sub>Br<sub>4</sub>(001), the latter height also indicates a change from an A to a B surface or vice versa, c.f. Fig. 4.2. In the SEM micrograph displayed in Fig. 5.2(d), six parallel step edges are visible due to the edge contrast created by secondary electrons [88, pp. 212-214]. It seems unlikely that the pronounced edge contrast is caused by a single monolayer high step. Instead, these steps are more than one monolayer high. This is consistent with the observation that it is impossible to image the area using the STM. Nevertheless, all steps are parallel, as expected from the quasi one-dimensional crystal structure of  $\alpha$ -Bi<sub>4</sub>Br<sub>4</sub>.

The STM topography [Fig. 5.2(a)] also shows atomic resolution, which is, however, invisible, due to the large contrast difference arising from the step. Therefore, the two terraces are displayed separately with individually adjusted contrast in Fig. 5.2(c). However, from this image, the surfaces of both terraces cannot be identified unambiguously. In order to identify the surface, it is necessary to analyze the vertical stacking of the

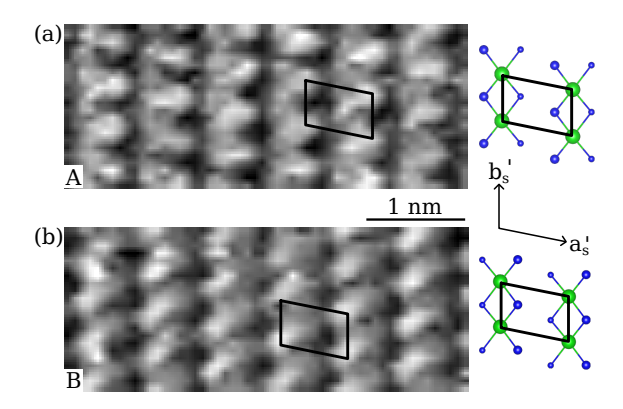


Fig. 5.3.: STM topographies of the lower terrace (a) and the upper terrace (b) in Fig. 5.2. Both images were recorded at  $I_{\rm t}=0.1\,{\rm nA}$  and  $V_{\rm tip}=0.4\,{\rm V}$ . They were upscaled using a linear interpolation. From the location of the dark contrast with in the surface unit cells (parallelogram), the surface can be identified: The lower terrace exposes an A surface, the upper terrace a B surface.

b/3 structure. Therefore, as on the b/2 structure [20], high resolution STM scans on the upper and the lower terrace were obtained. Two of these scans are presented in Fig. 5.3 showing the upper and the lower terrace. Figure 5.3(a) displays the lower terrace. The surface unit cell is marked with a parallelogram that was placed by using the large, bright contrasts as anchor points. In Fig. 5.3(a), the dark contrast is located in the left half of the parallelogram. As noted above, the large, bright contrasts are associated with the surface Bi atoms. Therefore, the parallelogram is also overlaid on the atomic model, using the Bi atoms as anchor points. The model shows, that the darker contrast in the STM topography is caused by the lower surface Br atom, which is located left of the chain. This arrangement of atoms (higher surface Br atom left and lower surface Br atom right of the Bi atoms) is a hallmark of the  $\alpha$ -Bi<sub>4</sub>Br<sub>4</sub>(001)A surface. The same parallelogram is also placed on the large bright contrasts in Fig. 5.3(b), showing the upper terrace. Here, the dark contrast is located in the right half of the surface unit cell. Comparing the topography to the atomic model indicates that the lower terrace exhibits a B surface. Therefore, the b/3 structure also exhibits AB stacking. The observation of AB stacking also excludes the possibility that the theoretical  $\beta$  polymorph of Bi<sub>4</sub>Br<sub>4</sub> was observed, as  $\beta$ -Bi<sub>4</sub>Br<sub>4</sub> is expected to feature AA stacking [111].

The observed surface structure differs significantly from the structural properties of  $\alpha$ -Bi<sub>4</sub>Br<sub>4</sub> under hydrostatic pressure [111]. The corresponding triclinic unit cell observed under these conditions is also clearly distinct from our observation of AB stacking [111]. Furthermore, the observation of a bulk band gap (see following section) disagrees with the metallic/superconducting properties of  $\alpha$ -Bi<sub>4</sub>Br<sub>4</sub> under hydrostatic pressure [111].

#### 5.2.2. Electronic structure

Now, scanning tunneling spectrocopy (STS) data is used in order to analyze the electronic properties of the b/3 structure. As already shown in section 4.3, the bulk band gap of

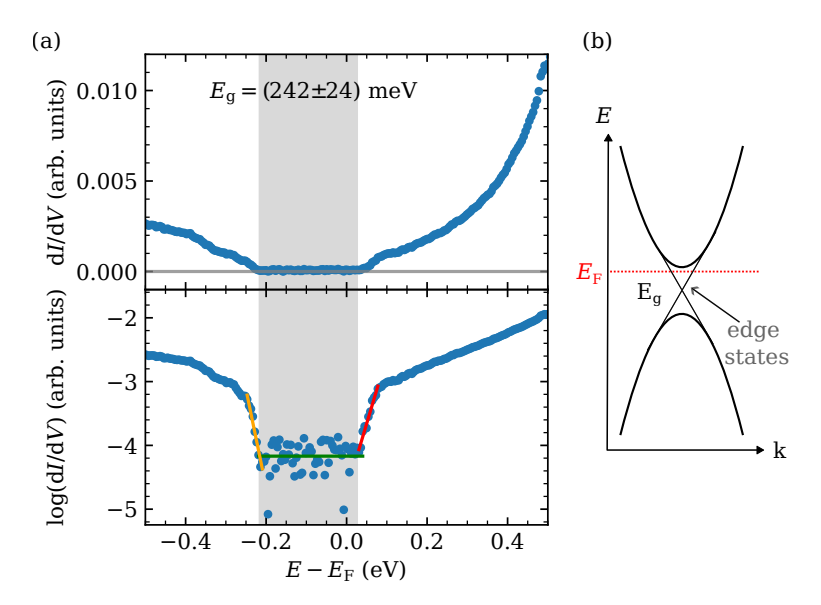


FIG. 5.4.: (a) Scanning tunneling spectrum of the b/3 surface with band gap  $E_{\rm g}$ , measured at  $V_{\rm set}=0.6\,{\rm V}$  and  $I_{\rm set}=50\,{\rm pA}$ . (b) Schematic band structure with topological gap and edge states. Adapted from Ref. [31].

 $\alpha$ -Bi<sub>4</sub>Br<sub>4</sub> can be observed on its (001) surface. The bulk band gap<sup>1</sup> is estimated using multiple spectra using the method described in Ref. [119]: The decadic logarithm of the measured differential conductance dI/dV is plotted as shown in the lower panel of Fig. 5.4(a). The plot shows three distinct ranges: the valence band at the left side, the band gap, and the conduction band at the right side. The width of the band gap is then extracted from the intersections of linear fits to the data in the three regions. In the present case, a band gap of  $E_{\rm g}=(242\pm24)\,{\rm meV}$  is obtained. Averaging results from multiple spectra yields a bulk band gap of  $E_{\rm g} = (234 \pm 14) \, {\rm meV}$ . The spectra are shown in Fig. E.1 on page 126 in the appendix. This result for  $E_{\rm g}$  falls into the range  $E_{\rm g} = 200 \dots 300 \,{\rm meV}$  reported in the literature for the b/2 structure using different methods: By combining angle-resolved photoemission spectroscopy (ARPES) with the deposition of K atoms on the surface, a band gap of  $E_{\rm g}=300\,{\rm meV}$  was obtained. A further ARPES study found  $E_{\rm g}=230\,{\rm meV}$  [112]. STS measurements on the  $\alpha$ -Bi<sub>4</sub>Br<sub>4</sub>(001) yield  $E_{\rm g}=260\,{\rm meV}$  [20, 108] and  $E_{\rm g}\approx200\,{\rm meV}$  [112]. Furthermore, from a (not further specified) optical measurement  $E_g = 220 \,\mathrm{meV}$  was obtained [96]. A schematic sketch of the band structure is depicted in Fig. 5.4(b).

The QSH edge states shown in gray in Fig. 5.4(b) are now addressed. Figure 5.5(a) shows a  $\sim 1$  nm deep trench, that formed by two parallel steps. A similar left step has already been discussed above. The atomic model in Fig. 5.5(b) indicates symbolically the location of the QSH edge states present at single monolayer steps on  $\alpha$ -Bi<sub>4</sub>Br<sub>4</sub>(001) [23,

<sup>&</sup>lt;sup>1</sup>STM/STS is a surface sensitive technique. Thus, in all cases, only the band gap at the surface can be measured. In contrast to other surfaces of  $\alpha$ -Bi<sub>4</sub>Br<sub>4</sub>, however, there are no topologically protected surface states on the  $\alpha$ -Bi<sub>4</sub>Br<sub>4</sub>(001) surface (c.f. section 4.3 on page 51). Thus, in principle, the bulk band gap is accessible at this surface.

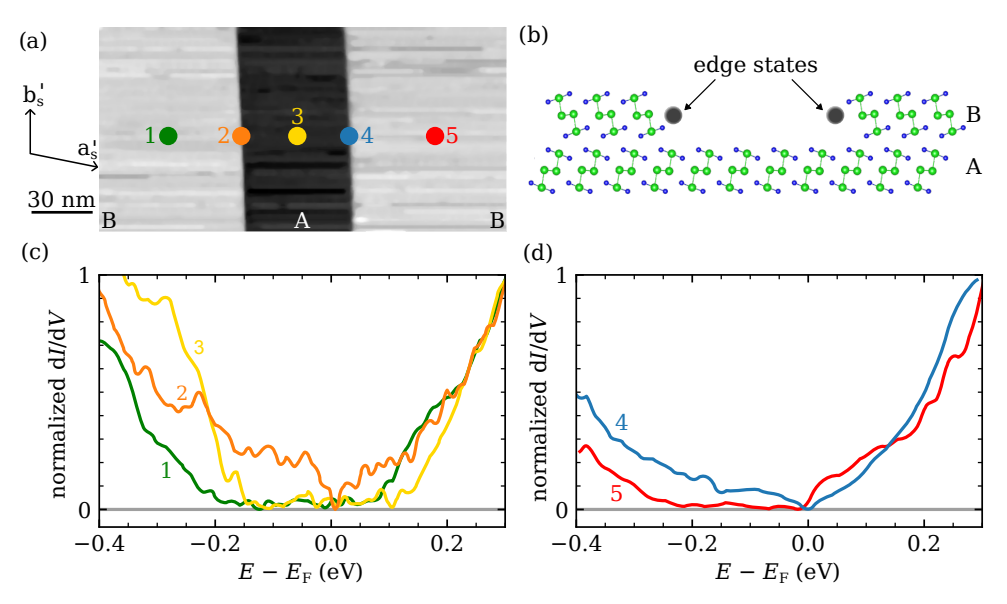


Fig. 5.5.: (a) STM topography of a  $\sim 1\,\mathrm{nm}$  deep trench on the surface, bordered by two  $\alpha$ -Bi $_4$ Br $_4$  monolayer steps. (b) An atomic model of the trench with the edge states indicated by the filled circles. Scanning tunneling spectra in (c) and (d) were recorded on terraces right and left of the trench and directly at the two step edges. The filled circles indicate the approximate positions where the spectra were measured. All spectra are normalized to 1 at 0.3 eV. Spectra at the step edges (orange and blue) show metallic edge states instead of a band gap. Note that the band gaps in the spectra from the terraces (green, yellow, and red) vary in width and alignment with the Fermi level. This is explained with sample degradation, see main text for more details. The spectra displayed in (c) and (d) were smoothed using a moving average with a 14 meV window.

99]. See also section 4.3 and Fig. 4.3. Figures 5.5(c) and (d) display scanning tunneling spectra taken at five different locations, indicated by numbers 1 to 5 and color-coded in Fig. 5.5(a). The spectra recorded on the terraces (green, yellow, and red; or 1,3, and 5), exhibit a vanishing density of states caused by the bulk band gap. Spectrum no 2 (orange) and spectrum no 4 (blue) show a metallic state with a non vanishing density of states inside the band gap. In the b/2 structure, such metallic states located at step edges on the  $\alpha$ -Bi<sub>4</sub>Br<sub>4</sub>(001) are explained by the presence of QSH edge states [20, 23, 96, 99, 108]. Thus, the non-vanishing density of states inside the band gap can be interpreted as evidence of the presence of edge states. To support this interpretation, DFT calculations are needed as discussed below.

The spectra 1, 3, and 5 recorded on the three terraces Fig. 5.5(a) differ somewhat in width and position of the bulk band gap. This effect can be attributed to an accumulation of adsorbates on the surface during the measurement (five days). The accumulation lead to a disordered surface and an eventual closing of the bulk band gap observed at the surface.

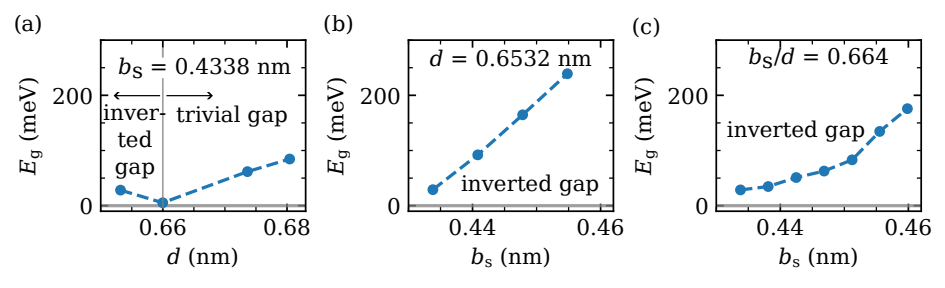


Fig. 5.6.: Evolution of the inverted band gap  $E_{\rm g}$  as a function of the inter-chain distance d and the lattice constant  $b_{\rm s}$ . The dashed lines are a guide for the eyes. The DFT calculations were performed by  $Mingqian\ Zheng\ and\ Jin-Jian\ Zhou$ . (a) Dependence of  $E_{\rm g}$  on the inter-chain distance d, when fixing  $b=0.4338\,{\rm nm}$ . The inverted band gap decreases, until it closes at  $d=0.66\,{\rm nm}$  and then transitions to a trivial gap. (b) Fixing  $d=0.6532\,{\rm nm}$  and increasing the lattice vector  $b_{\rm s}$  enhances the inverted band gap. (c) The same applies if the ratio  $b_{\rm s}/d=0.664$  is kept constant. Adapted from Ref. [31].

Using DFT calculations, the topological properties of the b/3 structure can be analyzed and its band structure can be compared to that of the b/2 ( $\alpha$ -Bi<sub>4</sub>Br<sub>4</sub>). DFT calculations of a monolayer of the b/3 structure were done by Minggian Zheng and Jin-Jian Zhou, numerical details are given in Ref. [31]. Since it is not possible to relax the b/3 structure, crystallographic data for the bulk of  $\alpha$ -Bi<sub>4</sub>Br<sub>4</sub> [12] and the surface structure presented here were combined. The inter-chain distance d' and the length of the surface lattice vector  $b'_{e}$ that were determined from the experiment, are somewhat larger than the values given in the literature for the b/2 structure [12]. The influence of these parameters on the topology of the b/3 structure will now be studied. As discussed in section 4.3, the van-der-Waals interaction between neighboring chains is closely related to the inverted band structure of  $\alpha$ -Bi<sub>4</sub>Br<sub>4</sub>. Therefore, the impact of the inter-chain distance d' on the band structure was analyzed using DFT simulations. First, the dependence of the inverted band gap  $E_{\sigma}$ on the inter-chain distance d' is considered. Figure 5.6(a) illustrates, how the inverted band gap closes at  $d' = 0.66 \,\mathrm{nm}$ , and then opens again as a trivial band gap. For this calculation,  $b_{\rm s} = 0.4338\,{\rm nm}$  was kept fixed. The experimentally obtained inter-chain distance  $d' = (0.68 \pm 0.04)$  nm is larger than the threshold d' = 0.66 nm. Thus, at first glance, the DFT calculations appear to contradict the previous conclusion that the b/3structure is a QSH insulator. This conclusion was drawn on the basis of the spectroscopic results. Note, however, that due to its measurement uncertainty,  $d' = (0.68 \pm 0.04)$  nm is still compatible with the calculated threshold. In addition, also the lattice vector  $b'_s$  was observed to be larger than the corresponding lattice vector of the b/2 structure. Thus, as a second step, the influence of  $\underline{b}_{s}$  on the band gap was analyzed.

As shown in Fig. 5.6(b), increasing  $b_{\rm s}'$  enhances the inverted band gap. This effect stabilizes the QSH properties of the b/3 structure and counteracts the effect of the inter-chain distance d'. For the calculation, the inter-chain distance was fixed at  $d=0.6532\,{\rm nm}$ , i.e., the value for the b/2 structure (calculated from the bulk  $\alpha$ -Bi<sub>4</sub>Br<sub>4</sub> lattice parameters [12]).

In the two cases above, one of the parameters was fixed to its respective value in the b/2 structure, while the other was varied. This contradicts the experimental observations. To explore the parameter space further, the ratio was fixed to  $b_s/d = 0.664$ , based on the

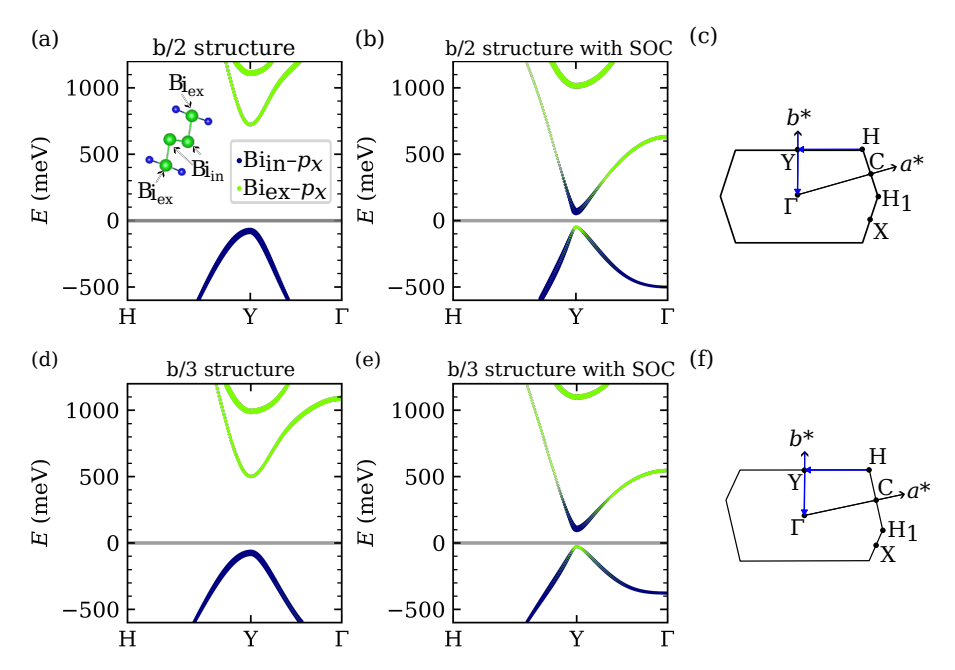


FIG. 5.7.: Band inversion in the b/2-structure and the b/3-structure. The DFT calculations were performed by  $Mingqian\ Zheng\ and\ Jin-Jian\ Zhou$ . (a) and (b) show the  $Bi_{in}-p_x$  and  $Bi_{ex}-p_x$  projected orbital character of the conduction and the valence bands around the Y point (a) without and (b) with spin orbit coupling (SOC) for the b/2 structure, see [23]. (c) Shows the 2D Brillouin zone of the b/2-structure. (d) and (e) show the same projected orbital character of the bands around the Y point for the b/3 structure. (d) and (e) were calculated using the lattice constants indicated in the main text. For both structures, SOC exchanges the two orbitals leading to an exchange of parity, which makes both the b/2 (b) and the b/3 (e) structure a QSH insulator. (f) Shows the 2D Brillouin zone of the b/3-structure. Panels (a), (b), (d), and (e) are adapted from Ref. [31].

experimental observation that  $b_{\rm s}'/d'=0.662$ . The results of these calculations, shown in Fig. 5.6(c) indicate that the effect of increasing  $\underline{b}_{\rm s}$  is stronger than the effect of increasing d. The band gap remains inverted over the complete range. Thus, the b/3 structure remains a QSH insulator, even if the mutual shift of  $\underline{b}/3$  should lead to a stronger repulsion between Br atoms and thus a larger inter-chain distance d'.

As noted above, the limit  $d=0.66\,\mathrm{nm}$  still lies within the uncertainty of experimentally obtained  $d'=(0.68\pm0.04)\,\mathrm{nm}$ . Increasing the length of the lattice vector  $\underline{b}_{\mathrm{s}}$  entails stretching the covalent bonds of the  $\mathrm{Bi}_4\mathrm{Br}_4$  chains. While stretching the van-der-Waals bonds connecting the individual chains appears to be plausible due to the weaker interaction, increasing the bond lengths of the  $\mathrm{Bi}\mathrm{-Br}$  and  $\mathrm{Bi}\mathrm{-Bi}$  bonds of the chains can be considered as less plausible. However, both  $b'_{\mathrm{s}}=(0.45\pm0.03)\,\mathrm{nm}$  and  $d'=(0.68\pm0.04)\,\mathrm{nm}$  contain the limit within their experimental uncertainty.

From the structures represented in Fig. 5.6(c), the best agreement to the experimentally derived values  $a_{\rm s}'=(0.69\pm0.04)\,{\rm nm},\ b_{\rm s}'=(0.45\pm0.03)\,{\rm nm},\ d'=(0.68\pm0.04)\,{\rm nm},\ {\rm and}$ 

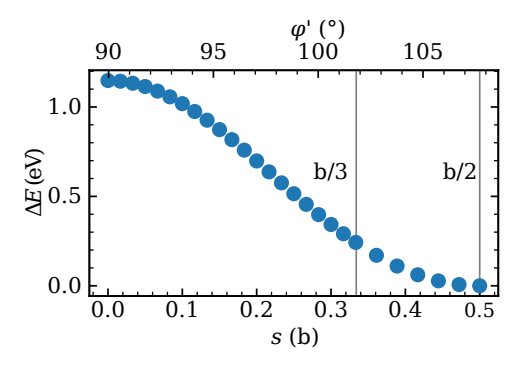


FIG. 5.8.: Total energy per unit cell relative to the b/2 structure as a function of the shift  $s = -d'\cot(\varphi')$  (plotted in units of b) between neighboring chains, where d is the inter-chain distance.  $\varphi'$  is the angle between the constant unit cell vector  $\underline{b'}_s$  and the changing  $\underline{a'}_s$  associated with s. The DFT calculations are performed by Tobias Wichmann. Adapted from Ref. [31].

 $\varphi' = (101 \pm 5)^{\circ}$ ) is found for the fifth data point form the left. The calculated parameters are  $a_{\rm s,c}'=0.6959\,{\rm nm},\,b_{\rm s,c}'=0.4512\,{\rm nm},\,d_{\rm c}'=0.6795\,{\rm nm},\,\varphi_{\rm c}'=102.48^{\circ}$  and a band gap of  $E'_{g,c} = 80 \text{ meV}$ . The calculated band gap is thus much smaller than the experimentally obtained  $E_{\rm g} = (234 \pm 14) \,\mathrm{meV}$ . As noted above, the experimental result falls within the range of the measured band gaps for the b/2 structure, but is slightly smaller than the band gap obtained by STS measurements on the b/2 structure yielding  $E_{\rm g}=260\,{\rm meV}$ [20, 108]. This indicates that the b/3 structure is closer than the b/2 structure to the transition to a trivial band gap. To demonstrate that the selected set of parameters indeed represents a QSH insulator, the band inversion due to the spin orbit coupling (SOC) is shown in Fig. 5.7. For comparison, also the band inversion for the b/2 structure is shown. As introduced in section 4.3, SOC exchanges the  $Bi_{in}$ - $p_x$  and  $Bi_{ex}$ - $p_x$  orbitals at the fundamental band gap [23, 99, 100]. In both the b/2 structure and the b/3 structure, the band gap is located at the Y point. Figure 5.7(a) and (b) show the  $Bi_{in}$ - $p_x$  and  $Bi_{ex}$ - $p_x$ orbital projected character of bands without and with SOC for the b/2, respectively. As noted above, SOC exchanges the two orbitals, leading to a change of parity at the Y point. Thus, the b/2 structure is a QSH insulator [23, 99, 100]. In Fig. 5.7(d) and (e), the same orbital projected character for the b/3 structure is displayed. Here as well, SOC exchanges the two orbitals leading to a non-trivial band gap. Consequently, also the b/3structure is a QSH insulator with  $\mathbb{Z}_2 = 1$ .

# 5.3. Origin of the b/3 structure

The b/3 structure has not been reported in the literature before. In this section, its origin will be discussed. It is well known, that STM only allows access to the sample surface. Consequently, it cannot be determined, whether the b/3 structure is also present in the bulk of the sample. From Fig. 5.2 and Fig. 5.3, the b/3 is present on the two adjacent surface terraces that were observed here. Thus, at least the two upper monolayers are in the b/3 structure. Alternatively, the b/3 structure could represent a surface reconstruction. However, a surface reconstruction of  $\alpha$ -Bi<sub>4</sub>Br<sub>4</sub> has not been observed in the literature. A

change from the b/2 to the b/3 structure, that coincides with a step edge seems to be unlikely.

Based on additional DFT calculations carried out by Tobias Wichmann (numerical details are given in Ref. [31]), a surface reconstruction can also be ruled out. The total energy per unit cell  $\Delta E_{\rm tot}$  was calculated as function of the shift s, with  $\Delta E_{\rm tot} = 0 \, {\rm eV}$ corresponding to the b/2 structure. The atom positions were not relaxed during the simulation. Figure 5.8 displays the resulting dependence of  $\Delta E_{\rm tot}$  on s in units of b. Obviously, the b/2 structure (s = b/2 and  $\varphi = 107.8^{\circ}$ ) corresponds to an energetic minimum. The energy  $\Delta E_{\text{tot}}$  increases monotonically, when the shift s is decreased. Thus, the DFT calculation suggests, that the b/3 structure does not represent a local energy minimum. As the calculation assumes rigid chains and an experimental interchain distance of  $d = 0.677 \,\mathrm{nm}$ , the effect of small relaxations of the atom positions are not included. In principle, such relaxation could stabilize the b/3 structure. At s=b/3, the total energy is  $\Delta E_{\rm tot}=250\,{\rm meV}$ . To stabilize the b/3 structure as a surface reconstruction, the value would have to be offset by the relaxation of atomic positions. This seems unlikely. Thus, the DFT calculation supports the earlier conclusion that the b/3 structure is not the result of a surface reconstruction. Note, for symmetry reasons, the function  $\Delta E_{\rm tot}$  has to be periodic:  $\Delta E_{\rm tot}(s) = \Delta E_{\rm tot}(s-b)$ . This can be understood by considering the application of a mutual shift of b. Shifting the neighboring chains by b starting from the b/2 structure, yields the b/2 structure again. Starting from the b/2structure, the b/2 structure is obtained again by shifting the neighboring chains by s = b.

A different explanation of the origin of the b/3 is strain. The quasi one-dimensional crystal structure should, in principle, allow the chains to glide past each other, if an external force is applied. External shear stress could, therefore, be the origin of the b/3 structure. In conventional two-dimensional van-der-Waals materials, a glide shift of planes due to external stress can significantly alter the electronic structure [120]. Due to the second van-der-Waals gap in a quasi-one dimensional van-der-Waals material, glide shifts of the chains are easily conceivable. The shear strain  $\gamma$  is denoted by [121, p. 245]

$$\gamma = \frac{\delta x}{l},\tag{5.1}$$

where  $\delta x$  is the displacement due to the shear stress and l is the size of the body, the stress is applied to. The strain due to the mutual shift of two neighboring chains is

$$\gamma = \frac{\frac{b}{2} - s}{d}.\tag{5.2}$$

Due to the periodicity of  $\Delta E_{\rm tot}$ , the maximum shear strain is found at s=0 ( $\varphi=90^{\circ}$ ) with  $\gamma=33\,\%$ . If the stress causes a shift of s>b, the chains can no longer spontaneously relax into their original positions. Instead, they relax into the closest minimum of the potential approximated by  $\Delta E_{\rm tot}$ . Therefore, a shift of s>b/2 will cause a plastic deformation of the crystal. Due to a lack of an external reference, it is not possible to discern such a large plastic deformation in the microscopic measurements presented here. Only a mutual shift of 0 < s < b/2 between two neighboring chains can be observed. In principle, there is no reason for the strain to lock at any given value of s, e.g., s=1/3 (corresponding to the b/3 structure and  $\gamma\approx7.5\%$ ) for the b/3 structure. However, small relaxations of the internal chain structure can make certain values of s metastable. In

contrast to the global energetic minimum required to stabilize a surface reconstruction, even a minor release of energy could create a local minimum around s=b/3, thus stabilizing the b/3 structure.

Explaining the origin of the b/3 structure using strain raises the question of how a stress was applied to the crystal. There are four possible ways of applying stress to the sample. First, during the handling of the sample, e.g., gluing it to the STM sample holder, the strain could have been applied. In this case, the b/3 structure should be present in the complete crystal. Second, cleaving the sample in UHV could have introduced the shear strain: The sample was cleaved by peeling off a tape in b direction. A minor misalignment might have applied stress to the crystal. Both of these cases should lead to a strain field on macroscopic length scales. In the third case, however, stress could have been applied by crystal inhomogeneities, e.g. domain boundaries. In this case, the stress would only be applied locally. During the experiment, only the b/3 structure was observed. Only a part of the crystal was accessible for the measurements, due to small flakes or "hairs" preventing a successful approach of a tunneling tip on other parts of the sample. The fourth possibility is thermal stress. This, however, seems unlikely, as STM measurements of the b/2 structure [20] were obtained at similar temperatures. Moreover, there is no obvious reason why cleaving at low temperature (as done in [20]) should stabilize the b/2structure.

#### 5.4. Résumé

In the present chapter, a new structure of  $\alpha$ -Bi<sub>4</sub>Br<sub>4</sub> observed at the surface is reported. In this structure, there is a mutual shift of the quasi one-dimensional chains of b/3, instead of b/2. Based on the experimental data and the DFT calculations, a surface reconstruction is excluded. The b/3 structure is attributed to shear strain instead. The quasi onedimensional van-der-Waals crystal structure allows neighboring chains to glide past each other. Thus a shear stress can modify the structure of the individual monolayers without changing the AB stacking. At step edges on the surface, states with a non-vanishing DOS inside the band gap were observed by STS. Since the b/2 structure is a QSH insulator, these metallic states are attributed to the QSH edge states. Furthermore, a DFT calculation confirms that the b/3 structure is a QSH insulator: Spin orbit coupling creates an inverted band gap at the Y point, which leads to a change of parity of the conduction and valence bands. Thus, the b/3 structure has the topological invariant  $\mathbb{Z}_2 = 1$ . In summary, the b/2 and the b/3 structures support almost identical electronic properties, although the DFT calculations indicate, that the b/3 structure is closer than the b/2 structure to the transition to a trivial topology. This is different from 2D vander-Waals materials, where a change in the stacking can drastically alter the electronic properties [120, 122].

Results and analysis presented here are largely published in Ref. [31].

# 6. Disentangling the anisotropic resistivity tensor of the topological insulator $\alpha$ -Bi<sub>4</sub>Br<sub>4</sub>

 $\alpha$ -Bi<sub>4</sub>Br<sub>4</sub> crystallizes in a highly anisotropic crystal structure featuring covalently bonded chains running in  $\underline{b}$  direction and two van-der-Waals gaps. See also section 4.2 for a more detailed description. The question of the electrical anisotropy of  $\alpha$ -Bi<sub>4</sub>Br<sub>4</sub> was first raised directly after its discovery [12]. However, at the time, it was only possible to measure the resistance of  $\alpha$ -Bi<sub>4</sub>Br<sub>4</sub> crystals along their long axis which coincides with the crystallographic  $\underline{b}$  axis [12]. While  $\alpha$ -Bi<sub>4</sub>Br<sub>4</sub> was reevaluated multiple times over the years [21, 94, 115, 123], the question of its electrical anisotropy was never tackled.

In order to separate the components of the resistivity tensor  $\underline{\rho}$ , first the ratio of the surface components is determined using resistance measurements in a square geometry on a bulk sample. In a second step, the magnitude of the component  $\rho_b$  is found from measurements on a long, thin flake. In a third step, the three components are calculated from the resistance measurements on the bulk sample.

# 6.1. The resistivity tensor of $\alpha$ -Bi<sub>4</sub>Br<sub>4</sub>

The resistivity tensor of a material does not only depend on material properties such as symmetries, but also on the coordinate system chosen. Therefore, there are conventions for the coordinate systems used when reporting tensors that describe physical properties [38, p. 282]. In the present case, all measurements were performed on the  $\alpha$ -Bi<sub>4</sub>Br<sub>4</sub>(001). The selected coordinate system coincides with the crystallographic spanning the surface. As discussed in section 4.2, the  $\alpha$ -Bi<sub>4</sub>Br<sub>4</sub>(001) surface is spanned by the bulk lattice vectors  $\underline{a}$  and  $\underline{b}$ , which are orthogonal. The chains run along the  $\underline{b}$ -direction. The coordinate system is chosen so that x is parallel to a and y is parallel to b. As described in section 2.4, the resistance measured in a square configuration depends on the direction of current flow. In the following, the tips are placed in a square configuration on the  $\alpha$ -Bi<sub>4</sub>Br<sub>4</sub>(001) surface, the sides of the square are oriented along the a- and b-directions. Thus, if the current injection tips are placed in corners adjacent the side running in  $\underline{a}$ -direction, the measured resistance will be referred to as  $R_{\rm a}$ . Similarly, if the current injection tips are placed in corners with an adjacent edge running in  $\underline{b}$ -direction, the four-point resistance  $R_{\rm b}$  is measured. As a third direction of the coordinate system, the surface normal  $c^*$  is selected. For convenience, this direction will be referred to as z-direction. The coordinate system is illustrated in Fig. 6.1(a).

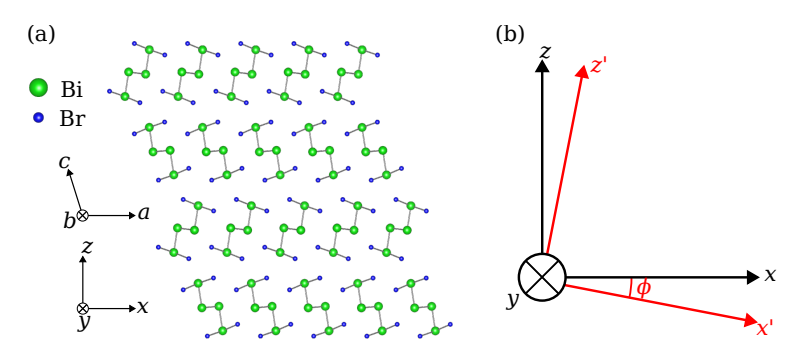


FIG. 6.1.: (a) Relation ship between the crystallographic coordinate system and the  $\underline{a}$ ,  $\underline{b}$ ,  $\underline{z}$  system. (b) Coordinate system K (black) and the coordinate system K' (red), with the axes x', and z', in which the conductivity tensor is diagonal. The angle  $\phi$  corresponds to the rotation needed to diagonalise  $\underline{\sigma}$ .

In this coordinate system, the conductivity tensor of  $\alpha$ -Bi<sub>4</sub>Br<sub>4</sub> is given by [38, Chapter 11; 54, 55]

$$\underline{\underline{\sigma}} = \begin{pmatrix} \sigma_{aa} & 0 & \sigma_{az} \\ 0 & \sigma_{bb} & 0 \\ \sigma_{az} & 0 & \sigma_{zz} \end{pmatrix}. \tag{6.1}$$

Compare also section 2.2. In the following, the contribution of the off-diagonal element  $\sigma_{az}$  to the four-probe resistance measurements in  $\alpha$ -Bi<sub>4</sub>Br<sub>4</sub> will be discussed. First  $\underline{\sigma}$  is diagonalized by rotation around the  $\underline{b}$  axis. In a second step, the magnitudes of different components of  $\underline{\sigma}$  are discussed.

# 6.1.1. Diagonalization of the resistivity tensor

As already noted in section 2.2, the conductivity tensor  $\underline{\underline{\sigma}}$  and thus also the resistivity tensor  $\underline{\underline{\rho}}$  is symmetric. Therefore, it is possible to find a coordinate system K', such that the tensor  $\underline{\underline{\sigma}}'$  becomes diagonal [54; 38, pp. 195-196; 56, pp. 218-220].

While this seems to be very useful at first glance, this transformation does not reduce the number of free parameters. Instead of the off-diagonal elements, now the numbers (or rather angles) pertaining to the transformation from the coordinate system K to the coordinate system K' have to be found. Furthermore, in most cases only certain crystallographic surfaces are accessible experimentally (e.g. low index cleavage planes). When measuring on such a plane, it is useful to write the resistivity tensor in a coordinate system particular to this surface, see also Ref. [124]. Thus, measuring the components of  $\underline{\sigma}'$  is not straightforward.

For monoclinic materials,  $\underline{\underline{\sigma}}$  can be diagonalised by rotating around the crystallographic y axis [124] by using the rotation matrix

$$R = \begin{pmatrix} \cos(\phi) & 0 & -\sin(\phi) \\ 0 & 1 & 0 \\ \sin(\phi) & 0 & \cos(\phi) \end{pmatrix}. \tag{6.2}$$

Figure 6.1(b) illustrates the relation between the coordinate system K and K'. The

conductivity tensor in the coordinate system K' is

$$\underline{\underline{\sigma}}' = R\underline{\underline{\sigma}}R^{-1}$$

$$= \begin{pmatrix} \frac{\sigma_{aa} + \sigma_{zz} + (\sigma_{aa} - \sigma_{zz})\cos(2\phi) - 2\sigma_{az}\sin(2\phi)}{2} & 0 & \sigma_{az}\cos(2\phi) + (\sigma_{zz} - \sigma_{aa})\cos(\phi)\sin(\phi) \\ 0 & \sigma_{bb} & 0 \\ \sigma_{az}\cos(2\phi) + (\sigma_{zz} - \sigma_{aa})\cos(\phi)\sin(\phi) & 0 & \frac{\sigma_{aa} + \sigma_{zz} + (\sigma_{zz} - \sigma_{aa})\cos(2\phi) + 2\sigma_{az}\sin(2\phi)}{2} \end{pmatrix}.$$

$$(6.3)$$

Finding the root of the off-diagonal element yields the angle of rotation  $\phi$  necessary to diagonalize  $\underline{\sigma}$ 

$$\phi = -\frac{1}{2}\arctan\left(\frac{2\sigma_{az}}{\sigma_{zz} - \sigma_{aa}}\right). \tag{6.4}$$

Thus, the diagonal tensor reads

$$\underline{\underline{\sigma}}' = \begin{pmatrix} \frac{\sigma_{aa} - \sigma_{zz} + \sqrt{(\sigma_{aa} - \sigma_{zz})^2 + 4\sigma_{az}^2}}{2} & 0 & 0\\ 0 & \sigma_{bb} & 0\\ 0 & 0 & \frac{\sigma_{aa} - \sigma_{zz} - \sqrt{(\sigma_{aa} - \sigma_{zz})^2 + 4\sigma_{az}^2}}{2} \end{pmatrix}.$$
(6.5)

See also appendix F on page 127.

#### 6.1.2. Contribution of the off-diagonal element

The relative sizes of the elements of  $\underline{\sigma}$  will be estimated based on the crystal structure of  $\alpha$ -Bi<sub>4</sub>Br<sub>4</sub>. As a simple qualitative estimate, the strength of the bonds is taken as an indication of the conductivity in a certain direction. The strength of the van-der-Waals interaction is assumed to be correlated with the size of the van-der-Waals gap. As already discussed in section 4.2, the atomic chains in b-direction are covalently bonded, thus the highest conductivity is expected along the <u>b</u>-direction. Note, however, that  $\sigma_{bb}$  has no effect on the off-diagonal element. Along the a-direction the atomic chains are bonded by weaker van-der-Waals forces, giving rise to a lower expected conductivity  $\sigma_{\rm aa} < \sigma_{\rm bb}$ . This is also true for the z-direction. However, in z-direction, the inter-chain distance is larger (0.48 nm, while in a-direction, the inter-chain distance is 0.44 nm) [12]. In addition, due to the monoclinic crystal structure (c.f. Fig.4.2), the chains stacked on top of each other in z-direction, are shifted slightly. It is therefore reasonable to assume that there is a greater overlap of the wave functions in the a-direction, which in turn leads to higher conductivity in z-direction. This conclusion is further substantiated by results of theoretical calculations showing that at the fundamental band gap, the lowest conduction band is mostly made up of  $Bi_{in}$ - $p_x$  orbitals [23, 99, 100] (see also section 4.3). These are oriented in the ab plane and stem from the inner Bi atoms. Consequently, their inter-layer coupling is small. As a result,  $\sigma_{zz} \ll \sigma_{aa}$  is expected. As a quantitative estimate,  $\sigma_{zz}$  is assumed to be one order of magnitude smaller than  $\sigma_{aa}$ .

The magnitude of the off-diagonal element  $\sigma_{\rm az}$  is considered. Based on the diagonal tensor  $\underline{\sigma}'$ , an upper limit for  $\sigma_{\rm az}$  is derived. If  $\sigma_{\rm zz} \ll \sigma_{\rm aa}$  is assumed, then  $\sigma'_{33}$  becomes negative for certain values of  $\sigma_{\rm az}$ . As  $\sigma'_{33}$  describes a current flowing in z' direction,  $\sigma'_{33} < 0$  would be associated with a negative resistance. A positive resistance is related to the Joule heat dissipated by the conductor [125, p. 109]. Negative resistances are forbidden

for passive electronic devices due to the first law [126, pp. 74-75] of thermodynamics: A negative resistance of a passive electronic device would violate the conservation of energy.<sup>1</sup>

Therefore, the roots of

$$\sigma_{33}' = \frac{\sigma_{aa} - \sigma_{zz} - \sqrt{(\sigma_{aa} - \sigma_{zz})^2 + 4\sigma_{az}^2}}{2}$$
 (6.6)

represent an upper limit. These roots are  $\sigma_{az_{max}} = \pm \sqrt{\sigma_{aa}\sigma_{zz}}$ . Neglecting the negative root, the maximum value of  $\sigma_{az}$  for given  $\sigma_{aa}$  and  $\sigma_{zz}$  is thus

$$\sigma_{\rm az_{max}} = \sqrt{\sigma_{\rm aa}\sigma_{\rm zz}}.\tag{6.7}$$

When  $\sigma_{aa}$  is assumed to be an order of magnitude higher than  $\sigma_{zz}$ , the upper limit of  $\sigma_{az_{max}} < 3.2 \,\sigma_{zz}$  results. Substituting Eq. (6.7) into Eq. (6.4) yields

$$\phi_{\text{max}} = \frac{1}{2} \arctan\left(\frac{2\sqrt{\sigma_{\text{aa}}\sigma_{\text{zz}}}}{\sigma_{\text{zz}} - \sigma_{\text{aa}}}\right). \tag{6.8}$$

Thus,  $|\phi_{\rm max}|=17.5^{\circ}$  results. The  $|\phi_{\rm max}|$  decreases when the ratio of the conductivities  $\sigma_{\rm aa}/\sigma_{\rm zz}$  increases. For example, in the case of  $\sigma_{\rm aa}=100\sigma_{\rm zz}$ , the upper limit for the off-diagonal element becomes  $\sigma_{\rm az_{max}}<10\,\sigma_{\rm zz}$ . And hence,  $|\phi_{\rm max}|=5.7^{\circ}$  is obtained.

According to Eq. (6.4), the angle  $\phi$  is a measure of the contribution of the off-diagonal element  $\sigma_{\rm az}$  to electrical transport through a monoclinic crystal in the ac plane. For  $\phi=0^{\circ}$  the coordinate systems K and K' are identical and the resistivity tensor  $\underline{\rho}$  is already diagonal. In this case, measuring the components of  $\underline{\rho}$  is greatly simplified, since only the elements on the main diagonal need to be determined. In general, however, the angle  $\phi$  is unknown and a surface, on which the components of  $\underline{\rho}'$  can be measured directly, is difficult to prepare.

Using the upper limit for  $\sigma_{\rm az}$ , the systematic error that is introduced, when  $\sigma_{\rm az}$  is neglected, is calculated. As long as the underlying assumption  $\sigma_{\rm aa}\gg\sigma_{\rm zz}$  holds, this systematic error is related to  $\cos(\phi_{\rm max})$ . The cosine  $\cos(\phi)$  gives the projection of the coordinate axes of K' onto the axes of K.Thus, assuming  $\sigma_{\rm aa}=10\sigma_{\rm zz}$ , the maximum systematic error is estimated to be  $1-\cos(17.5^\circ)=0.05$ . If the conductivity  $\sigma_{\rm aa}$  becomes even larger, the systematic error will decrease. Since the present thesis constitutes the first measurement of the anisotropy of  $\alpha$ -Bi<sub>4</sub>Br<sub>4</sub>, this systematic error of up to 5% is deemed acceptable. Thus, the off-diagonal element is neglected in the measurements presented here.

When neglecting the off-diagonal element  $\sigma_{az}$ , the conductivity tensor becomes

$$\underline{\underline{\sigma}} = \begin{pmatrix} \sigma_{\text{aa}} & 0 & 0\\ 0 & \sigma_{\text{bb}} & 0\\ 0 & 0 & \sigma_{\text{zz}} \end{pmatrix}. \tag{6.9}$$

The resistivity tensor is the inverse of the conductivity tensor. For a diagonal tensor  $\underline{\underline{I}}$ , the elements of its inverse  $\underline{I}$  are given by  $I_{ii} = 1/T_{ii}$ . Consequently, the resistivity tensor

<sup>&</sup>lt;sup>1</sup>Negative resistances can be realized using active components, see [34, pp. 380-382].

is

$$\underline{\rho} = \begin{pmatrix} \rho_{\text{aa}} & 0 & 0 \\ 0 & \rho_{\text{bb}} & 0 \\ 0 & 0 & \rho_{\text{zz}} \end{pmatrix}.$$
(6.10)

In the following, the elements of this tensor are to be measured. To simplify the nomenclature, the second, redundant index will be dropped hereafter.

# 6.2. Method to disentangle the diagonal components of the resistivity tensor

For this thesis, the following method was developed, in order to disentangle the three elements on the main diagonal of the resistivity tensor of  $\alpha$ -Bi<sub>4</sub>Br<sub>4</sub>. To measure all three diagonal components of the resistivity tensor, two different measurements are combined:

- 1. Measurements on a 3D crystal in a square geometry with current injected along the two orthogonal directions  $\underline{a}$  and  $\underline{b}$ , and
- 2. In-line measurements on exfoliated Bi<sub>4</sub>Br<sub>4</sub>-flakes, i.e. measurements on a rectangular cuboid with uniform current density.

The second step resembles a measurement on a sample that is cut in a low index direction, compare also [29, 60].

# 6.2.1. Determination of the anisotropy A (Square Measurement)

On the bulk sample, the tips were placed in a square geometry, with the sides of the square aligned with the lattice vectors  $\underline{a}$  and  $\underline{b}$ . As discussed in section 2.4, the resistance of a square measurement of a square tip geometry on a bulk sample is given by Eq. (2.51). Rewriting for the new coordinate system yields

$$R_{\text{square,b}} = \frac{\sqrt{\rho_{\text{b}}\rho_{\text{z}}}}{\pi s} \left( 1 - \frac{1}{\sqrt{1 + \frac{\rho_{\text{b}}}{\rho_{\text{a}}}}} \right)$$
 (6.11)

when the current is injected along b direction [30, 32].  $R_{\text{square,a}}$  is obtained by exchanging b and a in Eq. (6.11).

From  $R_{\text{square,b}}$  and  $R_{\text{square,b}}$ , the surface anisotropy

$$A = \frac{\rho_{\rm a}}{\rho_{\rm b}} \tag{6.12}$$

can be obtained by solving

$$\frac{R_{\text{square,a}}}{R_{\text{square,b}}} = \frac{\sqrt{1 + \frac{\rho_{\text{a}}}{\rho_{\text{b}}}} - 1}{\sqrt{1 + \frac{\rho_{\text{b}}}{\rho_{\text{a}}}} - 1}$$

$$(6.13)$$

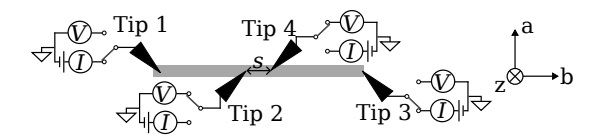


Fig. 6.2.: Linear, distance-dependent measurement on a long, thin flake (gray area). The current is injected using the two outer tips (Tips 1 and 3) while the voltage drop is measured using the inner tips 2 and 4.

[30, 32] numerically for the anisotropy  $A = \rho_a/\rho_b$ . See also section 2.4.

## 6.2.2. Determination of the resistivity $\rho_b$ (Linear Measurement)

In the second step, a single element of the resistivity tensor,  $\rho_b$ , is measured. The data is aquired on thin, long flakes.  $\alpha$ -Bi<sub>4</sub>Br<sub>4</sub> tends to form elongated flakes; the long edge of these flakes is parallel to the  $\underline{b}$ -direction [108].

As shown in Fig. 6.2, current is injected at the opposing short edges of the flake. In the center region of the flake, there will be uniform current flow in  $\underline{b}$ -direction. As Fig. 6.2 further shows, the two voltage probing tips are placed at the middle of the flake. From a measurement of R depending on the inter-tip distance s, the resistivity  $\rho_b$  can be extracted by using a linear fit described by

$$R = \frac{\rho_{\rm b}}{t_{\rm av}} s = f s,\tag{6.14}$$

where w is the flake width and t is its thickness.

## **6.2.3.** Determination of $\rho_a$ and $\rho_z$

Solving Eq. (6.11), an equation for  $\rho_z$  can be derived. Rewriting for  $R_{\text{square,a}}$  and some trivial rearranging results in

$$(R_{\text{square,a}}\pi s)^2 = \rho_z \rho_a \left(1 - \frac{1}{\sqrt{1+A}}\right)^2.$$
 (6.15)

With

$$\left(1 - \frac{1}{\sqrt{1+A}}\right)^2 = 1 - \frac{2}{\sqrt{1+A}} + \frac{1}{1+A} = \frac{1}{1+A}\left((1+A) - 2\sqrt{1+A} + 1\right) \qquad (6.16)$$

$$= \frac{1}{1+A}\left(\sqrt{1+A} - 1\right)^2 \qquad (6.17)$$

and  $\rho_a = A\rho_b$ , the resistivity  $\rho_z$  is thus given by

$$\rho_{\rm z} = \frac{\left(R_{\rm square,a}\pi s\right)^2 \cdot (1+A)}{A \cdot \left(\sqrt{1+A}-1\right)^2 \cdot \rho_{\rm b}}.$$
(6.18)

This now expresses  $\rho_z$  in terms of the anisotropy A and the resistivity  $\rho_b$ , that were measured before.

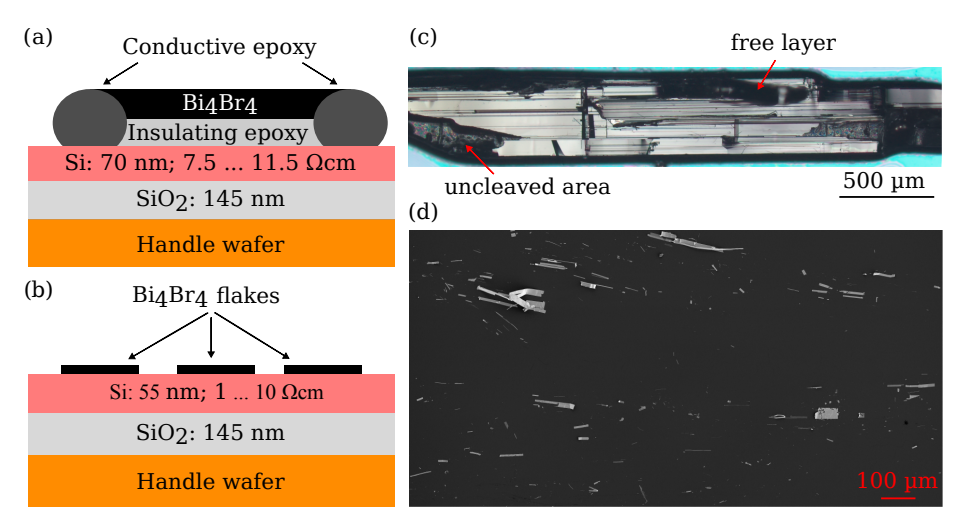


FIG. 6.3.: (a) Sample structure for bulk measurements (not to scale) at room temperature. (b) Sample structure for flake measurements (not to scale). (c) Optical micrograph of the bulk sample after completion of the measurements under ambient conditions. The crystal has an elongated shape due to its quasi one-dimensional structure. This structure is also the origin of the horizontal lines on the surface. Very typical for  $\alpha$ -Bi<sub>4</sub>Br<sub>4</sub> are layers that are still partially attached to the sample but do not lie flat on the surface. Such a layer is visible at the top as a dark contrast. At the lower left, there is a small rough area, that was not cleaved. (d) SEM micrograph of the flake sample after completion of the measurement. Note the random distribution of flakes due to exfoliation.

With known A and  $\rho_b$ , the resistivities  $\rho_a$  and  $\rho_z$  can be easily calculated. Thus, the elements on the main diagonal of  $\underline{\rho}$  have been disentangled. For computations using the Wasscher transformation (c.f. section 2.3), the mean resistivity

$$\bar{\rho} = \sqrt[3]{\rho_a \rho_b \rho_z} \tag{6.19}$$

is also needed. By substituting Eq. (6.18)  $\bar{\rho}$  can be computed directly from A,  $\rho_{\rm b}$ , and the inter-tip distance s:

$$\bar{\rho} = \sqrt[3]{\rho_{\rm a}\rho_{\rm b}\rho_{\rm z}} = \sqrt[3]{\rho_{\rm b}\frac{(R_{\rm square,a}\pi s)^2 \cdot (1+A)}{\left(\sqrt{1+A}-1\right)^2}}.$$
(6.20)

# 6.3. Samples

As noted above, two different samples were needed to measure the three components of the resistivity tensor, a bulk sample and a sample of exfoliated flakes. As substrates, silicon-on-insulator (SOI) substrates were used. The SOI substrates were cleaned by a wet etching process (RCA/hydrofluoric acid), leaving a hydrogen terminated surface. The bulk  ${\rm Bi_4Br_4}$  crystal (0.5 mm  $\times$  3.6 mm  $\times$  0.1 mm) was glued to the SOI substrate, using insulating epoxy (EPO-TEK® 323LP). To establish a conductive connection between

the crystal and ground via the device layer of the SOI substrate for tunneling, two drops of conductive epoxy (EPO-TEK<sup>®</sup> H20E) were applied on both ends of the crystal [Fig. 6.3(a)]. In this configuration, the insulating epoxy between these contacts prevents current from flowing from the Bi<sub>4</sub>Br<sub>4</sub> crystal to the substrate. The sample was then inserted into the UHV chamber and cleaved using Kapton tape before insertion into the STM. Figure 6.3(c) shows an optical microscope image of the sample after cleaving under ambient conditions.

The flakes were exfoliated from the same  $\alpha$ -Bi<sub>4</sub>Br<sub>4</sub> bulk crystal also used for the bulk sample using the technique detailed in section 4.4 on page 54. After thinning the flakes down by multiple cleaving steps inside the glovebox, the tape was placed onto a separate SOI substrate and left in place. The sample was transported through air and introduced to the UHV chamber. The tape was then peeled off under UHV conditions to expose the exfoliated flakes. A cross section of the second sample is shown in Fig. 6.3(b). Similar to the insulating epoxy of the bulk sample, the thin, highly insulating device layer of the SOI prevents the substrate from contributing significantly to the measured resistance. Figure 6.3(d) displays an SEM image of the flake sample after conclusion of the measurement. The flakes are distributed randomly on the surface. Their long axes, however, tend to be aligned with each other. This alignment corresponds to the alignment of the bulk crystal, from which the flakes were exfoliated.

#### 6.4. Results

#### 6.4.1. Sizes of the relevant flakes

Before the results of the transport measurements are presented, the sizes of the flakes used for the measurements are determined. The necessary measurements were obtained as the last step, as sample had to be transferred through air to an ambient atomic force microscope (AFM) and a scanning electron microscope (SEM). In order to determine the flake sizes, two different instruments were used; an SEM (Zeiss Sigma 500 with Gemini column) to find the lateral flake sizes (l and w) and an ambient AFM (Brucker Inova) for the flake thicknesses t. To accurately image the large heights, tapping mode AFM was used. To remove the effect of piezo creep, the forward (FWD) and backward (BWD) scan directions were averaged.

For the measurements, four flakes were used: flakes A, B, C, and D. Figure 6.4 depicts flakes A and B. The flake heights were extracted from height profiles of the AFM scan depicted in Fig. 6.4(a). The overview image [Fig 6.4(c)] and the SEM scan [Fig 6.4(d)] show significant damage to flake A sustained due to a transient over current event while

TA	в. 6.1.:	Sizes of	the	flakes	used	for tl	he me	asureme	$_{ m nts.}$
	_	w	(µm	)	l (μr	n)	t	$(\mu m)$	
	Flake	A 6!	5 + 0	1 5	9 0 +	0.5	0.64	1 + 0.04	_

_	$w$ ( $\mu$ m)	$l~(\mu { m m})$	$t~(\mu\mathrm{m})$
Flake A	$6.5 \pm 0.1$	$59.0 \pm 0.5$	$0.64 \pm 0.04$
Flake B	$3.8 \pm 0.1$	$59.5 \pm 0.5$	$0.57 \pm 0.03$
Flake C	$2.6 \pm 0.1$	$55.5 \pm 0.5$	$0.64 \pm 0.04$
Flake D	$16.0 \pm 0.2$	$55.0 \pm 0.5$	$1.13 \pm 0.06$

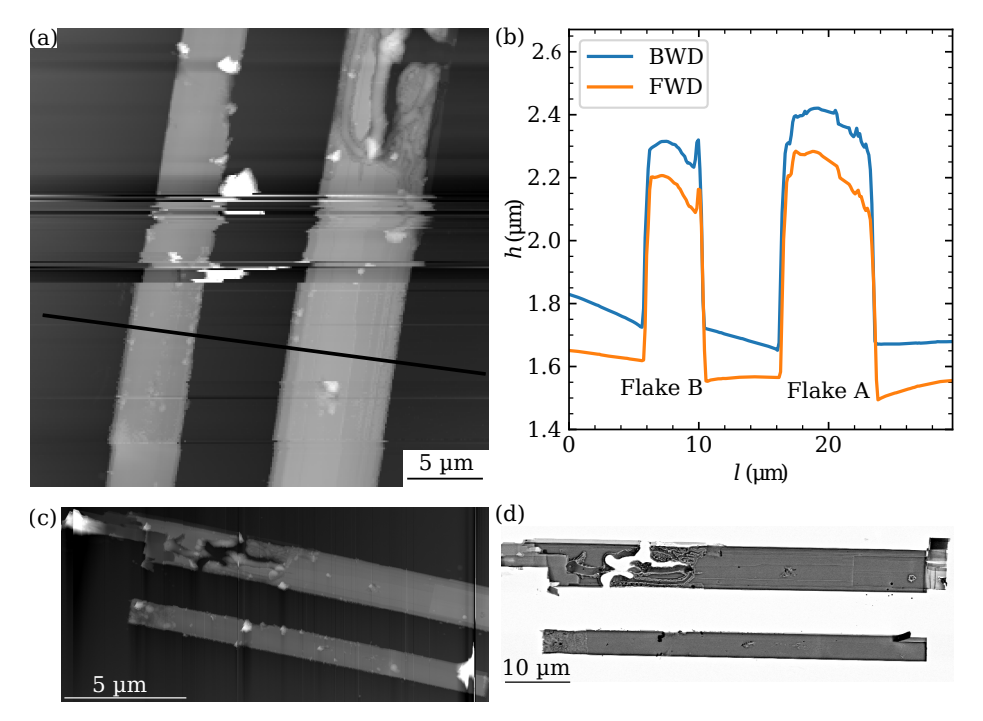


FIG. 6.4.: (a) AFM topograpy of a part of flakes A and B. (b) From the height profiles, the flake height are determined to be  $t_{\rm Flake~A}=(0.64\pm0.04)\,\mu{\rm m}$  and  $t_{\rm Flake~B}=(0.57\pm0.03)\,\mu{\rm m}$ . To minimize errors due to feedback overshoot, both the forward and the backward scanning direction are used. (c) AFM topography showing an overview of both flakes. The brightness represents the topographical height, with lower areas displayed as dark. (d) SEM micrographs of flakes A and B. flake A (upper) and flake B (lower). Flake A exhibits considerable damage caused by a transient high current event during contacting.

contacting. The high current destroyed a portion of the flake. The holes go down to the substrate level. Flake C is depicted in Fig. 6.5.

Figure 6.6 depicts flake D. Flake D was used to measure the bulk anisotropy at  $77\,\mathrm{K}$  in lieu of the bulk sample (see below for details). In the electron micrograph [Fig. 6.6(c)], a number of flakes are visible, peeling off from the surface and covering flake D. These flakes were already present during the measurements at low temperature, however, in the SEM micrographs taken after removing the sample from the UHV chamber, the flakes peeling off cover a larger part of flake D. While these flakes did prevent access to parts of flake D in the STM, they have considerably shifted after removing the sample from the vacuum system. These flakes also limited the area accessible to the AFM, thus the AFM topography in Fig. 6.6(a) corresponds to the top right corner of panel (c).

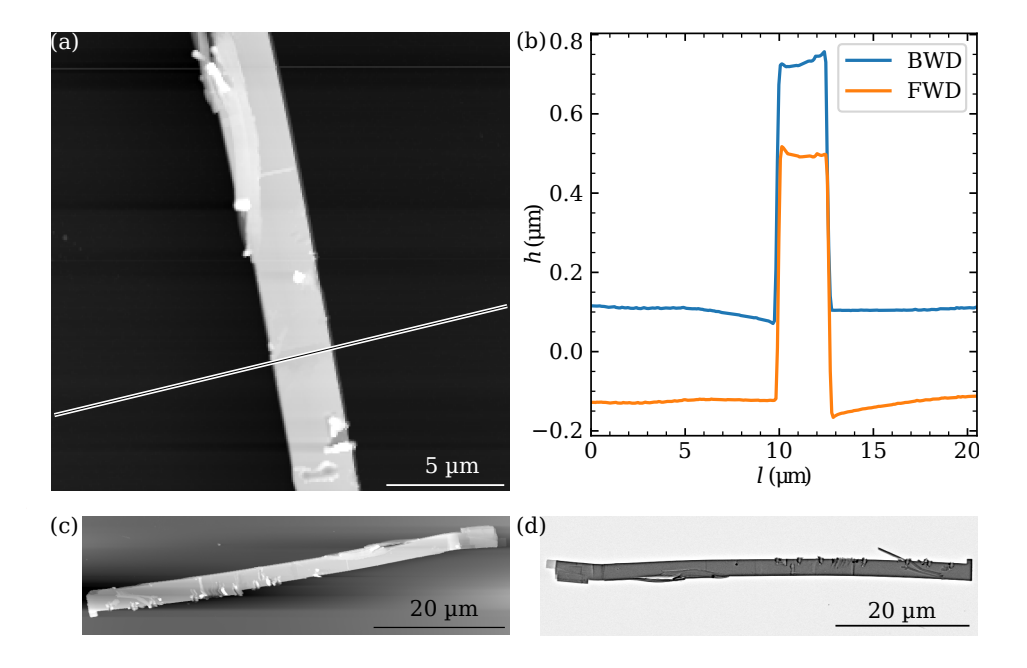


Fig. 6.5.: (a) AFM topograpy of a part of flake C. (b) From the height profiles, the thickness of flake C is determined:  $t=(0.64\pm0.04)\,\mu\text{m}$ . To minimize errors due to feedback overshoot, both the forward and the backward scanning direction are used. (c) Overview AFM topography showing the complete flake. The brightness represents the topographical height, with lower areas displayed as dark. (d) SEM micrograph of flake C.

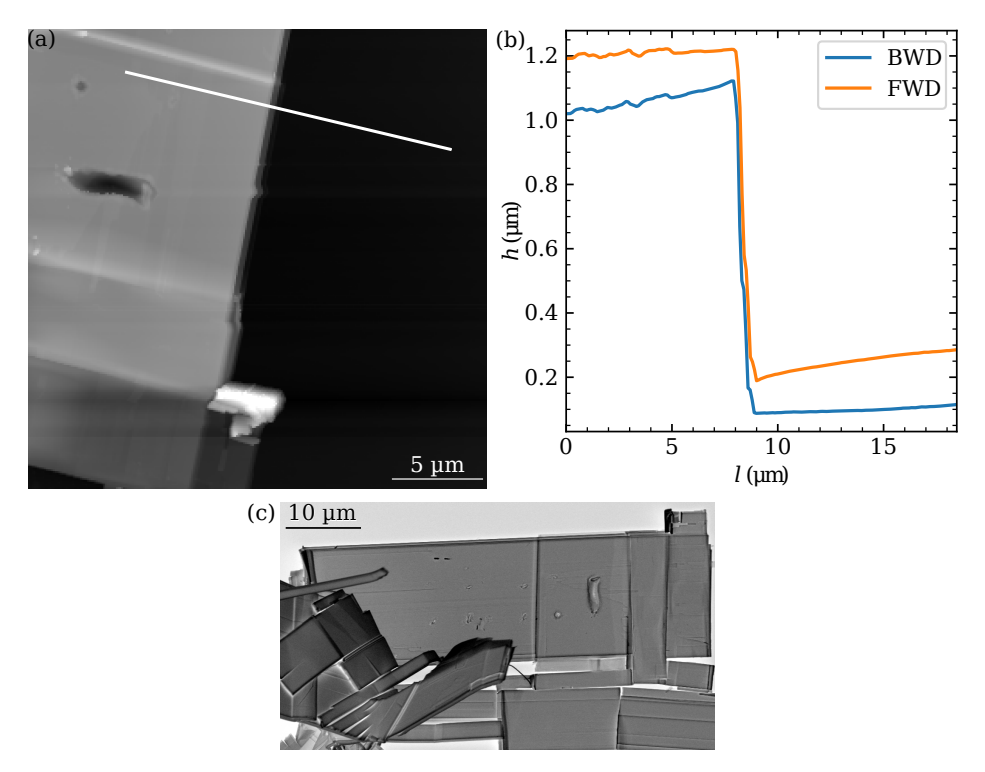


Fig. 6.6.: (a) AFM topograpy of a part of flake D; the flakes hanging above flake D [see panel (c)] prohibited a more complete AFM scan of flake D. The brightness represents the topographical height, with lower areas displayed as dark. (b) From the height profiles, the flake height are determined to be  $t=(1.13\pm0.06)\,\mu\text{m}$ . To minimize errors due to feedback overshoot, both the forward and the backward scanning direction are used. (c) SEM micrographs of flake D.

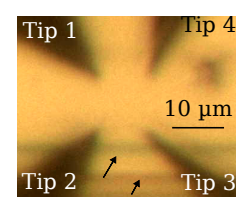


FIG. 6.7.: Photomicrograph of the bulk sample. The tips are placed in a square configuration. The horizontal lines indicated by the arrows result from step edges or small sections of the crystal peeling off, and are oriented along  $\underline{b}$ -direction. They were used to align the square. For convenience, this image, presented already in Fig. 3.1, is repeated here.

#### 6.4.2. Room Temperature

#### 6.4.2.1. Bulk measurements

For the transport measurements on the bulk sample, the tips were placed in a square with side-length  $s=10\,\mu\text{m}$ . Such a square placement of the tips is shown in Fig. 6.7. The square is oriented with one edge parallel to the parallel lines visible on the surface (pointed out by the arrows), which correspond to large step edges, compare also Fig. 6.3(c). Due to the quasi one-dimensional crystal structure of  $\text{Bi}_4\text{Br}_4$ , the step edges are parallel to the the lattice vector  $\underline{b}$  [20, 21].

The distance  $s = 10 \,\mu\text{m}$  is chosen as a compromise between two confounding factors:

- 1. According to Eq. (6.11) the resistance decreases with increasing s leading to a worse signal-to-noise ratio for large values of s.
- 2. Conversely, decreasing s leads to a greater influence of positioning errors, a major source of measurement uncertainty, as explained below.

Table 6.2 lists the resistances measured in five different transport experiments. Between these measurements, the tips were repositioned and reconditioned on stainless steel/gold as needed. The equivalent resistances (c.f. section 2.7) were averaged. The four-point resistance with current injection along the chain direction  $R_{\rm square,b}$  is  $\sim 20$  times smaller than the resistance  $R_{\rm square,a}$  perpendicular to the chain direction. Using Eq. (6.13), the

TAB. 6.2.: Measurement data of five measurements to determine the anisotropy of the  $\alpha$ -Bi<sub>4</sub>Br<sub>4</sub>(001) surface at room temperature. The anisotropy  $A=\rho_{\rm a}/\rho_{\rm b}$  obtained using Eq. (6.13) is also given.

No	$R_{\rm square,a} (\Omega)$	$R_{\text{square, b}}\left(\Omega\right)$	A
1	$157.2 \pm 0.3$	$8.4 \pm 0.2$	5.7
$^2$	$163.5 ~\pm~ 0.5$	$7.2 \pm 0.4$	6.4
3	$108.15 \pm 0.03$	$4.79 \pm 0.02$	6.4
4	$188.9 \pm 0.2$	$5.4 \pm 0.2$	8.4
5	$173.9 ~\pm~ 1.8$	$10.5 \pm 0.7$	5.4
Avg	$158 \pm 13$	$7.2 \pm 1.0$	$6.4 \pm 0.5$

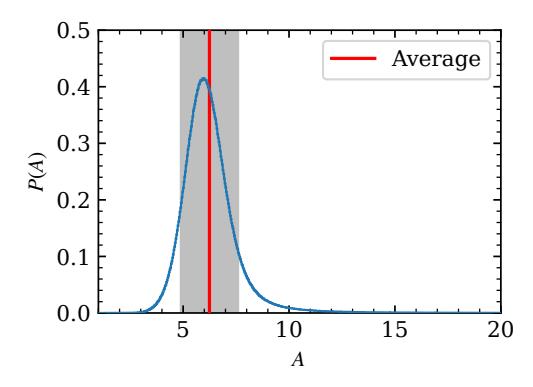


FIG. 6.8.: Histogram of A obtained from the Monte-Carlo propagation of uncertainty. The mean of 6.4 is indicated by the red line. The gray background indicates the range of  $\bar{A} \pm \sigma_{\rm A}$  with  $\sigma_{\rm A} = 1.4$ .

anisotropy  $A = \rho_{\rm a}/\rho_{\rm b}$  is calculated, it is also listed in Tab. 6.2. The average anisotropy is  $A = 6.4 \pm 0.5$ .

The resistances listed in Tab. 6.2 show also uncertainties. These uncertainties are related to the performance of the electronics, the noise in the current and voltage measurements, the tip-sample contacts etc. Therefore, this type of error is called *electrical error*. The uncertainties are calculated as the standard error of the mean: The resistance given in each individual cell is calculated first by averaging multiple repetitions of the same measurement (giving the average and the standard error of the mean) and then averaging the equivalent resistances. It is evident, that these uncertainties cannot explain the spread of the resistances between different measurement series. Accordingly, for the averages given in the last line of Tab. 6.2, the standard error of the mean was employed. The uncertainties listed in Tab. 6.2 only describe this electrical error. Obviously, the uncertainties cannot explain the deviations between the individual measurements.

A source of measurement uncertainty, that is not contained within the error bars given in Tab. 6.2 is the *tip-placement error*. The origin of the tip-placement error was already addressed in section 3.5 on page 44. A major source of this error is the resolution of the optical microscope, which is  $1\,\mu\text{m}$ . Since Eq. (6.13) has to be solved numerically for A, the standard Gaussian propagation of uncertainty cannot be applied. Therefore, to gain insight into the tip-placement error, a Monte-Carlo propagation of uncertainty is applied [91]. The Monte-Carlo propagation of uncertainty was likewise introduced in section 3.5, where it was used to calculate relative errors for the linear, equidistant tip configuration.

For the Monte-Carlo propagation of uncertainty,  $N=10\,000\,000$  samples of the resistances  $R_{\rm a}$  and  $R_{\rm b}$  were computed. The tips were placed in a square with  $s=10\,\mu{\rm m}$ . To each x and y positions N samples from a normal distribution with a standard deviation of  $1\,\mu{\rm m}$  were added. This standard deviation is based on the experimental error of  $1\,\mu{\rm m}$ . To compute the resistances, Eq. (2.48) was used. Eq. (2.48) describes the resistance measured in an arbitrary tip configuration on an anisotropic bulk sample. In addition to the tip positions also the resistivities are required to compute the resistance R. Therefore, the disentangled elements resistivity tensor at room temperature,  $\rho_{\rm a}$ ,  $\rho_{\rm b}$ , and  $\rho_{\rm z}$  given in Eq. (6.22), were plugged into Eq. (2.48).

Using Eq. (2.48),  $R_{\rm square,a}$  and  $R_{\rm square,b}$  are calculated for each set of samples. Then the anisotropy A for each set of samples could be calculated by solving Eq. 6.13 numerically. A histogram of the anisotropy obtained is plotted in Fig. 6.8. From this distribution,  $\bar{A}=6.3\pm1.4$  results. This uncertainty is almost three times larger than the experimental uncertainty  $\pm0.5$ . At the distance  $s=10\,\mu{\rm m}$ , the Monte-Carlo simulation finds a long tail for the anisotropy A. The long tail originates from very small values of  $R_{\rm square,b}$ , due to small inter-tip distances. These small inter-tip distances, and corresponding small resistances  $R_{\rm square,b}$ , are, however, unlikely to occur during the experiment, as small inter-tip distances are avoided to prevent tip crashes. Furthermore, as discussed in section 3.5, the point of contact will tend to move outwards. Therefore, modeling the tip-placement error with circular Gaussian distributions does not completely capture the true tip-placement error as observed during the experiments. Nevertheless, the naive simulation of the tip-placement error allows the conclusion that it can cause significantly larger uncertainties than the electrical errors listed in Tab. 6.2

#### 6.4.2.2. Linear measurements

From the available flakes [c.f. Fig. 6.3(d)], the long thin flakes A, B, and C were selected for the measurement. As described in section 6.2.2, the four-point resistances R of the flakes were measured as a function of the inner tip distance s. Figure 6.9(a), (b), and (c) depict the resulting curves for the three flakes. The resistance-distance curves do not exhibit any turn-off points that would indicate a strong deviation from uniform current flow. Flake C is depicted during the measurement in Fig. 6.9(d); the inter-tip distances s were measured using the optical microscope of the four tip STM. The uncertainty in inter-tip distance s results form the resolution of the optical microscope. An additional source of uncertainty is the width of the tips and the difficulty in identifying the point of contact. This is the tip-placement error discussed above. The measured data is fitted with a linear function according to Eq. (6.14). To account for the uncertainty in inter-tip distance s, the data were fitted using an orthogonal distance regression algorithm [127]. The resulting fit parameter s is given in the keys in Fig. 6.9.

From the fit,  $\rho_{\rm b}$  was extracted, based on the assumption that the current flows in  $\underline{b}$ -direction with a uniform current density close to the flake center. Using Eq. (6.14),  $\rho_{\rm b}$  is given by

$$\rho_{\rm b} = ftw. \tag{6.21}$$

As explained in detail in section 6.4.1, the flake sizes were measured at ambient conditions

Tab. 6.3.: Disentangled resistivities and the anisotropy  $A_z = \rho_z/\rho_b$  for three different Bi<sub>4</sub>Br<sub>4</sub> flakes, and their averages at room temperature.

	$\rho_{\rm b}~({\rm m}\Omega{\rm cm})$	$\rho_{\rm a}~({\rm m}\Omega{\rm cm})$	$\rho_{\rm z}~(\Omega{\rm cm})$	$A_{ m z}$	$\bar{\rho} \; (\Omega  \mathrm{cm})$
Flake A	$14.4 \pm 0.8$	$93 \pm 9$	$7\pm2$	460	0.20
Flake B	$9.2 \pm 0.6$	$59 \pm 6$	$10 \pm 3$	1100	0.18
Flake C	$6.9 \pm 0.5$	$44 \pm 5$	$14 \pm 4$	2000	0.16
Avg	10 ±3	$65 \pm 15$	$11 \pm 3$	1300	0.18

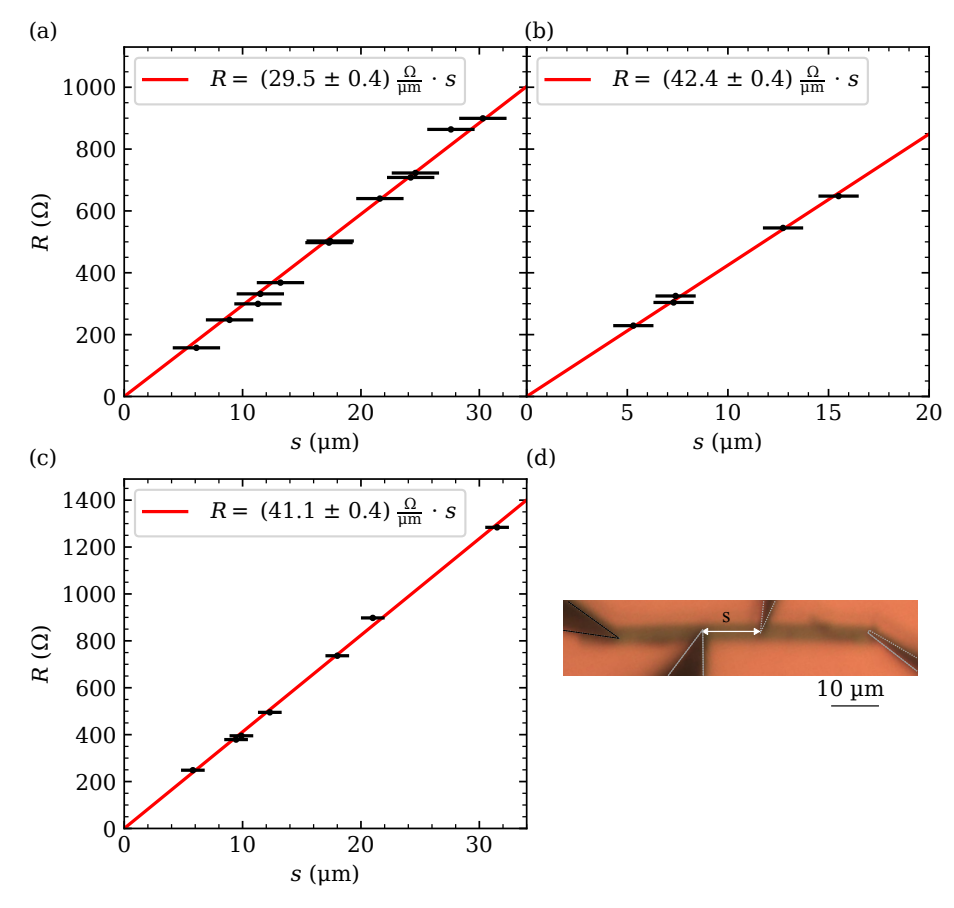


FIG. 6.9.: (a), (b), (c) show transport data on the long, thin  $\alpha$ -Bi<sub>4</sub>Br<sub>4</sub> flakes A, B, and C. The resistance is plotted as function of the distance s between the two voltage probing tips. The data was fitted with  $R = f \cdot s$  (red lines). (d) Flake C during measurement. The outlines of the the tips are highlighted by dashed lines.

once the electrical measurements were completed. For these measurements, an SEM and an ambient AFM were used. Table 6.3 lists the resistivities  $\rho_b$  of three different flakes.

The resistivity  $\rho_b$  shows a large spread. While the flakes were all exfoliated at the same time from the same crystal, minor differences in doping are conceivable. Moreover, during the room temperature measurements, the light of the optical microscope was kept on. In principle, minor changes in the intensity of the light source could induce a variation of the carrier density. However, as will be shown below, the spread of  $\rho_b$  is also present in the low temperature data taken without light. An alternative explanation is a small gating effect due to the SOI substrate.

#### 6.4.2.3. Calculation of the resistivity tensor

Using the previous results, the missing elements of the resistivity tensor,  $\rho_{\rm a}$  and  $\rho_{\rm z}$ , can now be computed as described in section 6.2.3.  $\rho_{\rm a}$  is calculated directly from Eq. (6.12). For  $\rho_{\rm z}$ , Eq. (6.18) with  $R_{\rm square,a} = (158 \pm 13)\,\Omega$  is used. The results are tabled in Tab. 6.3. The table also gives the average resistivity  $\bar{\rho}$  computed using Eq. (6.20) and the anisotropy  $A_{\rm z} = \rho_{\rm z}/\rho_{\rm b}$ .

Note that the large spread of  $\rho_a$  and  $\rho_z$  is induced by the spread of  $\rho_b$ . Keeping in mind that according to Eq. (6.18)  $\rho_z \propto 1/\rho_b$  and  $A_z \propto 1/\rho_b^2$ , the large discrepancies in  $\rho_z$  and  $A_z$  can be easily understood. On the other hand  $\bar{\rho} \propto \sqrt[3]{\rho_b}$ . Correspondingly, the spread of  $\bar{\rho}$  is much smaller. In summary, the resistivity tensor of  $\alpha$ -Bi<sub>4</sub>Br<sub>4</sub> is

$$\underline{\rho}_{\text{RT}} = \begin{pmatrix} (65 \pm 15) \,\text{m}\Omega \,\text{cm} & 0 & 0\\ 0 & (10 \pm 3) \,\text{m}\Omega \,\text{cm} & 0\\ 0 & 0 & (11 \pm 3) \,\Omega \,\text{cm} \end{pmatrix}$$
(6.22)

at room temperature (RT). The average resistivity is  $\bar{\rho}_{RT} = 180 \,\mathrm{m}\Omega\,\mathrm{cm}$ .

With  $\rho_{\rm a}$  and  $\rho_{\rm b}$ , the sheet resistivity  $R_{\rm S,avg}$  of the  $\alpha$ -Bi<sub>4</sub>Br<sub>4</sub> flakes can be calculated using Eq. (2.61).  $R_{\rm S,avg}$  then facilitates a retroactive justification of the chosen SOI substrate. According to Eq. (2.12), the (isotropic) SOI substrate ( $t=55\,{\rm nm},\,\rho\geq 1\,\Omega\,{\rm cm}$ ) has a sheet resistivity of  $R_{\rm S,SOI}\geq 0.18\,{\rm M}\Omega\,\Box^{-1}$ . Conversely, the sheet resistivity of the  $\alpha$ -Bi<sub>4</sub>Br<sub>4</sub> ( $\bar{t}=0.6\,\mu{\rm m}$ ) is  $R_{\rm S,\alpha\text{-Bi}_4\text{Br}_4}=410\,\Omega\,\Box^{-1}$ . Thus,  $R_{\rm S,SOI}/R_{\rm S,Bi_4\text{Br}_4}\gtrsim 430$ . While this ratio does not necessarily hold for the ratio of currents, it is a strong indication that the current density inside the  $\alpha$ -Bi<sub>4</sub>Br<sub>4</sub>-flakes dominates the current density flowing through the substrate.

Furthermore, the disentangled resistivity tensor allows to revisit the discussion on the contribution of the off-diagonal element  $\sigma_{\rm az}$ . The off-diagonal element  $\sigma_{\rm az}$  was neglected in the analysis of the measurement data. Therefore, the results cannot serve as experimental verification of the initial assumption, that  $\sigma_{\rm az}$  could be neglected. Nevertheless, a contradiction between the initial assumptions would point to a significant flaw in the reasoning. Initially it was assumed that  $\sigma_{\rm a}$  was an order of magnitude larger than  $\sigma_{\rm z}$ . From the results, the ratio  $\sigma_{\rm a}/\sigma_{\rm z}\approx 170$  is found.

# 6.4.3. Low temperature transport on flakes

Low-temperature transport data was obtained by Serhii Kovalchuk using the methods developed at room temperature. The analysis was done by Jonathan Karl Hofmann.

Measurements at 77 K were obtained on the flake sample, also used at room temperature. The flakes B and C were measured again. Furthermore, a new flake, flake D, was used. The sample was transferred to the low temperature STM using a vacuum suitcase at pressures no higher than  $\sim 1 \times 10^{-5}\,\mathrm{Pa}$ . As the low temperature STM was not baked prior to the measurements, its base pressure was  $\sim 2 \times 10^{-7}\,\mathrm{Pa}$ .

Note, at 77 K, also the surface anisotropy A was measured on a flake. This is possible due to the extremely high resistivity of  $\alpha$ -Bi<sub>4</sub>Br<sub>4</sub> in the  $\underline{z}$ -direction. Furthermore, the SEM installed in the low temperature four-tip STM enabled a smaller inter-tip distance of  $s=5\,\mu\mathrm{m}$ . The micrograph in Fig. 6.10 shows the flake during measurement. According to the Wasscher transformation, for each anisotropic flake, there exists an equivalent isotropic flake whose dimensions are scaled by a factor of  $\sqrt{\rho_i/\bar{\rho}}$  (c.f. section 2.3). In the

case of the Bi<sub>4</sub>Br<sub>4</sub> flakes, during the transformation the thickness is stretched, while both directions on the flake surface are compressed.

The influence of the flake boundaries on the measurement results can be judged using the correction factors derived in section 2.6.2 on page 22. While the tips are placed in a square on the flake surface, the Wasscher transformation will transform the square into a rectangle. This rectangle then has the edge lengths

$$s_{\rm a}' = s \sqrt{\frac{\rho_{\rm a}}{\bar{\rho}}}$$
 and  $s_{\rm b}' = s \sqrt{\frac{\rho_{\rm b}}{\bar{\rho}}}$ . (6.23)

As is shown in Fig. 6.10 the edges of the square are aligned with the lattice directions  $\underline{a}$  and  $\underline{b}$ , which themselves are aligned with the flake edges [108].

To evaluate the correction factors  $F_{\perp}$  [Eq. (2.84)],  $F_{\parallel}$  [Eq. (2.88)], and  $F_{\rm t}$  [Eq. (2.98)] numerically, the components of the resistivity tensor need to be known. In order to proceed with the analysis, the results for room temperature given in Eq. (6.22) are used. From Tab. 6.1, flake D has the dimensions  $t=1.13\,\mu{\rm m},\ l=55\,\mu{\rm m},\ {\rm and}\ w=16\,\mu{\rm m}.$  The distance from the current injection tips to the nearest flake boundary was  $d_{\rm a}=6\,\mu{\rm m}.$  For the resistance measurements, a square with  $s=5\,\mu{\rm m}$  was used. Applying the Wasscher transformation [Eq. (2.33)] gives the distances on the equivalent isotropic flake:  $w'=9.29\,\mu{\rm m},\ l'=31.9\,\mu{\rm m},\ t'=8.54\,\mu{\rm m},\ s'_{\rm a}=2.90\,\mu{\rm m},\ s'_{\rm b}=1.14\,\mu{\rm m},\ {\rm and}\ d'_{\rm a}=3.49\,\mu{\rm m}.$ 

First, the correction of  $R_{\rm square,a}$  is considered. Due to the high aspect ratio of the flake, the influence of the flake boundary parallel to the lattice vector  $\underline{a}$  is neglected. The injection of current along the lattice vector  $\underline{a}$  is described by the correction factors  $F_{\perp}$  and  $F_{\rm t}$  with  $s=s'_{\rm a}$  and  $v=s'_{\rm b}$ . The distance between the current injection tips is given by v, the distance between a current injection tip to a neighboring voltage probing tip by s. Thus, the aspect ratio of the square is  $s'_{\rm a}/s'_{\rm b}\approx 2.5$ . With  $d'_{\rm a}/s'_{\rm a}\approx 1.2$ , Fig. 2.12 indicates that the contribution of the higher order terms in  $F_{\parallel,\rm long}$  [Eq. (2.89)] can be neglected. The correction factors are then

$$F_{\perp} = 0.984 \tag{6.24}$$

$$F_{\rm t} = 0.996$$
 (6.25)

$$F_{\perp}F_{\rm t} = 0.980.$$
 (6.26)

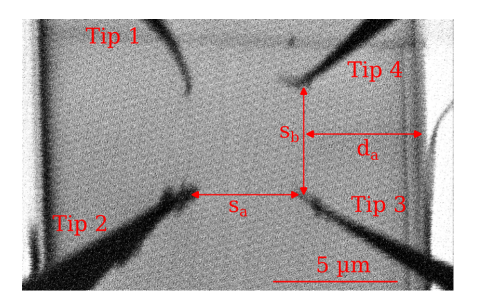


FIG. 6.10.: SEM micrograph of the square tip configuration on flake D. The dimensions of the square,  $s_{\rm a}$  and  $s_{\rm b}$ , and its distance from the flake boundary  $d_{\rm a}$  are indicated. These parameters are needed for the evaluation of the correction factors. The contrast of the SEM image was inverted for better visibility.

TAB. 6.4.: Measurement data to determine the anisotropy of the  $\alpha$ -Bi<sub>4</sub>Br<sub>4</sub>(001) surface at 77 K. The calculated anisotropy  $A = \rho_{\rm a}/\rho_{\rm b}$  calculated using Eq. (6.13) is also given.

No	$R_{ m squa}$	$_{\rm re,a} (\Omega)$	$R_{\rm square,b} (\Omega)$	A
1	806.3	$\pm 0.5$	$49 \pm 5$	5.3
<b>2</b>	829	$\pm 2$	$57.0 \pm 0.1$	5.3
3	840	$\pm 2$	$63.0 \pm 0.3$	4.6
Avg	825	± 10	$57 \pm 5$	$5.0 \pm 0.3$

These results show, that for current along the lattice vector  $\underline{a}$  the flake can be treated as an infinite 3D object. Additionally, the tips are far enough from the edge, that within the measurement error, a correction for this edge is not necessary.

Second, the correction of  $R_{\text{square,b}}$  is considered. In this case, the correction factors  $F_{\parallel}$  and  $F_{\text{t}}$  are to be computed. With  $s=s_{\text{b}}'$  and  $v=s_{\text{a}}'$ , the correction factors evaluate to

$$F_{\parallel} = 0.973 \tag{6.27}$$

$$F_{\rm t} = 0.987 \tag{6.28}$$

$$F_{\parallel}F_{\rm t} = 0.961. \tag{6.29}$$

Thus, during the measurement of  $R_{\text{square,a}}$  and  $R_{\text{square,b}}$ , flake D can be considered to be an infinitely large 3D sample, within the measurement error.

#### 6.4.3.1. Square measurements

The resistances measured in a square with  $s=5\,\mu\mathrm{m}$  are listed in Tab. 6.4. As described above, the measurements were obtained on flake D, which is large enough to behave like an infinite bulk sample at the used inter-tip distance. From the resistances, the anisotropy can be calculated using Eq. 6.13 as discussed above. At 77 K, the surface anisotropy is  $A=5.0\pm0.3$ 

#### 6.4.3.2. Linear measurements

Similar to the room temperature measurements, distance dependent measurements of the resistance of long, thin flakes were carried out. Figure 6.11(a) and (b) display the distance dependence of R on the inter-tip distance s for flakes B and C. As noted in section 6.4.1, flake A while measuring additional data at room temperature. An SEM micrograph of flake B during measurement is presented in Fig.6.11(c). Since the SEM offers a much better resolution, the uncertainty of s is much lower than it was for the RT measurements. During the analysis of the resistance data for flake C [depicted in Fig. 6.11(b)], the two

TAB. 6.5.: Disentangled resistivities of  $Bi_4Br_4$  and the anisotropy  $A_z = \rho_z/\rho_b$  at 77 K.

	$\rho_{\rm b}~({\rm m}\Omega{\rm cm})$	$\rho_{\rm a}~({\rm m}\Omega{\rm cm})$	$\rho_{\mathbf{z}} \; (\Omega  \mathrm{cm})$	$A_{ m z}$	$\bar{\rho} \; (\Omega  \mathrm{cm})$
Flake B	$19 \pm 1$	$93 \pm 7$	$51 \pm 12$	2800	0.45
Flake C	$9.7 \pm 0.8$	$48 \pm 5$	$99 \pm 24$	10300	0.36
Avg	$14.1 \pm 0.1$	$71 \pm 7$	$75 \pm 18$	6500	0.40

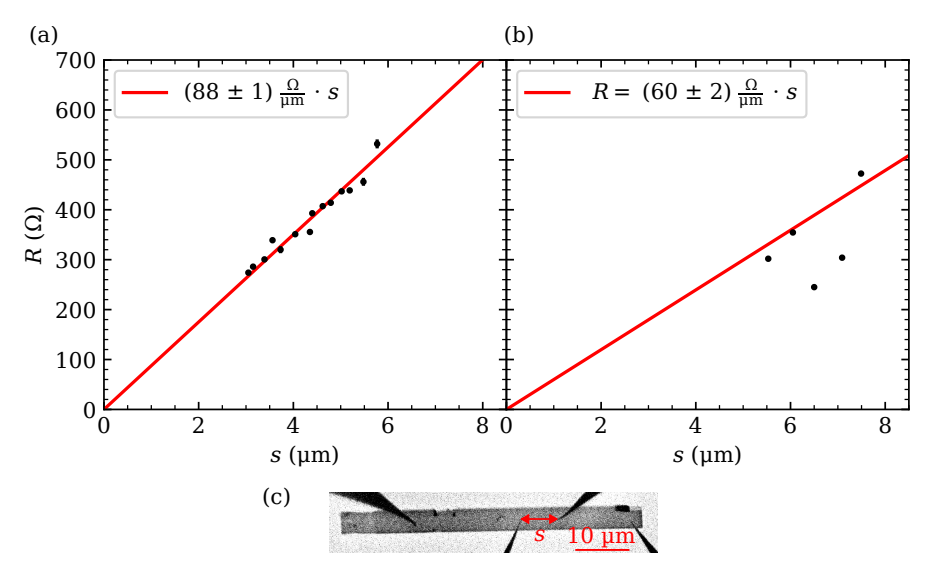


Fig. 6.11.: (a) and (b) show transport data on the long, thin  $\alpha$ -Bi<sub>4</sub>Br<sub>4</sub> flakes B, and C. The resistance is plotted as function of the distance s between the two voltage probing tips. (c) A flake during measurement. Note the superior resolution of the SEM compared to Fig. 6.9(d). The contrast of the SEM image was inverted for better visibility.

outliers were neglected. These outliers are probably the result of a bad contact with one of the voltage probing tips, leading to high noise in the four-probe measurement. Due to severe degradation of the tips, recording further data points on flake C was not possible. Removing the sample from the cryostat, however, would have lead to an accumulation of adsorbants on the flake surfaces. Experience shows that the adsorbants themselves also prohibit good ohmic contact for current injection. The resulting resistivities  $\rho_b$  are tabled in Tab. 6.5. Also at 77 K, there is a large difference on the resistivities of flakes B and C. In fact, compared to the room temperature results listed in Tab. 6.2,  $\rho_b$  of flake B doubles, while for flake C it only increases by a factor of  $\approx 1.4$ .

#### 6.4.3.3. Calculation of resistivity tensor

The diagonal elements of the resistivity tensor at 77 K are now calculated from A and  $\rho_b$  as outlined in section 6.2.3. Relative to the room temperature values,  $\rho_b$  increases by 40 % and  $\rho_z$  increases substantially (by a factor of seven) at 77 K. Correspondingly, the vertical anisotropy increases to  $A_z = 6500$ . The values calculated for flakes A and B are given in Tab. 6.5. From the averages, the resistivity tensor at 77 K is

$$\underline{\rho}_{=77 \,\mathrm{K}} = \begin{pmatrix} (71 \pm 7) \,\mathrm{m}\Omega \,\mathrm{cm} & 0 & 0 \\ 0 & (14.1 \pm 0.1) \,\mathrm{m}\Omega \,\mathrm{cm} & 0 \\ 0 & 0 & (75 \pm 18) \,\Omega \,\mathrm{cm} \end{pmatrix}.$$
(6.30)

The average resistivity is  $\bar{\rho}_{77\,\mathrm{K}} = 400\,\mathrm{m}\Omega\,\mathrm{cm}$ .

### 6.5. Discussion

As expected from the crystal structure (c.f. Fig. 4.2) the resistivity  $\rho_b$ , describing electrical current flow in  $\underline{b}$ -direction, is the smallest of the measured resistivities. In the literature, multiple measurements of the resistivity of  $\alpha$ -Bi<sub>4</sub>Br<sub>4</sub> can be found. However, not all experimental descriptions offer sufficient details to allow a proper identification of the measured components of  $\underline{\rho}$ . Nevertheless, since  $\alpha$ -Bi<sub>4</sub>Br<sub>4</sub> tends to form elongated crystals along the  $\underline{b}$ -direction, it can be assumed that  $\rho_b$  was measured in all of these studies. The values obtained for  $\rho_b$  at room temperature are  $13 \,\mathrm{m}\Omega\,\mathrm{cm}$  [94],  $60 \,\mathrm{m}\Omega\,\mathrm{cm}$  [21],  $35 \,\ldots\, 59 \,\mathrm{m}\Omega\,\mathrm{cm}$  [115]. The present value  $\rho_b = 10 \,\mathrm{m}\Omega\,\mathrm{cm}$  agrees reasonably with [94] and is considerably lower than the values reported in [21] and [115]. However, it is known that the resistivities can vary from sample to sample. For instance for two samples measured in [115] the resistivities differ by  $68 \,\%$ .

The values for  $\rho_b$  obtained on different flakes stemming from the same  $\alpha$ -Bi<sub>4</sub>Br<sub>4</sub> crystal given in Tab. 6.3 deviate up to 40 % from the average. These variation of the resistivities can be attributed to a different density of defects for the different samples. The flakes with the lowest defect density are the ones with the lowest resistivity  $\rho_b$ . A difference between the measurements presented here and the measurements in the literature is the distance over which the four-point measurements are performed. In the literature, distances in the millimeter range are used, whereas here, the distances are in the  $\mu$ m range. Larger fluctuations of the defect density on small length scales can explain the relatively large differences between the measured resistivities for different flakes (see Tab. 6.3 and 6.5).

From the literature, the resistivity at 77 K increases by a factor of  $\sim 2$  [12, 21, 94, 115], which is also supported by a measurement of the resistance [128]. Only the result in Ref. [94] is quite different, with a decrease of the resistivity from room temperature to 77 K. In the present thesis, an increase by a factor of 1.4 was observed.

All previous measurements of the resistivity of  $\alpha$ -Bi<sub>4</sub>Br<sub>4</sub> samples were limited to  $\rho_{\rm b}$ . In this work, all three components on the main diagonal were measured. By measuring the four-point resistances in a square configuration along the  $\underline{a}$ -direction and  $\underline{b}$ -direction, the resistivity  $\rho_a$  and correspondingly the lateral anisotropy  $A = \rho_{\rm a}/\rho_{\rm b} = 6.4 \pm 0.5$  at room temperature and a somewhat smaller value of  $A = 5.0 \pm 0.3$  at 77 K were obtained.

For the conductivity<sup>2</sup>  $\sigma$ , it holds in general [121, p. 406]

$$\sigma = en\mu_{\rm n} + ep\mu_{\rm n},\tag{6.31}$$

where e is the elementary charge and n and p are the electron and hole densities, respectively. The mobilities  $\mu_n$  and  $\mu_p$  are denoted by [121, p. 406]

$$\mu_v = \frac{e\tau_{\rm n}}{m_{\rm n}^*}$$
 and  $\mu_{\rm p} = \frac{e\tau_{\rm p}}{m_{\rm p}^*}$ , (6.32)

with the mean relaxation time  $\tau$ , describing the scattering of charge carriers, and the effective mass  $m^*$ . Since in  $\alpha$ -Bi<sub>4</sub>Br<sub>4</sub> the Fermi level is close to the conduction band [20, 108, 115], the contribution of the holes to the conductivity can be neglected. The electron density is a scalar, thus the measured anisotropies A and  $A_z$  stem from the electron mobility  $\mu_n$  [59]. Both, the relaxation time  $\tau$  and the effective mass  $m^*$  can contribute to

<sup>&</sup>lt;sup>2</sup>To follow the convention of the literature, the conductivity is used here. For an diagonal resistivity tensor,  $\sigma_i = 1/\rho_i$ . Thus  $A = \rho_a/\rho_b = \sigma_b/\sigma_a$ .

the anisotropy of  $\mu$ , compare also Ref. [124] for an example in a different material of the same space group. In the case of  $\alpha$ -Bi<sub>4</sub>Br<sub>4</sub>, no measurements of  $\tau$  exist in the literature. However, the different scatter mechanisms in a semiconductor are temperature dependent [121, pp. 408-413]. Cooling the sample to 77 K changed the measured anisotropies of the conductivity (or resistivity). This observation indicates that the measured anisotropies may be partly due to corresponding anisotropies of the relaxation time  $\tau$ .

The anisotropy of the effective mass  $m^*$  can be extracted from DFT calculations. However, as the fundamental band gap is located at the boundary of the Brillouin zone, the necessary k-paths are not included in the calculations in the literature [22, 99, 103, 111, 115]. Therefore, a phenomenological explanation of anisotropy using the crystal structure of  $\alpha$ -Bi<sub>4</sub>Br<sub>4</sub> (c.f. Fig. 4.2) is given. The in-plane anisotropy A of the resistivity can be explained by a larger overlap of the wave functions, due to the covalent bonds, in b-direction along the atomic rows than in a-direction, where weaker van-der-Waals forces connect different rows. Since there are no measurements of the lateral anisotropy of  $\alpha$ -Bi<sub>4</sub>Br<sub>4</sub> available in the literature, the results are compared to other anisotropic 2D materials. For thin flakes of black phosphorus, an in-plane anisotropy of 1.5 was measured using two-probe measurements with lithographic contacts placed in a circle 30° apart [129]. For the transition metal dichalcogenides 1T'-MoS<sub>2</sub> and 1T'-WTe<sub>2</sub> a dependence of the two-point resistance on the direction of current flow with respect to crystallographic axes was observed using similar setup of electrodes [130, 131]. For 1T'-MoS<sub>2</sub>, the ratio between highest and lowest resistance is 1.8, which indicates a low anisotropy [130] The in-plane anisotropy is lower in both of these materials as both materials consist of layers that are internally bonded with covalent bonds. On the other hand, in 1T'-WTe<sub>2</sub> a surprisingly large ratio of the two-point resistances of  $\sim 10^3$  was observed [131]. This result indicates a strong in-plane anisotropy of 1T'-WTe<sub>2</sub>, even though the intra-layer bonds of this material are covalent bonds. In principle, transport through the topological hinge states, present at step edges on the (001) surface [20, 21, 108], could contribute to the anisotropy A observed here. However, transport in  $\alpha$ -Bi<sub>4</sub>Br<sub>4</sub> is bulk dominated until below 20 K [108, 115]. Consequently, the anisotropy A observed here is due to the bulk transport properties of  $\alpha$ -Bi<sub>4</sub>Br<sub>4</sub>.

Finally, the resistivity along the vertical direction  $\rho_z$  was also disentangled. This resistivity is much larger than the in-plane resistivities, with a room temperature value of  $\rho_z = 11 \Omega$  cm, corresponding to an lateral anisotropy of  $A_z = \rho_z/\rho_b = 1300$  at room temperature. The low temperature value is even much larger with a value of  $\rho_z = 75 \,\Omega$  cm, corresponding to  $A_z = 6500$ . As before, there are no measurements of  $\rho_z$  or  $A_z$  available from the literature. Thus, a comparison to other layered van-der-Waals materials, where anisotropies were measured between the base-plane and the c-axis, is drawn. For Bi<sub>2</sub>Te<sub>3</sub>, an anisotropy of  $\sim 4$  was obtained [132], while for  $\mathrm{Sb_2Te_3}$ , anisotropies of 1.9 [133] and 2.3 [134] were measured. In the case of these two topological insulators, the anisotropy is obviously much smaller than the  $A_z = 1300$ , observed in  $\alpha$ -Bi<sub>4</sub>Br<sub>4</sub>. In graphite, on the other hand, there is a pronounced anisotropy between  $\rho_a$ , measured in the basal plane and  $\rho_{\rm c}$  [135–139]. At room temperature,  $\rho_{\rm a}/\rho_{\rm c}=300\ldots 600$  has been measured for natural single crystal graphite [136]. The difference between the in-plane anisotropy A and the out-of-plane anisotropy  $A_z$  is remarkably large. While the difference can be attributed to the larger van-der-Waals gap in  $\underline{z}$ -direction than in  $\underline{a}$ -direction and to the fact that the cross-section of two adjacent chains is larger in a-direction than in z-direction (c.f. section 4.2 on page 49), a more thorough understanding is needed. While only a study of scattering of charge carriers in  $\alpha$ -Bi<sub>4</sub>Br<sub>4</sub> will shed some light on the influence of the scattering time  $\tau$ , DFT calculations can, even without supplying the anisotropy of the effective mass, offer an explanation. As already noted in section 4.3 on page 51,  $\alpha$ -Bi<sub>4</sub>Br<sub>4</sub> exhibits a weak inter-layer coupling [99, 100]. The weak inter-layer coupling arises from the fact that the lowest energy bands close the the fundamental band gap consist of Bi- $p_x$  orbitals, that are oriented in the ab plane [23, 99]. In addition, at the fundamental band gap, due to the band inversion, the lowest conduction band predominately consists of Bi<sub>in</sub>- $p_x$  orbitals, which belong to the two inner atoms of the Bi<sub>4</sub>Br<sub>4</sub> chains [23, 99, 100]. See also Fig. 5.7(a) and (b) on page 64.

#### 6.6. Résumé

A method to disentangle the three components on the main diagonal of the resistivity tensor describing an anisotropic crystal was presented. The method involves two measurements on a bulk sample in a square tip configuration and one distance-dependent measurement on a long, thin flake in a linear configuration. The alignment of the square with the two primary crystallographic axes spanning the investigated surface was known from typical surface properties of the quasi one-dimensional crystal structure. In principle, the method presented here can be extended for samples where this alignment is unknown, e.g. by rotating the square tip configuration around its center [42, 140]. The ability to evaluate data without relying on correction factors is the main advantage of the linear distance dependent measurement used here.

This method was then applied to disentangle three principal resistivities of the HOTI  $\alpha$ -Bi<sub>4</sub>Br<sub>4</sub>, under the assumption that the off-diagonal element of the resistivity tensor only has a negligible impact on the resistances. Measurements were obtained at room temperature and at 77 K using a four-tip STM. On the commonly used  $\alpha$ -Bi<sub>4</sub>Br<sub>4</sub>(0 0 1) surface, the resistivity at room temperature along the chain direction ( $\rho_{\rm b}$ ) is 6.4 times smaller than the resistivity perpendicular to the chain direction ( $\rho_{\rm a}$ ), i.e.  $A = \rho_{\rm a}/\rho_{\rm b} = 6.4 \pm 0.5$ . At 77 K, this anisotropy decreases to  $A = \rho_{\rm a}/\rho_{\rm b} = 5.0 \pm 0.3$ . This decrease of A may indicate, that the anisotropy is not only governed by the effective mass  $m^*$ , but also by an anistorpy scattering time scale  $\tau$ . On the other hand, the resistivity  $\rho_{\rm z}$  (normal to the (0 0 1) surface) is  $\sim$  1300 times larger than  $\rho_{\rm b}$  at room temperature, i.e.  $A_{\rm z} = \rho_{\rm z}/\rho_{\rm b} = 1300$ . At 77 K, this anisotropy increases to  $A_{\rm z} \approx 6500$ . The notably larger anisotropy  $A_{\rm z}$  can be attributed to the weak inter-layer coupling of  $\alpha$ -Bi<sub>4</sub>Br<sub>4</sub> [99], which is also evident in the larger van-der-Waals gap in z-direction.

Results and analysis presented here are to be published in <u>Jonathan K. Hofmann</u>\*, Serhii Kovalchuk\*, et al., Disentangling three anisotropic resistivities of the topological insulator  $\alpha$ -Bi<sub>4</sub>Br<sub>4</sub>, in preparation.

<sup>\*</sup> These authors contributed equally.

# 7. Measuring the anisotropy of an $\alpha$ -Bi<sub>4</sub>Br<sub>4</sub> flake by the Bierwagen-Simon method

In the previous chapter, the surface anisotropy A of  $\alpha$ -Bi<sub>4</sub>Br<sub>4</sub> was determined from measurements on the bulk crystal. A subsequent measurement of  $\rho_{\rm b}$  using a flake then allowed for all three components on the main diagonal of  $\underline{\rho}$  to be disentangled. However, as shown in section 2.4 on page 14, there are multiple different measurements that, in principle, lead to the same result. In the present chapter, the anisotropy A and the two in-plane components  $\rho_{\rm a}$  and  $\rho_{\rm b}$  are measured on thin flakes. For  $\rho_{\rm z}$ , the results for  $R_{\rm square,a}$  measured on the bulk sample is reused.

## 7.1. Disentagling the three components of an orthorombic resistivity tensor

To measure the anisotropy  $A = \rho_{\rm a}/\rho_{\rm b}$ , a number of different approaches can be used:

- For rectangular flakes, the Bierwagen-Simon or the Montgomery method can be used.
- Otherwise, the tips can be placed in a square on the 2D sample and Eq. (2.58) can be applied, see e.g. Refs. [32, 140].

While a measurement of the anisotropy A according to the Bierwagen-Simon method is not exclusive to the 2D case, on a 2D sample, the same tip configuration can be used to measure the average sheet resistivity  $R_{\rm S,avg}$  using the van-der-Pauw method. Therefore, a thin sample is still required. To apply the Bierwagen-Simon method, the flake has to be rectangular and the main resistivity directions need to be aligned with the flake edges. This is the case for  $\alpha$ -Bi<sub>4</sub>Br<sub>4</sub> [108], but not necessarily for other materials.

If the flake is not of rectangular shape, the tips can be placed on its surface in a square geometry, and the anisotropy can be obtained from Eq. (2.58). The square formed by the tips still needs to be aligned with the main resistivity directions. If those are unknown, the square can be rotated around its center axis. This allows to extract both the anisotropy A and the angle of the main resistivity direction with respect to an arbitrary point of reference on the surface. If atomic resolution can be measured on the flake surface, using the four-tip STM, in principle this angle can also be referenced a lattice direction [32, 140].

This method, however, has an additional requirement: The tips must be positioned sufficiently distant from the sample edges to avoid the necessity for the application of

TAB. 7.1.: Measurement data of three measurements used to determine the anisotropy of a  $\alpha$ -Bi<sub>4</sub>Br<sub>4</sub> flake using the Bierwagen-Simon method at room temperature. The anisotropy  $A = \rho_{\rm a}/\rho_{\rm b}$  obtained using Eq. (2.67) is also given.

No	$R_{\rm a}~(\Omega)$	$R_{ m b} \; (\Omega)$	A	$R_{ ext{S,avg}}\left(rac{\Omega}{\Box} ight)$	$\rho_{\rm avg}~({\rm m}\Omega{\rm cm})$
1	$177.4 \pm 0.9$	$191.7 \pm 0.1$	3.0	834	$55 \pm 7$
2	$180.0 \pm 0.7$	$196 \pm 2$	3.0	847	$56 \pm 7$
3	$163.9 \pm 0.5$	$226.0 \pm 0.1$	2.8	876	$58 \pm 7$
Avg	174 $\pm 5$	$204 \pm 11$	$2.9\pm0.1$	$852 \pm 13$	$56 \pm 7$

correction factors (see below). While there is a large body of literature on correction factors for different measurement geometries and sample shapes as elaborated in section 2.6 (see also e.g. [28, 32, 37, 45]), the special case of an irregularly shaped flake is not found in the literature: Correction factors are calculated only for highly symmetrical sample shapes. Furthermore, most correction factors are calculated only for the isotropic case. While correction factors can be easily applied to anisotropic samples using the Wasscher transformation, this procedure requires knowledge of the value of the anisotropy A. Therefore, some sort of self consistent solution would need to be implemented. Instead of correction factors, also finite-element modeling (FEM) could be applied to the problem. However, a fitting procedure of some sort would still be necessary.

Once the two lateral components of the resistivity ( $\rho_a$  and  $\rho_b$ ) are known, the third component ( $\rho_z$ ) can be measured. For this measurement, there are different methods, as well:

- 1.  $\rho_z$  can be measured on a bulk sample, showing the same crystallographic surface as the flake sample, using e.g. a linear, equidistant tip configuration and Eq. 2.50.
- 2. A thin flake sample showing a different crystallographic surface (e.g. the surfaces is spanned by x and z) is prepared. Then the procedure described above is applied.

#### 7.2. Results

From measurements of the resistance on flake E, the anisotropy can be found using the Bierwagen-Simon method. Figure 7.1 depicts flake E. The optical micrograph [Fig. 7.1(a)] shows the sample during measurement, in Fig. 7.1(b) an SEM micrograph is depicted. Similar to flake A, also flake E was damaged by a transitory high current during contacting. This accident prevented further measurements. The damage is also visible in the optical microscope (compare appendix G on page 129). Figure 7.1(a) depicts the flake prior to sustaining the damage.

From the SEM micrograph the flake size  $w_{\rm a}=57\,\mu{\rm m}$  and  $l_{\rm b}=32.5\,\mu{\rm m}$  is determined. Using these values, the anisotropy is calculated using Eq. (2.67). Figure 7.1(a) depicts the flake before it was damaged.

$$A = \frac{\rho_{\rm a}}{\rho_{\rm b}} = 2.9 \pm 0.1. \tag{7.1}$$

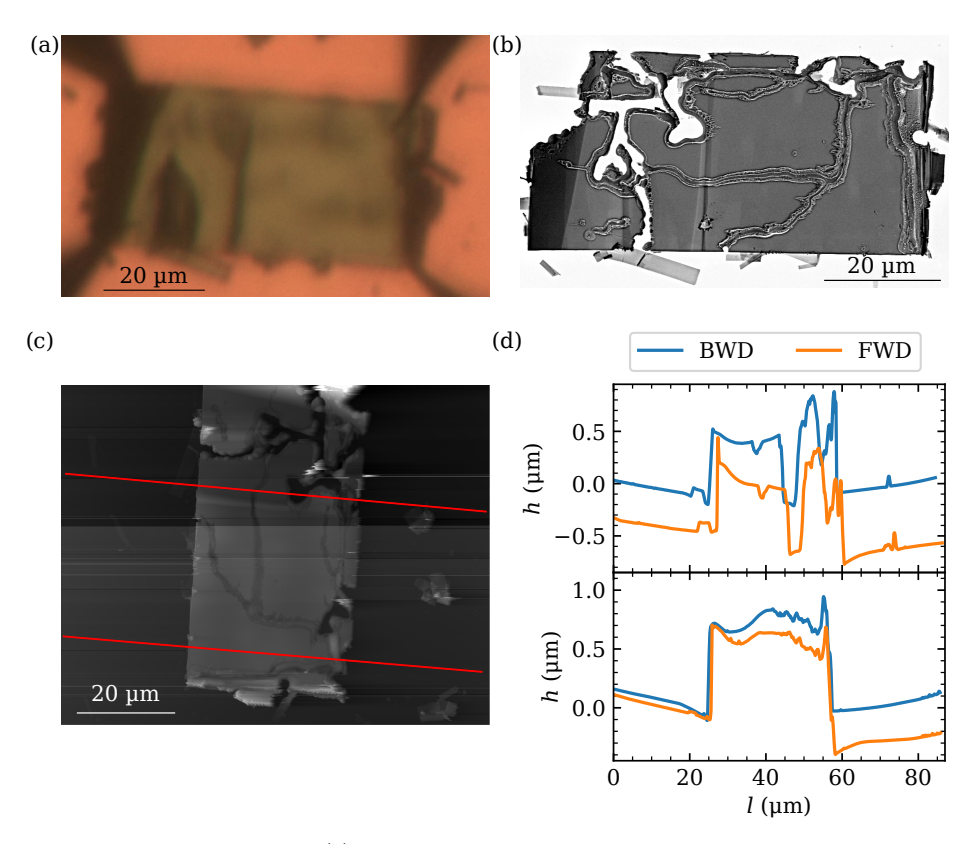


FIG. 7.1.:  $\alpha$ -Bi<sub>4</sub>Br<sub>4</sub> flake E. (a) Bierwagen measurement on flake E with four tips placed in the corners. (b) SEM micrograph after the completion of the measurements. The flake shows damage from a high current event during contacting. (c) AFM topography under ambient conditions. The same damage as in (b) is visible. (d) Height profiles along the two red lines in (c). The average flake thickness was evaluated using the forward and backward scan directions. The upper panel corresponds to the upper profile indicated in (c).

This result for the room temperature anisotropy obviously does not agree with the result obtained on the bulk sample in the previous chapter.

According to the Bierwagen-Simon method [59, 64] as introduced in section 2.5.1 on page 17, as a next step the average sheet resistivity  $R_{\rm S,avg}$  is determined. To this end, the resistances given in Tab. 7.1 are plugged into the van-der-Pauw equation [Eq. (2.64)], which is then solved numerically. The resulting sheet resistances are also given in Tab. 7.1. With<sup>1</sup>

$$R_{\rm S,avg} \cdot t = \sqrt{\rho_{\rm a}\rho_{\rm b}} = \rho_{\rm avg}$$
 (7.2)

[c.f. Eq. (2.61)], where t is the flake thickness, the geometric mean of the two in-plane components of  $\underline{\rho}$  is found.

<sup>&</sup>lt;sup>1</sup>Bierwagen *et al.* use the symbol  $\rho_{\text{avg}}$  for the average sheet resistivity, given in in units of  $\Omega$ . They also use  $\rho_x$  and  $\rho_y$  for the components of the 2D resistivity tensor [59].

The thickness of flake E was measured using an AFM in tapping mode under ambient conditions. There appears to be a boundary on the flake, that manifests itself differently in Fig. 7.1(a), (b), (c), due to different contrasts mechanisms. Consequently, two different height profiles of the AFM topography were taken. Their locations are indicated by the red lines in Fig. 7.1(c). The height profiles are plotted in Fig. 7.1(c). Averaging the two profiles per scan direction, flake thickness  $t=(0.66\pm0.08)\,\mu\mathrm{m}$  was obtained.

From Eq. (7.2) and (7.1), the two components of the anisotropy tensor can be calculated:

$$\rho_{\rm a} = \sqrt{A}\rho_{\rm avg} \quad \text{and} \quad \rho_{\rm b} = \frac{\rho_{\rm avg}}{\sqrt{A}}.$$
(7.3)

Using Eq. (7.2), the average of the two in-plane resistivities  $\rho_{\rm avg}$  can the be calculated. The results for the three measurements are given in Tab. 7.1. The average of the measurements is  $\rho_{\rm avg} = (56 \pm 7) \, \rm m\Omega \, cm$ . Thus, using Eq. (7.3), the two in-surface components  $\rho_{\rm a} = (96 \pm 12) \, \rm m\Omega \, cm$  and  $\rho_{\rm b} = (33 \pm 4) \, \rm m\Omega \, cm$ . As already noted above, this result deviates from results obtained on the bulk sample in the previous chapter.

To demonstrate a complete disentanglement of the main diagonal of the resistivity tensor  $\underline{\rho}$ , results measured on the bulk crystal of the previous chapter are used. There,  $R_{\rm square,a}=(158\pm13)\,\Omega$  was measured in a square tip configuration with  $s=10\,\mu{\rm m}$ . Plugging the bulk results into Eq. (6.18) yields  $\rho_{\rm z}=(10\pm3)\,\Omega$  cm. Thus, the completed resistivity tensor reads

$$\rho_{\text{RT}} = \begin{pmatrix}
(96 \pm 12) \,\text{m}\Omega \,\text{cm} & 0 & 0 \\
0 & (33 \pm 4) \,\text{m}\Omega \,\text{cm} & 0 \\
0 & 0 & (10 \pm 3) \,\Omega \,\text{cm}
\end{pmatrix}.$$
(7.4)

The mean resistivity is  $\bar{\rho} = 320 \,\mathrm{m}\Omega\,\mathrm{cm}$ .

#### 7.3. Discussion

Regarding the discrepancy between the bulk data presented in the previous chapter and the flake measurements a number of possible reasons will be discussed in the following section. As already noted in the previous chapter, transport in  $\alpha$ -Bi<sub>4</sub>Br<sub>4</sub> is bulk dominated until below 20 K [108, 115]. Thus, the topological hinge states are not the source of the anisotropy observed here.

### 7.3.1. Effect of moving the tips out of the corners

First, the effect of tip positioning is addressed: While the effect of shifting the contacts off the circumference of the sample for resistivity measurements using the van-der-Pauw method is discussed extensively in the literature, e.g. [52, 141], the corresponding effect on the Bierwagen-Simon method has not been investigated in detail.

To examine the influence of the tip positioning on the resulting anisotropy finite-element modeling (FEM) was used. The FEM simulations were performed by *Helmut Soltner*. The results of these FEM calculations are presented in Fig. 7.2. A rectangular flake of dimensions  $w_a = 32.5 \,\mu\text{m}$ ,  $l_b = 55 \,\mu\text{m}$ , and  $t_z = 0.6 \,\mu\text{m}$  (dimensions of flake E) with the three resistivities determined in the previous chapter was simulated. Three different

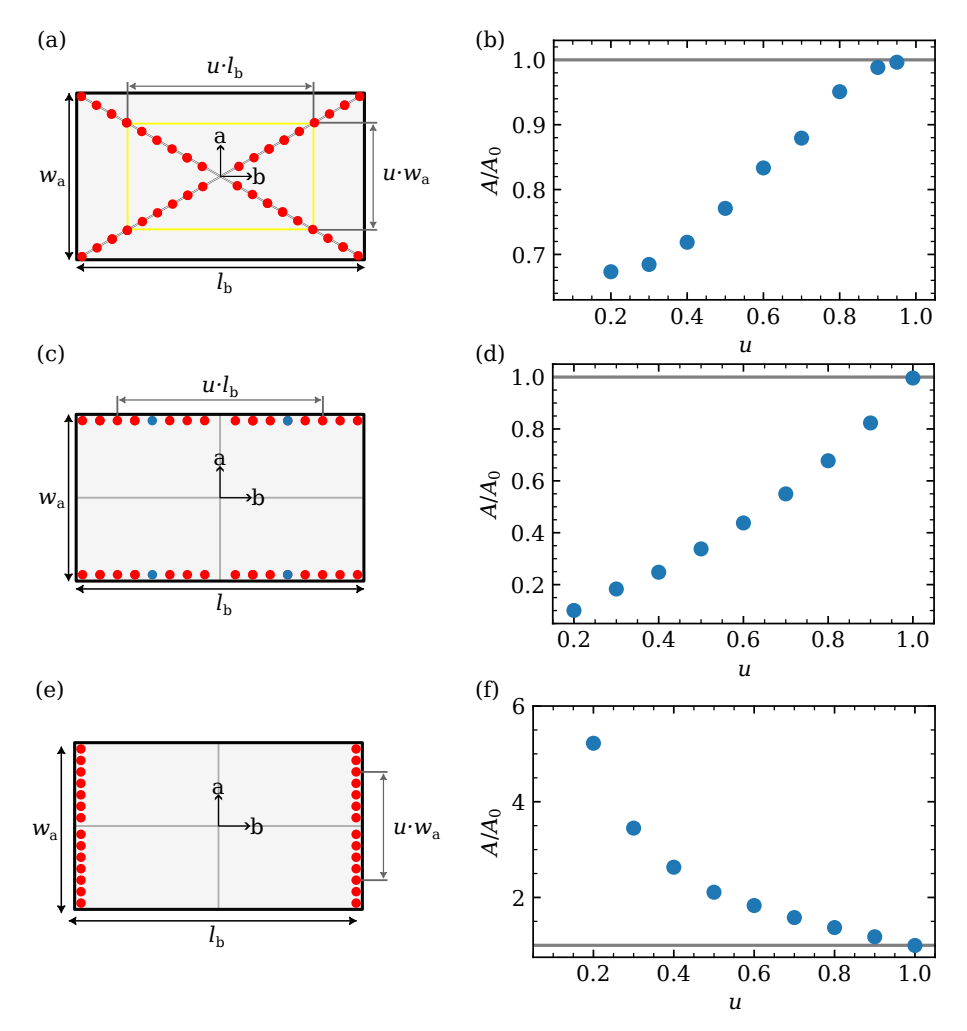


FIG. 7.2.: Results of FEM calculation by  $Helmut\ Soltner$  to investigate the dependence of the measured anisotropy A on the tip placement. (a) The tip placements for the diagonal tip movement. (b) The normalized anisotropy  $A/A_0$  for the diagonal tip movement. The measured anisotropy decreases, when the tips are placed closes to the flake center. (c) Tip placements for tip movement along the long edge. The blue point indicates the tip positions needed to explain the deviations between the measurement on the flake and the measurement on the bulk. (d) Normalized anisotropy  $A/A_0$  for tip movement along the long edge. Also this movement leads to a decrease of the anisotropy when the tips are moved closer to the flake center. (e) Tip placements for tip movement along the short edge of the flake. (f) Normalized anisotropy  $A/A_0$  for tip movement along the short edge. In this case, the measured anisotropy is increased by placing the tips closed to the flake center.

cases were examined: movement of the tips along the diagonals to the center of the flake [Fig. 7.2(a)], movement of the tips along the short edge [Fig. 7.2(c)] and movement along the long edge [Fig. 7.2(e)]. In all cases, the tip movement was performed symmetrically, i.e. the tips were placed in a rectangle centered on the flake center. For the diagonal movement, the aspect ratio of the rectangle formed by the tips did not change, while, naturally, movement along the two edges increases or decreases the aspect ratio.

The resistances calculated using the FEM method were then evaluated using the Bierwagen-Simon method, c.f. section 2.5.1. The anisotropies normalized to the input anisotropy of  $A_0 = 6.4$  are plotted in Fig. 7.2(b) for the diagonal movement, in Fig. 7.2(d) for the movement along the long edge, and in Fig. 7.2(f) for movement along the short edge as a function of the simulation parameter u. The parameter u describes how far the tips are moved away from the corner, with the tips being placed in the corners at u=1and close to the center axes, when u approaches zero. As a first result, at u=1, the value  $A_0$  is found, providing a verification that the analysis methods and the FEM simulations are working correctly. As expected, moving the tips out of the corners has a significant impact on the measured anisotropy. The plot in Fig. 7.2(d) shows that  $u \approx 0.5$  would explain the observed discrepancy of bulk and flake data. The corresponding tip positions are indicated in blue in the drawing in Fig. 7.2(c). The tip displacement necessary to explain the observed deviations should be visible during the measurement. However, while the tips are obviously not in the corners of flake E in Fig. 7.1, the displacements are not consistent with the results of the FEM calculations. Thus, the tip displacement from the corners during the measurement cannot explain the measured lower anisotropy.

For the diagonal tip movement, the normalized anisotropy appears to reach saturation for low values of u. At the same time, at  $u \approx 1$ , the decrease is much slower than for the tip movement along the flake edges. This might be explained by the fact, that for the diagonal tip movement, the aspect ratio of the rectangle does not change. The two cases of tip movement along the flake edges are more similar than they appear at first glance. As a first approximation, the normalized anisotropy of the tip movement along the short edge [Fig. 7.2(d)] can be understood as the inverse of the tip movement along the long edge [Fig. 7.2(f)]

#### 7.3.2. Influence of flake defects of flake E

The AFM topography of flake E presented in Fig. 7.1 indicates that the thickness of flake E is not uniform. In order to analyze the influence of the thickness on the aniostropy obtained by the Bierwagen-Simon method, another FEM simulation was performed by  $Helmut\ Soltner$ : Based on the AFM topography, flake E was approximated as two connected cuboids with different thicknesses. The thinner section makes up  $\sim 1/3$  of the flake length. For the other parameters and dimensions, the values of the previous simulations were retained. Figure 7.3(a) displays a side view of the modeled flake. Form the simulated potential in the two configurations the anisotropy

$$A_{\text{step}} = 1.7 \tag{7.5}$$

was obtained.

This result indicates that, unsurprisingly, in addition to the tip placement the quality of the flake itself can have a pronounced influence on the measured result. The anisotropy

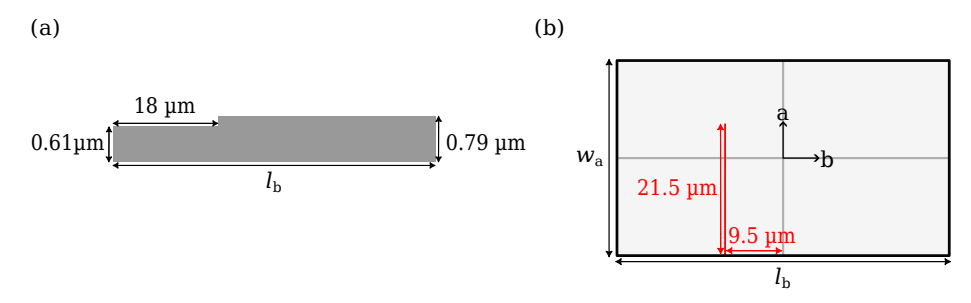


FIG. 7.3.: FEM calculations by Helmut Soltner to analyze the effect of two different imperfections of the flake on the measured anisotropy. In both cases, a flake with the parameters  $w_{\rm a}=32.5\,\mu{\rm m},\ l_{\rm b}=55\,\mu{\rm m},\ {\rm and}\ t_{\rm z}=0.6\,\mu{\rm m}$  was used. (a) The AFM image [Fig. 7.1(c)] indicates that the flake exhibits a large surface step. As a simple model, a flake with two different thicknesses was simulated. (b) The optical microscope micrograph [Fig. 7.1(a)] indicates that there might be a line shaped defect in the flake separating it into two parts. To simulate this kind of defect, a thin stripe of insulating material (red line) was inserted into the flake.

obtained from this simulation is much lower than the measured value of  $A = 2.9 \pm 0.1$ . This discrepancy may be due to the simplified model of flake E used in the simulation. Furthermore, this simulation does not take into account any effects of tip placement.

A further FEM simulation was performed to analyze the influence of a long defect extending in  $\underline{a}$  direction. The defect was simulated by a layer of air in the flake, producing a 0.1  $\mu$ m wide defect extending over the complete thickness of the flake. This is displayed in Fig. 7.3(b). The anisotropy obtained from this simulation is

$$A_{\text{line defect}} = 0.37. \tag{7.6}$$

An anisotropy of A < 1 indicates, that the resistivity  $\rho_b$  appears to be larger than  $\rho_a$   $(A_0 = \rho_a/\rho_b = 6.4$  was used as an input parameter in all calculations). This is primarily an effect of the measurement of  $R_a$ . Due to the placement of the voltage probing tips, they are almost cut off from the potential landscape on the other side of the defect. Consequently, the measured resistance is extremely small. Obviously, the effect of such a linear defect strongly depends on its size and its actual resistivity. In the FEM simulation presented here, the effect of the defect is rather pronounced, as the defect is rather long and approximated as non conductive material.

Based on the available data of the actual flake and its complexity presented in Fig. 7.1, it is not possible to accurately simulate the measurement. However, the simulations indicate that the differences in thickness across the flake and possible defects can explain the lower anisotropy, that was observed here. During the measurement in the four-tip STM, it is very difficult to obtain accurate measurements of the flake thickness using a tip of the four-tip STM, as the flake is substantially larger than the maximum nominal scan size of  $\sim 3\,\mu\text{m}$  and the large thickness requires a good linearity of the z-scanner piezos over almost their entire range. The non-linearities of the x- and y-scanner piezos can be calibrated using a method developed by Leis et al. [142].

## 7.4. Résumé

In this chapter, an alternative approach to measure the elements on the main diagonal of the resistivity tensor  $\underline{\rho}$  was introduced. This method was applied to the resistivity tensor of  $\alpha$ -Bi<sub>4</sub>Br<sub>4</sub> using the sample simplification already introduced in the precious chapter. In contrast to the method presented in the previous chapter, the surface anisotropy  $A = \rho_{\rm a}/\rho_{\rm b}$  was measured on  $\alpha$ -Bi<sub>4</sub>Br<sub>4</sub> flakes using the Bierwagen-Simon method. While it is possible to demonstrate the disentanglement of the three elements of  $\underline{\rho}$ , the anisotropy obtained here diverges significantly form the anisotropy obtained on the bulk sample. Thus, the resistivity tensor presented in this chapter is different from the one found before.

Based on FEM simulations of the Bierwagen-Simon measurements, the tip-placement error could be excluded as the sole source of the deviation. However, when measuring on smaller flakes, it could become a more significant source of error. The FEM simulations indicate that the cause of the deviation are imperfections of the flake used for the measurements.

## 8. Conclusion and outlook

In the present thesis, two different properties arising from the quasi one-dimensional crystal structure of the higher-order topological insulator (HOTI)  $\alpha$ -Bi<sub>4</sub>Br<sub>4</sub> were studied: its topological properties under shear strain and its electrical anisotropy.  $\alpha$ -Bi<sub>4</sub>Br<sub>4</sub> possesses two van-der-Waals gaps: One separating the layers stacked in the crystallographic  $\underline{c}$ -direction, and the other separating the individual chains within the layers. The chains extend into the b-direction and are bonded together by covalent bonds.

In chapter 5, one consequence of this quasi one-dimensional crystal structure is studied: As the van-der-Waals bonds joining the adjacent chains are comparatively weak, the crystal can easily be deformed by external shear stress. Using STM measurements on the  $\alpha$ -Bi<sub>4</sub>Br<sub>4</sub>(001) surface, a new monolayer structure of  $\alpha$ -Bi<sub>4</sub>Br<sub>4</sub> was observed. In this structure, there is a mutual shift of the quasi one-dimensional chains of b/3, instead of b/2as observed for the known surface structure of  $\alpha$ -Bi<sub>4</sub>Br<sub>4</sub>. This b/3 structure is attributed to shear strain, as the experimental data and DFT calculations allowed to exclude a surface reconstruction. At step edges on the surface, states with a non-vanishing density of states inside the band gap were observed by STS. Since the b/2 structure is a quantum spin Hall (QSH) insulator, these metallic states are attributed to the QSH edge states. A band inversion makes  $\alpha$ -Bi<sub>4</sub>Br<sub>4</sub> a QSH insulator [23, 99, 100]. This band inversion depends on the van-der-Waals interaction between neighboring chains. Therefore, DFT calculations were performed by Minggian Zheng and Jin-Jian Zhou [31] to study the dependence of the band inversion on the lattice parameters of the b/3 structure. These DFT calculations corroborate the earlier conclusion that a monolayer of the b/3 structure is also a QSH insulator, as the topological invariant  $\mathbb{Z}_2 = 1$  is obtained. This behavior is radically different from conventional 2D van-der-Waals materials where a change in the stacking (which is similar to an in-plane change in  $\alpha$ -Bi<sub>4</sub>Br<sub>4</sub>) can drastically alter the electronic properties [120, 122].

A second property arising from its crystal structure is the electrical anisotropy of the resistivity of  $\alpha$ -Bi<sub>4</sub>Br<sub>4</sub>. The resistivity of  $\alpha$ -Bi<sub>4</sub>Br<sub>4</sub> is addressed in chapters 6 and 7. In chapter 6, a method is developed to disentangle the three components on the main diagonal of the resistivity tensor. This method involves three measurements: Two on a bulk sample in a square tip configuration and one distance-dependent measurement on a long, thin flake in a linear configuration. It is long known that mechanical exfoliation of  $\alpha$ -Bi<sub>4</sub>Br<sub>4</sub> tends to produce flakes, that are elongated in <u>b</u>-direction, e.g. [108]. Surface properties of the  $\alpha$ -Bi<sub>4</sub>Br<sub>4</sub>, that are closely related to the quasi-one dimensional crystal structure were used to align the square during the measurements. In principle, this method could be extended by measuring the square resistances as a function of the rotation angle. This would allow to apply the method to crystals where the orientation of the lattice vectors on the surface is harder to ascertain. Furthermore, the measurements do not necessarily rely on correction factors. For the measurements at low temperature, however, correction factors had to be applied due to experimental difficulties with the bulk sample.

The method outlined above was subsequently applied to  $\alpha$ -Bi<sub>4</sub>Br<sub>4</sub> under the assumption that the off-diagonal elements of the resistivity tensor  $\underline{\rho}$  could be neglected. At room temperature, the resistivity along the chains (in  $\underline{b}$ -direction) is  $6.4 \pm 0.5$  times smaller than the resistivity perpendicular to the chains. Since only the  $\alpha$ -Bi<sub>4</sub>Br<sub>4</sub>(0 0 1) surface was used for the measurements, the result obtained for  $\rho_z$  is subject to a considerable measurement uncertainty. Nevertheless, the results show that  $\rho_z$  is  $\sim 1300$  times larger than  $\rho_b$ . This high out-of plane anisotropy can be attributed to the weak inter-layer coupling, i.e. the larger van-der-Waals gap between the layers. At 77 K, the in-plane anisotropy reduces to  $A = 5.0 \pm 0.3$ . The out of plane anisotropy increases to  $\sim 6500$ . The notably larger anistorpy  $A_z$  can be attributed to the weak inter-layer coupling of  $\alpha$ -Bi<sub>4</sub>Br<sub>4</sub> [99], which is also evident in the larger van-der-Waals gap in  $\underline{z}$ -direction.

An alternative method to measure the in-plane anisotropy of  $\alpha$ -Bi<sub>4</sub>Br<sub>4</sub> on the (001) surface is described in chapter 7. This second method relies on the Bierwagen-Simon method to measure the anisotropy of a flake and the van-der-Pauw method to find its sheet resistivity. Using data from the bulk sample discussed in chapter 6, it was possible to disentangle the three components on the main diagonal. However, the surface anisotropy A obtained here is considerably different from the results obtained on the bulk sample. Based on FEM simulations of the Bierwagen-Simon measurements, the tip-placement error could be excluded as the sole source of the deviation. However, it could become a more significant source of error when measuring smaller flakes. The FEM simulations of the internal defects indicate that the cause of the deviation are imperfections in the flake used for the measurements.

As a next step, measurements of the ballistic transport through a hinge or edge state are planned. Such measurements were previously attempted by Leis et al. [143]. The hallmark property of ballistic transport, the quantized conductance, could, however, not be observed [143]. Such measurements are performed on a thin, finite 2D sample, where the hinge/edge states form the boundary. In such a measurement, the edge or hinge state is not contacted directly. Instead, the current is injected into the 2D sample. A part of this current then flows through the 2D material into the edge state. This is referred to as distributed injection [143, 144]. The problem of distributed injection is treated in Ref. [144] for a ballistic channel adjacent to a conductive half-plane. To account for the anisotropy of  $\alpha$ -Bi<sub>4</sub>Br<sub>4</sub>, the Wasscher transformation can then be used to extend the treatment of an isotropic 2D half-plane to an anisotropic 2D half-plane. The presence of a ballistic edge channel (compared to an Ohmic edge channel) strongly influences the interface potential between the edge channel and the conductive half-plane. The potential on the conductive half-plane can be calculated from the interface potential using analytic continuation [144]. Thus, the effect of a ballistic edge channel can be pinpointed by comparing the calculated potential to the data collected on a sample using either scanning tunneling potentiometry [81, 83] or four-probe resistance measurements with a mobile tip voltage-probing tip as in Ref. [143].

## **Bibliography**

- <sup>1</sup>Paolo Gargini, SIEEE International Roadmap for Devices and Systems Semconductor crises and roadmap rescues, (2023) https://irds.ieee.org/images/files/pdf/2023/2023IRDS Perspectives.pdf, pre-published.
- <sup>2</sup>Anshul A. Vyas, Arvind Kumar, Bich-Yen Nguyen, Boshen Liang, Charles Kin P. Cheung, Cheng-tzung Tsai, Chorng-Ping Chang, Christiane Le Tiec, Christopher Henderson, Digh Hisamoto, Francis Balestra, Fred Kuper, Geoffrey Yeap, Gerben Doornbos, Gerhard Klimeck, Guillaume Bouhe, Hajime Nakabasyashi, Hiroshi Iwai, Hitoshi Wakabayashi, Huiming Bu, James Stathis, Jim Fonseca, Jiro Ida, Joe Brewer, Joel Barnett, Jurgen Lorenz, Karim Cherkaoui, Kazuyuki Tomida, Krishna Bhuwalka, Kunihiko Iwamoro, Kuniyuki Kakushima, Lars Liebmann, Laurent Le-Pailleur, Malgorzata Jurczak, Mark van Dal, Masako Kodera, Masami Hane, Matthias Passlack, Mehdi Salmani, Moon-Young Jeong, Mustafa Badaroglu, Olivier Faynot, Paul Mertens, Peter Ramm, Philip Wong, Prasad Sarangapani, Ray Duffy, Rich Liu, Robert Lander, SangBum Kim, Saumitra Mehrotra, Sergei Drizlikh, Shinichi Ogawa, Shinichi Takagi, SungGeun Kim, Takashi Matsukawa, Takeshi Nogami, Tatsuva Ohguro, Tesuo Endoh, Tetsu Tanaka, Thierry Poiroux, Toshiro Hiramoto, Wilman Tsai, Witek Maszara, Yannick Le Tiec, Yanzhong Xu, Yasutoshi Okuno, and Yoshihiro Hayashi, IEEE International Roadmap for Devices and Systems - More Moore, (2023) https://irds. ieee.org/images/files/pdf/2023/2023IRDS MM.pdf, pre-published.
- <sup>3</sup>R. P. Feynman, "There's Plenty of Room at the Bottom", Engineering and Science **23**, 22-6 (1960), https://calteches.library.caltech.edu/47/3/ES.23.5.1960.0.pdf.
- <sup>4</sup>I. Byun, M. Cuthbert, E. DeBenedictis, K. Delfanazari, R. L. Fagaly, G. Fagas, P. Febvre, T. Filippov, C. Fourie, M. Frank, D. Gupta, A. Herr, Q. Herr, D. S. Holmes, T. Humble, A. Leese de Escobar, D. Min, P. Mueller, O. Mukhanov, K. Nemoto, S. Papa Rao, E. Pelucchi, B. Plourde, I. Soloviev, G. Tzimpragos, A. Van Horn, M. Weides, N. Yoshikawa, and L. You, *IEEE International Roadmap for Devices and Systems Cryogenic Electronics and Quantum Information Processing*, (2023) 10.60627/042B–J892, pre-published.
- <sup>5</sup>National Academies of Sciences, Engineering, and Medicine, *Quantum Computing: Progress and Prospects*, edited by E. Grumbling and M. Horowitz (National Academies Press, Washington, D.C., 2019), 25196, ISBN: 978-0-309-47969-1, 10.17226/25196.
- $^6$ J. Alicea, "New directions in the pursuit of Majorana fermions in solid state systems", Reports on Progress in Physics **75**, 076501, ISSN: 0034-4885, 1361-6633 (2012) 10. 1088/0034-4885/75/7/076501.
- <sup>7</sup>L. Fu and C. L. Kane, "Superconducting Proximity Effect and Majorana Fermions at the Surface of a Topological Insulator", Physical Review Letters **100**, 096407, ISSN: 0031-9007, 1079-7114 (2008) 10.1103/PhysRevLett.100.096407.

- <sup>8</sup>M. Z. Hasan and C. L. Kane, "Colloquium: Topological insulators", Reviews of Modern Physics **82**, 3045–3067, ISSN: 0034-6861, 1539-0756 (2010) 10.1103/RevModPhys.82. 3045.
- $^9\mathrm{C.}$  L. Kane and E. J. Mele, "Z $_2$  Topological Order and the Quantum Spin Hall Effect", Physical Review Letters **95**, 146802, ISSN: 0031-9007, 1079-7114 (2005) 10.1103/PhysRevLett.95.146802.
- <sup>10</sup>M. König, S. Wiedmann, C. Brüne, A. Roth, H. Buhmann, L. W. Molenkamp, X.-L. Qi, and S.-C. Zhang, "Quantum Spin Hall Insulator State in HgTe Quantum Wells", Science 318, 766-770, ISSN: 0036-8075, 1095-9203 (2007) 10.1126/science.1148047.
- <sup>11</sup>L. Fu, C. L. Kane, and E. J. Mele, "Topological Insulators in Three Dimensions", Physical Review Letters **98**, 106803, ISSN: 0031-9007, 1079-7114 (2007) 10.1103/PhysRevLett.98.106803.
- <sup>12</sup>H. von Benda, A. Simon, and W. Bauhofer, "Zur Kenntnis von BiBr und BiBr<sub>1,167</sub>",
   Zeitschrift für anorganische und allgemeine Chemie 438, 53–67, ISSN: 1521-3749 (1978)
   10.1002/zaac.19784380105.
- <sup>13</sup>H. G. Von Schnering, H. Von Benda, and C. Kalveram, "Wismutmonojodid BiJ, eine Verbindung mit Bi(0) und Bi(II)", Zeitschrift für anorganische und allgemeine Chemie **438**, 37–52, ISSN: 0044-2313, 1521-3749 (1978) 10.1002/zaac.19784380104.
- $^{14}$  J. Han, W. Xiao, and Y. Yao, "Quasi-one-dimensional topological material Bi $_4$ X $_4$  (X=Br,I)", Advances in Physics: X **7**, 2057234, ISSN: 2374-6149 (2022) 10.1080/23746149.2022.2057234.
- <sup>15</sup>C. D. Hinostroza, L. Rodrigues De Faria, G. H. Cassemiro, J. Larrea Jiménez, A. Jefferson Da Silva Machado, W. H. Brito, and V. Martelli, "Structural investigation of the quasi-one-dimensional topological insulator Bi<sub>4</sub>I<sub>4</sub>", Physical Review B 109, 174105, ISSN: 2469-9950, 2469-9969 (2024) 10.1103/PhysRevB.109.174105.
- <sup>16</sup>R. Noguchi, "Stacking-Dependent Topological Phases in Quasi-1D Bismuth Halides", in, Designing Topological Phase of Bismuth Halides and Controlling Rashba Effect in Films Studied by ARPES (Springer Nature Singapore, Singapore, 2022), 77–120, ISBN: 978-981-19-1873-5, 10.1007/978-981-19-1874-2\_5.
- <sup>17</sup>R. Noguchi, T. Takahashi, K. Kuroda, M. Ochi, T. Shirasawa, M. Sakano, C. Bareille, M. Nakayama, M. D. Watson, K. Yaji, A. Harasawa, H. Iwasawa, P. Dudin, T. K. Kim, M. Hoesch, V. Kandyba, A. Giampietri, A. Barinov, S. Shin, R. Arita, T. Sasagawa, and T. Kondo, "A weak topological insulator state in quasi-one-dimensional bismuth iodide", Nature 566, 518–522, ISSN: 0028-0836, 1476-4687 (2019) 10.1038/s41586-019-0927-7.
- <sup>18</sup>R. Noguchi, "Backgrounds", in, Designing Topological Phase of Bismuth Halides and Controlling Rashba Effect in Films Studied by ARPES (Springer Nature Singapore, Singapore, 2022), 3–19, ISBN: 978-981-19-1873-5, 10.1007/978-981-19-1874-2\_2.
- <sup>19</sup>S. Yu, J. Deng, W. Liu, Y. Zhang, Y. Sun, N. Dhale, S. Li, W. Ma, Z. Wang, P. Wu, Z. Liang, X. Zhang, B. Lv, Z. Wang, Z. Wang, and X. Chen, "Observation of Robust One-Dimensional Edge Channels in a Three-Dimensional Quantum Spin Hall Insulator", Physical Review X 14, 041048, ISSN: 2160-3308 (2024) 10.1103/PhysRevX. 14.041048.

- <sup>20</sup>N. Shumiya, M. S. Hossain, J.-X. Yin, Z. Wang, M. Litskevich, C. Yoon, Y. Li, Y. Yang, Y.-X. Jiang, G. Cheng, Y.-C. Lin, Q. Zhang, Z.-J. Cheng, T. A. Cochran, D. Multer, X. P. Yang, B. Casas, T.-R. Chang, T. Neupert, Z. Yuan, S. Jia, H. Lin, N. Yao, L. Balicas, F. Zhang, Y. Yao, and M. Z. Hasan, "Evidence of a room-temperature quantum spin Hall edge state in a higher-order topological insulator", Nature Materials 21, 1111–1115, ISSN: 1476-1122, 1476-4660 (2022) 10.1038/s41563-022-01304-3.
- <sup>21</sup>R. Noguchi, M. Kobayashi, Z. Jiang, K. Kuroda, T. Takahashi, Z. Xu, D. Lee, M. Hirayama, M. Ochi, T. Shirasawa, P. Zhang, C. Lin, C. Bareille, S. Sakuragi, H. Tanaka, S. Kunisada, K. Kurokawa, K. Yaji, A. Harasawa, V. Kandyba, A. Giampietri, A. Barinov, T. K. Kim, C. Cacho, M. Hashimoto, D. Lu, S. Shin, R. Arita, K. Lai, T. Sasagawa, and T. Kondo, "Evidence for a higher-order topological insulator in a three-dimensional material built from van der Waals stacking of bismuth-halide chains", Nature Materials 20, 473–479, ISSN: 1476-4660 (2021) 10.1038/s41563-020-00871-7.
- <sup>22</sup>W. Zhao, M. Yang, R. Xu, X. Du, Y. Li, K. Zhai, C. Peng, D. Pei, H. Gao, Y. Li, L. Xu, J. Han, Y. Huang, Z. Liu, Y. Yao, J. Zhuang, Y. Du, J. Zhou, Y. Chen, and L. Yang, "Topological electronic structure and spin texture of quasi-one-dimensional higher-order topological insulator Bi<sub>4</sub>Br<sub>4</sub>", Nature Communications 14, 8089, ISSN: 2041-1723 (2023) 10.1038/s41467-023-43882-z.
- <sup>23</sup>J.-J. Zhou, W. Feng, C.-C. Liu, S. Guan, and Y. Yao, "Large-Gap Quantum Spin Hall Insulator in Single Layer Bismuth Monobromide Bi<sub>4</sub>Br<sub>4</sub>", Nano Letters 14, 4767–4771, ISSN: 1530-6984 (2014) 10.1021/nl501907g.
- <sup>24</sup>I. Shiraki, F. Tanabe, R. Hobara, T. Nagao, and S. Hasegawa, "Independently driven four-tip probes for conductivity measurements in ultrahigh vacuum", Surface Science 493, 633–643, ISSN: 00396028 (2001) 10.1016/S0039-6028(01)01276-6.
- <sup>25</sup>G. Binnig and H. Rohrer, "Scanning tunneling microscopy", Helvetica Physica Acta **55**, 726–735 (1982) 10.5169/seals-115309.
- <sup>26</sup>G. Binnig, H. Rohrer, Ch. Gerber, and E. Weibel, "7 × 7 Reconstruction on Si(111) Resolved in Real Space", Physical Review Letters 50, 120–123, ISSN: 0031-9007 (1983) 10.1103/PhysRevLett.50.120.
- <sup>27</sup>F. Wenner, "A method of measuring earth resistivity", Bulletin of the Bureau of Standards 12, 469–478 (1916) 10.6028/bulletin.282.
- <sup>28</sup>L. Valdes, "Resistivity Measurements on Germanium for Transistors", Proceedings of the IRE 42, 420–427, ISSN: 0096-8390 (1954) 10.1109/JRPROC.1954.274680.
- <sup>29</sup>L. J. van der Pauw, "Determination of resistivity tensor and Hall tensor of anisotropic shape", Philips Research Reports **16**, 187–195 (1961).
- <sup>30</sup>J. D. Wasscher, "Note on four-point resistivity measurements on anisotropic conductors", Philips Research Reports 16, 301–306 (1961).
- <sup>31</sup> J. K. Hofmann, H. Jeon, S. M. Hus, Y. Zhang, M. Zheng, T. Wichmann, A.-P. Li, J.-J. Zhou, Z. Wang, Y. Yao, B. Voigtländer, F. S. Tautz, and F. Lüpke, "Shear-resistant topology in the quasi-one-dimensional van der Waals material Bi<sub>4</sub>Br<sub>4</sub>", Physical Review B 111, 245415, ISSN: 2469-9950, 2469-9969 (2025) 10.1103/tdp5-wmqc.

- <sup>32</sup>I. Miccoli, F. Edler, H. Pfnür, and C. Tegenkamp, "The 100th anniversary of the four-point probe technique: the role of probe geometries in isotropic and anisotropic systems", Journal of Physics: Condensed Matter 27, 223201, ISSN: 0953-8984, 1361-648X (2015) 10.1088/0953-8984/27/22/223201.
- <sup>33</sup>K. Knödel, H. Krummel, and G. Lange, eds., *Geophysik: mit ... 57 Tabellen*, 2., überarb. Aufl, Handbuch zur Erkundung des Untergrundes von Deponien und Altlasten / BGR, Bundesanstalt für Geowissenschaften und Rohstoffe Bd. 3 (Springer, Berlin, 2005), 1102 pp., ISBN: 978-3-540-26606-8.
- <sup>34</sup>U. Tietze and C. Schenk, *Halbleiter-Schaltungstechnik*, 10th ed. (Berlin Heidelberg New York, 1993), ISBN: 3-540-56184-6.
- <sup>35</sup>W. Thomson, "New Electrodynamic Balance for resistance of short bars or wires", Philosophical Magazine and Journal of Science **24**, 149–162 (1862), https://zs.thulb.uni-jena.de/rsc/viewer/jportal\_derivate\_00126615/PMS\_1862\_Bd24\_%200157.tif?logicalDiv=jportal\_jpvolume\_00126094.
- <sup>36</sup>F. Wenner, "The four-terminal conductor and the Thomson bridge", Bulletin of the Bureau of Standards 8, 559, ISSN: 0096-8579 (1912) 10.6028/bulletin.197.
- <sup>37</sup>F. M. Smits, "Measurement of Sheet Resistivities with the Four-Point Probe", Bell System Technical Journal **37**, 711–718, ISSN: 00058580 (1958) 10.1002/j.1538-7305.1958.tb03883.x.
- <sup>38</sup>J. D. Nye, *Physical properties of crystals* (Oxford University Press, London, 1957).
- <sup>39</sup>A. Uhlir, "The Potentials of Infinite Systems of Sources and Numerical Solutions of Problems in Semiconductor Engineering", Bell System Technical Journal 34, 105–128, ISSN: 00058580 (1955) 10.1002/j.1538-7305.1955.tb03765.x.
- <sup>40</sup>B. Voigtländer, V. Cherepanov, S. Korte, A. Leis, D. Cuma, S. Just, and F. Lüpke, "Invited Review Article: Multi-tip scanning tunneling microscopy: Experimental techniques and data analysis", Review of Scientific Instruments 89, 101101, ISSN: 0034-6748 (2018) 10.1063/1.5042346.
- <sup>41</sup>D. K. Schroder, Semiconductor Material and Device Characterization, 3rd ed. (Wiley, Oct. 21, 2005), ISBN: 978-0-471-73906-7, 10.1002/0471749095.
- <sup>42</sup>S. Just, "Disentangling parallel conduction channels by charge transport measurements on surfaces with a multi-tip scanning tunneling microscope" (RWTH Aachen University, 2021), 10.18154/RWTH-2021-05732.
- <sup>43</sup>A. Leis, "Nanoscale four-point charge transport measurements in topological insulator thin films" (RWTH Aachen University, 2021), 10.18154/RWTH-2021-08176.
- <sup>44</sup>M. Blab, "Ladungstransportmessungen an Si(111)-Oberflächen mit einem Multispitzen-Rastertunnelmikroskop" (RWTH Aachen University, Aachen, 2015), https://publications.rwth-aachen.de/record/463827/files/5251.pdf.
- <sup>45</sup>D. S. Perloff, "Four-point sheet resistance correction factors for thin rectangular samples", Solid-State Electronics **20**, 681–687, ISSN: 00381101 (1977) 10.1016/0038-1101(77)90044-2.
- <sup>46</sup>L. J. van der Pauw, "A method of measuring specific resistivity and hall effect of disc of arbitrary shape", Philips Research Reports 13, 1–9 (1958).

- <sup>47</sup>L. J. van der Pauw, "A method of measuring the resistivity and hall coefficient on lamellae of arbitrary chape", Philips Technical Review **20**, 220–224 (1958).
- <sup>48</sup>Z.-H. Sun, J. Zhou, X.-J. Xia, and D.-M. Zhou, "Two-dimensional electrostatic model for the Van der Pauw method", Physics Letters A **381**, 2144–2148, ISSN: 03759601 (2017) 10.1016/j.physleta.2017.04.020.
- <sup>49</sup>S. Hurand, T. Chommaux, P.-O. Renault, T. Girardeau, and F. Paumier, "Easy and computer-time-saving implementation of the van der Pauw method including anisotropy and probe positioning correction factors using approximate closed-form analytical functions", Review of Scientific Instruments 93, 053907, ISSN: 0034-6748, 1089-7623 (2022) 10.1063/5.0068682.
- <sup>50</sup>W. K. Chan, "On the calculation of the geometric factor in a van der Pauw sheet resistance measurement", Review of Scientific Instruments 71, 3964–3965, ISSN: 0034-6748, 1089-7623 (2000) 10.1063/1.1290496.
- <sup>51</sup>S. Thorsteinsson, F. Wang, D. H. Petersen, T. M. Hansen, D. Kjær, R. Lin, J.-Y. Kim, P. F. Nielsen, and O. Hansen, "Accurate microfour-point probe sheet resistance measurements on small samples", Review of Scientific Instruments 80, 053902, ISSN: 0034-6748, 1089-7623 (2009) 10.1063/1.3125050.
- <sup>52</sup>J. D. Weiss, "Generalization of the van der Pauw relationship derived from electrostatics", Solid-State Electronics **62**, 123–127, ISSN: 00381101 (2011) 10.1016/j.sse. 2011.04.006.
- <sup>53</sup>J. D. Weiss, "A comparison of two van-der-Pauw measurement configurations of resistivity", Materials Science in Semiconductor Processing 16, 1637–1644, ISSN: 13698001 (2013) 10.1016/j.mssp.2013.05.013.
- <sup>54</sup>C. S. Smith, "Macroscopic Symmetry and Properties of Crystals", in *Solid State Physics*, 6 (Elsevier, 1958), 175–249, ISBN: 978-0-12-607706-3, 10.1016/S0081-1947(08)60727-4.
- <sup>55</sup>T. Okada, "The Phenomenological Theory of the Galvanomagnetic Effect", Memoirs of the Faculty of Science, Kyusyu University 1, 157–167 (1955).
- <sup>56</sup>K. Jänich, *Lineare Algebra*, 11. Edition (Springer, Heidelberg Dordrecht London New York, 2008), ISBN: 978-3-540-75501-2.
- <sup>57</sup>B. J. Hornstra and L. J. Van Der Pauw, "Measurement of the Resistivity Constants of Anistotropic Conductors by means of Plane-Parallel Discs of Arbitrary Shape", Journal of Electronics and Control 7, 169–171, ISSN: 0368-1947 (1959) 10.1080/00207215908937197.
- <sup>58</sup>J. J. Wasscher, "Electrical transport phenomena in MnTe, an antiferromagnetic semi-conductor" (Technische Universiteit Eindhoven, Eindhoven, 1969), https://research.tue.nl/en/publications/electrical-transport-phenomena-in-mnte-an-antiferromagnetic-semiconductor(2c43dfc2-56d7-497f-b02b-21ba9915b081).html.
- <sup>59</sup>O. Bierwagen, R. Pomraenke, S. Eilers, and W. T. Masselink, "Mobility and carrier density in materials with anisotropic conductivity revealed by van der Pauw measurements", Physical Review B 70, 165307, ISSN: 1098-0121, 1550-235X (2004) 10.1103/PhysRevB.70.165307.

- <sup>60</sup>E. G. Víllora, K. Shimamura, Y. Yoshikawa, K. Aoki, and N. Ichinose, "Large-size β-Ga<sub>2</sub>O<sub>3</sub> single crystals and wafers", Journal of Crystal Growth **270**, 420–426, ISSN: 00220248 (2004) 10.1016/j.jcrysgro.2004.06.027.
- <sup>61</sup>S. V. Airapetyants and M. S. Bresler, "Measurement of the anisotropy of electrical conductivity of semiconductors by the four-probe method", Sovjet Physics Solid State 1, 134 (1959).
- <sup>62</sup>H. C. Montgomery, "Method for Measuring Electrical Resistivity of Anisotropic Materials", Journal of Applied Physics 42, 2971–2975, ISSN: 0021-8979, 1089-7550 (1971) 10.1063/1.1660656.
- <sup>63</sup>C. A. M. Dos Santos, A. De Campos, M. S. Da Luz, B. D. White, J. J. Neumeier, B. S. De Lima, and C. Y. Shigue, "Procedure for measuring electrical resistivity of anisotropic materials: A revision of the Montgomery method", Journal of Applied Physics 110, 083703, ISSN: 0021-8979, 1089-7550 (2011) 10.1063/1.3652905.
- <sup>64</sup>S. H. Simon, "Comment on "Evidence for an Anisotropic State of Two-Dimensional Electrons in High Landau Levels", Physical Review Letters 83, 4223–4223, ISSN: 0031-9007, 1079-7114 (1999) 10.1103/PhysRevLett.83.4223.
- <sup>65</sup>B. F. Logan, S. O. Rice, and R. F. Wick, "Series for Computing Current Flow in a Rectangular Block", Journal of Applied Physics 42, 2975–2980, ISSN: 0021-8979, 1089-7550 (1971) 10.1063/1.1660657.
- <sup>66</sup>R. A. Weller, "An algorithm for computing linear four-point probe thickness correction factors", Review of Scientific Instruments **72**, 3580–3586, ISSN: 0034-6748, 1089-7623 (2001) 10.1063/1.1394186.
- <sup>67</sup>J. Albers and H. L. Berkowitz, "An Alternative Approach to the Calculation of Four-Probe Resistances on Nonuniform Structures", Journal of The Electrochemical Society 132, 2453–2456, ISSN: 0013-4651, 1945-7111 (1985) 10.1149/1.2113598.
- <sup>68</sup>M. Yamashita and M. Agu, "Geometrical Correction Factor for Semiconductor Resistivity Measurements by Four-Point Probe Method", Japanese Journal of Applied Physics 23, 1499, ISSN: 0021-4922, 1347-4065 (1984) 10.1143/JJAP.23.1499.
- <sup>69</sup>M. Yamashita, "Geometrical Correction Factor for Resistivity of Semiconductors by the Square Four-Point Probe Method", Japanese Journal of Applied Physics 25, 563, ISSN: 0021-4922, 1347-4065 (1986) 10.1143/JJAP.25.563.
- <sup>70</sup>M. Yamashita, T. Nishi, H. Kurihara, H. Enjoji, and A. Iwata, "Resistivity Correction Factor for the Four-Probe Method: Experiment III", Japanese Journal of Applied Physics 29, 776, ISSN: 0021-4922, 1347-4065 (1990) 10.1143/JJAP.29.776.
- <sup>71</sup>M. Abramowitz and I. A. Stegun, Handbook of mathematical functions: with formulas, graphs and mathematical tables, Unabridged, unaltered and corr. republ. of the 1964 ed, Dover Books on Advanced Mathematics (Dover publ, New York, 1972), ISBN: 978-0-486-61272-0.
- <sup>72</sup>D. C. Worledge, "Reduction of positional errors in a four-point probe resistance measurement", Applied Physics Letters 84, 1695–1697, ISSN: 0003-6951, 1077-3118 (2004) 10.1063/1.1655697.

- <sup>73</sup>R. Rymaszewski, "Relationship between the correction factor of the four-point probe value and the selection of potential and current electrodes", Journal of Physics E: Scientific Instruments 2, 170–174, ISSN: 00223735 (1969) 10.1088/0022-3735/2/2/312.
- <sup>74</sup>G. R. Kirchhoff, "Ueber die Auflösung der Gleichungen, auf welche man bei der Untersuchung der linearen Vertheilung galvanischer Ströme geführt wird", Annalen der Physik und Chemie. **72**, 497–508 (1847).
- <sup>75</sup>E. A. Guillemin, *Introductory circuit theory* (John Wiley & Sons, Inc, New York, 1953).
- <sup>76</sup>D. S. Perloff, "Four-Point Probe Correction Factors for Use in Measuring Large Diameter Doped Semiconductor Wafers", Journal of The Electrochemical Society 123, 1745–1750, ISSN: 0013-4651, 1945-7111 (1976) 10.1149/1.2132683.
- <sup>77</sup>V. Cherepanov, E. Zubkov, H. Junker, S. Korte, M. Blab, P. Coenen, and B. Voigtländer, "Ultra compact multitip scanning tunneling microscope with a diameter of 50 mm", Review of Scientific Instruments 83, 033707, ISSN: 0034-6748, 1089-7623 (2012) 10.1063/1.3694990.
- <sup>78</sup>G. Binnig, H. Rohrer, Ch. Gerber, and E. Weibel, "Tunneling through a controllable vacuum gap", Applied Physics Letters **40**, 178–180, ISSN: 0003-6951, 1077-3118 (1982) 10.1063/1.92999.
- <sup>79</sup>C. J. Chen, *Introduction to scanning tunneling microscopy*, Third edition, Monographs on the Physics and Chemistry of Materials 69 (Oxford University Press, Oxford, 2021), 452 pp., ISBN: 978-0-19-885655-9.
- <sup>80</sup>B. Voigtländer, Scanning probe microscopy: atomic force microscopy and scanning tunneling microscopy, Nanoscience and Technology (Springer, Heidelberg New York Dordrecht London, 2015), 382 pp., ISBN: 978-3-662-45239-4.
- <sup>81</sup>P. Muralt and D. W. Pohl, "Scanning tunneling potentiometry", Applied Physics Letters 48, 514–516, ISSN: 0003-6951, 1077-3118 (1986) 10.1063/1.96491.
- <sup>82</sup>W. Huang, J. A. Seo, M. P. Canavan, P. Gambardella, and S. Stepanow, "Observation of different Li intercalation states and local doping in epitaxial mono- and bilayer graphene on SiC(0001)", Nanoscale 16, 3160–3165, ISSN: 2040-3364, 2040-3372 (2024) 10.1039/D3NR03070A.
- <sup>83</sup>F. Lüpke, S. Korte, V. Cherepanov, and B. Voigtländer, "Scanning tunneling potentiometry implemented into a multi-tip setup by software", Review of Scientific Instruments 86, 123701, ISSN: 0034-6748, 1089-7623 (2015) 10.1063/1.4936079.
- <sup>84</sup>R. Hobara, N. Nagamura, S. Hasegawa, I. Matsuda, Y. Yamamoto, Y. Miyatake, and T. Nagamura, "Variable-temperature independently driven four-tip scanning tunneling microscope", Review of Scientific Instruments 78, 053705, ISSN: 0034-6748, 1089-7623 (2007) 10.1063/1.2735593.
- <sup>85</sup> J. P. Ibe, P. P. Bey, S. L. Brandow, R. A. Brizzolara, N. A. Burnham, D. P. DiLella, K. P. Lee, C. R. K. Marrian, and R. J. Colton, "On the electrochemical etching of tips for scanning tunneling microscopy", Journal of Vacuum Science & Technology A: Vacuum, Surfaces, and Films 8, 3570–3575, ISSN: 0734-2101, 1520-8559 (1990) 10.1116/1.576509.

- <sup>86</sup>FEMTO Messtechnik GmbH, Datasheet: Variable Gain Low Noise Transimpedance Amplifier (Current Amplifier) DLPCA-200 Current amplifier, DLPCA-200 (Berlin), https://www.femto.de/images/pdf-dokumente/de-dlpca-200.pdf.
- <sup>87</sup>R. Lerch, Elektrische Messtechnik: Analoge, digitale und computergestützte Verfahren, 4., neu bearbeitete Aufl (Springer-Verlag Berlin Heidelberg, Berlin, Heidelberg, 2007), ISBN: 978-3-540-75727-6.
- <sup>88</sup>L. Reimer, Scanning electron microscopy: physics of image formation and microanalysis, 2., completely rev. and updated ed, Springer Series in Optical Sciences 45 (Springer, Berlin Heidelberg, 1998), 527 pp., ISBN: 978-3-642-08372-3.
- <sup>89</sup>S. Korte, Ladungstransport durch Graphenschichten und GaAs-Nanodrähte untersucht mit einem Multispitzen-Rastertunnelmikroskop, Schriften des Forschungszentrums Jülich / Reihe Schlüsseltechnologien 90 (Hochschulbibliothek der Rheinisch-Westfälischen Technischen Hochschule Aachen, Aachen, 2014), ISBN: 978-3-89336-990-4.
- <sup>90</sup>D. Cuma, "Multi-tip scanning tunneling potentiometry on thin bismuth films and topological insulators in a cryogenic system" (RWTH Aachen University, 2023), https://publications.rwth-aachen.de/record/963395.
- <sup>91</sup>BIPM, IEC, IFCC, ILAC, ISO, IUPAC, IUPAP, and OIML, Evaluation of measurement data Supplement 1 to the "Guide to the expression of uncertainty in measurement" Propagation of distributions using a Monte Carlo method, Joint Committee for Guides in Metrology, JCGM 101:2008, 2008, https://www.bipm.org/documents/20126/2071204/JCGM\_101\_2008\_E.pdf/325dcaad-c15a-407c-1105-8b7f322d651c.
- $^{92}$ B. Predel, "Bi-I (Bismuth-Iodine)", in  $B\text{-}Ba-C\text{-}Zr,~\mathbf{5b},$ edited by O. Madelung (Springer-Verlag, Berlin/Heidelberg, 1992), 1–3, ISBN: 978-3-540-55115-7, 10.1007/10040476 554.
- $^{93}\text{C.-C.}$  Liu, J.-J. Zhou, Y. Yao, and F. Zhang, "Weak Topological Insulators and Composite Weyl Semimetals:  $\beta-\text{Bi}_4\text{X}_4$  ( X = Br , I)", Physical Review Letters **116**, 066801, ISSN: 0031-9007, 1079-7114 (2016) 10.1103/PhysRevLett.116.066801.
- <sup>94</sup>T. Filatova, P. Gurin, L. Kloo, V. Kulbachinskii, A. Kuznetsov, V. Kytin, M. Lindsjo, and B. Popovkin, "Electronic structure, galvanomagnetic and magnetic properties of the bismuth subhalides Bi<sub>4</sub>I<sub>4</sub> and Bi<sub>4</sub>Br<sub>4</sub>", Journal of Solid State Chemistry 180, 1103–1109, ISSN: 00224596 (2007) 10.1016/j.jssc.2007.01.010.
- $^{95}$ X. Zhang, X. Xing, J. Li, X. Peng, L. Qiao, Y. Liu, X. Xiong, J. Han, W. Liu, W. Xiao, and Y. Yao, "Controllable epitaxy of quasi-one-dimensional topological insulator  $\alpha$  -Bi<sub>4</sub>Br<sub>4</sub> for the application of saturable absorber", Applied Physics Letters **120**, 093103, ISSN: 0003-6951, 1077-3118 (2022) 10.1063/5.0083807.
- <sup>96</sup>X. Peng, X. Zhang, X. Dong, D. Ma, D. Chen, Y. Li, J. Li, J. Han, Z. Wang, C.-C. Liu, J. Zhou, W. Xiao, and Y. Yao, "Observation of Topological Edge States on α-Bi<sub>4</sub>Br<sub>4</sub> Nanowires Grown on TiSe<sub>2</sub> Substrates", The Journal of Physical Chemistry Letters 12, 10465–10471, ISSN: 1948-7185, 1948-7185 (2021) 10.1021/acs.jpclett.1c02586.
- <sup>97</sup>J. Zhuang, J. Li, Y. Liu, D. Mu, M. Yang, Y. Liu, W. Zhou, W. Hao, J. Zhong, and Y. Du, "Epitaxial Growth of Quasi-One-Dimensional Bismuth-Halide Chains with Atomically Sharp Topological Non-Trivial Edge States", ACS Nano 15, 14850–14857, ISSN: 1936-0851, 1936-086X (2021) 10.1021/acsnano.1c04928.

- <sup>98</sup>Bureau international des poids et mesures, ed., Comptes rendus de la 26 e réunion de la Conférence générale des poids et mesures (Sèvres Cedex, France, 2018), ISBN: 978-92-822-2276-8, https://www.bipm.org/documents/20126/17314988/CGPM26.pdf.
- $^{99}$ J.-J. Zhou, W. Feng, G.-B. Liu, and Y. Yao, "Topological edge states in single- and multi-layer Bi<sub>4</sub>Br<sub>4</sub>", New Journal of Physics **17**, 015004, ISSN: 1367-2630 (2015) 10.1088/1367-2630/17/1/015004.
- <sup>100</sup>C. Yoon, C.-C. Liu, H. Min, and F. Zhang, Quasi-One-Dimensional Higher-Order Topological Insulators, (May 29, 2020) http://arxiv.org/abs/2005.14710, prepublished.
- <sup>101</sup>S. Wu, V. Fatemi, Q. D. Gibson, K. Watanabe, T. Taniguchi, R. J. Cava, and P. Jarillo-Herrero, "Observation of the quantum spin Hall effect up to 100 kelvin in a monolayer crystal", Science 359, 76–79, ISSN: 0036-8075, 1095-9203 (2018) 10.1126/science.aan6003.
- <sup>102</sup>F. Schindler, A. M. Cook, M. G. Vergniory, Z. Wang, S. S. P. Parkin, B. A. Bernevig, and T. Neupert, "Higher-order topological insulators", Science Advances 4, eaat0346, ISSN: 2375-2548 (2018) 10.1126/sciadv.aat0346.
- <sup>103</sup>C.-H. Hsu, X. Zhou, Q. Ma, N. Gedik, A. Bansil, V. M. Pereira, H. Lin, L. Fu, S.-Y. Xu, and T.-R. Chang, "Purely rotational symmetry-protected topological crystalline insulator α-Bi<sub>4</sub>Br<sub>4</sub>", 2D Materials 6, 031004, ISSN: 2053-1583 (2019) 10.1088/2053-1583/ab1607.
- $^{104}\mathrm{L}.$  Fu, "Topological Crystalline Insulators", Physical Review Letters  $\mathbf{106},\,106802,\,\mathrm{ISSN}:\,0031\text{-}9007,\,1079\text{-}7114$  (2011)  $10.1103/\mathrm{PhysRevLett.106.106802}.$
- <sup>105</sup>P. Roushan, J. Seo, C. V. Parker, Y. S. Hor, D. Hsieh, D. Qian, A. Richardella, M. Z. Hasan, R. J. Cava, and A. Yazdani, "Topological surface states protected from backscattering by chiral spin texture", Nature 460, 1106–1109, ISSN: 0028-0836, 1476-4687 (2009) 10.1038/nature08308.
- <sup>106</sup>A. Leis, M. Schleenvoigt, A. R. Jalil, V. Cherepanov, G. Mussler, D. Grützmacher, F. S. Tautz, and B. Voigtländer, "Room temperature in-situ measurement of the spin voltage of a BiSbTe3 thin film", Scientific Reports 10, 2816, ISSN: 2045-2322 (2020) 10.1038/s41598-020-59679-9.
- <sup>107</sup>A. Leis, M. Schleenvoigt, V. Cherepanov, F. Lüpke, P. Schüffelgen, G. Mussler, D. Grützmacher, B. Voigtländer, and F. S. Tautz, "Lifting the Spin-Momentum Locking in Ultra-Thin Topological Insulator Films", Advanced Quantum Technologies 4, 2100083, ISSN: 2511-9044 (2021) 10.1002/qute.202100083.
- <sup>108</sup>M. S. Hossain, Q. Zhang, Z. Wang, N. Dhale, W. Liu, M. Litskevich, B. Casas, N. Shumiya, J.-X. Yin, T. A. Cochran, Y. Li, Y.-X. Jiang, Y. Zhang, G. Cheng, Z.-J. Cheng, X. P. Yang, N. Yao, T. Neupert, L. Balicas, Y. Yao, B. Lv, and M. Z. Hasan, "Quantum transport response of topological hinge modes", Nature Physics 20, 776–782, ISSN: 1745-2473, 1745-2481 (2024) 10.1038/s41567-024-02388-1.
- <sup>109</sup>F. Lüpke, D. Waters, S. C. De La Barrera, M. Widom, D. G. Mandrus, J. Yan, R. M. Feenstra, and B. M. Hunt, "Proximity-induced superconducting gap in the quantum spin Hall edge state of monolayer WTe<sub>2</sub>", Nature Physics 16, 526–530, ISSN: 1745-2473, 1745-2481 (2020) 10.1038/s41567-020-0816-x.

- <sup>110</sup>K. S. Novoselov, D. Jiang, F. Schedin, T. J. Booth, V. V. Khotkevich, S. V. Morozov, and A. K. Geim, "Two-dimensional atomic crystals", Proceedings of the National Academy of Sciences 102, 10451–10453, ISSN: 0027-8424, 1091-6490 (2005) 10.1073/pnas.0502848102.
- <sup>111</sup>X. Li, D. Chen, M. Jin, D. Ma, Y. Ge, J. Sun, W. Guo, H. Sun, J. Han, W. Xiao, J. Duan, Q. Wang, C.-C. Liu, R. Zou, J. Cheng, C. Jin, J. Zhou, J. B. Goodenough, J. Zhu, and Y. Yao, "Pressure-induced phase transitions and superconductivity in a quasi-1-dimensional topological crystalline insulator α-Bi<sub>4</sub>Br<sub>4</sub>", Proceedings of the National Academy of Sciences 116, 17696–17700 (2019) 10.1073/pnas.1909276116.
- <sup>112</sup>M. Yang, Y. Liu, W. Zhou, C. Liu, D. Mu, Y. Liu, J. Wang, W. Hao, J. Li, J. Zhong, Y. Du, and J. Zhuang, Large-Gap Quantum Spin Hall State and Temperature-Induced Lifshitz Transition in Bi<sub>4</sub>Br<sub>4</sub>, (Oct. 13, 2021) 10.48550/arXiv.2110.06658, prepublished.
- <sup>113</sup>E. Khalaf, H. C. Po, A. Vishwanath, and H. Watanabe, "Symmetry Indicators and Anomalous Surface States of Topological Crystalline Insulators", Physical Review X 8, 031070, ISSN: 2160-3308 (2018) 10.1103/PhysRevX.8.031070.
- <sup>114</sup>Z. Song, T. Zhang, Z. Fang, and C. Fang, "Quantitative mappings between symmetry and topology in solids", Nature Communications 9, 3530, ISSN: 2041-1723 (2018) 10.1038/s41467-018-06010-w.
- <sup>115</sup>D.-Y. Chen, D. Ma, J. Duan, D. Chen, H. Liu, J. Han, and Y. Yao, "Quantum transport evidence of boundary states and Lifshitz transition in Bi<sub>4</sub>Br<sub>4</sub>", Physical Review B 106, 075206, ISSN: 2469-9950, 2469-9969 (2022) 10.1103/PhysRevB.106.075206.
- <sup>116</sup>S.-L. Wu, Z.-H. Ren, Y.-Q. Zhang, Y.-K. Li, J.-F. Han, J.-X. Duan, Z.-W. Wang, C.-Z. Li, and Y.-G. Yao, "Gate-tunable transport in van der Waals topological insulator Bi<sub>4</sub>Br<sub>4</sub> nanobelts", Journal of Physics: Condensed Matter 35, 234001, ISSN: 0953-8984, 1361-648X (2023) 10.1088/1361-648X/acc3eb.
- <sup>117</sup>A. Castellanos-Gomez, X. Duan, Z. Fei, H. R. Gutierrez, Y. Huang, X. Huang, J. Quereda, Q. Qian, E. Sutter, and P. Sutter, "Van der Waals heterostructures", Nature Reviews Methods Primers 2, 58, ISSN: 2662-8449 (2022) 10.1038/s43586-022-00139-1.
- <sup>118</sup>Z. Gong, X. Lai, W. Miao, J. Zhong, Z. Shi, H. Shen, X. Liu, Q. Li, M. Yang, J. Zhuang, and Y. Du, "Br-Vacancies Induced Variable Ranging Hopping Conduction in High-Order Topological Insulator Bi<sub>4</sub>Br<sub>4</sub>", Small Methods, 2400517, ISSN: 2366-9608, 2366-9608 (2024) 10.1002/smtd.202400517.
- <sup>119</sup>F. Lüpke, A. D. Pham, Y.-F. Zhao, L.-J. Zhou, W. Lu, E. Briggs, J. Bernholc, M. Kolmer, J. Teeter, W. Ko, C.-Z. Chang, P. Ganesh, and A.-P. Li, "Local manifestations of thickness-dependent topology and edge states in the topological magnet MnBi<sub>2</sub>Te<sub>4</sub>", Physical Review B 105, 035423, ISSN: 2469-9950, 2469-9969 (2022) 10.1103/PhysRe vB.105.035423.
- <sup>120</sup>K. Sugawara, N. Yamamura, K. Matsuda, W. Norimatsu, M. Kusunoki, T. Sato, and T. Takahashi, "Selective fabrication of free-standing ABA and ABC trilayer graphene with/without Dirac-cone energy bands", NPG Asia Materials 10, e466–e466, ISSN: 1884-4049, 1884-4057 (2018) 10.1038/am.2017.238.

- <sup>121</sup>C. Weissmantel and C. Hamann, Grundlagen der Festkörperphysik (Springer, Berlin Heidelberg, 1980), 807 pp., ISBN: 978-3-540-09072-4.
- <sup>122</sup>F. Lüpke, D. Waters, A. D. Pham, J. Yan, D. G. Mandrus, P. Ganesh, and B. M. Hunt, "Quantum Spin Hall Edge States and Interlayer Coupling in Twisted Bilayer WTe<sub>2</sub>", Nano Letters 22, 5674–5680, ISSN: 1530-6984, 1530-6992 (2022) 10.1021/acs.nanolett.2c00432.
- <sup>123</sup>E. V. Dikarev, B. A. Popovkin, and A. V. Shevelkov, "New polymolecular bismuth monohalides. Synthesis and crystal structures of  $Bi_4Br_xI_{4-x}$  (x = 1, 2, or 3)", Russian Chemical Bulletin **50**, 2304–2309, ISSN: 1573-9171 (2001) 10.1023/A:1015010907973.
- <sup>124</sup>C. Golz, Z. Galazka, J. Lähnemann, V. Hortelano, F. Hatami, W. T. Masselink, and O. Bierwagen, "Electrical conductivity tensor of β-Ga<sub>2</sub>O<sub>3</sub> analyzed by van der Pauw measurements: Inherent anisotropy, off-diagonal element, and the impact of grain boundaries", Physical Review Materials 3, 124604, ISSN: 2475-9953 (2019) 10.1103/PhysRevMaterials.3.124604.
- <sup>125</sup>W. Raith, *Lehrbuch der Experimentalphysik: Elektromagnetismus*, 9th edition (De Gruyter, Inc, Berlin/Boston, 2008).
- <sup>126</sup>F. Schlögl, *Probability and Heat* (Vieweg+Teubner Verlag, Wiesbaden, 1989), ISBN: 978-3-528-06343-6, 10.1007/978-3-663-13977-5.
- <sup>127</sup>P. T. Boggs and J. E. Rogers, "Orthogonal distance regression", in *Statistical analysis of measurement error models and applications (Arcata, CA, 1989)*, **112**, Contemp. Math. (Amer. Math. Soc., Providence, RI, 1990), 183–194, ISBN: 0-8218-5117-9, 10.1090/conm/112/1087109.
- <sup>128</sup>L. Qiao, X. Xiong, H. Yang, D. Chen, Y. Li, J. Li, X. Peng, Z. Xu, J. Han, W. Xiao, and Y. Yao, "Ultralong Single-Crystal α-Bi<sub>4</sub>Br<sub>4</sub> Nanobelts with a High Current-Carrying Capacity by Mechanical Exfoliation", The Journal of Physical Chemistry C 125, 22312–22317, ISSN: 1932-7447, 1932-7455 (2021) 10.1021/acs.jpcc.1c06702.
- <sup>129</sup>F. Xia, H. Wang, and Y. Jia, "Rediscovering black phosphorus as an anisotropic layered material for optoelectronics and electronics", Nature Communications 5, 4458, ISSN: 2041-1723 (2014) 10.1038/ncomms5458.
- <sup>130</sup>G.-H. Nam, Q. He, X. Wang, Y. Yu, J. Chen, K. Zhang, Z. Yang, D. Hu, Z. Lai, B. Li, Q. Xiong, Q. Zhang, L. Gu, and H. Zhang, "In-Plane Anisotropic Properties of 1T+-MoS<sub>2</sub> Layers", Advanced Materials 31, 1807764, ISSN: 0935-9648, 1521-4095 (2019) 10.1002/adma.201807764.
- <sup>131</sup>Q. Zhang, R. Zhang, J. Chen, W. Shen, C. An, X. Hu, M. Dong, J. Liu, and L. Zhu, "Remarkable electronic and optical anisotropy of layered 1T'-WTe<sub>2</sub> 2D materials", Beilstein Journal of Nanotechnology 10, 1745–1753, ISSN: 2190-4286 (2019) 10.3762/bjnano.10.170.
- <sup>132</sup>J. H. Dennis, Anisotropy of thermoelectric power in bismuth telluride, Technical Report 337 (Massachusetts Institute of Technology, Research Laboratory of Electronics, 1961), https://dspace.mit.edu/bitstream/handle/1721.1/4445/RLE-TR-377-0474098 3.pdf?sequence=1.
- <sup>133</sup>L. D. Ivanova, Y. V. Granatkina, and Y. A. Sidorov, "Anisotropie Electrical Properties of Tin-doped Antimony Telluride Single Crystals", Inorganic Materials 34, 26 (1998).

- <sup>134</sup>M. Stordeur and W. Heiliger, "Anisotropy of the thermopower of p-Sb<sub>2</sub>Te<sub>3</sub>", physica status solidi (b) **78**, ISSN: 0370-1972, 1521-3951 (1976) 10.1002/pssb.2220780255.
- <sup>135</sup>K. S. Krishnan and N. Ganguli, "Large Anisotropy of the Electrical Conductivity of Graphite", Nature **144**, 667–667, ISSN: 0028-0836, 1476-4687 (1939) 10.1038/144667a0.
- <sup>136</sup>W. Primak and L. H. Fuchs, "Electrical Conductivities of Natural Graphite Crystals", Physical Review 95, 22–30, ISSN: 0031-899X (1954) 10.1103/PhysRev.95.22.
- <sup>137</sup>D. Tsang and M. Dresselhaus, "The c-axis electrical conductivity of kish graphite", Carbon 14, 43–46, ISSN: 00086223 (1976) 10.1016/0008-6223(76)90081-6.
- <sup>138</sup>C. A. Klein, "Electrical Properties of Pyrolytic Graphites", Reviews of Modern Physics **34**, 56–79, ISSN: 0034-6861 (1962) 10.1103/RevModPhys.34.56.
- <sup>139</sup>K. Matsubara, K. Sugihara, and T. Tsuzuku, "Electrical resistance in the c direction of graphite", Physical Review B 41, 969–974, ISSN: 0163-1829, 1095-3795 (1990) 10.1103/PhysRevB.41.969.
- <sup>140</sup>S. Just, M. Blab, S. Korte, V. Cherepanov, H. Soltner, and B. Voigtländer, "Surface and Step Conductivities on Si(111) Surfaces", Physical Review Letters 115, 066801, ISSN: 0031-9007, 1079-7114 (2015) 10.1103/PhysRevLett.115.066801.
- <sup>141</sup>M. G. Buehler and W. Thurber, "Measurement of the resistivity of a thin square sample with a square four-probe array", Solid-State Electronics 20, 403–406, ISSN: 00381101 (1977) 10.1016/0038-1101(77)90130-7.
- <sup>142</sup>A. Leis, V. Cherepanov, B. Voigtländer, and F. S. Tautz, "Nanoscale tip positioning with a multi-tip scanning tunneling microscope using topography images", Review of Scientific Instruments 93, 013702, ISSN: 0034-6748, 1089-7623 (2022) 10.1063/5.0073059.
- <sup>143</sup>A. Leis, M. Schleenvoigt, K. Moors, H. Soltner, V. Cherepanov, P. Schüffelgen, G. Mussler, D. Grützmacher, B. Voigtländer, F. Lüpke, and F. S. Tautz, "Probing Edge State Conductance in Ultra-Thin Topological Insulator Films", Advanced Quantum Technologies 5, 2200043, ISSN: 2511-9044 (2022) 10.1002/qute.202200043.
- <sup>144</sup>K. Moors, C. Wagner, H. Soltner, F. Lüpke, F. S. Tautz, and B. Voigtlander, "Distributed Current Injection into a 1D Ballistic Edge Channel", in preparation.
- <sup>145</sup>I. S. Gradštejn and I. M. Ryžik, *Table of integrals, series and products*, 4. ed. (Academic Press, New York, 1965).

## 9. Acknowledgment

The research presented in this thesis was carried out at the Peter-Grünberg Institute (PGI-3) at the Forschungszentrum Jülich GmbH in the group of Prof. Dr. Bert Voigtländer.

First and foremost, I would like to thank my supervisor PROF. DR. BERT VOIGT-LÄNDER for his continuous, patient and always encouraging guidance. He was always available, even during his holidays, to discuss possible ways forward, addressing the challenges occurring at critical points of this study. I am very grateful for his indispensable and emphatic support during the hectic months of writing this thesis

Furthermore, I would like to thank PROF. DR. MARKUS MORGENSTERN for agreeing to be associate assessor for this thesis.

I would also like to thank PROF. DR. STEFAN TAUTZ for the opportunity to conduct my research at the PGI-3 Institute and for his comments on my research and publications.

Special thanks go to Dr. Felix Lüpke for introducing me to  $\alpha$ -Bi<sub>4</sub>Br<sub>4</sub>, our time together measuring in Oak Ridge, his support and suggestions during data analysis and drafting the publications.

I would like to thank SERHII KOVALCHUK for the close collaboration, especially for the measurements on the low-temperature four-tip STM. I would also like to thank DR. VASILY CHEREPANOV for his help with sample preparation, helpful comments, and last but not least, for building and maintaining the four-tip STMs. I also thank DR. TIMOFEY BALASHOV for many interesting discussions. Furthermore, I thank TOBIAS WICHMANN for his help with the glovebox and the ambient AFM, for calculating DFT results, and for many constructive discussions. I would also like to thank DR. SVEN JUST for sharing his experience with the four-tip STM and with anisotropy measurements. I would also like to thank all my colleagues at the PGI-3 Institute, especially PROF. DR. MARKUS TERNES. PROF. DR. CHRISTIAN KUMPF, DR. CHRISTIAN WAGNER, DR. SABINE WENZEL, JANINE LORENZ, MARK HUTTER, ABHISEK KOLE, and KEDA JIN for their time and discussions. Thank you to HELMUT STOLLWERK, FRANZ-PETER COENEN, CLAUDIA FUNK, and SILKE BEHLAU for your technical and administrative support.

Moreover, I thank Dr. Helmut Soltner at the Zentralinstitut für Engineering, Elektronik und Analytik (ZEA-1) for the FEM calculations he performed, even on short notice, and for his general advise and sharing his deep knowledge of mathematics.

At the Helmholtz Nano Facility, I thank FENGBEN XI and MICHAEL SCHLEEN-VOIGT.

I also thank Priv.-Doz. Dr. Holger Eisele for comments and suggesting literature on crystal physics. I acknowledge helpful discussions on STS with Dr. Michael Schnedler and Dr. Philipp Ebert at Ernst Ruska-Centre for Microscopy and Spectroscopy with Electrons (ER-C). Special thanks to Dr. Dorothee Rosenzweig (also at ER-C) for reading and commenting on a draft of this thesis.

I am very grateful to Dr. An-Ping Li, Dr. Saban Hus, and Dr. Hoyeon Jeon at the Center for Nanophase Materials Sciences of the Oak Ridge National Laboratory, Tennessee, USA for their extensive support during the measurements at the DOE User Facility in Oak Ridge.

At the Beijing Institute of Technology, I thank Yuqi Zhang and Prof. Dr. Zhiwei Wang for providing us with the  $\alpha$ -Bi<sub>4</sub>Br<sub>4</sub> crystals and Mingqian Zheng and Prof. Dr. Jin-Jian Zhou for DFT calculations presented in this thesis.

Finally, I would like to thank MY PARENTS for always supporting me through the good and bad times during my studies.

## A. Solving Eq. 2.50 and 2.51 for the three components of the resistivity tensor

For a bulk sample, when measuring in both in a square and in a linear, equidistant configuration, there a four different resistances, that can be measured:

$$R_{\text{line},x} = \frac{\sqrt{\rho_{yy}\rho_{zz}}}{2\pi s}$$
 (in-line for  $x$ ) (A.1)  

$$R_{\text{line},y} = \frac{\sqrt{\rho_{xx}\rho_{zz}}}{2\pi s}$$
 (in-line for  $y$ ) (A.2)

$$R_{\text{line},y} = \frac{\sqrt{\rho_{xx}\rho_{zz}}}{2\pi s}$$
 (in-line for y) (A.2)

$$R_{\text{square},x} = \frac{\sqrt{\rho_{xx}\rho_{zz}}}{\pi s} \left( 1 - \frac{1}{\sqrt{1 + \frac{\rho_{xx}}{\rho_{yy}}}} \right)$$
 (square for  $x$ )

$$R_{\text{square},y} = \frac{\sqrt{\rho_{yy}\rho_{zz}}}{\pi s} \left( 1 - \frac{1}{\sqrt{1 + \frac{\rho_{yy}}{\rho_{xx}}}} \right)$$
 (square for y). (A.4)

While, at first glance, this system appears to be overdetermined, the system is in fact underdetermined. This can be demonstrated by substituting

$$\rho_{xx} = \alpha r \tag{A.5}$$

$$\rho_{yy} = r \tag{A.6}$$

$$\rho_{zz} = \frac{\beta}{r},\tag{A.7}$$

where  $\alpha, \beta \in \mathbb{R}$ . This yields

$$R_{\text{line},x} = \frac{\sqrt{\beta}}{2\pi s} \tag{A.8}$$

$$R_{\text{line},y} = \frac{\sqrt{\alpha\beta}}{2\pi s} \tag{A.9}$$

$$R_{\text{square},x} = \frac{\sqrt{\alpha\beta}}{\pi s} \left( 1 - \frac{1}{\sqrt{1+\alpha}} \right) \tag{A.10}$$

$$R_{\text{square},y} = \frac{\sqrt{\beta}}{\pi s} \left( 1 - \frac{1}{\sqrt{1 + \frac{1}{\alpha}}} \right). \tag{A.11}$$

Obviously, the system separates into two systems, one for the linear measurement and the other for the square measurement. From both of these systems, the parameters  $\alpha$ and  $\beta$  can be determined. The third component (the parameter r in the substitution), however, has to determined by an independent measurement.

## **B.** Calibration Procedures

The calibration procedures given here are intended for the old Createc four-tip STM electronics, using a single DSP, two ADDA boards, and 16 bit DACs for the bias voltages.

#### **B.1.** Bias DAC Calibration

In the following the DACs generating the bias voltages for the four tips will be calibrated. A good calibration of the bias voltage DACs is useful for four-probe resistance measurements and necessary for STP. Furthermore, calibrated bias DACs are needed for two-probe measurements. Use a Keithley 2000 digital multimeter or a similar device with  $6\frac{1}{2}$  digits.

- 1. Set gain and offset of the bias DACs to 1 and 0, respectively.
- 2. For each bias DAC, measure the output voltage  $U_{\rm DAC}$  as a function of the voltage set in the software  $U_{\rm set}$ . To ensure a good calibration, use enough points: e.g.  $U_{\rm set} = 0\,\mathrm{V};\,\pm0.1\,\mathrm{V};\,\pm0.5\,\mathrm{V};\,\pm1\,\mathrm{V};\,\pm2\,\mathrm{V};\,\pm3\,\mathrm{V};\,\pm4\,\mathrm{V};\,\pm5\,\mathrm{V};\,\pm6\,\mathrm{V};\,\pm7\,\mathrm{V};\,\pm8\,\mathrm{V};\,\pm9\,\mathrm{V}.$  Select appropriate measurement ranges at the digital multimeter.
- 3. Plot  $U_{\text{set}}$  as a function of  $U_{\text{DAC}}$  and fit it with  $y = A \cdot x + B$ . A is then the gain, and B the offset. Note, the offset is given in mV in the old software.
- 4. Verify the quality of the calibration. Especially close to  $U_{\text{set}} = 0 \,\text{V}$ .

#### **B.2. ADC Calibration**

This calibration is needed both for four-tip transport measurements and for STP. Use a Keithley 2000 digital multimeter or a similar device with  $6\frac{1}{2}$  digits.

- 1. Set gain and offset of all ADCs to 1 and 0, respectively.
- 2. In principle, all ADCs can be measured simultaneously using the Mulitspec feature of the software, if they all connected to the same voltage source.
- 3. As a voltage source, a DAC can be used. If the electronics only features 16 bit bias DACs, another DAC (e.g. the x output of tip 1 can be used.) In any case, one mulitmeter should be used to measure the voltage  $U_{\rm set}$  applied to the ADCs to be independent of the DAC calibration.
- 4. Measure the ADC input voltage  $U_{\rm ADC}$  as a function of the voltage set in the software  $U_{\rm set}$ . To ensure a good calibration, use enough points: e.g.  $U_{\rm set}\approx 0\,{\rm V};\ \pm\,0.1\,{\rm V};\ \pm\,0.5\,{\rm V};\ \pm\,1\,{\rm V};\ \pm\,2\,{\rm V};\ \pm\,3\,{\rm V};\ \pm\,4\,{\rm V};\ \pm\,5\,{\rm V};\ \pm\,6\,{\rm V};\ \pm\,7\,{\rm V};\ \pm\,8\,{\rm V};\ \pm\,9\,{\rm V}.$  Since the

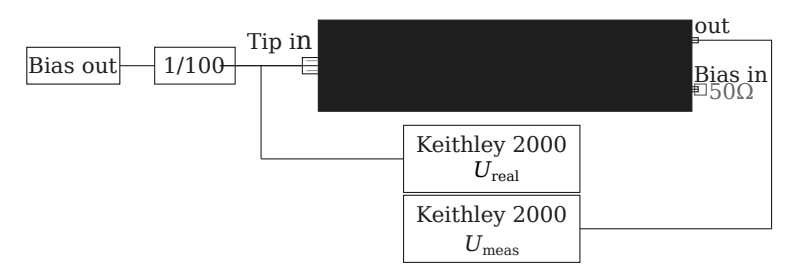


Fig. B.1.: Calibration of the voltage-probe mode of the Black Box, using a bias output DAC, 1/100 voltage divider and two Keithley 2000 multimeters.

applied voltage  $U_{\rm set}$  is measured with the multimeter, small deviations from the voltages given here are permissible. Select appropriate measurement ranges at the digital multimeter.

- 5. For each ADC, plot  $U_{\text{set}}$  as a function of  $U_{\text{ADC}}$  and fit it with  $y = A \cdot x + B$ . A is then the gain, and B the offset. Note, the offset is given in mV in the software.
- 6. Verify the quality of the calibration. Especially close to  $U_{\text{set}} = 0 \,\text{V}$ .

## B.3. Calibrating the offset of the current amplifier

The current amplifier of the Black Box also has a gain and an offset. Due to the lack of calibrated current source, only the offset can be calibrated for. This procedure requires calibrated ADCs and DACs. This calibration is necessary for STP. The gain of the Black Box is not calibrated.

- 1. Connect a  $1\,\mathrm{G}\Omega$  resistor to the tip input of the Black Box to simulate the tunnel resistance.
- 2. Measure a voltage ramp from +1 V to -1 V and back to +1 V.
- 3. Both the forward part of the ramp (FWD) and the backward part of the ramp (BWD) do not pass though  $I=0\,\mathrm{A}$ . Due to some parasitic capacitances, the two parts of the voltage ramp will not coincide. Adjust the offset of the ADC such that  $I=0\,\mathrm{A}$  is at an equal distance from both FWD and BWD.

#### B.4. Calibrating the gain of the voltage-probe mode

Each voltage follower in the Black Box has two gains and two offsets. Which one needs to be calibrated, depends on whether 100 times amplification is used. For transport-measurements, only the gains are actually relevant. STP does not use the voltage-probe mode. Use two Keithley 2000 digital multimeters or a similar devices with  $6\frac{1}{2}$  digits. The drawing in Fig. B.1 clarifies the measurement set up.

1. Switch the Black Box into the voltage-probe mode.

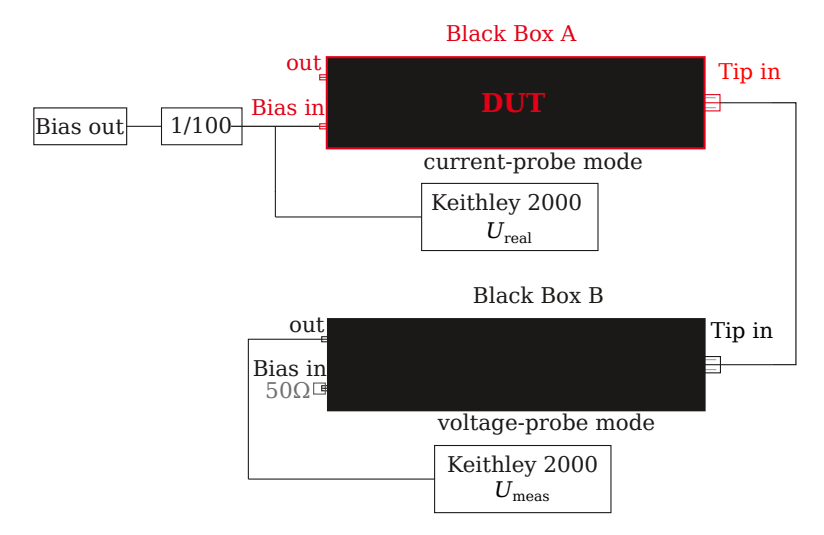


Fig. B.2.: Setup to measure  $U_{\rm bias}$  that the Black Box under testing (DUT) puts out using a second Black Box in voltage-probe mode.

- 2. Apply the voltage  $U_{\rm set}$  to triaxial input of the Black Box. Use one multimeter, to measure the  $U_{\rm set}$  in order to be independent of the calibration of the voltage source. If the 100 times amplification is used, place a 1/100 voltage divider between voltage source and Black Box, and measure  $U_{\rm set}$  after the divider. As coaxial to triaxial plug adapter, use one, that drops the guard, i.e. the inner shield.
- 3. Terminate the bias input of the Black Box with a 50  $\Omega$  resistor.
- 4. Measure the output voltage of the voltage follower  $U_{\rm VF}$  using the second multimeter at  $U_{\rm set}\approx 0\,{\rm V};\ \pm 0.1\,{\rm V};\ \pm 0.5\,{\rm V};\ \pm 1\,{\rm V};\ \pm 2\,{\rm V};\ \pm 3\,{\rm V};\ \pm 4\,{\rm V};\ \pm 5\,{\rm V};\ \pm 6\,{\rm V};\ \pm 7\,{\rm V};\ \pm 8\,{\rm V};\ \pm 9\,{\rm V}$  using the appropriate measurement ranges.
- 5. Plot  $U_{\text{set}}$  as a function of  $U_{\text{VF}}$  and fit it with  $y = A \cdot x + B$ . A is then the gain, and B the offset.
- 6. During data analysis of the four-probe transport data, the calibration factors then have to applied to the measured voltages before numerically calculating the voltage drop.

Note, if the Black Boxes with different gains are used for the voltage measurement, reading the voltage drop in differentially, using only one ADC, is impossible.

## B.5. Calibrating the offset of the bias voltage in the Black Box

If deemed necessary, also the offset of the bias voltage applied by the Black Box to the tip can be measured. This calibration can help to suppress small, spurious currents from

flowing in very conductive samples, when (nominally)  $0\,\mathrm{V}$  is applied to both current injection tips. To measure the applied bias of one Black Box, a second black in voltage probe mode is used. The calibration factors for the latter Black Box for 100 times amplification must be known. Figure B.2 displays a drawing of the measurement setup.

- 1. Switch Black Box A to be measured to current-probe mode.
- 2. Switch the measuring Black Box B to the voltage-probe mode, connect a multimeter to its output and terminate its bias input with a 50  $\Omega$  resistor
- 3. Terminate the bias input of the Black Box to be measured with a  $50\,\Omega$  resistor, as well, or connect it to the bias output of the respective tip.
- 4. Connect the triaxial inputs of both Black Boxes.
- 5. Measure the output voltage  $U_{\rm meas}$  using the second multimeter at  $U_{\rm set}\approx 0\,\rm V;\,\pm\,0.1\,V;\,\pm\,0.5\,V;\,\pm\,1\,V;\,\pm\,2\,V;\,\pm\,3\,V;\,\pm\,4\,V;\,\pm\,5\,V;\,\pm\,6\,V;\,\pm\,7\,V;\,\pm\,8\,V;\,\pm\,9\,V$  using the appropriate measurement ranges.
- 6. Plot  $U_{\text{set}}$  as a function of  $U_{\text{meas}}$  and fit it with  $y = A \cdot x + B$ . A is then the gain, and B the offset.
- 7. Adjust the offset of the bias DAC accordingly.

If during a measurement in hard contact a spurious current is observed even though all bias voltages are set to 0 V and the ADCs and DACs are well calibrated, a different method can be used. To correct the effect of the offset, change the setting of one bias output (DAC 6-9) in hard contact until there is no current flowing when 0 V are applied to both current injection tips.

## C. Contacting procedure

This procedure was used on samples of  $\alpha$ -Bi<sub>4</sub>Br<sub>4</sub> with a high resistance to ground due to the SOI substrate used ( $R \approx 500\,\mathrm{M}\Omega$ ). Depending on the resistance of the sample-to-ground connection, the response of the sample material to high current densities, and the tunneling parameters suitable for a stable tunneling contact, this procedure may need to be modified. Also note that switching the light of the optical microscope on and off can cause drift in the position of the tip. Therefore, switching the light on and off during tunneling or hard contact should be avoided. If a transport measurement is to be performed without illumination, the tip positions in tunneling contact should be checked before switching off the light to ensure accurate positioning, as the z fine piezo drives can also move the tip laterally. Also, no coarse steps should be done, while a tip is in tunneling or hard contact, if it can be avoided.

- 1. Verify that the sample is grounded.
- 2. Approach all tips into tunneling contact with e.g.  $I = 100 \,\mathrm{pA}$  and  $V_{\mathrm{bias}} = 0.3 \,\mathrm{V}$
- 3. Retract the tips a few coarse steps and move them into the desired configuration. For precise positioning, a small amplitude of the sawtooth pulse and the fine-motion piezo drives (offsets) can be used.
- 4. Sequentially approach each tip in turn into tunneling contact and verify accurate positioning and then retract it using the fine motion piezo-drive. At this point, do not keep multiple tips in tunneling contact at the same time.
- 5. Set slightly different bias voltages at the tips, so that there is never a net zero voltage difference between the sample and any given tip once the first tip is lowered into hard contact.
- 6. Approach all tips into tunneling contact, one after the other. The creep of the piezo must be allowed to decay at each tip, which takes at least several minutes. Waiting for all tips to decay can be done simultaneously to save time.

#### 7. Contacting procedure:

- a) Once no creep is visible in the Data Recorder (long term graph), retract a tip by 1 nm using the z-limiter of the control software. The tunneling current should vanish.
- b) Change the tunneling set point to a sufficiently high value, it should be at least one order of magnitude higher than the highest expected current of the four-probe transport experiment. In the Parameters window of the Createc software, it is possible to easily set  $I = 10^{-1}$  A.

- c) Change the current gain to  $\sim 10^6\,\mathrm{V\,A^{-1}}$ . Doing this after changing the setpoint will prevent the feedback loop from retracting the tip if it registers the higher amplifier noise as tunneling current
- d) Set  $V \approx 0.1 \,\mathrm{V}$  to prevent sample damage from too high a current and tip crashes of the other, still tunneling tips. (This is a precautionary measure; it may not always be necessary.)
- e) Use the z-limiter up-button to move the tip back towards the sample in steps of 1 nm or less until a visible change in the measured current can be seen: There should be sudden, step-like increase of the measured current to at least 0.01  $\mu$ A. If the sample-to-ground contact is highly insulating, this current may be hard to detect. In this case, stop after  $\sim 10$  steps ( $\sim 10$  nm) and approach a second tip.
- f) Set  $V_{\text{bias}} = 0 \text{ V}$ , and repeat for the next tip.
- 8. Once all tips are in hard contact, the quality of the contacts can be checked:
  - a) Place all tips in voltage-probe mode: The voltage should read 0. Drifting voltages indicate bad contact.
  - b) Remove the sample ground.
  - c) Place all but one tip in voltage-probe mode: The voltage-probe tips should follow the voltage of the current injection tips without any delay. Slow drift towards the applied voltage indicates bad contact of the tip.
  - d) Place the tips needed for current injection (depending on the measurement, that may comprise all four tips) in current injection mode and verify, that a reasonable current (e.g.  $1\,\mu\text{A}$ ) can be injected.
- 9. If a contact is not satisfactory:
  - a) Press more steps, or
  - b) Re-contact the tip: Remember to reconnect the sample ground and to set  $V_{bias} \neq 0 \, \text{V}!$  Experience shows, that moving the tip a little to the side (e.g. changing an offset by  $0.1 \, \text{V} \, [= 14 \, \text{nm}]$ ) and then contacting it again can lead to good contact.
- 10. The ultimate judge of good contact is the transport measurement! The voltage drop needs to attain a reasonable value (i.e. more than 1 mV peak-to-peak) and the four-probe (and perhaps two-probe) resistances must make sense.

## D. Crystal structures of Bi<sub>4</sub>I<sub>4</sub>

- Figure D.1 shows atomic models of the crystal structure of  $\beta$ -Bi<sub>4</sub>I<sub>4</sub>.
- Figure D.2 shows atomic models of the crystal structure of  $\alpha$ -Bi<sub>4</sub>I<sub>4</sub> and its AA' stacking.

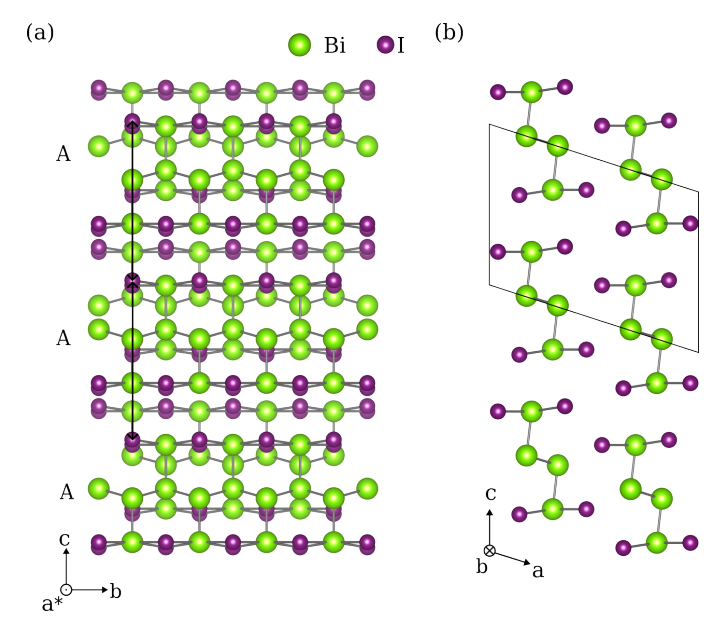


Fig. D.1.: Atomic crystal models of  $\beta\text{-Bi}_4\mathrm{I}_4$ . [13] (a) shows the projection along the lattice vector  $\underline{a}^*$ . The AA stacking is indicated using the two black horizontal arrows connecting two corresponding I atoms of two chains laying on top of each other. (b) side view of the unit cell. The unit cell is indicated in black. Note, in contrast to  $\alpha\text{-Bi}_4\mathrm{Br}_4$  and  $\alpha\text{-Bi}_4\mathrm{I}_4$ , the unit cell height corresponds to the height of a monolayer.

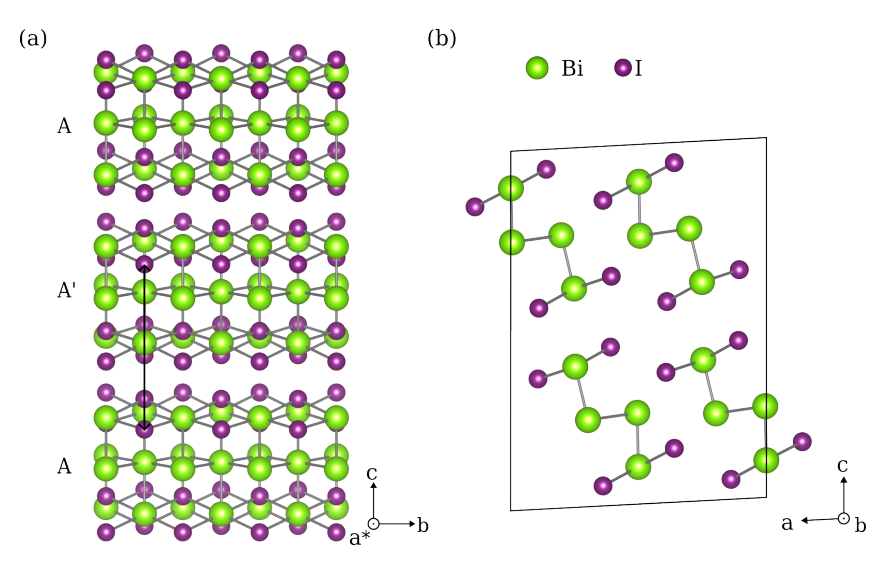


Fig. D.2.: Atomic crystal models of  $\alpha$ -Bi<sub>4</sub>I<sub>4</sub>. [13] (a) shows the projection along the lattice vector  $\underline{a}^*$ . The AA' stacking is indicated using the black horizontal arrow connecting two corresponding I atoms of two chains laying on top of each other. The AA' stacking is due to the b/2 shift present in this structure: In the ab-plane, two neighboring chains are shifted by b/2. (b) side view of the unit cell. The unit cell is indicated in black.

## E. Extended data: evaluation of the band gap of the b/3 structure

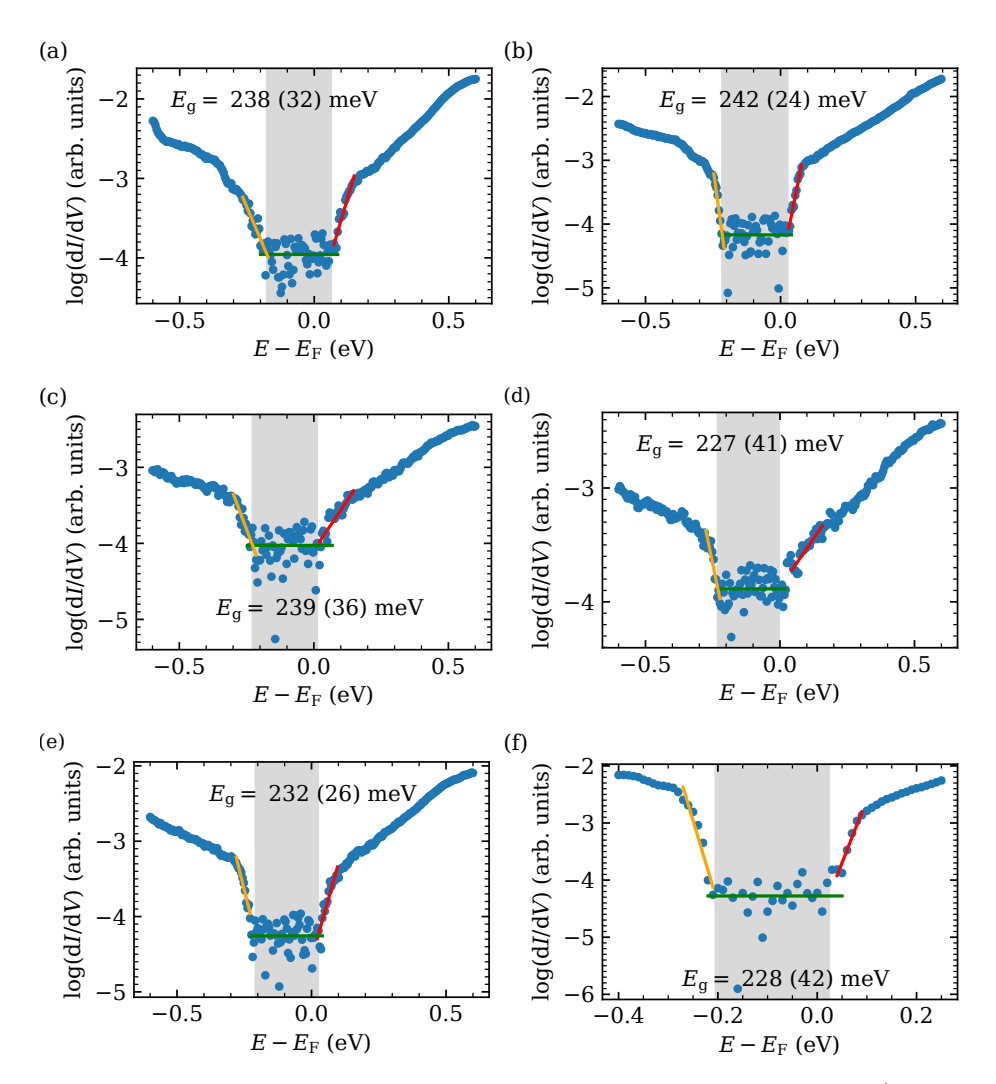


FIG. E.1.: Extended data for experimental determination of the band gap of the b/3 structure.: (a)  $I_{\rm set}=50\,{\rm pA},\ V_{\rm set}=-0.6\,{\rm V}.$  (b)  $I_{\rm set}=50\,{\rm pA},\ V_{\rm set}=-0.6\,{\rm V}.$  (c)  $I_{\rm set}=50\,{\rm pA},\ V_{\rm set}=+0.6\,{\rm V}.$  (e)  $I_{\rm set}=100\,{\rm pA},\ V_{\rm set}=+0.6\,{\rm V}.$  (f)  $I_{\rm set}=100\,{\rm pA},\ V_{\rm set}=-0.4\,{\rm V}.$ 

## F. Diagonalisation of the conductivity tensor

In the coordinate system K, the conductivity tensor of  $\alpha$ -Bi<sub>4</sub>Br<sub>4</sub> is given by [38, Chapter 11; 54, 55]

$$\underline{\underline{\sigma}} = \begin{pmatrix} \sigma_{aa} & 0 & \sigma_{az} \\ 0 & \sigma_{bb} & 0 \\ \sigma_{az} & 0 & \sigma_{zz} \end{pmatrix}. \tag{F.1}$$

The conductivity tensor in the coordinate system K' is found by rotation around  $\underline{b}$ . This is achieved by the rotation matrix

$$R = \begin{pmatrix} \cos(\phi) & 0 & -\sin(\phi) \\ 0 & 1 & 0 \\ \sin(\phi) & 0 & \cos(\phi) \end{pmatrix}. \tag{F.2}$$

The conductivity tensor in the coordinate system K' is

$$\underline{\sigma}' = R\underline{\underline{\sigma}}R^{-1}$$

$$= \begin{pmatrix} \frac{\sigma_{\text{aa}} + \sigma_{\text{zz}} + (\sigma_{\text{aa}} - \sigma_{\text{zz}})\cos(2\phi) - 2\sigma_{\text{az}}\sin(2\phi)}{2} & 0 & \sigma_{\text{az}}\cos(2\phi) + (\sigma_{\text{zz}} - \sigma_{\text{aa}})\cos(\phi)\sin(\phi) \\ 0 & \sigma_{\text{bb}} & 0 \\ \sigma_{\text{az}}\cos(2\phi) + (\sigma_{\text{zz}} - \sigma_{\text{aa}})\cos(\phi)\sin(\phi) & 0 & \frac{\sigma_{\text{aa}} + \sigma_{\text{zz}} + (\sigma_{\text{zz}} - \sigma_{\text{aa}})\cos(2\phi) + 2\sigma_{\text{az}}\sin(2\phi)}{2} \end{pmatrix}.$$
(F.3)

To find the angle  $\phi$ , by which the coordinate system has to be rotated around  $\underline{b}$  to obtain a diagonal tensor  $\underline{\sigma}'$ , the roots of the off-diagonal elements have to be considered:

$$\sigma_{\rm az}\cos(2\phi) = -\left(\sigma_{\rm zz} - \sigma_{\rm aa}\right)\cos(\phi)\sin(\phi) \tag{F.4}$$

$$\frac{\sigma_{\rm az}}{(\sigma_{\rm zz} - \sigma_{\rm aa})} = -\frac{\cos(\phi)\sin(\phi)}{\cos(2\phi)}.$$
 (F.5)

Using the multiple-angle formula  $\sin(2\phi) = 2\cos(\phi)\sin(\phi)$  [71, p. 72] the rotation angle  $\phi$  needed for diagonalization is given by

$$2\phi = -\arctan\left(\frac{2\sigma_{az}}{\sigma_{zz} - \sigma_{aa}}\right). \tag{F.6}$$

In the next step, the element  $\sigma'_{11}$  is considered.

$$\sigma'_{11} = \frac{\sigma_{aa} + \sigma_{zz} + (\sigma_{aa} - \sigma_{zz})\cos(2\phi) + 2\sigma_{az}\sin(2\phi)}{2}$$
 (F.7)

To simplify the following algebraic manipulations, only the  $\sigma_{aa} - \sigma_{zz}$ )  $\cos(2\phi) + 2\sigma_{az}\sin(2\phi)$ is considered. Plugging in Eq. (F.6) using the two identities [145, p. 48]

$$cos(arctan(x)) = \frac{1}{\sqrt{1+x^2}}$$
 and (F.8)

$$\sin(\arctan(x)) = \frac{x}{\sqrt{1+x^2}},\tag{F.9}$$

yields

$$(\sigma_{\rm aa} - \sigma_{\rm zz}) \cdot \frac{-1}{\sqrt{1 + \left(\frac{2\sigma_{\rm az}}{(\sigma_{\rm zz} - \sigma_{\rm aa})}\right)^2}} - 2\sigma_{\rm az} \cdot \frac{-\left(\frac{2\sigma_{\rm az}}{(\sigma_{\rm zz} - \sigma_{\rm aa})}\right)}{\sqrt{1 + \left(\frac{2\sigma_{\rm az}}{(\sigma_{\rm zz} - \sigma_{\rm aa})}\right)^2}}$$
(F.10)

$$= \frac{-1}{\sqrt{1 + \left(\frac{2\sigma_{\rm az}}{(\sigma_{\rm zz} - \sigma_{\rm aa})}\right)^2}} \left( (\sigma_{\rm aa} - \sigma_{\rm zz}) - \left(\frac{(2\sigma_{\rm az})^2}{(\sigma_{\rm zz} - \sigma_{\rm aa})}\right) \right) \tag{F.11}$$

$$= \frac{-1}{\sqrt{1 + \left(\frac{2\sigma_{az}}{(\sigma_{zz} - \sigma_{aa})}\right)^2}} \left( (\sigma_{aa} - \sigma_{zz}) - \left(\frac{(2\sigma_{az})^2}{(\sigma_{zz} - \sigma_{aa})}\right) \right)$$
(F.11)  
$$= \frac{1}{(\sigma_{zz} - \sigma_{aa})} \cdot \frac{1}{\sqrt{1 + \left(\frac{2\sigma_{az}}{(\sigma_{zz} - \sigma_{aa})}\right)^2}} \cdot \left( (\sigma_{aa} - \sigma_{zz})^2 + (2\sigma_{az})^2 \right)$$
(F.12)

$$= \frac{(\sigma_{aa} - \sigma_{zz})^2 + (2\sigma_{az})^2}{\sqrt{(\sigma_{aa} - \sigma_{zz})^2 + (2\sigma_{az})^2}}$$
(F.13)

$$= \sqrt{(\sigma_{aa} - \sigma_{zz})^2 + (2\sigma_{az})^2}$$
 (F.14)

Consequently, the element  $\sigma'_{11}$  is

$$\sigma'_{33} = \frac{\sigma_{aa} - \sigma_{zz} + \sqrt{(\sigma_{aa} - \sigma_{zz})^2 + 4\sigma_{az}^2}}{2}.$$
 (F.15)

The element the element  $\sigma'_{33}$  is can be calculated in a similar manner.

Thus, the diagonal tensor is

$$\underline{\underline{\sigma}}' = \begin{pmatrix} \frac{\sigma_{aa} - \sigma_{zz} + \sqrt{(\sigma_{aa} - \sigma_{zz})^2 + 4\sigma_{az}^2}}{2} & 0 & 0\\ 0 & \sigma_{bb} & 0\\ 0 & 0 & \frac{\sigma_{aa} - \sigma_{zz} - \sqrt{(\sigma_{aa} - \sigma_{zz})^2 + 4\sigma_{az}^2}}{2} \end{pmatrix}.$$
 (F.16)

## G. Extended data: Damage to flake E

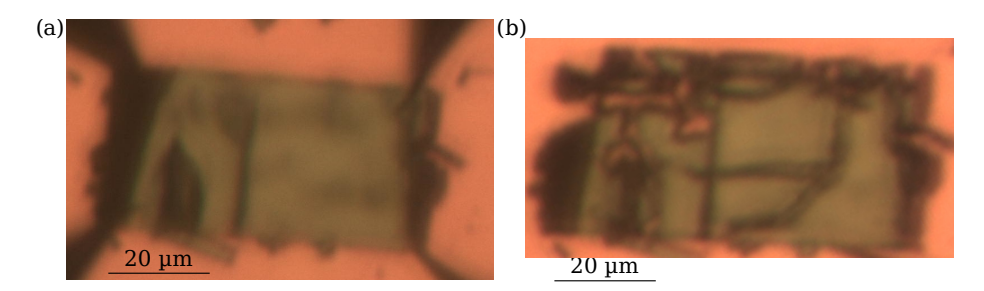


Fig. G.1.: Damage to flake E seen with the optical microscope. (a) Undamaged flake during measurement. (b) Flake E after sustaining damage from a transitory high current event.

Band / Volume 104

#### **Advances in Photoemission Orbital Tomography**

A. Haags (2024), ix, 254 pp ISBN: 978-3-95806-766-0

Band / Volume 105

## Quantitative investigation of point defects and their dynamics in focused ion beam-prepared group III-nitride lamellas by off-axis electron holography

K. Ji (2024), 164 pp ISBN: 978-3-95806-782-0

Band / Volume 106

#### NeuCoNS and Stacked-Net: Facilitating the Communication for Accelerated Neuroscientific Simulations

R. Kleijnen (2024), xx, 110, xxi-xxxiv pp ISBN: 978-3-95806-788-2

Band / Volume 107

#### **Construction of a Spiking Network Model of Macaque Primary Visual**

Cortex: Towards Digital Twins

A. Kurth (2024), xvi, 207 pp ISBN: 978-3-95806-800-1

Band / Volume 108

#### Spin selectivity of chiral molecules on surfaces

M.R. Safari (2025), xiv, 165 pp ISBN: 978-3-95806-810-0

Band / Volume 109

## Redox-based Random Access Memory Arrays for Computing-In-Memory and Neuromorphic Computing

H. Chen (2025), x, 154 pp ISBN: 978-3-95806-814-8

Band / Volume 110

#### Mechanics of deep neural networks beyond the Gaussian limit

K. Fischer (2025), xvi, 138 pp ISBN: 978-3-95806-815-5

Band / Volume 111

#### Characteristics of plastically deformed fcc and bcc High-Entropy Alloys

T. Meenen (2025), x, 115 pp ISBN: 978-3-95806-820-9 Band / Volume 112

## Software-Configurable Analog-To-Digital Converters for Configurable Pulse Detection

L. Krystofiak (2025), xvii, 113 pp, xxix

ISBN: 978-3-95806-826-1

Band / Volume 113

#### Development of Superparamagnetic Based Biological Sensor for the Detection of Brucella DNA Using Frequency Mixing Magnetic Detection

A. Abuawad (2025), X, 129 pp ISBN: 978-3-95806-836-0

Band / Volume 114

## A System for the Cryogenic Power Management of Quantum Computing Electronics: Development, Integration, and Test

A. R. Cabrera Galicia (2025), xxv, 110, lviii pp

ISBN: 978-3-95806-844-5

Band / Volume 115

## Investigation of 2D Materials using Low Energy Electron Microscopy (LEEM)

H. Yin (2025) viii, 137 pp ISBN: 978-3-95806-848-3

Band / Volume 116

## Topotactic phase transition in La<sub>0.6</sub>Sr<sub>0.4</sub>CoO<sub>3- $\delta$ </sub> thin films: oxygen content, dynamics and reversibility

S. He (2025) ix, 137 pp ISBN: 978-3-95806-868-1

Band / Volume 117

## Electrical anisotropy and shear-resistant topology in the quasi one-dimensional van-der-Waals material $\alpha$ -Bi<sub>4</sub>Br<sub>4</sub>

J.K. Hofmann (2025) xv, 129 pp ISBN: 978-3-95806-869-8

Weitere Schriften des Verlags im Forschungszentrum Jülich unter http://wwwzb1.fz-juelich.de/verlagextern1/index.asp

Information Band / Volume 117 ISBN 978-3-95806-869-8

